N°d'ordre NNT : 2019LYSEC010

THESE de DOCTORAT DE L'UNIVERSITE DE LYON
opérée au sein de
l'Ecole Centrale de Lyon

Ecole Doctorale n° 34
Ecole Doctorale Matériaux de Lyon

Spécialité de doctorat : Physique des Matériaux

Soutenue publiquement le 16/04/2019, par :

Marco Vettori

Growth optimization and characterization of regular arrays of GaAs/AlGaAs core/shell nanowires for tandem solar cells on silicon

---

Devant le jury composé de :

HARMAND Jean-Christophe	Directeur de Recherche CNRS, C2N Palaiseau	Président
MARIETTE Henri	Directeur de Recherche CNRS, I. Néel/CEA Grenoble	Rapporteur
DURAND Olivier	Professeur, I. FOTON, INSA Rennes	Rapporteur
KAMINSKI-CACHOPO Anne	Professeure, IMEPH-LAHC/PHELMA Grenoble	Examinatrice
PLISSARD Sébastien	Chargé de Recherche CNRS, LAAS Toulouse	Examinateur
GENDRY Michel	Directeur de Recherche CNRS, INL ECL Ecully	Directeur de thèse
FAVE Alain	Maitre de conférences, INL INSA Lyon	Co-Directeur de thèse

In loving memory
of my grandfather
Dario Devescovi,
who taught me
to be meticulous,
and rigorous,
and to love my work.

Contents

Acknowledgements

The work reported here has taken almost three and a half years of my life, as well as the effort and help of many people without whom it would not have been possible to achieve it. I would therefore like to thank them all most sincerely.

Firstly, I would like to express all my deepest gratitude and affection for my supervisors, Michel Gendry and Alain Fave, who have granted me the privileges of enjoying their trust, learning from them and benefitting from their knowledge, and who have undertaken the task of following my work through all these years and correcting my manuscript. Working under their leadership has been one of the best experiences not only of my career but also of my whole life, because Michel and Alain have always shown me great fairness, respect and humanity, three important qualities which unfortunately are not always present in the relationship between supervisors and subordinates. For all these reasons I hope to carry with me the spirit that has characterized the collaboration with them wherever I go, and that they can be proud of what I will do in the future, because any future achievement of mine will be obtained also thanks to them.

I sincerely want to thank the members of my thesis jury for having accepted the task of reading my manuscript and evaluating my work: Jean-Christophe Harmand from C2N, for accepting to be examiner and president of the jury. Henri Mariette from Institut Néel and CEA Grenoble, and Olivier Durand from Institut FOTON and INSA Rennes for being my thesis reporters. Sébastien Plissard from LAAS, and Anne Kaminski-Cachopo from IMEP-LAHC, for having accepted to be examiners of this work.

I acknowledge the direction of INL, Catherine Bru-Chevallier and Christian Seassal, for making it possible for me to be hired and for the support provided to my research activity.

The research work here reported could be carried out only thanks to the technical, financial and theoretical support of several INL research groups. Therefore, I want to thank the leaders of the Heteroepitaxy and Nanostructures group, Guillaume Saint-Girons and Alexandre Danescu, for the financial support of my PhD work, in particular in the last months. Also, I would like to thank Alexandre Danescu for its valuable help in the development of the model proposed by Michel and for the theoretical study of our results: together with Michel and Alain he has been an inspiring figure, and I feel privileged to have collaborated with him. José Penuelas, for all his help in the interpretation of our results and for his support during our collaboration, as well as for his friendliness. Philippe Regreny, for the difficult task of repairing and maintaining operative the reactors, for all the fruitful discussions and suggestions in the HETONAN project, for the help in the preparation of patterned substrates at INL, but in particular for his adrenaline injection! I will always be grateful to Jean-Baptiste Goure, “oncle JB”, for his kindness and profound humanity as well

as for all the maintenance and reparations of the UHV compartments, and to Claude Botella, for all his help in the MBE reactor automating and in the interpretation of the XPS spectra, the last task having been carried out with Genevieve Grenet, whom I also thank. Hervé Dumont, for teaching me how to use SEM. Romain Bachelet, Yves Robach and Bertand Vilquin for their support in the H&N group.

I also want to thank the Photovoltaic group with which I have worked a great deal and in which I have been integrated in the last months of my PhD work. Erwann Fourmond, leader of the photovoltaic group, for the financial support in the last months of my research work. Céline Chevalier, for her precious help in the fabrication and development of the cell technology, and also for the development of patterned substrates at INL. Fabien Mandorlo, for his theoretical contribution and related simulations. Danièle Blanc-Pélissier, for the help with the laser. And Mustapha Lemiti and Mohamed Amara, for their kindness and their suggestions.

I also would like to thank people from other groups who made my work possible. Xavier Letartre, for the financial support provided in the last months. Jean-Louis Leclercq, for the access to the Nanolyon platform. Nicolas Chauvin, for all the PL analysis and the fruitful discussions about the optoelectronic properties of the nanowires. Emmanuel Drouard, for his simulations. Cécile Jamois, for all the precious help provided at the SEM.

The technical team played a fundamental role in my research: without them my work would have not been possible at all. Therefore, I would like to thank Aziz Benamrouche for AFM analysis, Radek Mazurczyk and Brice Devif for the help during the fabrication steps, Solène Brottet for helping me at SEM and for realising the thin lamellae by FIB, and Joëlle Grégoire and Jordan Ndong Abessolo for the access to the instruments at INSA.

I would like to thank Sylvie Goncalves for her patience in answering my numerous questions and acting as a tax consultant, and Patricia Dufaut, for the nice conversations had while brushing our teeth, and for enduring me as “her worst nightmare”. I am also grateful to Bénédicte André, Thérèse Martin, Emmanuelle Foltzer, Virginie Lagarde, Raphaël Lopez and Laurent Carrel for all the administrative and informatics support provided in these years.

As supported by ANR, the HETONAN project was carried out in collaboration with other French groups. I want therefore to thank our partners at C2N: Jean-Christophe Harmand, for the fruitful discussion and his boundless knowledge of nanowires. Gilles Patriarche, for all the TEM analysis of our nanowire samples. Andrea Cattoni, for providing the patterned substrates and for the fruitful discussions about them. A special mention should be reserved to three other persons at C2N, to whom I am not only grateful for their cooperation but whom I also appreciate very much for their kindness and deep humanity: Andrea Scaccabarozzi, whose contributions in both the experimental work and the discussion of the results were essential. Maria Tchernycheva, without whom I would never have been able to work on this project since she was the first person to inform me of the existence of this PhD

position at INL, and who helped us out considerably in the optoelectronic characterization of our core-shell nanowires. Valerio Piazza, who carried out the EBIC measurements and who explained to me the mechanisms and the principles of this technique. I also want to thank our partners at IMEP-LAHC, who carried out optical and electronic simulations to define the proper geometric parameters of our tandem cell; in particular, I want to acknowledge Anne Kaminski-Cachopo for her kindness and helpfulness, as well as Vladimir Maryasin.

I must definitely thank all the PhD students and post-docs who shared their company with me in these years making me feel like at home in Lyon. Ali, who kept my spirits up with fully-balanced Italian curses and with whom I shared many bottles of whisky. Thomas, diner of spaghetti eaten together at 2 pm to prevent hangover and narrator of interesting tales about Tahiti. Eirini, μια φάτσα μια ράτσα, whose contagious laughter has often given me a good mood. Rahma, person of great determination and kindness: she has my full support to become president of Tunisia. Louise, whom I especially thank for letting me hear the song "Libertine." François, who is probably the best dancer in Lyon. Hà My, whose ability to tolerate all my jokes at all times is a sign of her great friendship with me, for which I am very grateful. Alberto, who has immediately aroused my instinctive sympathy. Milan, with whom I was immediately in tune thanks to our Balkan spirit, and with whom I share the love for history and rakija. Michele, to whom I say “Caro amico, fatti un campo di nanofili tutto tuo, che ti fai la crana”. Li Xiao, whom I thank for the precious help during the manufacture step of the solar cell. Nelly, for all the interesting philosophical discussions. I also want to thank Mohamed and Dong, fellow travellers in the adventure of the doctorate. To all of you I wish the best and hope you have a bright future, whatever you decide to do.

Two of the doctoral students I met at INL have become so important to me that they deserve a separate thank you, because their friendship is a cornerstone of my life. Nasser and Li Hui became my best friends in Lyon, and despite the distance which separates us the bond between us is still very strong, and for that I am grateful.

Undoubtedly, I have to acknowledge my family for all the moral and material support given to me over these years, without which not a single page of this manuscript could have been written: the things they have done to help me are so many and so important that they cannot be summed up here. Therefore, I simply say thanks for everything to my parents Oscar and Antonella, and to my grandmother Irene Giuditta.

Finally, the most important thanks of all: to Guan Xin. For everything that has happened to us since I met her.

Introduction

Nowadays one of the main issues that the nations of the planet are facing is the development of cheap and sustainable technologies for energy harvesting, so as to supply their constantly increasing need for energy while minimizing the negative impact on the environment. This research is an issue of enormous importance not only from the scientific and technological points of view, but also from the geopolitical, military and economic profiles. It is thus clear the importance that renewable energy sources have recently acquired in the global scenario.

In this context, photovoltaics (PV) undoubtedly appears as one of the preferential solutions, being a more available and more versatile approach than others (e.g. wind farming or geothermal or hydroelectric energy), due to the fact that it can be employed not only in massive production plants, but also on domestic (or even device) scale. Ultimately, photovoltaics has all the potential to represent an effective and elegant answer to a complex issue.

For this reason, many efforts have been spent in the last decades both to reduce the cost of the devices and to improve their performances. Most of the PV technology for commercial uses is currently based on crystalline Si (c-Si), a low-cost material whose properties have been very well investigated and mastered for decades. As a matter of fact, fabrication costs of c-Si PV modules drop from 4 $ in 2008 to less than 0.3 $ now per Watt-peak,[1] corresponding to an energy cost below 0.2 €/kWh and a grid parity within a large part of Europe. However, this drastic improvement in competitiveness is coming to a limit and some new directions should be investigated.

Regarding the reduction of the material cost, much attention has been paid to the use of alternative materials to replace Si, which currently dominates the market thanks to its large availability and cheapness but whose intrinsic properties prevents significant increases in cell efficiency. Among the alternative materials, we can mention for example CIGS (copper indium gallium selenide) alloys, organic materials and perovskites. Nevertheless, all of them have shown intrinsic limitations which prevent them to replace silicon in commercial applications. As far as CIGS materials are concerned, although relatively affordable, they do not present efficiencies as high as those ones of traditional Si cells. Organic materials are particularly interesting for the possibility of achieving flexible devices, but their photoconversion efficiencies and life times are not comparable to those ones of Si cells. Perovskites have been arousing great interest in the PV sector, thanks to high efficiency performances. However, the short life time of these materials due to their organic nature and their highly eco-unfriendly Pb-based composition still restrict their use to the development of prototypes only.

In this context, a further cost reduction for devices based on Si requires to overcome its maximum theoretical efficiency limit (29.1 %),[2,3] which is due to different physical loss mechanisms. The best approach to increase the PV cell efficiency would consist in the development of multi-junction (MJ) solar cells, whose fundamental principle is to connect in series several sub-cells made of different materials with different band-gaps. Multi-junction structures, usually fabricated using a combination of III-V alloys as upper cells and Ge substrate as bottom cell, present the advantage of reducing the losses caused by thermalization. Notwithstanding, the costliness of Ge substrates or wafer bonding techniques still restrict their use to a narrow field of applications, e.g. in photovoltaics under concentrated light or in the aerospace industry.

A simple way to reduce the cost is to develop bottom cells based on Si substrates, which also offers the advantages of a well-established manufacture. In the case of a tandem cell with Si as bottom cell and top cell having a band-gap of 1.7 eV, efficiencies up to 41.9% can be theoretically achieved.[4] In the last years, many efforts have been devoted to obtaining this kind of structure, and several materials have been employed to realise the top cell, e.g. perovskites[5,6] and III-V alloys,[7] although these generally require very complex architectures.

Therefore, a monolithic approach based on heteroepitaxy may appear as the most convenient to integrate III-V top cells on Si substrates. However, it must be considered that the high lattice mismatch between the two materials would cause the presence of misfit and threading dislocations acting as recombination centers for carriers, thus decreasing the performances of the cells.

A possible solution to this issue could come from the use of nanowires (NWs) in the photovoltaic domain: already employed with promising results in the development of single-junction cells, thanks to their peculiar structural and optoelectronic properties, they may also constitute an alternative approach to overcome the drawbacks of the III-V/Si integration and potentially lead to the achievement of cheap yet highly efficient tandem solar cells.

Based on these considerations, we developed the French ANR funded project HETONAN (http://inl.cnrs.fr/projects/hetonan/) to achieve a prototype of tandem solar cell based on ordered arrays of $Al_{0.2}Ga_{0.8}As$ NWs (top cell) monolithically integrated on Si (bottom cell) via molecular beam epitaxy.

The results of the last three years of experimental work in this regard are reported in this thesis as follows:

Chapter 1: The background and state of the art of III-V photovoltaics and of its integration on Si are briefly presented, with particular attention to the chronological evolution of the issue. After that, we expose thoroughly the evolution and state of the art of the NWs-based single junction cells, before introducing the most important theoretical studies developing the concept of NWs-based tandem solar cells on

Si. This is followed by the presentation of the only tandem solar cell prototype so far achieved, and finally by the definition of our targeted cell.

Chapter 2: The second chapter concerns the solid-source molecular beam epitaxy (ss-MBE). After introducing the salient concepts of its principles, we describe our experimental setup and the Reflection High Energy Electron Diffraction (RHEED) technique we have used to calibrate the V and III element fluxes and to follow the growth of NWs *in situ*.

Chapter 3: The experimental results achieved during this thesis are started to be reported in this chapter. After introducing the general principles of the vapour-liquid-solid (VLS) assisted MBE growth of III-V NWs and the main theoretical models so far developed, we present our experimental results concerning the self-assisted growth of GaAs NWs on epi-ready Si(111) (as a preliminary step for the further development of core/shell structures). Firstly, we expose the influence of the growth temperature and the role of the Ga pre-deposition on the NW growth. Then, we conducted a very thorough study on the impact of the incidence angle of the Ga flux on the self-assisted GaAs NW growth, with particular attention to the NW length and diameter. In order to better explain these experimental results, we report on a semi-empiric growth model and numerical simulations (performed in our group by A. Danescu) to better explain the influence of the incident angle of the Ga flux on the self-assisted growth kinetic of GaAs NWs.

Chapter 4: Our work continues with the presentation of the results achieved in the growth of core/shell $Al_{0.2}Ga_{0.8}As$-based NWs on epi-ready Si substrates, a preliminary step before switching to patterned substrates. The first part is dedicate to present our attempts to achieve the axial growth of $Al_{0.2}Ga_{0.8}As$ NWs on epi-ready Si substrates (the originally targeted structures), and to explain the reasons of our failures. Subsequently, we treat the growth of core/shell NWs and we expose the results concerning the growth and structural characterization of p-n GaAs core/shell NWs and of p-GaAs/p.i.n-$Al_{0.2}Ga_{0.8}As$ core/shell NWs. A second part is dedicated : 1- to the characterization of the optoelectronic properties of these core/shell NWs and of the study of the "passivation" shell by photoluminescence (PL), and 2- to the study of the p-n and p-i-n junctions by Electron Beam Induced Current (EBIC) (performed by the partner group of M. Tchernycheva at C2N).

Chapter 5: This chapter deals with the growth of self-assisted core/shell NWs on patterned substrates. Firstly, we present the results of the numerical simulations performed by the partner group of A. Kaminski-Cachopo at IMEP-LAHC to define the optimal parameters of the top cell. Then, we present the results concerning the selective pre-deposition of Ga to form ordered arrays of Ga droplets as a necessary condition to grow ordered arrays of self-assisted NWs with GaAs core.

Subsequently, we present the growths of NWs performed on patterned substrates (provided by A. Cattoni from C2N) with a focus on our protocol, which allows achieving remarkably high vertical yields of both GaAs NWs and p-core GaAs/ p.i.n-$Al_{0.2}Ga_{0.8}As$ shell NWs thanks to a soft thermal pre-treatment of the patterned substrate before the NW growth. Then we present a TEM characterization of these NWs and an EBIC study of the p-i-n junctions. Finally, we show the first results obtained on substrates patterned at INL and, based on these results, we advance a hypothesis to explain the role of the thermal pre-treatment in determining high vertical yields.

Chapter 6: This last chapter shows the preliminary results obtained in the fabrication process undertaken to achieve the targeted tandem solar cell. We firstly expose some preliminary results concerning the fabrication of the Si bottom cell and the general process to develop the architecture of the targeted tandem solar cell. Then, we show the results concerning the encapsulation of NWs, which is eventually performed with polymer resine BCB after experiencing failures with inorganic compound HSQ. Finally, we conclude by presenting the results achieved in the NW top contacting with ITO by magnetron sputtering.

We reported also two annexes: a brief summary of the characterization techniques employed (Annex 1) and an additional document by A. Danescu to provide more insights about the simulation work (Annex 2).

1 State of the art of photovoltaics and the potential of nanowires in the new generation of solar cells

1.1 State of the art of photovoltaics

Among all the possible options in the field of "green energies", photovoltaics (PV) is for sure the one which draws most of the attention, thanks to the possibility to exploit a stable and *de facto* unlimited source. The main consequence of this interest has been a continuous quest to increase the competitiveness of the PV cells on the energy market, which lead to good results in terms of costs. As a matter of fact, fabrication costs of PV modules drop from 4 $ in 2008 to less than 0.3 $ now per Watt-peak[1]. As these costs appear to reach a limit for Si modules, it follows that the only way to increase the competitiveness of the PV technology is to enhance its efficiency, so as to increase the power delivered per m^2.

1.2 Si-based photovoltaics

Most of the PV technology for commercial uses is currently based on crystalline Si, a low-cost material whose properties have been very well investigated and mastered for decades. Nevertheless, the efficiency of high-quality commercial modules is still slightly less than 20 %. In order to achieve higher performances, many efforts in the latest years have been devoted to the development of prototypes,[8] and promising results have been reached in this field. For example, in 2014, Masuke et al obtained a cell efficiency η equal to 25.6 %,[9] a result approached one year later by Adachi et al with a device providing η = 25.1 %.[10] Smith et al reached η = 25.2 % in 2016,[11] although the current efficiency record of 26.6 % is held by Yoshikawa et al (at Kaneka corporation) since 2017.[12] However, in spite of these remarkable performances, the further development of this technology is intrinsically affected by the maximum theoretical efficiency limit reachable by a Si-based cell, better known as Shockley-Queisser limit and corresponding to η = 29.1 %.[2,3]

As a consequence, researchers have been focusing on materials other than Si to push the efficiency beyond the Shockley-Queisser limit.

1.2.1 Multi-junction solar cells

The best approach to increase the efficiency would consist in the development of multi-junction (MJ) solar cells, whose fundamental principle is to connect in series several sub-cells

made of different materials with different band-gaps. This allows collecting photons from a broader range of wavelengths of the solar spectrum, with remarkable enhancement of the performances (Figure 1.1). The theoretical maximum efficiency of a MJ cell composed by an infinite number of sub-units would be indeed around 87 %,[4] and experimental results obtained so far are also very promising, the current efficiency records in the field of MJ cells (and generally speaking of all PV) being held by 3- and 4-junction cells (η = 44.4 and 46 %, respectively) under concentrated sunlight (508 suns).[8]

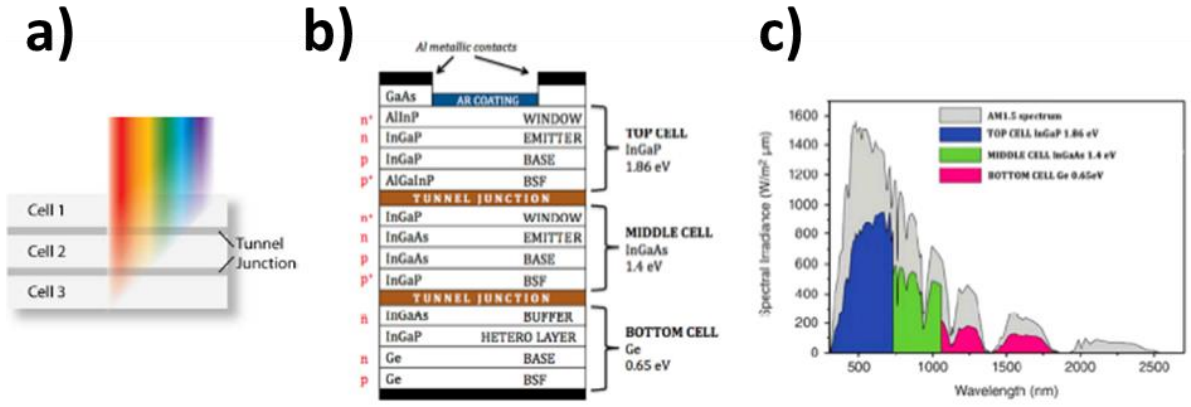

Figure 1.1. (a) Schematics of the main concept of a MJ cell. (b) Schematics of the structure of a 3-junction cell. (c) Graph of spectral irradiance as a function of the wavelength over a 1 sun AM 1.5G solar spectrum. The maximum electricity conversion efficiency for each junction as a function of the wavelength is also reported.[13]

Nevertheless, the production of MJ cells presents some problematic aspects. Indeed, the different sub-cells must be connected in series by tunnel junctions which are quite difficult to design and produce, because the electrical characteristics of each individual junction must be matched, and the values of photo-generated currents should be as close as possible in each junction. Since the optimal materials for this purpose are the III-V semiconductors, much more expensive and difficult to process than Si, the drawbacks of MJ-based systems are a high complexity and high material and manufacture costs. As a consequence, MJ cells are currently unsuitable for mass production and limitedly utilized to specific applications such as aerospace and concentrated photovoltaics (CPV) plants, whereas they are not adopted for commercial uses and to replace the Si-based cell technology. Thus, a different approach to increase efficiency in the PV market is still needed.

1.2.2 III-V semiconductor/Si planar tandem solar cells

A feasible solution to the cost issues related to MJ cells has come from the possibility of developing III-V semiconductor/Si planar tandem solar cells (TSC). These can be defined as hybrid systems consisting of only two different sub-units connected in series by a tunnel

junction: a bottom cell made of Si and a top cell made of III-V materials, as schematized in Figure 1.2.

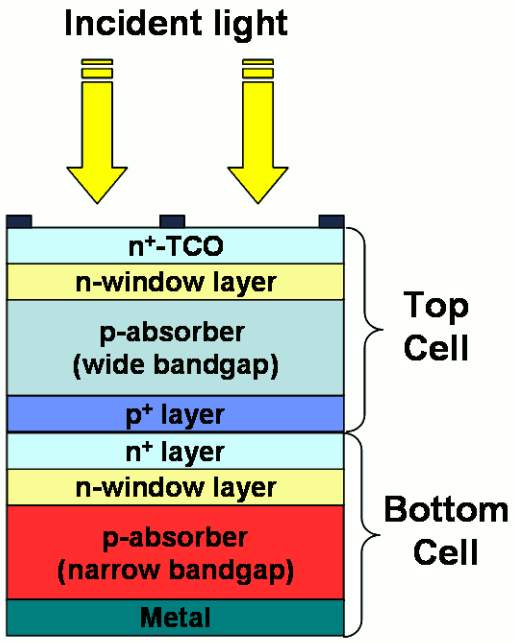

Figure 1.2. Schematics of a TSC.[14]

The purpose of such a configuration is still to exploit the solar radiation more efficiently, yet employing a cheap substrate. Although a double junction implies less efficiency than in a MJ system, the low cost of Si substrates, their well-established manufacturing and the lower complexity of the device can make TSC more advantageous than MJ cells for commercial uses. Theoretical calculations showed indeed that TSCs can largely exceed the Shockley-Queisser limit of Si cells, their maximal efficiency having been estimated around 42 % for planar devices under 1 sun illumination.[4] The choice of III-V semiconductors as constituents of the top cell is not accidental, but due to the fact that the optimal band-gap for this sub-unit is 1.7 eV,[15] and III-V ternary or quaternary alloys (like GaAsP, AlGaAs, InGaN, GaAsPN and others) can provide for this function, since their composition can be tuned to achieve this value.

Based on these considerations, a monolithic approach based on heteroepitaxy may appear as the most convenient to integrate III-V top cells on Si substrates. However, it must be considered that the high lattice mismatch between the two materials would cause the presence of misfit and threading dislocations acting as recombination centers for carriers, eventually decreasing the performances of the cells. Moreover, since the growth of polar III-V materials on non-polar Si would originate other structural defects such as anti-phase domains, the direct epitaxy process turn out as extremely challenging and has not been resolved until now.

The solution to this problem may consist in the introduction between the two sub-units of a buffer layer, which is expected to be optically transparent and thin enough to actually exploit the Si substrate as bottom cell, and also conductive enough to reduce the series resistance.[16] In 2005 Geisz et al achieved a conversion efficiency of 5.2 % with open circuit voltage (V_{OC}) equal to 1.53 V under 1 sun AM 1.5G on a $GaN_xP_{1-x-y}As_y$/Si TSC, in which the adoption of a buffer layer of diluted nitrides ($GaN_{0.02}P_{0.98}$) made most of the III-V layers nearly lattice-matched to the Si substrate.[17] A similar result was obtained three years later by Ager et al thanks to an InGaN/Si TSC with an AlN buffer layer,[18] a configuration adopted also by Train et al, who achieved V_{OC} = 1.52 and η = 7.1 % in 2012.[19] However, the current efficiency record for a monolithically integrated III-V/Si planar system was achieved in 2007 by Geisz et al, with a $GaAs_{0.7}P_{0.3}$/Si TSC providing η = 9.8 % under 1 sun AM 1.5 G thanks to a buffer layer whose composition changes progressively from $GaAs_{0.07}P_{0.93}$ to $GaAs_{0.63}P_{0.37}$.[20]

Despite the introduction of buffer layers, experimental results are evidently inferior to theoretical expectations. Although efficiencies above 16 % were obtained by other groups,[21,22] it should be noticed that in these cases both top and bottom cells were made of III-V materials, Si being used just as substrate for the growth and not as PV-active component. Moreover, the performances achieved by this type of devices were still lower than those ones of Si-based commercial modules and this fact lead to reconsider the monolithic approach in favour of other methods.

In such a context, post-growth wafer bonding turned out to be the most promising technique. This approach generally consists in growing the III-V top cell on GaAs (or other III-V substrates), so as to prevent dislocations caused by lattice mismatch. Subsequently, the top cell is removed by epitaxial lift-off (usually by wet etching) and fusion bonded on the Si bottom cell. The whole procedure can be carried out at relatively low temperature, so as to minimize the number of defects at the interface and prevent cracks due to the different thermal expansion of Si and III-V materials,[23] and as a matter of fact it has led to much more performing devices than those obtained by monolithic approach. In the above-quoted article, Dimroth et al compared the results obtained for two GaInP/GaAs TSCs on Si substrates prepared by wafer bonding and by epitaxial growth (Figure 1.3): it was thus observed that, although the cells had formally the same structure, conversion efficiencies were as high as 26 and 16.4 %, respectively.[22]

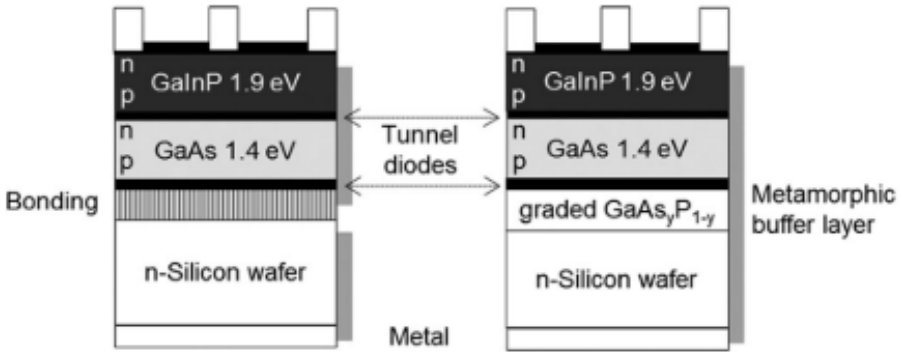

Figure 1.3: Schematics of the two GaInP/GaAs TSCs realized by Dimroth et al on Si substrates.[22] Although the structure is formally the same, the cell prepared by wafer bonding showed much higher efficiency (26 %) than the monolithic one (16.4 %), realised with a metamorphic buffer layer.[22]

Thanks to wafer bonding, significant improvements were observed also for TSCs with Si bottom cells. In 2003, Taguchi et al almost equalled the efficiency of commercial modules with a GaAs/Si TSC providing η = 19.4 %,[24] whereas in 2012, Tanabe et al surpassed Si-based commercial modules realising an AlGaAs/Si TSC exceeding 25 % efficiency.[25] However, the most important result so far achieved in this field was realized in 2017, as Essig et al developed two 4-terminal GaInP/Si and GaAs/Si TSCs (Figure 1.4), with efficiency equal to 32.4 and 32.8 %, respectively.[7] Such an outcome is particularly significant not only because it sets a new high efficiency record, but also because it is the first example of III-V/Si TSCs actually capable to overcome the Shockley-Queisser limit of Si.

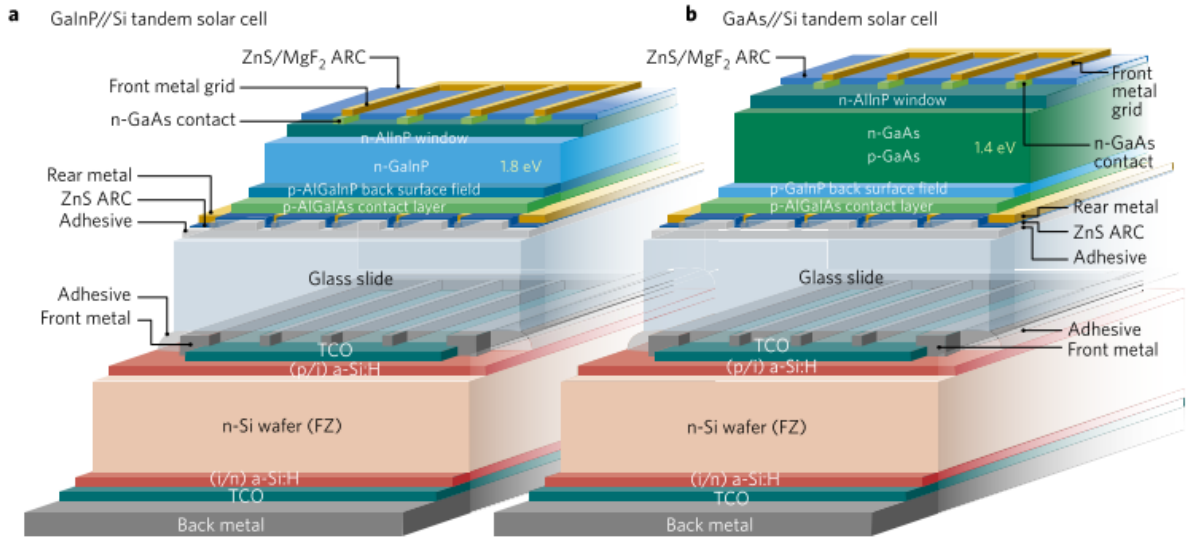

Figure 1.4. Schematics of (a) GaInP/Si and (b) GaAs/Si TSCs realised by Essig et al in 2017.[7] These devices, with η = 32.4 and 32.8 %, respectively, provided the current efficiency record for III-V/Si TSCs and are the first example of such a cell overcoming the Shockley-Queisser limit of Si.

Despite this very remarkable result, the cost of such a device would still be too high if compared to conventional Si cells. As a matter of fact, this is estimated as one order of magnitude higher than for commercially available Si cells, the disparity being caused by the high cost of GaAs wafers and of the epitaxy of III-V solar cell stacks. Moreover, its integration in mass production appears difficult because of the 4 terminals, whereas devices adapted for commercial uses generally consist of 2-terminals technology. As a consequence, these problems set once again the question which triggered the quest for innovation, i.e. how to combine higher performances with low costs?

The solution, as shown in the next paragraphs, might come from dismissing the concept of planar TSC to embrace the opportunities offered by unidimensional structures.

1.3 The role of nanowires in photovoltaics

Thanks to their high aspect ratio, nanowires (NWs) are *de facto* unidimensional nanostructures whose electronic, optoelectronic, mechanical and thermal properties are much different from those of their corresponding two-dimensional (2D) and bulk materials, and because of this peculiarity they have been object of studies in many fields. The interest aroused by those nanostructures involves also energy harvesting, due their potential use in photovoltaics and water splitting.

As far as photovoltaics is concerned, in the last two decades a lot of attention has been paid to research on NWs,[26–30] since solar cells based on these nanostructures have indeed some potential benefits over planar devices. These advantages consist mainly in superior electronic and optoelectronic properties, capacity of strain relaxation, effective charge separation and cheapness. Therefore, although NW-based solar cells are not meant to exceed the thermodynamic efficiency limits of corresponding planar devices, they still do represent a chance to closely approach those limits.

As a consequence, many prototypes of NW-based PV devices have been realized with a large variety of materials, such as Si,[31] Ge,[32] metal oxides,[33–36] II-VI semiconductors[37–39], nitrides[40] and also combination of NWs and polymers[41–43], without forgetting to mention all the solar cells based on III-V NWs that will be discussed in paragraph 1.3.2.

1.3.1 The benefits of unidimensional nanostructures

If we look into the microscopic nature of photovoltaics, we can see that the conversion of sunlight into electricity is a process consisting of many consecutive steps such as photon absorption, carrier generation, carrier separation and finally carrier collection. Therefore,

minimizing all possible causes of losses in every step is the keystone to optimize performances. As already mentioned in the previous paragraphs, one of the main drawbacks in thin-film technology is the high density of structural defects at the interface between Si and III-V materials which act as recombination centres for the free carriers. This issue can be overcome thanks to NWs. As a matter of fact, semiconductor NWs show a very high degree of crystallinity even when grown on highly mismatched substrates, since these free-standing nanostructures are capable to release the stress induced by the lattice mismatch through elastic relaxation on their surface,[44,45] as shown in Figure 1.5, and also to prevent the formation of anti-phase domains. Small foot print and strain accommodation are also extremely eligible characteristics during the integration process, since they can prevent the risk of cracks which may occur as a consequence of the different thermal expansion coefficients.[16]

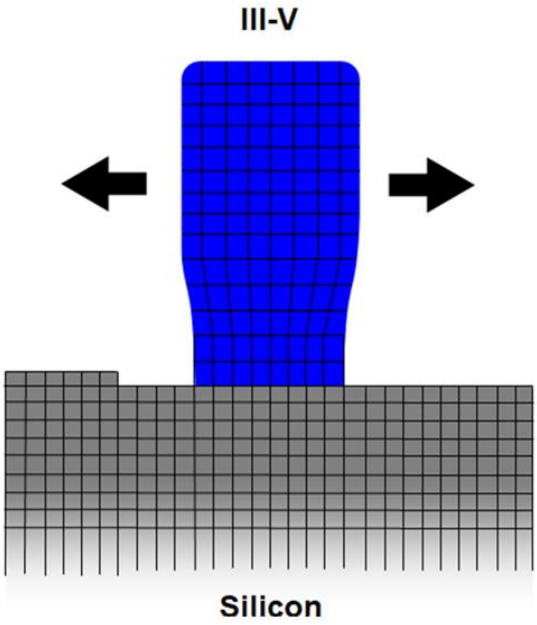

Figure 1.5. Schematic of a free-standing III-V semiconductor NW on Si substrate; the strain induced by lattice mismatch is released through elastic relaxation at the NW surface, and the formation of anti-phase boundaries is prevented.

The contribution of NWs in the improvement of PV performances is not limited to the prevention of structural defects, but it involves the rest of the steps of the photogeneration process. As a matter of fact, another very important characteristic of NWs is the possibility to strongly reduce the so-called absorption losses: these can be divided into losses caused by reflection, in which not all photons enter the semiconductor being reflected from the surface, and transmission losses, in which part of the photons passes through the active region without causing carrier separation.

Reflection losses can constitute an extremely serious issue for PV considering that most of the semiconductors would reflect from 10 to 50 % of the sunlight,[46] and since reflection

originates from a difference in refractive index between two media[47], the most common solution to this problem is to provide a cell with coatings whose refractive indexes are intermediate between that one of the semiconductor and that one of the air.[48] Although this approach is widely used in the fabrication of planar cells, it is still not that efficient since every layer can completely prevent reflection only for a single wavelength at normal incidence, thus being less effective for the rest of the spectrum. However, if we consider that an ideal coating should have a continuously graded refractive index to be totally anti-reflective, NWs appear indeed close to this ideal case thanks to the fact that they actually show a gradual change in it. As a matter of fact, experiments carried out on different types of semiconductors (e.g. c-Si, GaN, GaAs, InP, GaP, Ge, CdS) eventually proved that NWs are actually capable to reduce drastically the reflection of light.[38,49–55]

In the case of transmission losses, the main advantage of NWs is the possibility for these nanostructures to act as a resonant light trap:[56–58] while random arrays of semiconductor NWs can act as strong scattering and resonance centres,[59] ordered arrays of structures benefit also from diffraction effects, collective resonance and changes in the optical density of states,[60] thus further reducing absorption losses and their detrimental effects.

Although absorption issues are potentially very detrimental for the PV process, they still do not constitute the biggest threat for the cell efficiency, as the main cause of losses in the photocurrent generation process is normally related to the second step, i.e. the carrier formation, in which carrier-phonon coupling can waste from 30 to 40 % of the incident sunlight.[61] As far as planar cells are concerned, the solution to this problem could consist in employing materials with optimal band-gap, which can be obtained by tuning the composition of semiconductor alloys. However, this possibility is strongly limited in the case of planar films by the fact that many 2D alloys can be subject to miscibility gaps and strain-induced defects. On the contrary, NWs can overcome the miscibility gap induced by strain, thanks to the possible strain relaxation, thus offering the chance to achieve completely tuneable compositions at will.[62]

Finally, further benefits can occur during the last phase of the PV process, i.e. the carrier collection by the electrodes, when the NW geometry can provide rapid radial large separation and efficient carrier collection through band conduction.[63]

Apart from potentially enhancing the PV efficiency by increasing the material quality and performances, all the above-mentioned properties can contribute also in lowering the cost of solar cells. The reason for cost reductions lies mainly in the reduced amount of material needed to fabricate a device due to the shorter NW growth times compared to those of equivalent 2D layers, the better absorption properties of NWs, as well as in the wider choice of eligible semiconductors offered by the possibility of easily tuning the band-gap.[60] However, the most attractive aspect of this kind of nanostructures is perhaps the possibility of achieving defect-free monolithic integration via bottom up synthesis on substrates as chip as Si, a characteristic which can significantly reduce the overall cost of a PV cell. Based on

these considerations, a strong impetus was given to the development of prototypes of NW-based PV cells: the main achievements in this field will be summarized in the next paragraph.

1.3.2 State of the art of single junction NW solar cells

Generally speaking, NWs can be classified according to the type of p-n (or p-i-n) junction, which constitutes the PV active region of these nanostructures, and can be distinguished into axial or radial, depending on whether it is located respectively along the NW length or diameter, as shown in Figure 1.6.

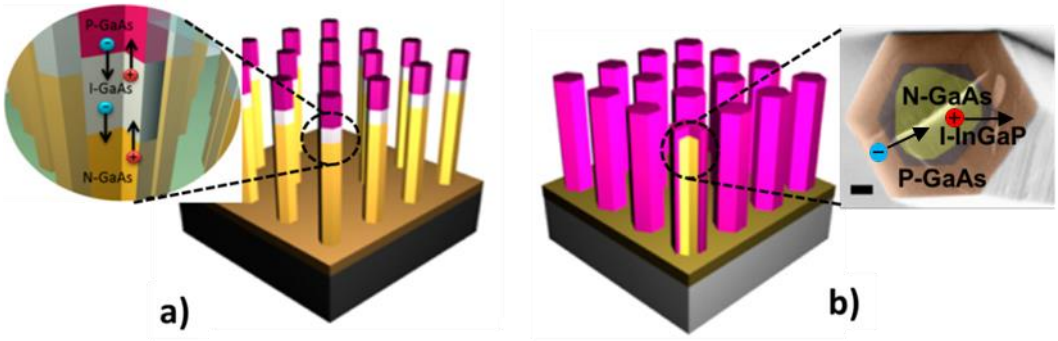

Figure 1.6. Schematics[64] of NWs with axial (a) and radial (b) p-i-n junction (right inset from Tegude et al[65] to exemplify a cleaved core/shell structure in top view).

NWs with radial junctions are commonly reputed as the most performing ones for PV applications, because apart from all the benefits offered by 1-D nanostructures they can also take advantage of a high charger collection efficiency due to the fact that the charge separation occurs along the shortest dimension of the NWs, thus making the carrier collection distance comparable to the minority carrier diffusion length.[63] Moreover, radial junctions are also more tolerant of the presence of defects[60] and surface states[66] than the axial ones, providing also a bigger PV active region at the same NW diameter.

On the other hand, although NWs with axial junctions do not benefit from these factors, they offer some advantages which make them still attractive as building blocks for solar cells, since according to a study conducted at Povinelli's group[64] they can provide higher open circuit voltage (V_{OC}) and more flexibility in designing the structure of the junction than radial ones. Moreover, theoretical comparisons showed that radial junctions are expected to be more tolerant to doping variation and capable to provide quite stable performances in terms of current density (J_{SC}), V_{OC} and η even on doping ranges as big as two orders of magnitude (10^{16}-10^{18} cm^{-3}), not omitting that thanks to the possibility of employing lower doping levels (< 10^{17} cm^{-3}) they lower the risk of reduced carrier mobility and diffusion, thus providing margin for optimization and robust design.[64]

These opposite considerations, together with the fact that the choice of the type of structure may be influenced by the versatility of the material and the fabrication technique adopted, have caused a flowering of theoretical and experimental studies aimed at the realization of NW-based solar cells based either on radial or axial single junctions.[29,61,62,64-91] As a consequence, the history of the research in this field records numerous important results, of which the most prominent ones are summarized below.

In 2007, Lieber's group at Harvard University succeeded in the purpose to obtain solar cells based on individual Si NWs with a p-i-n radial junction. Those nanostructures proved to be capable to achieve individually energy conversion efficiencies up to 3.4 % and maximal power outputs of 200 pW under 1 sun AM 1.5G illumination.[67] Moreover, the authors investigated in detail the role of the intrinsic layer in the junctions by comparing the I(V) curves of p-n and p-i-n structures: the results are extremely important since they show that p-i-n junctions have a better ideality factor in forward bias and a much larger breakdown voltage in reverse, which suggests the presence of lower tunnelling or leakage currents than in their p-n counterparts. These characteristics (later found also in GaAs NWs[77]) make p-i-n NWs much more performing as diodes and thus more suitable for the fabrication of solar cells.

Although very interesting under the aspect of the fundamental properties of NWs and constituting a milestone in the history of this topic, this study was nevertheless very far from the concept of solar cells based on a NW array. This was put into practice for the first time one year later thanks to the pioneering work of LaPierre's group, which fabricated a solar cell based on a disordered array of GaAs NWs with a radial p-n junction grown by molecular beam epitaxy (MBE) on GaAs(111) substrate via Au-assisted vapour-liquid-solid (VLS) growth:[70] the choice of such material was widely motivated by the fact that thanks to his band-gap of 1.42 eV, it has the best-matching absorption with solar spectrum among semiconductors.[94] Despite the poor cell performance in terms of efficiency (0.83 % under 2.6 suns illumination) caused by the lack of optimization due to the originality of the structure, this study constituted a very impressive results since it demonstrated the feasibility of a novel approach, thus becoming indeed the first in a long series of works.

In 2009, Goto et al extended the range of semiconductors with a 7.0 x 2.6 mm^2 solar cell based on InP NWs grown on the same substrate by Metal Organic Vapour Phase Epitaxy (MOVPE) and including a radial p-n junction (Figure 1.7).[72] Some of the interesting points of this research (which eventually broke the 1 % efficiency barrier reaching η = 3.37 % under 1 sun AM 1.5G illumination) consist in the use of selective area growth so as to obtain ordered arrays of NWs, which are expected to have better light trapping properties than the unordered ones,[60] and of a transparent resin for encapsulating the NWs so as to protect them from mechanical stresses. Another remarkable result was achieved in the same year by Fontcuberta's group at EPFL with a solar cell based on individual GaAs NWs with a radial p-i-n junction showing efficiency equal to 4.5 %,[55] thus exceeding Lieber's previous record.

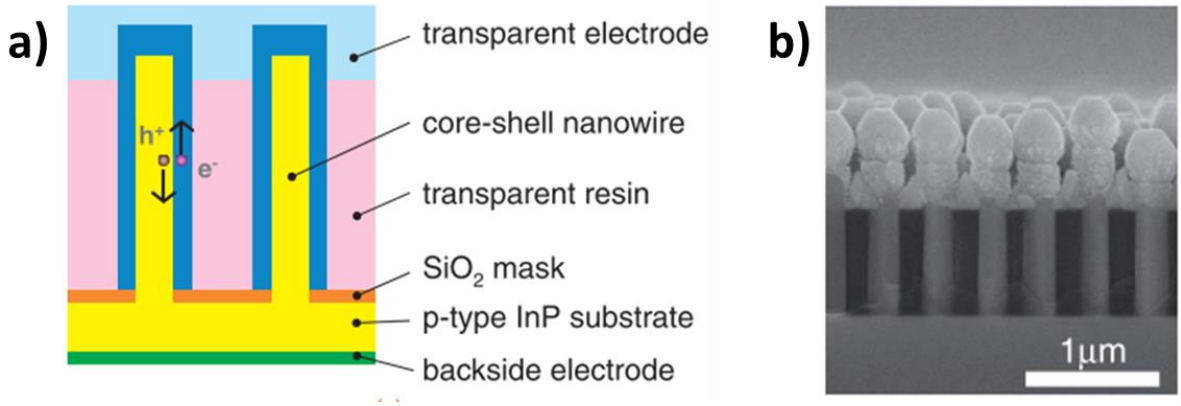

Figure 1.7. (a) Schematics of the solar cell developed by Goto et al. and (b) cross-sectional SEM image of the device in question.[72]

Afterwards, Garnett and Yang applied the concept of ordered arrays to Si NWs and in order to exploit the enhanced light trapping properties offered by relatively long nanostructures they developed a solar cell based on 8 µm long NWs on an area equal to 16 cm^2 which reached efficiency above 5 %.[31] Apart from the remarkable efficiency which constituted a new record at that time, the element of novelty in that work is the use for the first time of a top-down approach, the NWs having been obtained by deep reactive ion etching (RIE) of a n-doped Si wafer, and subsequently doped by boron diffusion so as to form radial p-n junctions.

In 2011, Mariani et al at Huffaker's group succeeded in fabricating the first example of PV devices based on an 0.25 mm^2 ordered array of catalyst-free GaAs nanopillars with a radial p-n junction grown on a GaAs substrate by Selective-Area Metal Organic Chemical Vapour Deposition (SA-MOCVD).[78] Although the efficiency of 2.54 % under 1 sun AM 1.5G illumination is lower than those ones previously achieved by other groups mentioned above, this work is nevertheless noteworthy because by tripling the result of LaPierre's first cell, it shows the importance not only of ordered arrays but also of Au-free nanostructures: as a matter of fact, the diffusion of Au into the NWs originates mid-gap trap states which degrade the minority carrier lifetime and diffusion length not only in Si[95,96] but also in GaAs,[97–99], thus diminishing the process efficiency.

The research at Huffaker's group provided further results between 2012 and 2013, when Mariani et al adopted for the first time a higher band-gap passivation shell of InGaP so as to suppress surface recombinations in ordered arrays of radial n-i-p GaAs NWs grown by catalyst-free SA-MOCVD on a GaAs substrate.[92] However, the passivation shell was not the only element of novelty introduced by this study: as a matter of fact, in order to determine the optimal parameters of diameter and pitch so as to maximize the absorption, the authors performed simulations taking into account an encapsulation by a benzocyclobutene (BCB) layer and a transparent conductive indium-tin-oxide (ITO) layer as top contact, this being a quite original innovation considering that until then simulations had been performed only on

bare NW structures.[100,101] Moreover, thanks to the sputtering deposition and thermal annealing of Ti/ITO on the NW tips, the authors were capable to obtain a good ohmic contact at the top of the cell and this measure, added to the previous one, eventually allowed them to achieve an efficiency equal to 6.63 % on a PV cell as broad as 0.25 mm^2. Such a solar cell configuration was used also in a later work, in which Mariani et al showed the possibility to exploit the appreciable optical focusing effect originated by the dome-shaped ITO layer obtained on the NW tips by a conformal sputter deposition so as to attenuate light reflection from the surface, thus increasing the PV efficiency up to 7.43 %.[82]

Apart from Mariani's works, the two-year period 2012-2013 turned out to be very productive for the research in the field of NW-based solar cells also because four different groups proved to be able of breaking the barrier of 10 % efficiency with different materials. The first remarkable result came from Samuelson's group at Lund University, where a 1 mm^2 broad ordered array of InP NWs with axial p-i-n junction was epitaxially grown on the same material; after removing the Au nanoparticles used as catalyst from the top of the NWs by wet etching, so as to reduce light reflection, the manufacturers were finally able to obtain a device with η = 13.8 % (Figure 1.8).[84] However, the high efficiency was not the only considerable aspect of this work, since the cell showed significant performances also in terms of J_{SC} and V_{OC}; in particular, the former proved to be as high as 83 % of that for the best performing InP planar cell (despite only 12 % of surface coverage), whereas the latter one was even higher than in the planar counterpart.

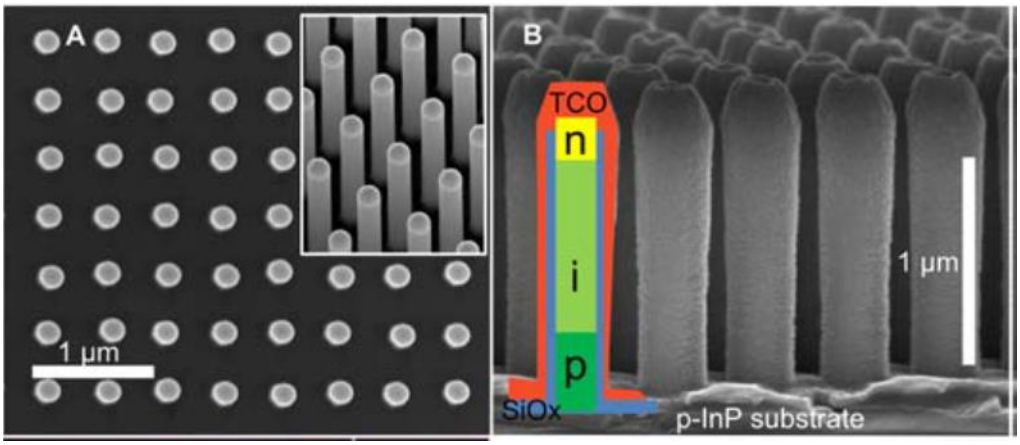

Figure 1.8. (a) Top view SEM image of the ordered array of p-i-n InP NWs (inset tilted 30°). (b) SEM image and schematics of the NWs after fabrication.[84]

The second important work consists in a study which shows the possibility to obtain efficiencies above Shockley-Queisser limit with single NWs.[93] As a matter of fact, Krogstrup et al report the fabrication of a PV device constituted of a single GaAs NW epitaxially grown by MBE on a Si substrate, encapsulated with a SU-8 photoresist and top-contacted with ITO, having efficiency as high as 40 % with J_{SC} and V_{OC} equal to 180 mA/cm-2 and 0.43 V, respectively, on an area of $1.42 \cdot 10^{-9}$ cm^{-2}. Although obtained on a single NW, such a result is

undeniably remarkable, and in order to explain it the authors advanced the hypothesis that the high efficiency is caused by the significant light concentration due to the fact that the absorption cross-section of NWs is several times larger than their physical cross-section. This explanation eventually appeared consistent with the results of their Finite Difference Time Domain (FDTD) simulations, proving that light absorption in a single NW can be enhanced from 10 to 70 times than in a thin film of the same material. Apart from the extremely high efficiency, this study introduced other original aspects, being not only the first example of device obtained with a free-standing NW, but also the first case in PV history of III-V NWs epitaxially grown on Si substrates, a result achieved thanks to the catalyst-free (or self-catalysed) method previously developed by Fontcuberta et al[102] (cf. Chapter 3). These results opened up the possibility of a direct integration of III-V NWs on Si overcoming the drawbacks due to Au incompatibility with this substrate[103] and to its detrimental effect on NW optoelectronics.[99]

The third main contribution was achieved by Holm et al at the University of Copenhagen, with a PV device made of a single $GaAs_{0.8}P_{0.2}$ NW with radial p-i-n junction grown by MBE and achieving η = 10.2 %.[85] Beside the performance, this is the first example of a NW-based cell made of a ternary alloy, $GaAs_{0.8}P_{0.2}$, having been chosen for its band-gap (1.7 eV), which made it a candidate for the possible development of a NW-based TSC in the future. Moreover, this work stands out once again the importance of passivation shells (also in this case InGaP) to prevent the surface recombination of the carriers, a precaution which eventually turned out to be crucial for improving the cell performances according to the authors.

The importance of reducing the defects at the interface was further demonstrated by the fourth work, carried out by Cui et al in Eindhoven and consisting in the fabrication of a 0.25 mm^2 PV device based on InP NWs with axial p-n junction epitaxially grown in a regular array on InP substrate by MOVPE with Au as catalyst.[86] The peculiarity of this study consists in the quest for reducing the parasitic radial growth on the NW side facets, which causes short circuit shunting paths as well as the presence of non-radiative recombination centers on the NW surface. This purpose was achieved by a sidewall etching, performed both *in situ* adding HCl to the precursors during the MOVPE synthesis, and *ex situ* dipping the NWs into piranha solution after the growth: such a procedure eventually leads to PV devices providing 11.1 % efficiency.

The research continued in the following years. In 2014, Yao et al from Povinelli's group were the first to introduce axial rather than radial p-i-n junctions in ordered arrays of GaAs NWs.[64] Thanks to the optimization of the junction geometry the authors were then able to develop a solar cell showing η = 7.58 % over a 1 mm^2 area, a lower value if compared to other prototypes but still a record for devices based on GaAs NWs and which appears even more remarkable considering that the nanostructures in question were grown without passivation shell. The importance of the latter one was put in evidence once again one year

later, as Aberg et al from Samuelson's group fabricated a 1 mm^2 broad cell with ordered arrays of GaAs NWs with axially p-n junction grown by Au-assisted MOCVD on GaAs substrates:[89] As a matter of fact, thanks to the addition of a radial AlGaAs passivation shell to suppress surface states, the manufacturers were eventually able to develop a device showing 15.3 % efficiency and V_{OC} equal to 0.906 V under 1 sun AM1.5G illumination. Such a result is extremely important not only because it constituted a new efficiency record but also because it showed how a passivation shell allowed to double the result obtained by Yao et al on a similar device with yet non-passivated NWs.

The last important progress so far realised in terms of high performances dates to the end of 2016 and comes from Bakkers' group. Here van Dam et al fabricated a solar cell made of NWs with axial p-n junction obtained by dry etch of InP substrate (Figure 1.9).[91] Drawing inspiration from the above-mentioned works at Huffaker's group, their research also focuses on the role played by Indium-Tin Oxide as top-contact layer for the NWs: as a matter of fact, one of the problem introduced by this material is the light reflectance due to the high refractive index, which can strongly reduce absorption. By controlling the size and shape of the deposited ITO it is nevertheless possible to reduce the reflection. This approach allowed the authors to fabricate a 0.25 mm^2 PV device with 17.8 % efficiency under 1 sun AM1.5G illumination: such a value is remarkably high, and beside being comparable to the best performances of III-V single junction planar cells,[8] it also consists in the highest efficiency record so far achieved by a NW-based solar cell.

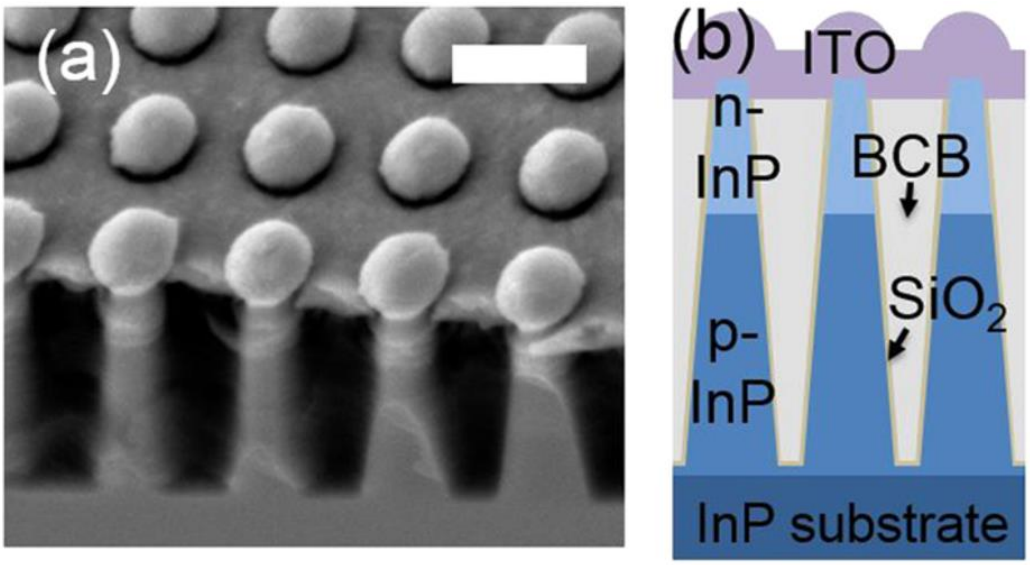

Figure 1.9: (b) SEM image of the cleaved solar cell (tilt angle 30°; white scale bar corresponding to 500 nm). (b) Schematics of the device.[91]

The results summarized here above do not only represent a remarkable progress in the scientific research about NW-based single junction solar cells themselves, but they also form a robust background for that one about TSCs, which can benefit from the experience

acquired in the former field. Based on these considerations, the main topic of this thesis can be finally introduced.

1.4 III-V semiconductor NW tandem solar cells on Si substrates

When it comes to NW-based TSCs, it is necessary to distinguish between two different concepts: those devices made of a dual junction inside the NWs themselves, i.e. without a PV-active substrate, and those ones constituted by a NW-based top cell coupled to a substrate working as bottom cell.

In the first case both junctions are located inside the NWs, which can consist either of Si[104] or III-V semiconductors,[105] whereas the substrate plays no role in photogeneration, acting just as a support for the nanostructures.

In the second case, III-V NWs contain only one junction and are connected in series to the Si substrate, provided with the second active zone. This configuration is *de facto* the nanostructured counterpart of the III-V/Si planar solar cells, and appears particularly attractive for the chance to exploit the technology of Si manufacturing, cheap substrates and coupling between 1.7 and 1.1 eV band-gap to maximize the photoconversion. Such a configuration is also the subject of this thesis, therefore from now on when we mention NW-based TSCs we refer only to those cells with a NW-based top cell and a substrate-based bottom one.

As mentioned at the end of the previous paragraph, it was the development of NW-based single junction solar cells which triggered the idea of employing these nanostructures to fabricate TSCs by monolithic integration of III-V semiconductors on Si substrates. In particular, the driving force of this process was the above-mentioned possibility for NWs to release the mismatch-induced strain via surface relaxation, thus preventing the formation of structural defects at the interface which deteriorate the performances of planar TSCs.

Based on these considerations, the concept of III-V NW-based TSC was finally proposed by LaPierre in 2011: in an article which became a milestone of the research in this topic,[106] the author described the configuration of such a device and provided a first estimation of its performances. The results of this work are briefly summarized in the next paragraph to provide a general example of the general characteristics and properties expected from this type of devices.

1.4.1 Theoretical maximum efficiency of NW tandem solar cells

In his work, LaPierre conceived the geometry of the system as a radial p-i-n junction in NWs of $GaAs_{0.77}P_{0.23}$, having a band gap of 1.7 eV, connected to the p-doped Si substrate through a p+/n+ tunnel diode. The NW structure is approximated to a cylindrical rod and a silica mask separates the n- and i-shells of the NWs from the p-doped substrate, which includes a n-doped emitter to form the PV-active region (see Figure 1.10).

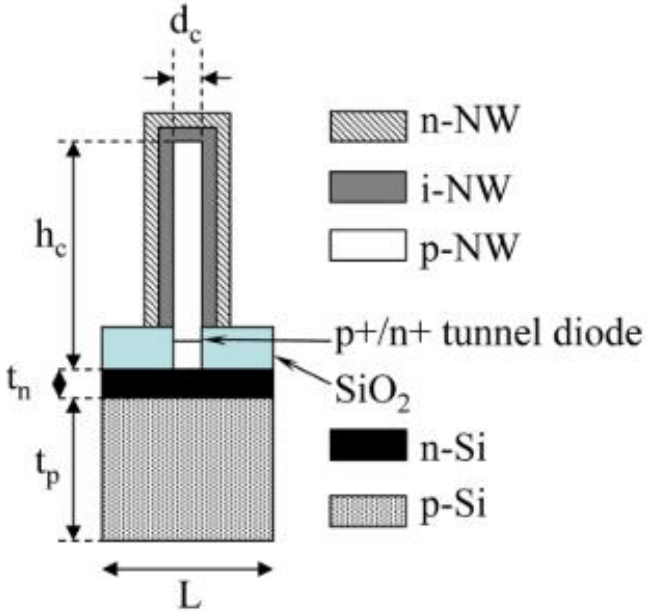

Figure 1.10: Schematics of the NW geometry (not to scale) adopted by LaPierre to model his NW-based TSC.[106]

The author solved numerically the continuity and Poisson equations in the single NW to obtain the photoconversion efficiency and the J(V) curve of the cell by employing the COMSOL Multiphysics code. The parameters adopted in the simulation are reported in Table 1.1.

Parameter	Description	Nominal values
d_c	p-doped NW core diameter	44 nm
h_c	p-doped NW core height	740 nm
$t_{nw\text{-}i}$	NW i-shell thickness	16.5 nm
$t_{nw\text{-}n}$	NW n-shell thickness	21.5 nm
t_n	n-doped Si emitter thickness	50 nm
t_p	p-doped Si base thickness	400 μm
μ_n	NW electron mobility	402 $cm^2/V{\cdot}s$
μ_p	NW hole mobility	4.9 $cm^2/V{\cdot}s$
τ_{nw}	SRH recombination lifetime in NW	2.5 ns
τ_{Si}	SRH recombination lifetime in Si	1 ms
D	Donor- and acceptor-like surface trap density	10^{12} cm^{-2}
S_{nw}	NW surface recombination velocity	3000 $cm{\cdot}s^{-1}$
S_{Si}	Si surface recombination velocity	10 $cm{\cdot}s^{-1}$
n_i	NW intrinsic carrier concentration	1.3×10^4 cm^{-3}
$N_{d,nw}$	NW donor concentration (n-doping)	5×10^{18} cm^{-3}
$N_{a,nw}$	NW acceptor concentration (p-doping)	5×10^{18} cm^{-3}
$N_{d,Si}$	Si donor (emitter) concentration	10^{20} cm^{-3}
$N_{a,Si}$	Si acceptor (base) concentration	10^{16} cm^{-3}
L	Diameter of substrate surrounding NW	200 nm
G	Illumination	1 Sun, AM 1.5G 500 Suns, AM1.5D

Table 1.1: Parameters used by LaPierre to model his NW-based TSC.[106]

It is noteworthy that the donor and acceptor concentrations in the NW were both set equal to $5{\cdot}10^{18}$ cm^{-3}, whereas the intrinsic shell was supposed to be also n-doped at 10^{16} cm^{-3} in consequence of the really occurring background doping.

In order to offer a comparison between a totally ideal case and a non-ideal one, the author investigated the properties of a cell with both perfectly and imperfectly passivated NW. In the first case, he assumed the lack of nominal donor and acceptor surface traps and a NW surface recombination velocity (S_{NW}) equal to zero; in the second, the surface trap density D was set equal to 10^{12} cm^{-2} and S_{NW} equal to 3000 cm s^{-1}.[107] The results of the simulations for these structures (assuming 1 sun AM1.5 G illumination) are reported in Figure 1.11. The bottom cell shows J_{SC} = 19.4 mA cm^{-2} and V_{OC} = 0.67 V, whereas the response of the top cell is J_{SC} = 20.8 or 20.5 mA cm^{-2} and V_{OC} = 1.27 or 1.23 V for the perfectly or non-perfectly passivated case, respectively: this is consistent with the presence of surface recombinations and depletion in non-perfectly passivated NWs, which reduce the performances of the top cell.[77]

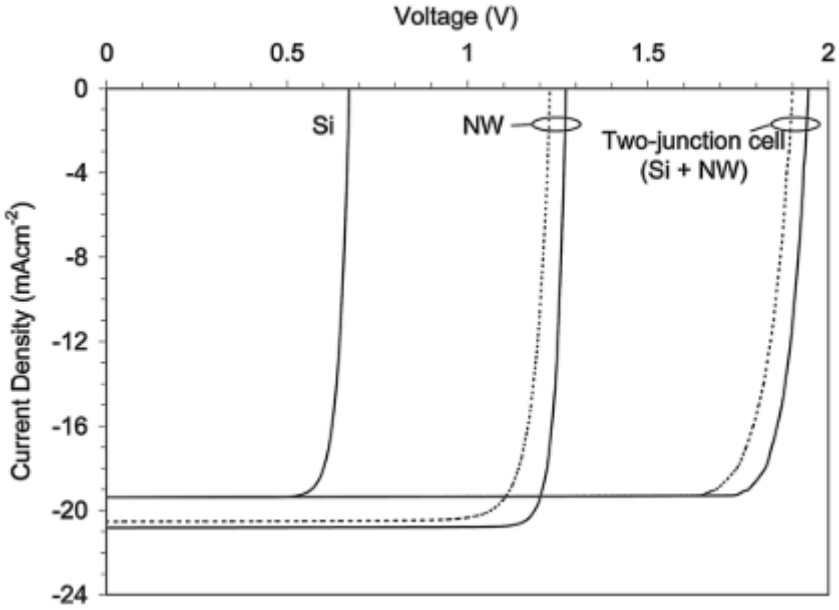

Figure 1.11: J(V) behaviour for bottom, top and tandem cells simulated by LaPierre. The dashed lines correspond to a perfect NW passivation (D = 0; S_{NW} = 0), while the solid one to an imperfect one (D = 10^{12} cm^{-2}; S_{NW} = 3000 cm s^{-1}).[106]

As far as the tandem device is concerned, it should be noticed that the overall J_{SC} is limited by the smallest short-circuit current generated by one of the sub-units (in this case the bottom one) and therefore is equal to 19.4 mA cm^{-2}, in line with what is expected for two cells connected in series. For the same reason, the overall V_{OC} of the tandem cell corresponds on the contrary to the sum of those ones provided by each sub-unit, thus being equal to 1.94 and 1.90 V for the perfectly and non-perfectly passivated case, respectively.

These J(V) curves determine quite the high fill factor (FF) and efficiencies, with FF = 0.90 and η = 33.8 % (FF = 0.87 and η = 32.1 %) for the perfectly (non-perfectly) passivated cell. Such a result is very encouraging, because it shows that a NW-based TSC can potentially overcome the Shockley-Queisser limit of Si-based cells and offer performances comparable to those ones expected from planar TSCs, plus all the benefits that 1D nanostructures offer over their 2D counterparts, particularly in terms of costs.

Although this study was limited to the theoretical calculation of the maximal limiting efficiency and did not consider all the possible sources of non-ideality (e.g. contact resistance, Auger losses and thermal effects), it definitely served as starting point for other works aiming at determining which is the effective efficiency value that can be reasonably expected in a NW-based TSC. As a matter of fact, in the following years several works were fulfilled with the aim to evaluate the performances which can be expected from real devices.

1.4.2 Estimation of the efficiency in a real case

The first step in this direction was carried out once again by LaPierre et al with a new study focusing on the effects of a square array of NWs with radial p-i-n junction.[108] In this case, the aim of the authors was to optimize the cell efficiency by finding the best condition to obtain a favourable current matching between the two sub-units. In order to do so, they fixed the NW length (L) at 5 μm and calculated the optimal diameter (D) and period (P) for different band-gaps. The numerical simulations were performed assuming a hexagonal rather than circular NW section so as to be closer to real cases, despite the fact that no encapsulation or contact layer was assumed, so that the nanostructures resulted directly in contact with air. The approach to the problem consisted in firstly solving Maxwell's equations in the NWs to determine the absorptance values of square arrays with different D and P, and then, assuming a system of perfect carrier extraction, to employ the absorptance values to obtain the photogenerated current by solving the following equation

$$J = \frac{q}{hc} \int \lambda A(\lambda) I(\lambda) d\lambda$$

(where q is the elementary charge, h the Planck's constant, c the light speed, A the absorptance, I the AM1.5G spectrum and λ the wavelength), whose solution depends on the NW geometry through A(λ).

With this approach the authors eventually found an optimal value of photocurrent equal to 17.8 mA cm^{-2} generated by NWs with D = 180 nm, P = 350 nm and band-gap equal to 1.72 eV; the consequent J(V) curve showed V_{OC} = 1.94 V, FF = 0.90 and overall efficiency equal to 33.1 %.

This study constituted an important result because the calculations performed on an ordered array of NWs offered a more realistic evaluation of the cell performances, which appeared still very promising. However, the fact that this theoretical optimization had been carried out only on the D and P parameters but at constant L left room for further improvements, achievable by adapting also the NW length.

That was actually one of the main ideas of the work of Huang et al, consisting in a similar study to optimize the structural parameters and maximize the detailed balanced efficiency of a TSC based on a hexagonal array of NWs on Si:[66] compared to the previous case, herein the system considered by the authors provided a higher level of complexity, since they set also the NW length among the tuneable parameters and introduced a transparent encapsulation and contact layers in the architecture of the device. Moreover, they took into account the effects of surface recombinations and lattice mismatch with Si so as to better approximate the real conditions, and they performed a comparison between the performances of the radial junctions and those of the axial ones. Eventually, the realistic efficiency limit in presence of surface recombinations was calculated as still higher than 30

%, while the radial junction came out as more tolerant to surface recombinations than its axial counterpart.

Despite the greater accuracy of these results, the evaluation of the real efficiency of the cell could still be improved. For this reason, in 2013 Bu et al decided to perform calculations taking into account not only the influence of surface recombinations but also the effects of Femi-level pinning in the NWs and of Shockley-Read-Hall recombinations in the Si sub-cell.[109] Moreover, contrary to the authors of the previous studies, they assumed more severe non-ideal conditions in terms of surface recombinations, setting a S_{NW} equal to $7 \cdot 10^4$ cm s^{-1}. The final result of the simulations, performed on a cell virtually constituted by a square array of cylindrical $Ga_{0.35}In_{0.65}P$ NWs with axial p-n junction on Si, provided an overall efficiency equal to 27.1 %.

Wang et al confirmed these results in a similar study carried out two years later.[110] Although the model adopted was quite similar to the previous one, herein the authors investigated also the effect induced by different minority carrier lifetimes for Shockley-Read-Hall recombinations, so as to reproduce varying densities of mid band-gap trap states. In this case, the practical efficiency resulted equal to 27.5 %.

In conclusion, based on the simulation performed so far it seems reasonable to expect efficiencies above 27 % for fully optimized NW-based TSCs operating in reality. This result is quite promising considering that such a value is higher than the current efficiency record for both planar TSCs and the most advanced Si-based prototypes, thus making NW-based TSCs a potentially effective solution which is worth to be tried.

1.4.3 State of the art of NW tandem solar cells

In spite of the large amount of single junction NW-based prototypes already developed and of the theoretical studies showing the possibility to achieve higher efficiencies, to the best of our knowledge only one attempt to realize such a device has been so far undertaken. This was reported by Yao et al from Povinelli's group in an article[111] which became a point of reference in this field and explains how the authors were eventually able to fabricate a GaAs NWs/Si TSC with current matching and voltage addition.

The TSC in question consists of a 1 mm^2 broad ordered array of GaAs NWs with axial p-i-n junction monolithically integrated via selective area MOCVD on a n-doped Si substrate covered with a Si_3N_4 mask (Figure 1.12). Ion implantation and rapid thermal annealing (RTA) were used to introduce p+ emitter and n+ back surface field in the bottom cell, with boron and phosphorus, respectively. The NW growth started with the deposition of a highly n-doped GaAs stem, so as to provide a good connection with the n-doped Si substrate, before introducing the axial p-i-n sequence with a high p-dopant concentration. The NWs were

subsequently encapsulated with transparent and insulating benzocyclobutene (BCB) so as to provide a mechanical stability; the polymer was then etched to expose the NW tips and allow their top contact through a sputtered layer of a transparent conductive ITO layer. The ohmic top contact was finally formed by AuGe/Ni/Au deposition followed by RTA, while the back one was obtained by e-beam evaporation of Al.

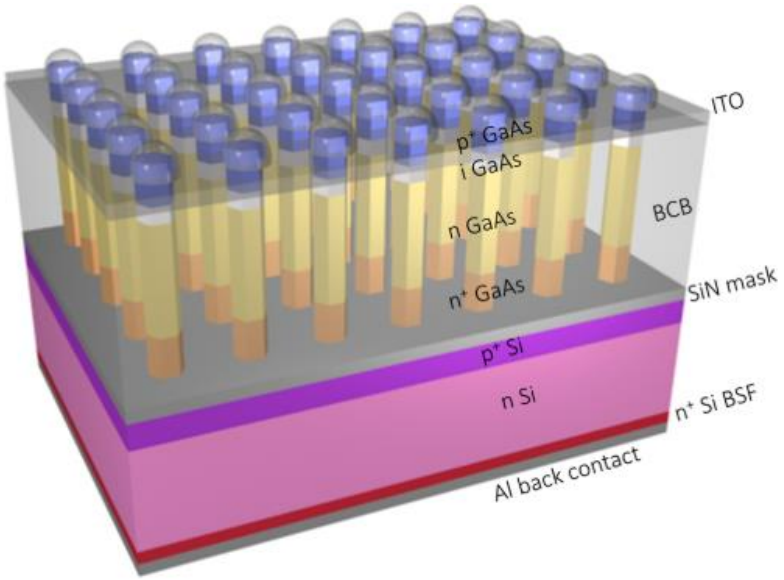

Figure 1.12: Schematics of the TSC realised by Yao et al.[111]

The NWs were grown with diameter, period and length equal to 300, 600 and 900 nm, respectively. In particular, the first two values were chosen on the basis of optical simulations previously performed by the same group to maximize the light absorption,[64] whereas the latter one was calculated as the optimal one for current matching.

The performances of the two individual sub-units and of the whole TSC were measured under 1 sun AM1.5 G illumination, the latter one showing J_{SC} = 20.64 mA/cm^2, V_{OC} = 956 V, FF = 0.578 and η = 11.4 %. By observing their corresponding J-V curves reported in Figure 1.13, it can be noticed that a good current matching was eventually achieved between bottom and top cells, whereas there is a slight difference between the V_{OC} of the TSC and the summation of those of the two sub-units (0.547 and 0.518 V for bottom and top cells, respectively): this voltage drop is likely due to surface recombinations at the heterointerface of the bottom cell and to nonradioactive recombinations in the heavily doped NW stem. Based on these considerations, the authors concluded that the two sub-units of the TSC were ultimately connected in series with nearly matched currents.

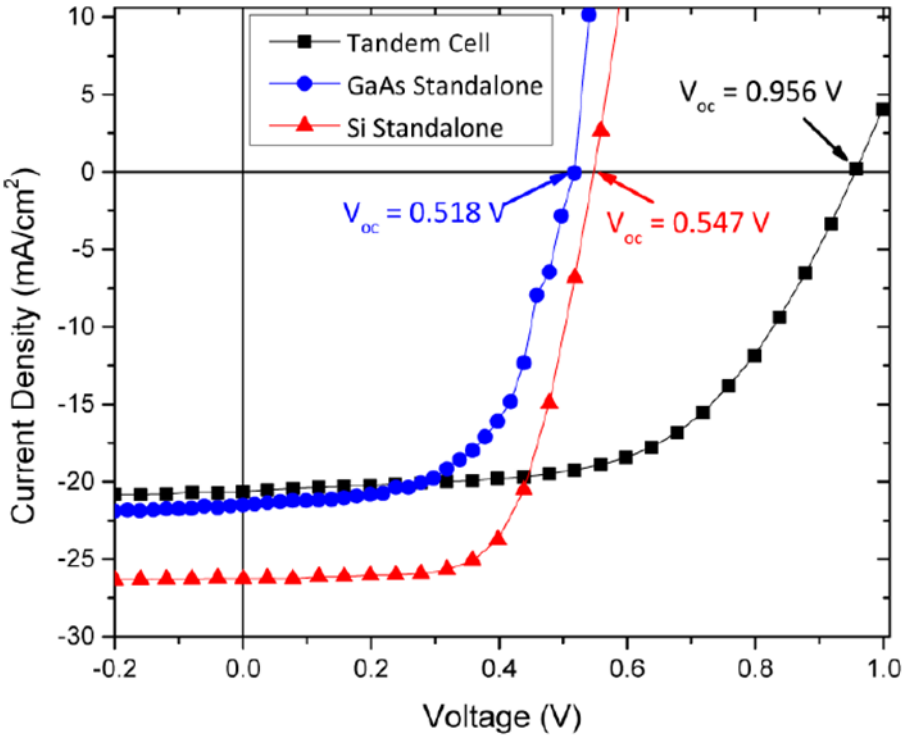

Figure 1.13: J-V curves for the tandem (black), bottom (red) and top (blue) cells developed by Yao et al.[111]

Although this result appears still low in terms of efficiency if compared to the current planar devices or to the most advanced NW-based single junction prototypes, such an outcome is nevertheless very significant, since it finally demonstrates the possibility to put into practice a NW-based TSC, thus making this study a good starting point for the research in this field. This structure offers indeed an ample room for optimization: such a purpose could be surely achieved by using ternary alloys with band-gap equal to the optimal value of 1.7 eV like AlGaAs, GaAsP or GaInP instead of GaAs, and by introducing back surface and shell passivation in the bottom and top cells, respectively, so as to strongly reduce the recombination losses.

It is therefore possible to conclude that NW-based TSCs appear as a promising and still improvable solution to the quest for combining higher efficiencies with lower costs, so that these characteristics make them one of the possible candidates to develop the next generation of PV devices.

1.5 The aim and scope of this thesis

The work herein reported is part of the HETONAN (acronym for "High efficiency tandem solar cells based on III-V nanowires on silicon") project, a research founded by ANR (Agence Nationale de Recherche) whose ultimate purpose is to develop prototypes of high-efficiency TSCs based on NWs of III-V ternary alloys with radial p-n junction, monolithically integrated on a Si sub-cell. The project, involving several public and private laboratories such as the CNRS-affiliated INL, C2N, IMEP-LAHC and the start-up SILSEF, was divided into several tasks, each of which was entrusted to some of the partners.

This PhD thesis focuses particularly on the growth by MBE on Si substrates of p-n and p-i-n core/shell AlGaAs-based heterostructured NWs (AlGaAs is one of the candidate materials for the development of the final structure), that being the main task assigned to us. At the same time, it presents also some parallel studies of their structural and optoelectronic properties carried out in collaboration with other groups at INL and C2N, which were employed to optimize the configuration of the NWs with particular regards to their junctions and passivation shells.

Our work started from the optimization of the growth conditions of self-catalysed GaAs NWs on epi-ready Si substrates as a preparatory step for the growth of AlGaAs NWs, which were initially expected to form the top cell of the TSC. However, having encountered many difficulties in growing this ternary alloy by vapour-liquid-solid (VLS) mechanism on Si substrates covered with an oxide layer, we decided to adopt a more feasible NW configuration consisting in GaAs/AlGaAs core/shell structures including the radial p-n or p-i-n junction inside the AlGaAs shell.

Once this objective has been achieved, we committed to transferring onto patterned Si substrates the know-how so far acquired on epi-ready Si, so as to obtain ordered arrays of NWs for the top cells. The main difficulty encountered in this step consisted in the quest for maximizing the yield of vertical NWs, a necessary condition to develop the TSC, but this problem was eventually solved with the development of a growth protocol leading to vertical yields around 90 %.

Moreover, other preliminary studies concerning the encapsulation and top contacting of the NWs have been performed, in order to eventually advance towards the fabrication of a NW-based TSC.

2 Molecular beam epitaxy

2.1 Epitaxial growth by MBE

2.1.1 The principle of epitaxial growth

The word epitaxy (from the Greek "*epì*"-above and "*taxis*"-order) defines the deposition of thin layers of crystalline material on a crystalline substrate, which directs the growth of the former one thus determining its structural properties.

The epitaxial growth can be divided into homoepitaxy and heteroepitaxy, depending respectively on whether the substrate and the grown layers are composed of the same or of different materials. As far as heteroepitaxy is concerned, if the lattice parameter mismatch between materials is not excessive, the grown layer can adapt to the substrate lattice parameter: the epitaxial growth is then defined as pseudomorphic. In the case of cubic materials, the epitaxial layer will be subject to a quadratic strain due to the fact that the material adopts a different lattice parameter in the surface plane, and will consequently undergo a different elastic deformation determined by its own Poisson's modulus perpendicularly to the surface plane. This fact will determine compressive or tensile stresses in the grown layer depending on whether it adopts a smaller or bigger in plane parameter, respectively.

As the deposition proceeds, the pseudomorphic layer grows while the elastic energy stored inside it is increasing. This process continues until the thickness reaches a critical value in which it is energetically favourable to relax the stress through either the formation of misfit dislocations at the interface (plastic relaxation) or the formation of 3D islands via a 2D/3D growth mode transition (elastic relaxation): after that, the layer material can regain its original lattice parameter and the growth continues without mismatch-induced stresses.

As far as the dynamics of the growth process are concerned, the atoms or molecules initially arriving on the substrate from the vapour phase can be either chemisorbed or physisorbed; subsequently, they can re-evaporate, interdiffuse in the first atomic layers of the substrate, or diffuse on the surface until they meet nucleation centres to grow a subsequent monolayer. The prevalence of one of these three behaviours over the others depends on the conditions of the system, such as the nature and temperature of the substrate and the chemical nature and ratio of the reagent flows; this causes the growth process to occur under kinetic rather than thermodynamic control.

As far as 2D- and 3D structures are concerned, epitaxial growth of thin films or bulks can take place in three different ways (Figure 2.1): the Frank-van der Merwe mode (also called "2D" or "layer-by-layer" mode), the Volmer-Weber mode (also called "island growth") and the Stranski-Krastanov mode. In the first case, the growth of a new atomic layer occurs only

after the completion of the underlying one: this happens if the interactions between substrate and overlayer are stronger than the lateral interactions between overlayer atoms. In the second case, the atoms form discontinuous structures of one or more atomic layers called “islands”, which eventually merge together originating a single epitaxial layer; in this case the interactions between atoms close to the deposited material are stronger than those with the substrate below. In the third case, which is *de facto* a mix of the previous one, the deposition of some complete atomic layers is followed by the formation of islands until the surface is completely covered.

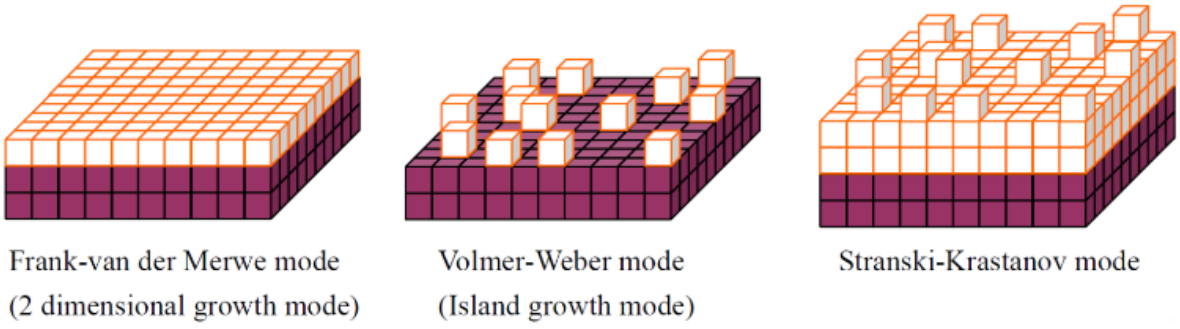

Figure 2.1. Schematics of the three possible epitaxial growth modes of 2D- and 3D materials.[112]

NWs on the contrary are grown through different mechanisms, notably the already-mentioned VLS, which will be exposed in detail in Chapter 3.

Generally speaking, epitaxial growth can be performed through different techniques, such as CVD, MOCVD, MOVPE and MBE. In particular, the latter one was adopted to carry out the growth of the NWs studied in this work thesis, therefore a description of this technique is summarized in the next paragraph.

2.1.2 Molecular Beam Epitaxy (MBE)

The main concept of MBE consists in employing localized beams of atoms or molecules in an ultra-high vacuum (UHV) environment, which provide precursors for the growing material: this technique is successfully employed to synthetize epitaxial layers and nanostructures of semiconductors, metals and oxides. Modern MBE systems may consist of several growth chambers (also called reactors) connected in UHV, which often include integrated surface characterization systems to analyse the growing surface in real time. A schematic representation of this type of reactor is reported in Figure 2.2. UHV conditions, corresponding to pressures in the 10^{-10}–10^{-11} Torr range, are obtained by employing ionic pumps, cryogenic panels and Ti sublimation.

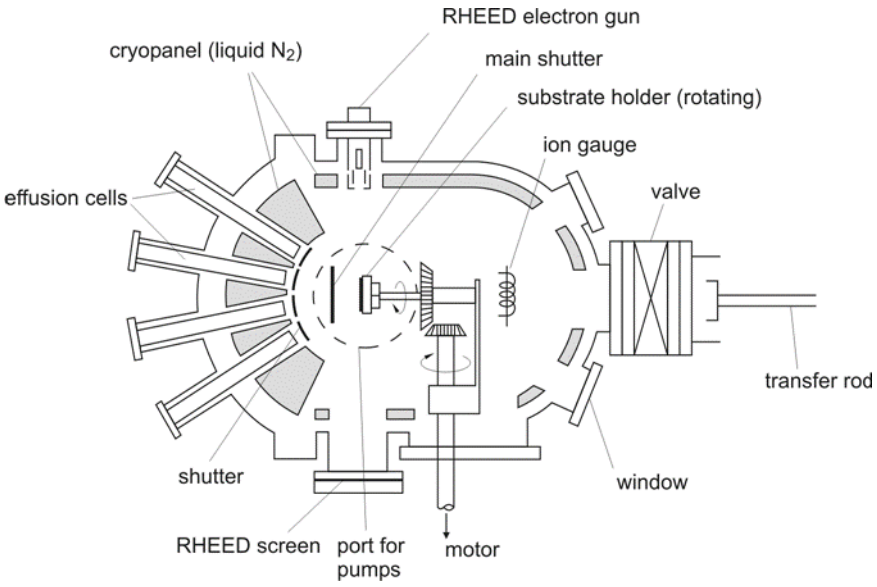

Figure 2.2. Top section of a MBE growth chamber.[113]

In MBE of III-V semiconductor compounds, atomic or molecular beams are thermally produced by effusion cells (also known as Knudsen's cells) containing elements or compounds in equilibrium with their own vapour and directed onto the substrate. Effusion cells are heated through filaments of refractory metals connected to external power suppliers; the cell temperatures are measured using thermocouples and regulated by a system based on PID controls and thermocouple feedback. Since the cells can reach extremely high temperatures, it is necessary to keep them thermally insulated and to refrigerate the whole system. This function is performed by a set of panels filled with liquid nitrogen (cryopanels), whose refrigeration contributes also in maintaining the reactor in UHV conditions.

Some cells, like those of V-group elements, are equipped with valves for flux control, whereas the flux of the others, like those of III-group elements, are tuned by varying their temperature. Indeed, the flux of atoms or molecules of a certain species i arriving on a unit area of the substrate per second is related to the cell temperature T_i through the following equation:[114]

$$J_i = \sqrt{\frac{N_A}{2k_B\pi}} \cdot \frac{p_i}{\sqrt{M_i T_i}}$$

Where J_i is the flux of atoms or molecules, N_A the Avogadro number, k_B the Boltzmann constant, p_i the pressure measured in the flux by the ion gauge, also expressed as the beam equivalent pressure (BEP), M_i the atomic or molecular mass.

Cells can be opened or closed at will, thanks to mechanical shutters made of high purity refractory metal (Ta), so as to measure the flux of a single cell without interference from the others and to carry out the growth of heterostructures with highly synchronised change of materials: speed of action of the shutters is indeed so high to allow the growth of structures with good compositional control and with well-defined interfaces control at atomic scale. Therefore, thanks to the extremely clean growth environment and to the precise control achieved over precursor purity and fluxes, MBE systems permit to obtain very abrupt interfaces, thus constituting a versatile technique for the fabrication of structures such as quantum dots, quantum wells, superlattices and heterojunctions.

Generally speaking, the substrates are fixed on molybdenum disks (called molyblocks) either with tungsten pins or with molten indium. A molyblock can be introduced inside the reactor and placed on its sample-holder: in order to perform uniform deposition, the sample holder is connected to a motor which allows the rotation of the substrate during the growth. The sample holder is provided with an ion gauge (Bayard-Alpert gauge) used to measure the fluxes, expressed in terms of BEP. Once a sample is introduced inside the reactor, its temperature can be adjusted with a heating filament and controlled with a thermocouple located on the sample holder. The thermocouple, not being in direct contact with the substrate but measuring only its radiant heat flux, cannot provide the exact value temperature, which nevertheless can be measured through an optical pyrometer. In order to correlate the temperature set by the thermocouple (T_{th}) with the temperature measured by the pyrometer (T_{pyro}), it is possible to plot the latter value as a function of the former one (Fig. 2.3). Since the thermal response is peculiar for every molyblock, depending on the chemical species deposited on it, and type of substrate, depending on composition, doping and crystal orientation of the surface, such calibration should be performed for all molyblocks and types of substrate adopted. This type of graph indicates the approximate value of T_{th} to be set in order to obtain a certain T_{pyro}, although during a growth process it is still advisable to monitor the temperatures and to correct T_{th} in real time if needed, so as to achieve the required T_{pyro}.

From now on, all the temperatures adopted during the NW growths reported in this manuscript (cf. Chapter 3, 4 and 5) refer to values measured by pyrometer, unless elsewhere specified.

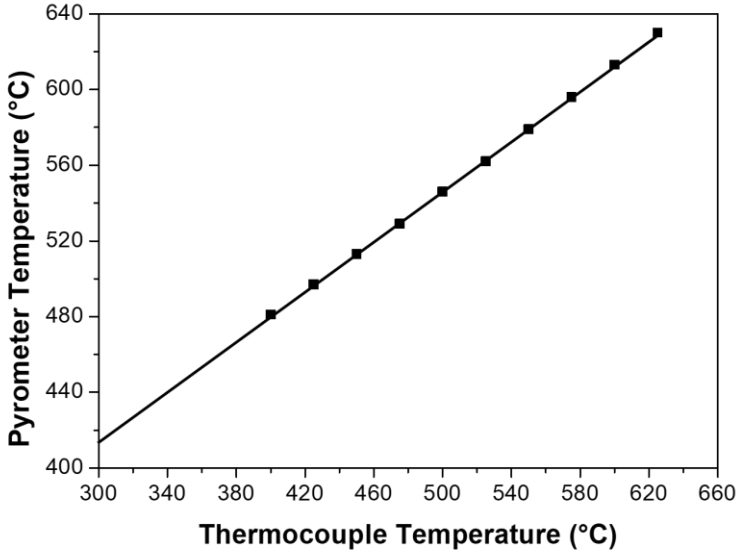

Figure 2.3. Graph reporting T_{pyro} as a function of T_{th} measured on a substrate consisting of boron-doped Si(111) (0.02-0.06 Ω·cm).

All samples reported in this thesis were realised using EPISURE, a software which automatizes the growth procedure providing precise control over the opening of shutters and valves and over the temperature of heating of the effusion cells and of the sample holder. The files containing all the specifics for a certain sample and selected to perform the growth procedure are commonly known as recipes. The possibility of automatizing the growth procedures is a very powerful tool which allows to keep the growth parameters extremely stable and to obtain a high degree of reproducibility, thus providing great control over the composition and configuration of the structures.

2.1.3 Reflection High Energy Electron Diffraction

Reflection High Energy Electron Diffraction (RHEED) is an *in situ* surface analysis technique, which allows monitoring the growth on a substrate by providing information about the structural quality of the surface of the growing material in real time throughout all the phases of a recipe.

In RHEED analysis, the surface of the sample is hit by high-energy electrons (20-30 kV) with grazing incidence (1°-3°) with respect to the surface. Diffracted electrons are observed on a fluorescent screen in front of the electron gun placed on the opposite side of the reactor (Fig. 2.4). Because of the angle of incidence, electron penetration is limited only to the first atomic layers of the surface; as a consequence, the diffraction pattern puts in

evidence the characteristics of the substrate surface, whereas it does not provide any information about the substrate bulk.

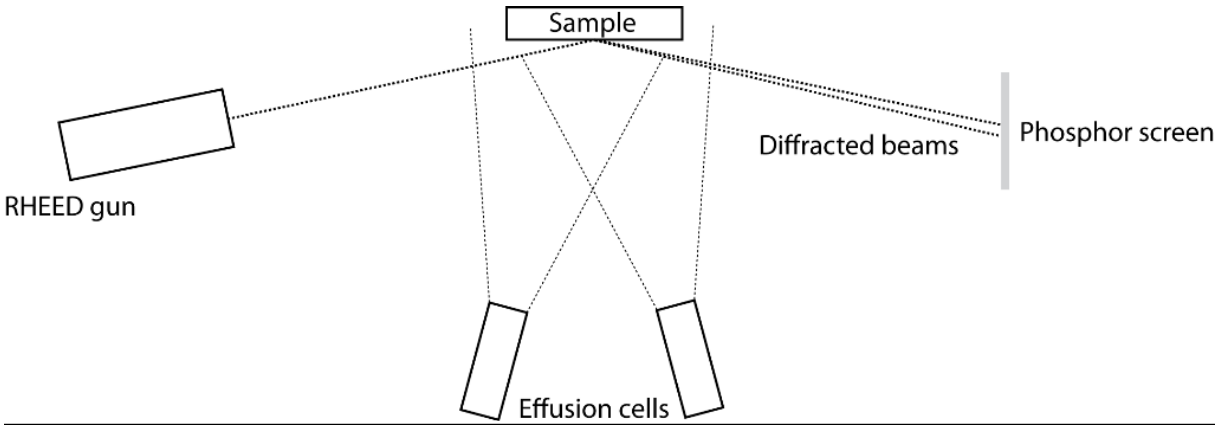

Figure 2.4. Schematics of a RHEED system integrated into a MBE reactor.[115]

The diffraction pattern originated is consistent with Laue's theory on the amplitude of the wave diffused by a crystal lattice, so that the incident wave is not attenuated by diffusion processes due to any crystalline defects, thus meaning that inelastic scattering is not considered. As a consequence, the diffraction will occur only if the Ewald sphere associated to the electron beam intersects points of the reciprocal lattice.

Since in the case of a smooth surface the direct lattice can be approximated to a 2D-only layer, the reciprocal lattice does not consist of points because they tend to degenerate into infinite 1D rods along the direction perpendicular to the surface. In an ideal case, the RHEED pattern (observed on the screen) of the reciprocal lattice should therefore consist of fine spots arranged in a semicircle (the so-called Laue's rings, shown in Fig. 2.5) because of the intersection between the 1D rods and the Ewald sphere. However, in reality: 1- the electronic beam is not perfectly monochromatic and originates an Ewald sphere with a certain thickness and 2- the surface in not completely smooth and originates 1D rods with a certain diameter. As a consequence, the intersection between the Ewald sphere and these 1D rods forms segments instead of spots. As a consequence, RHEED patterns of real smooth 2D surfaces will appear as sets of lines.

On the contrary, rough surfaces and 1D or 0D nanostructures (like NWs or quantum dots, respectively) present reciprocal lattices formed by large points instead of 1D rods, originating from diffraction by transmission mode instead of from a reflection mode; as a consequence, the Ewald sphere intersecting with such set of points originates also a set of points, which appears as a network of spots on the RHEED pattern observed on the screen.

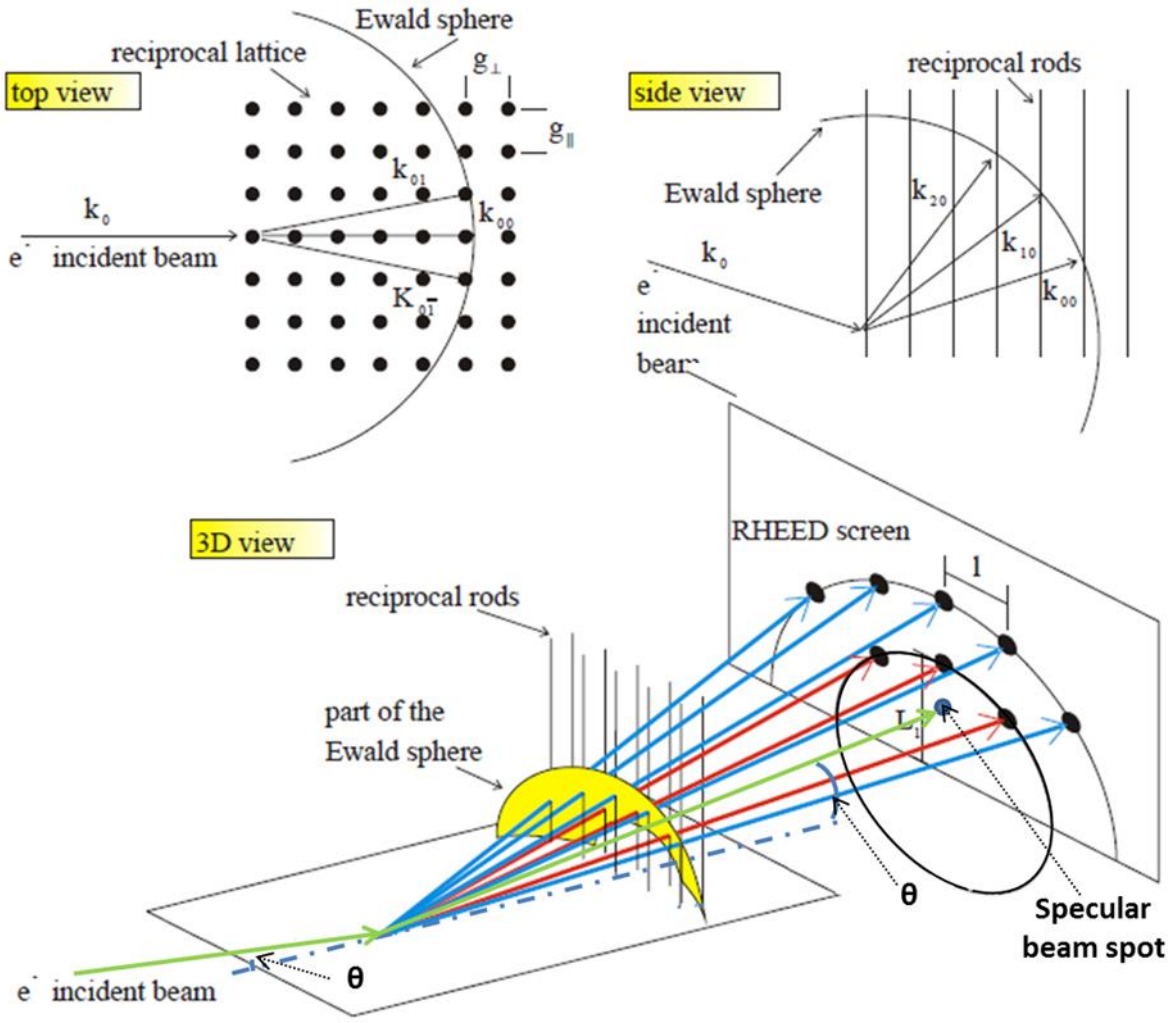

Figure 2.5. Principe of the RHEED diffraction: the case of an ideal 2D surface.[116]

As far as grown layer surfaces are concerned, one of the main advantages of this technique consists in the possibility of investigating their reconstruction or roughness.

However, an important application of the RHEED pattern is the so-called RHEED oscillations which makes it possible to measure the growth rate of a layer by following the intensity of the specular beam spot (i.e. the beam as purely reflected by the surface, cf. Figure 2.5) during this growth. As reported in Figure 2.6, in the case of a 2D growth the surface can be initially intended as a smooth plane with coverage ϑ equal to zero; in this case, the electrons of the incident beam are diffused in the same direction, so that the intensity of the specular beam spot results the highest as possible. Then, when a new layer starts to form, covering for example a quarter of the surface (ϑ = 0.25), part of the electrons are necessary diffused in other directions, and the intensity of the specular beam spot is consequently decreased. When the growing layer reaches half of its coverage (ϑ = 0.5) the intensity is at its minimum, then increasing again as the growth continues (e.g. ϑ = 0.75). Finally, when the new layer is completely filled, the intensity of the specular beam spot is

once again maximized; as a consequence, by observing the oscillations of the specular beam spot intensity during the growth (and especially at the beginning of it), it is possible to measure the period of this oscillation, which corresponds to the growth time of 1ML, and therefore the growth rate of the layer.

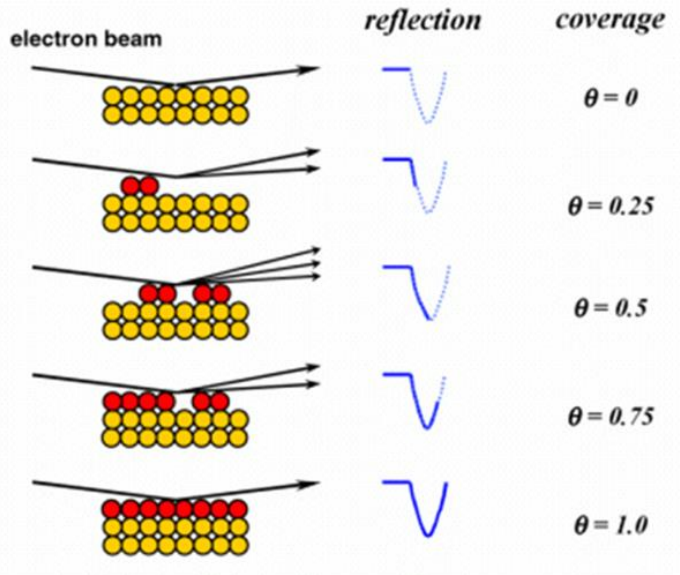

Figure 2.6. Relationship between the intensity of the specular beam spot and the surface coverage during the growth of 1ML of a layer.[117]

For the growth of III-V materials, growth rate measurements by RHEED were used in determining the fluxes of group III and V elements, which were expressed in terms of equivalent 2D growth rates of the III-V material.[118] For example, the flux of Ga can be expressed through the growth rate of a 2D GaAs layer on the same substrate while performing the measurements in excess of As (when the growth rate is limited by the Ga flux). In such conditions, it is possible to measure the growth rate of the III-V material for different temperatures of the Ga cell and, knowing their corresponding BEP measured by the Bayard-Alpert gauge, to link these values to those of Ga flux. The Ga flux can therefore be expressed in terms of equivalent growth rate of 2D GaAs and quantified either in monolayers of GaAs per second (ML/s) or in Å of GaAs per second (Å/s). This allows to plot a graphic showing the correlation between the Ga flux (F_{Ga}), obtained as GaAs equivalent growth rate and measured in Å/s, and the Ga BEP (P_{Ga}), as reported in Figure 2.7.

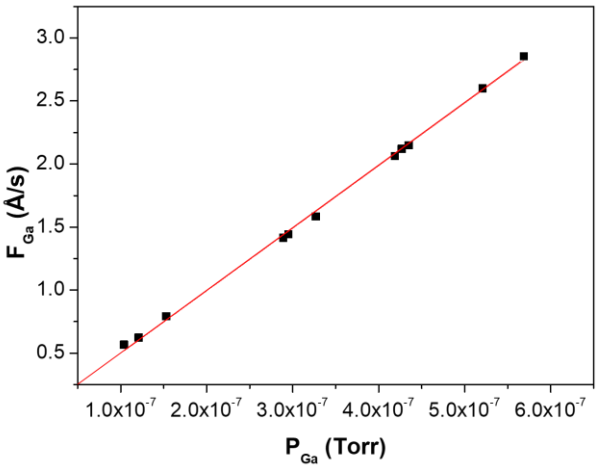

Figure 2.7. Flux of Ga (F_{Ga}) as a function of the BEP of Ga (P_{Ga}).

This method can be adopted to express also the fluxes of elements of group V. In the latter case, for example, the flux of As can be determined by performing the same type of measurements in excess of Ga (when the growth rate is limited by the As flux). In this case the flux of As is kept constant while that one of Ga is constantly increased until saturation of the growth rate is reached: this corresponds to the moment in which the oscillation period of the specular beam spot remains stable despite the increasing Ga flux, thus meaning that the growth has switched from a Ga-limited regime to an As-limited one. This can be seen in practice by plotting the equivalent growth rate of GaAs as a function of the Ga flux for increased As flux, as reported in Figure 2.8(a). This shows that at saturation, experimental points deviate from linearity and stabilize on a constant value: this allows As flux to be also quantified in terms of ML/sec or Å/sec as equivalent growth rate of 2D GaAs and, subsequently, to relate the As flux F_{As} to the As BEP (P_{As}), as shown in Figure 2.8(b).

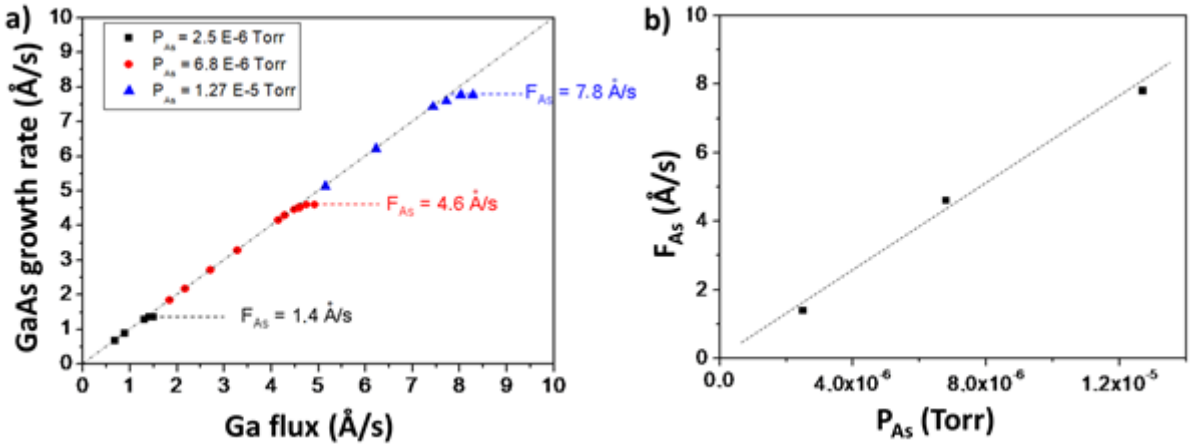

Figure 2.8. (a) Ga-As flux measurements obtained by monitoring RHEED oscillations. (b) Flux of As (F_{As}) as a function of As BEP (P_{As}).

Another application of the RHEED pattern obtained in transmission mode is the indexation of spots so as to determine their corresponding plane family; this is particularly useful when it comes to determine the crystallographic structure of nanostructures. For example, in the case of GaAs NWs, the indexation of the spots allows to distinguish between two crystallographic structures, i.e. the cubic Zinc Blende (ZB) (Figure 2.9(a)) and the hexagonal Wurtzite (Wz) (Figure 2.9(b)) ones, respectively with ABCA and ABA stacking sequence in the equivalent close-packed directions <111> and <0001>.

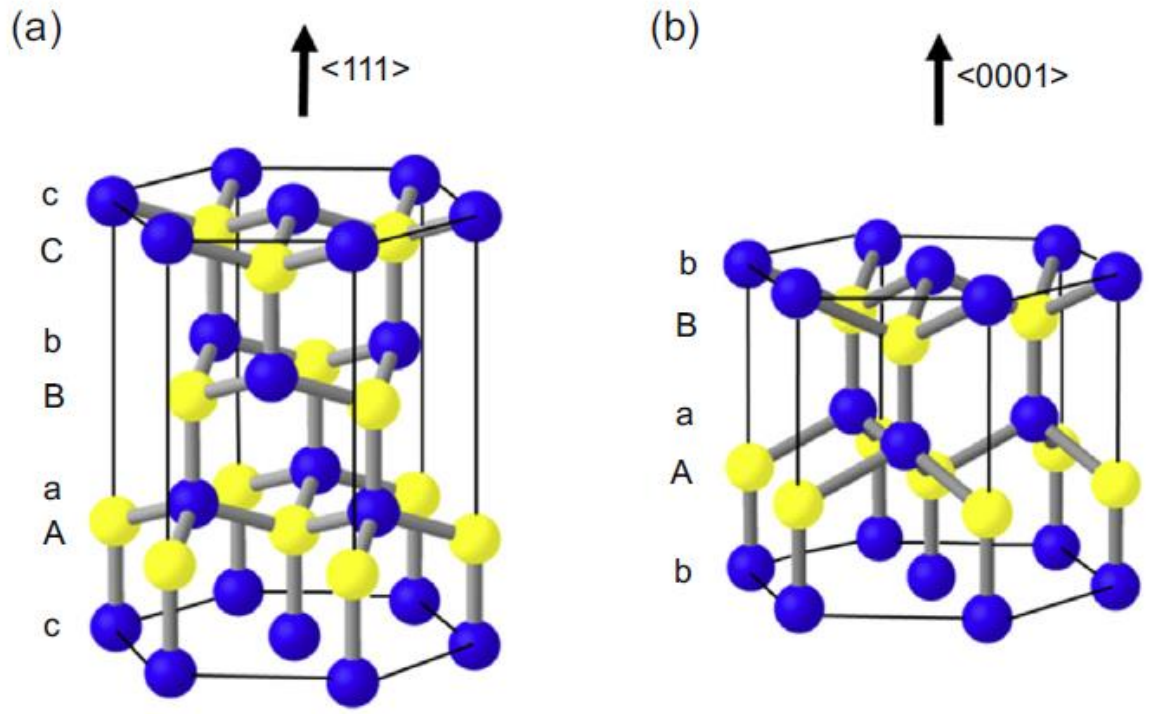

Figure 2.9. Illustrations of the (a) ZB and (b) Wz crystal structures.[119] ZB structure is characterized by an ABCA sequence of III-V planes, while Wz structure is characterized by an ABA sequence. III and V atoms are in yellow and blue, respectively.

Thus, considering a RHEED pattern taken from [1-10] azimuth, the ZB and/or Wz crystal structures of GaAs NWs can be detected. As an example,[120,121] Figure 2.10 shows a typical RHEED pattern measured along the [1-10] azimuth of GaAs NWs (grown on a Si substrate) for which the two phases were present (from Master 2 report of T. Dursap).[120] The position of the spots is indeed in agreement with an epitaxial growth of the NWs on the silicon substrate: the GaAs [111] and $[1\bar{1}0]$ axis are parallel to the Si [111] and $[1\bar{1}0]$ axis, respectively. The RHEED diagram shows the presence of the mixture of ZB and Wz structures and the corresponding spots were indexed.

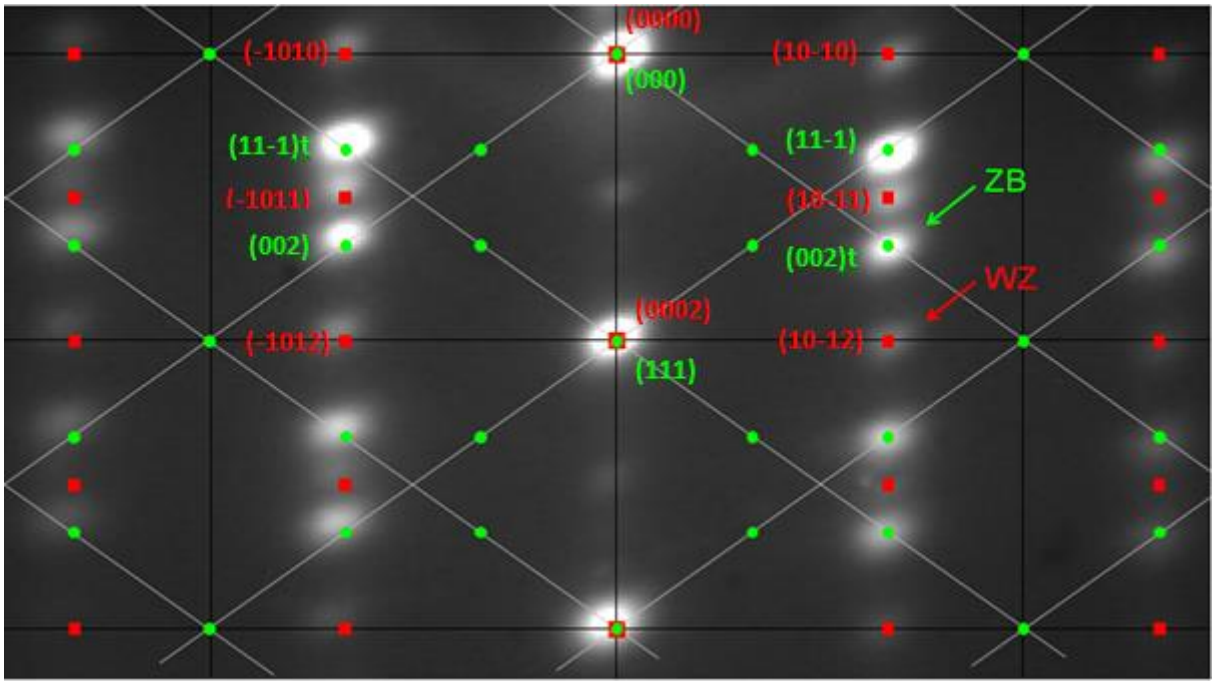

Figure 2.10: RHEED diagram recorded along the $[1\bar{1}0]$ azimuth of self-catalysed GaAs NWs grown on Si(111) substrate, where ZB and Wz spots are visible and indexed. Green dots report ZB plans taking into account the two ZB variants. Red squares reports Wz plans. An extinction of the structure factor F_{hkl} is responsible for the missing spots of one ZB column over two, and for the one over two Wz spots along the growth axis. From master report 2 of T. Dursap,[120] in collaboration with J. Penuelas.[121]

3 The growth of self-catalysed GaAs nanowires on epi-ready Si substrates

3.1 Introduction

As far as the fabrication of NWs is concerned, the already mention VLS growth is undeniably the most common mechanism, and the correct understanding of the experimental work reported in this thesis cannot be separated from the understanding of this mechanism. Therefore, the first part of this chapter will focus the explanation of the VLS growth of NWs; after that, it will be finally possible to present the experimental results concerning the nucleation and growth of self-catalysed GaAs NWs on epi-ready Si substrates, in particular as a function of the incident angle of the Ga flux.

3.2 The Vapour-Liquid-Solid mechanism

By definition, VLS growths are all those mechanisms of NW synthesis in which beams or flows of molecular or atomic gaseous precursors (vapour) impinge or diffuse into droplets of molten metals (liquid) randomly dispersed or orderly arranged on a substrate (solid). Once the droplets are supersaturated by the precursors, these react causing nucleation at the droplet/substrate interface and subsequent growth of the first monolayer of the NWs; as a consequence, a new solid/liquid interface forms between the droplets and the grown NWs, and as long as precursors are provided the process can continue, thus determining the axial growth of the NWs, as illustrated in Figure 3.1.

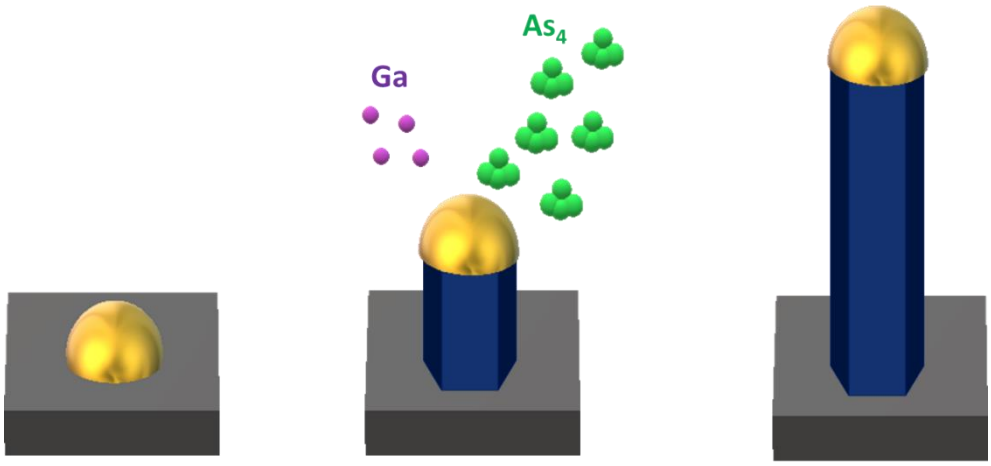

Figure 3.1. Schematics of metal assisted VLS growth of NWs.

Although the metal droplets act only as gathering centres, the literature concerning this topic often reports of metal-catalysed growths. Such definition is undoubtedly not correct, since metal atoms of droplets do not form chemical bonding with the precursors and do not affect the activation energies of their reactions. For this reason, chemists generally prefer the more proper definition of metal-assisted growths. However, the term "catalysed" has become so widespread over the years to be nowadays commonly accepted by the scientific community; therefore, in this thesis we will use the two terms as equivalent and refer to metal droplets as catalysts.

VLS growths of NWs can be mainly classified in two types: those processes carried out using a foreign metal as catalyst, and those ones (also called self-catalysed growths) assisted by a metal droplet constituted of an element which is also one of the components of the NWs. Growths catalysed with foreign metals are widely adopted with all epitaxial techniques in the synthesis of IV, II-VI and III-V semiconductor NWs; generally speaking, the most common catalyst adopted in this case is Au, although other metals such as Ni, Pd, Pt, Mn, Cu, Ag, Bi and Fe can also be used.[122] Self-catalysed process on the contrary are employed in the growth of III-V NWs by MBE, such as Ga in the case of GaAs, GaP, In in the case of InAs, InP and related ternary alloys.

3.2.1 Theoretical models of NW growth

When Wagner and Ellis synthesized the first NWs in 1964,[123] they already assumed VLS growth to explain their results. The first model describing their growth mechanism was developed 11 years later by Givargizov,[124] but after this work there was no further progress for the following three decades, until Dubrovskii and Sibirev extended and generalized Givargizov's model in an article published in 2004.[125] This work became the first of many publications realized until nowadays,[126–134] as evidence of the renewed interest developed in this topic as the potential of NWs was understood by the scientific community. Some of these results have proved to be of inestimable importance and usefulness thanks to the possibility of explaining the experimental data and providing insight about the physical processes occurring during the VLS growth, especially in the case of GaAs NWs: it is thus worthwhile to describe the most significant results in this regard.

One of the main questions about the growth of Au-catalysed GaAs NWs was why these nanostructures can grow also with a WZ crystalline phase, whereas the bulky counterpart usually presents a ZB phase.[135] The answer was finally achieved in 2007 through the model developed by Glas et al,[130] which constitutes a milestone in the literature about this subject, and although this research takes into consideration the case of Au-catalysed GaAs NWs, this model can be adopted also for self-catalysed ones. According to this work, nucleation occurring at the liquid-solid (LS) interface (Figure 3.2(a)) is less favourable and originates the ZB phase, whereas the nucleation at the triple phase line (TPL) is thermodynamically

favoured and forms preferentially the WZ phase (Figure 3.2(b)). As a matter of fact, assuming that the nucleation at LS interface occurs with the formation of a 2D island nucleus of height h, perimeter P and surface A, the change of free enthalpy ΔG for the nucleation process eventually results equal to:

$$\Delta G = -Ah\Delta\mu + Ph\gamma_{lL} + A(\gamma_{SN})$$

where Δμ> 0 is the difference of chemical potential for III-V pairs between liquid and solid phases per unit volume of nucleus, γ_{lL} the energy of the lateral interface between nucleus and liquid per unit area and γ_{SN} the energy of the substrate-nucleus interface per unit area. Since Δμ and γ_{lL} are equal for both ZB and WZ phases, whereas γ_{SN} > 0 for WZ phase and = 0 for ZB phase, the latter results the preferential crystal phase in the thermodynamically less favourable case of nucleation at LS interface.

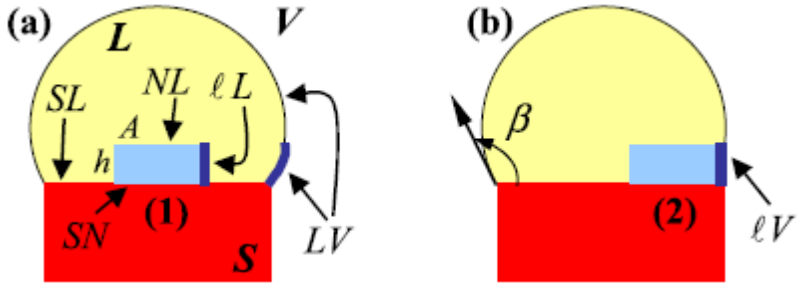

Figure 3.2. Schematics of the nucleation and of the surfaces of interest at (a) the NW/liquid interface and (b) at TPL.[130]

Concerning the nucleation at TPL, this can be thought as a shift of the nucleus from the centre (site (1), Figure 3.2(a)) to the edge (site (2), Figure 3.2(b)) of the NW; in this case, the area s formed at the nucleus-vapour (lV) interface eliminates a part **τS** of the previous LV one. The difference in formation enthalpies between nucleation sites (1) and (2) reported in Figure 3.2 is:

$$\Delta G(\alpha) - \Delta G(0) = \alpha Ph(\gamma_{lV} - \gamma_{lL} - \tau\gamma_{LV})$$

where α is the fraction of the island perimeter in contact with the vapour and γ_{lV}, γ_{LV} the energies of nucleus-vapour and liquid-vapour interfaces per unit area, respectively. Assuming that γ_{lV} is close to γ_{lL}, the equations can be approximated to:

$$\Delta G(\alpha) - \Delta G(0) = \alpha Ph(-\tau\gamma_{LV})$$

Considering an artificial cylindrical nucleus, it is argued that **τ** = sinβ, with β the contact angle between the NW and the droplet.

As a consequence, a nucleus tends to form at TPL provided - γ_{LV} sinβ < 0: considering that γ_{LV} is a positive value, the difference in energy depends on sinβ which is also positive

regarding the value of the contact angle is always $90° \leq \beta \leq 125°$. The above inequality is therefore safely satisfied and consequently the preferential nucleation should always take place at the TPL.

Afterwards, the authors demonstrate that nucleation of WZ phase for each successive monolayer is favoured at TPL when the droplet superstation is higher than a critical value. This result is of extreme importance, because it introduces the possibility to tune the phase composition of the NWs through the control the droplet supersaturation by tuning the flux of gaseous precursors.

The study of Glas served as a starting point for the work of other groups. In particular, Krogstrup et al[134,136] and Yu et al[137] carried out some relevant studies, respectively on Au and Ga-assisted GaAs NWs, to demonstrate that it is the catalyst droplet wetting angle the main parameter to determine the crystal phase.

The investigation of the droplet-NW (LS) interface and the role of the V/III ratio of flux precursors in the formation of different crystal phases was further deepened by Jacobsson et al,[138] who exploited the novel technique of *in situ* TEM to study the LS interface of Au-catalysed GaAs NWs during the growth. Thanks to this novel approach, the authors were capable to observe the nucleation and growth of single GaAs monolayers in real time, and confirming that the key parameter in determining the crystal phase consists in the geometry of the droplet and notably in its contact angle. As a matter of fact, they noticed that As-poor fluxes of precursors originate big droplets with a high contact angle ϕ typically > 125°, determining also a truncated LS interface with edge facet and letting GaAs monolayer nucleation occur at the edge N, so as to lead to a ZB phase (as illustrated in Figure 3.3(e)). On the contrary, for As-rich fluxes of precursors, smaller droplets with lower droplet contact angles $\phi < 125°$) and a sharp LS interface are observed (as illustrated in Figure 3.3(d)), on which GaAs monolayers nucleate at the TPL so as to lead to a WZ phase.

These experimental results can be explained considering that reducing the As/Ga ratio in the precursor determines a lower axial growth rate of the GaAs NWs and consequently a higher amount of metallic Ga in the droplet (which consists of an Au-Ga-As liquid solution), thus letting it swollen and increasing its contact angle. On the contrary, increasing the As/Ga ratio will enhance the NW axial growth rate and consequently the consumption of Ga from the droplet and let it shrink, reducing the contact angle. Based on these considerations, the authors developed a model to calculate the edge facet length y (in the NW growth direction) (cf. Fig. 3.3(a)) as a function of ϕ for low and high values of gold droplet supersaturation. The results, reported in Figure 3.3(b), show that NWs can assume truncated shape not only for $\phi > 125°$, but also for values lower than 55°. This fact suggests that, although not observed by the authors because their experimental setup did not allow TEM imaging at high supersaturation, the nucleation of ZB can occur also at very high As/Ga ratio corresponding to low ϕ as reported in Figure 3.3(c), while decreasing the V/III ratio and consequently

increasing ϕ leads first to a sharp interface (Figure 3.3(d)) for 55° < ϕ < 125° where WZ nucleates and then to a truncated one when ϕ > 125° (Figure 3.3(e)), where ZB forms again.

These results are not in contrast with Glas' previous model but rather represent an integration of it, since they allow explaining the correlation between the changes in the droplet composition and volume and the switches in the NW crystal structure with microscopic phenomena such as variations of the interface profile.

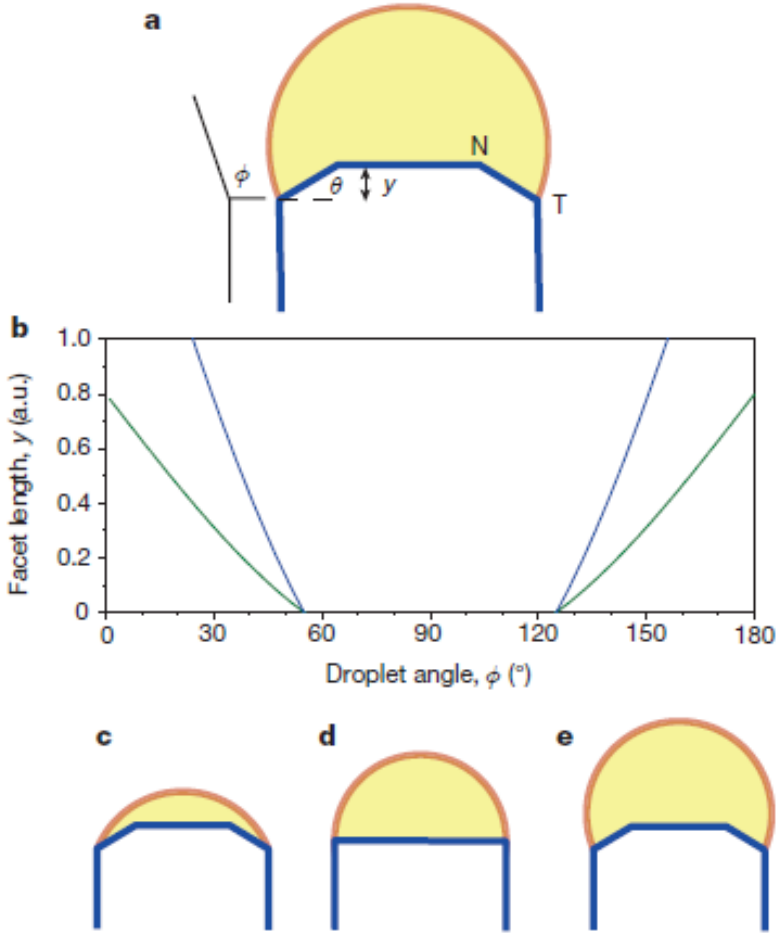

Figure 3.3. (a) Schematics of the NW/droplet interface profile defining the nucleation site N, the triple phase line T, the edge facet length y (in the NW growth direction) and the droplet contact angle ϕ. (b) Graphic reporting the edge facet length y as a function of the droplet contact angle ϕ, as calculated for low (blue line) and high (green line) supersaturations. Schematics relating droplet size to interface profile with (c) ϕ < 55°, (d) 55° < ϕ < 125°, (e) ϕ > 125°.[138]

Although Jacobsson et al carried out their experiments only on Au-assisted NWs, their model can be applied also to describe the growth of self-assisted GaAs NWs, as shown by Kim et al.[139]

3.2.2 Self-assisted growth of GaAs NWs

The possibility to perform self-assisted growth of III-V NWs by MBE constitutes for sure an important progress in the synthesis of these nanostructures. It avoids the use of foreign catalysts such as Au and thus prevents the incorporation of impurities into the NWs preserving their optoelectronic properties. Moreover, at the end of the NW growth it is easy to evaporate or to consume the remaining droplet. Self-assisted growths allow greater control over axial growth in the case of the synthesis of core/shell structures: as a matter of fact, when shell growth is performed on NWs catalysed with foreign metals, the molten metal at the top of the NW is still present so that the VLS axial growth continues to occur at the same time as the vapour-solid (VS) radial one, and this fact tends to originate structures with tapered geometry. On the contrary, in the case of self-assisted NWs the VLS growth can be totally suppressed by exposing the III-group droplet to a flux of V-group precursors only, so as to consume the droplets progressively. After that, it is possible to perform a conformal shell growth, while the axial growth is reduced to the VS growth of material at the top facet of the NWs.

The first example of self-assisted GaAs NWs obtained by MBE dates back to 2008, as Fontcuberta's group synthesized this kind of structures on a GaAs(111)B substrates.[102] After that, many other studies have been carried out to investigate the possibility to extend the self-catalysed growth to other substrates; in particular, great interest was aroused by the possibility of achieving self-assisted monolithic integration of GaAs NWs on Si substrates. In this case, it has been observed that the silicon oxide layer present on the surface of the sample plays a key role in the growth process, both in the case of epi-ready silica with low thicknesses[140] and in that one of specimens covered with thicker patterned masks of SiO_2.[141]

As far as the self-assisted growth of GaAs NWs on epi-ready substrate is concerned, because of the roughness of the surface, Ga droplets tend to form spontaneously on it when the sample is exposed to the flux of precursors. Indeed, part of the silica layer can be reduced by Ga at the usual growth temperature (around 600°C), in the following reactions:[142]

$$SiO_2 + 4\,Ga \rightarrow Si + 2\,Ga_2O$$

$$SiO_2 + Si \rightarrow 2\,SiO$$

$$SiO_2 + 2\,Ga \rightarrow SiO + Ga_2O$$

Since both SiO and Ga_2O desorb around 600 °C, the products of the reactions will evaporate, thus causing the presence of pinholes on the epi-ready silica and exposing the bare silicon surface at their bottom. Subsequently, Ga droplets are formed in these pinholes which constitute the nucleation point for epitaxial growth of NWs. As a consequence, no preliminary treatment of the surface is needed to obtain self-assisted growth. However, in order to control the NW density, it is possible to perform a pre-deposition step to form Ga

droplets at lower temperature, followed by a controlled thermal annealing to let the metal reduce the oxide so as to form the pinholes. Subsequently, once the substrate is exposed to the flux of precursors, the droplets will re-form and the NWs nucleate in these pinholes. For a detailed explanation of this mechanism we refer the reader to the paragraph 3.3.3.

3.3 The axial growth of NWs on Si(111)

In this section we will present experimental results concerning the axial growth of self-assisted GaAs NWs on epi-ready Si(111) substrates. Since our group had already performed systematic studies[143–145] of the influence of growth temperature, V/III flux ratio and Ga pre-deposition on the NW growth, we did not further investigate the impact of these parameters, rather using the know-how previously developed as the starting point of this research, the growth parameters having been already optimized. Therefore, our preliminary studies were initially limited to checking the influence of the growth temperature (Paragraph 3.3.2), particularly in order to adapt the thermocouple based temperatures to the molyblock employed for this work: 1- to verify whether we could reproduce properly the optimal growth conditions, and 2- to investigate the role of Ga pre-deposition (Paragraph 3.3.3). However, we have also decided to study the influence of another parameter on the NW growth: the incident angle of the Ga flux with the substrate normal which is the NW growth direction for vertical NWs. As a matter of fact, since our MBE reactor is equipped with two Ga cells having different angles with respect to the substrate normal (≈9.3° for the so-called Ga(7) cell and ≈27.9° for the so-called Ga(5) cell), it was possible to carry out a detailed and systematic analysis to determine the influence of this parameter on the NW growth. The results of this broad study are reported in Paragraph 3.4, and show that different angles can have significant effects on the NW growth. When non-mentioned, the NW growths were realised with the Ga(5) cell.

3.3.1 The growth protocol

The protocol developed in our group requires that before growth a pre-deposition of Ga for 2 sec is performed at temperature $T_{pre\text{-}dep}$ of 510-530 °C with Ga flux (f_{Ga}) equal to 0.5 ML/sec in terms of equivalent growth rate of 2D GaAs layers on GaAs(001) substrate. This allows the formation of Ga droplets on the epi-ready substrates. Subsequently, the temperature is raised with a slow ramp (7 °C/minute) up to the growth temperature T_{growth} ≈ 600-610 °C (a temperature range which provides a high density of NWs and a low presence of parasitic structures). This raise in temperature permits the reduction of SiO_2 by the Ga droplets and the formation of holes in the oxide layer whose thickness was estimated to ≈ 2 nm. Once T_{growth} is reached and stabilised, the growth is started by opening the effusion cells

of Ga(5) and As at the same time. As for pre-deposition, the value of F_{Ga} is set equal to 0.5 ML/sec also during the growth, whereas the flux of As_4 tetramers (F_{As}) is equal to 1.15 ML/sec: this corresponds to As/Ga flux ratio equal to 2.3, a value chosen to produce ZB GaAs NWs with a low density of twin planes and/or Wz segments and with a good morphology, the as-obtained NWs presenting almost constant diameter along their whole length (in the 1-2 µm range) (Figure 3.4). The growth is finally stopped by closing the effusion cells of Ga and As at the same time. After that, the temperature is decreased as fast as possible to prevent As desorption from the NWs and to preserve the Ga droplets at the NW tips. Throughout the whole procedure the sample is rotated at 5 rpm.

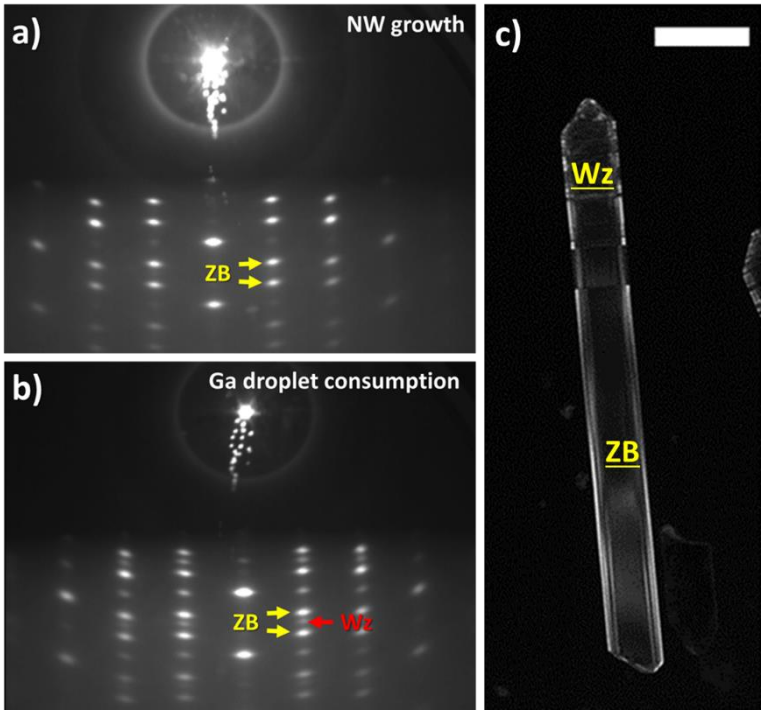

Figure 3.4: (a, b) RHEED diagrams along 1-10 azimuth recorded respectively during the NW growth and the droplet consumption: (a) pure ZB structure with the two variants indicating the presence of twin planes in some parts of the NWs, and (b) apparition of the Wz structure when the droplet is consumed. (c) 2 waves dark field TEM image of core/shell GaAs/AlGaAs NWs grown (with Ga(5) source, cf. Paragraph 3.4) with the optimal growth procedure. The detail of the NW structure will be better described in Chapter 4. Note that all the TEM imaging of NWs presented in this thesis was realised by G. Patriarche at C2N.

This protocol is the standard one adopted in this work; therefore, from now on it is to be assumed that each sample of GaAs NWs reported herein, unless otherwise specified, was realized according to this procedure.

The molyblock employed for this work is in a 2-inches In-free molyblock covered with GaAs and capable to carry a 1 cm x 1 cm sample. The Si substrates adopted consisted of 0.02-0.06 Ω·cm B-doped epi-ready Si(111), with SiO_2 surface layer about 2 nm thick. Before

the growth, all substrates were sonicated for 10 minutes in acetone and ethanol to remove possible contaminants from the surface, and dried under nitrogen flow; subsequently, they were degassed at 200 °C in UHV and finally introduced into the MBE reactor.

3.3.2 The influence of the growth temperature

The influence of the growth temperature was investigated with a series of samples realised at different T_{growth}. In particular, the purpose of this analysis was to evaluate the impact of T_{growth} on the surface density of NWs and on the presence of parasitic structures, so as to verify the reproducibility of the results previously obtained in our group with this protocol. The results are reported in Figure 3.5 where it can be noticed that parasitic structures, largely present at lower T_{growth} such as 585 °C (Figure 3.5(a)), are progressively decreasing as T_{growth} is increased up to 610 °C (Figure 3.4(b, c, d)). The graphic in Figure 3.5(e) reports the density of vertical NWs and parasitic structures as a function of T_{growth}. It can be noticed that a NW density maximum at T_{growth} = 590 °C (d = 2.1 NW/μm^2): this can be likely explained assuming that at the lower growth temperature of 585 °C, the Ga droplets tend to evolve more into a large population of parasitic structures at the expense of the vertical NWs (d =1.2 NWs/μm^2). On the contrary, increasing the temperature at 600 and 610 °C reduces the parasitic structure density, but it also disadvantages the nucleation and growth of NWs due to increased desorption of Ga and As adatoms from the sample surface, leading to lower densities (1.4 and 1.0 NWs/μm^2, respectively). Such results are consistent with those ones previously reported by our group,[143–145] and confirm the reproducibility of the protocol. As far as the NW length L and diameter D are concerned, it can be noticed that in the range of T_{growth} here adopted, there are no significant differences on these values (Figure 3.5(f, g).

We remind the reader that all the values of NW diameters reported in this thesis were obtained by measuring the very NW top (right below the Ga droplet).

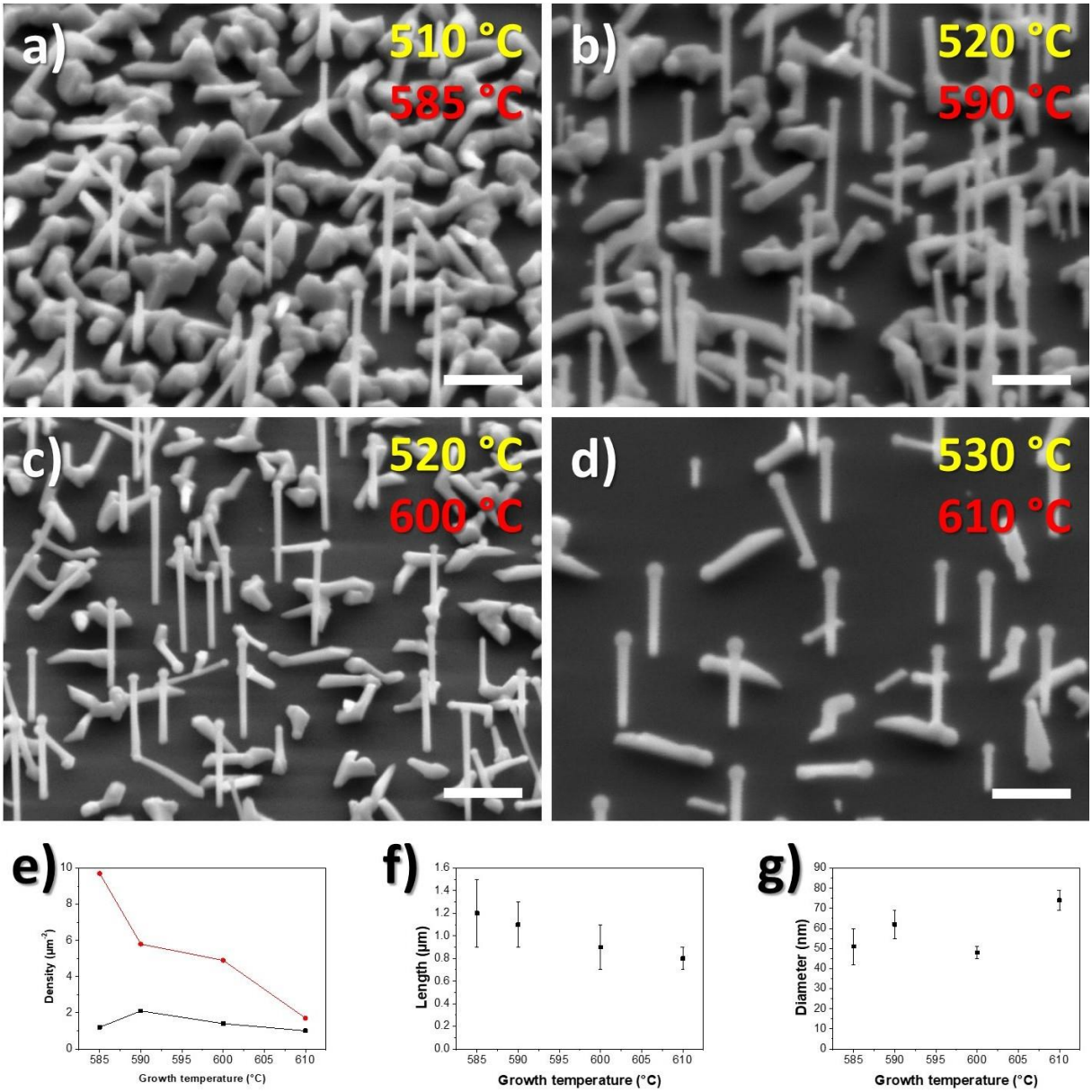

Figure 3.5. (a-d) SEM images (45°-tilted) of GaAs NWs grown for 10 min at different T_{growth}. The values reported in yellow corresponds to $T_{pre\text{-}dep}$, whereas those in red are T_{growth} adopted in each case. The white scale bar corresponds to 500 nm. Graphic reporting (e) the density of NWs and parasitic structures, (f) the NW length and (g) diameter as a function of T_{growth}.

Generally speaking, the choice of the growth temperature depends on two main needs: 1- maximizing the rate of vertical NWs and 2- minimizing the density of parasitic structures. As shown by the experimental results, T_{growth} = 590 °C is particularly favourable in the first case, but not in the second one. For this reason, we came up with the conclusion that T_{growth} in the 600-610 °C range is the best compromise for our purpose.

3.3.3 The role of Ga pre-deposition

Performing a Ga pre-deposition before the growth, the overall process can be exemplified by the following Figure 3.6. It, illustrates the formation of droplet at 520 °C (Figure 3.6(a,b)), the formation of holes as a result of silica reduction while increasing the temperature (Figure 3.6(c)), the re-formation of Ga droplets at 610 °C when the sample is exposed to Ga and As fluxes (Figure 3.6(d)), and finally the nucleation and axial growth of the NWs (Figure 3.6(e)).

This type of procedure has been already employed by Tauchnitz et al[146] and is considered a very advantageous approach, since it permits to decouple the NW density and diameter from their length.

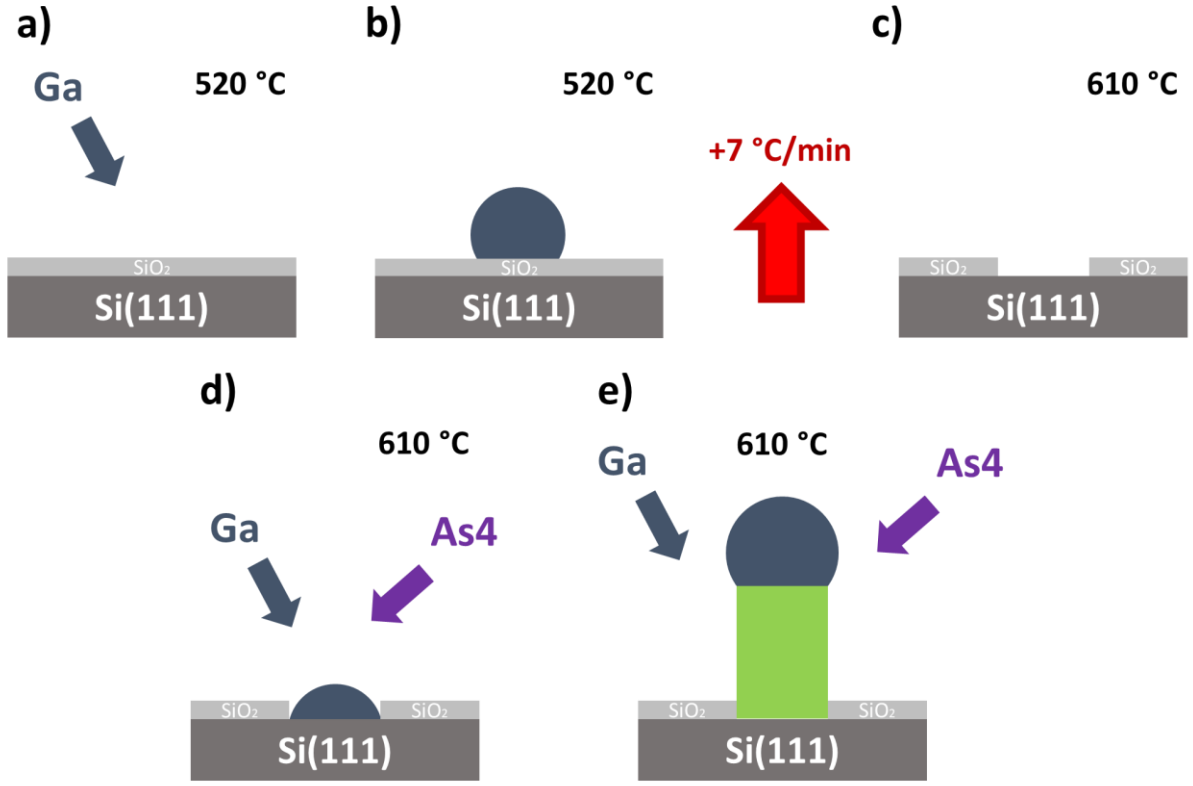

Figure 3.6. Schematics of the process of Ga pre-deposition and growth. (a) The epi-ready Si substrate is exposed to a flux of Ga (2 sec with F_{Ga} = 0.5 ML/sec). (b) Ga droplets form on the surface. (c) While raising the temperature to T_{growth}, Ga reduces SiO_2 forming holes in the surface layer. (d) When the sample is exposed to the Ga and As fluxes, Ga droplets re-form inside the holes and in contact with the bare Si. (e) When the Ga droplet is saturated by As, nucleation occurs at Ga/Si interface and the axial growth starts.

In order to verify and illustrate this mechanism, we took SEM images for each step of the procedure from Ga pre-deposition to the very beginning of the NW growth (using a different sample for each stage, due to the impossibility of stopping and re-starting the growth to check).

Results are reported in Figure 3.7. Generally speaking, Ga pre-deposition on Si(111) in standard conditions (2 sec with a F_{Ga} = 0.5 ML/sec) leads to droplets having diameter around 15 nm and density in the 15-40 units/μm^2 range: this is confirmed in Figure 3.7(a), where the density (d) ≈ 30 /μm^2 and the diameter (D) ≈ 16 ± 3 nm. While increasing the temperature gradually up to 600 °C, we expected Ga to reduce SiO_2 forming holes, as mentioned above, until all Ga_2O desorbs: this is consistent with Figure 3.7(b), where no more droplets are visible on the surface after the thermal treatment. Once stabilized the growth temperature, we performed a first growth exposing the substrates to both Ga and As for 2 sec only. As expected, this caused the re-formation of Ga droplets on the surface (Figure 3.7(c)), whose values of density is slightly lower but still consistent with those observed in Figure 3.7(a), in this case d ≈ 25 /μm^2, whereas D ≈ 22 ± 3 nm is higher than in the previous case. Such a value can be probably attributed to the higher temperature employed in this case, since to higher temperature corresponds a higher Ga mobility,[136] which can increase the diameter of the droplets at expense of density. A high magnification image of these droplets is reported in Figure 3.7(d): it is possible to measure the droplet contact angle (ϑ) which is ≈ 51° ± 4°. This value is consistent with that one reported for Ga on bare Si(111),[147] whereas ϑ for Ga on SiO_2 is known to be ≈ 116°.[147] This result is quite significant, since it corroborates the hypothesis that Ga droplets reform preferentially in the holes originated by silica reduction, thus being in contact with the underlying bare Si rather than with the silica surface layer. After 12 sec of GaAs deposition the system appears as essentially unchanged as shown in Figure 3.7(f): only the droplet density increases to ≈ 40 /μm^2 and while D ≈ 22 ± 3.0 nm and ϑ ~ 51° ± 6° (measured from Figure 3.7(f)) remain unchanged. After 20 seconds, the first NWs have already formed and the sample surface is covered by NWs and droplets (Figure 3.7(g, h)), with an overall density of structures ≈ 25 units/μm^2. The diameter of the droplets has slightly increased to ≈ 27 ± 4 nm while the contact angle has not changed significantly (ϑ ≈ 56° ± 4°). Vertical NWs have length (L) and diameter equal to 58 ± 4 nm and 11 ± 4 nm, respectively, and a density of ≈ 1.2 NWs/μm^2. Such a value is much smaller than the total density of structures, and still in the density range measured for longer growth times at these conditions (d = 1.0-1.5 NWs/μm^2 in the case of NWs grown for 10 minutes with this procedure, as shown in Figure 3.8). This means that only a fraction of the droplets take part in the axial growth and that the droplets which evolve into NWs nucleate at the very beginning of the growth, rather than at a later time.

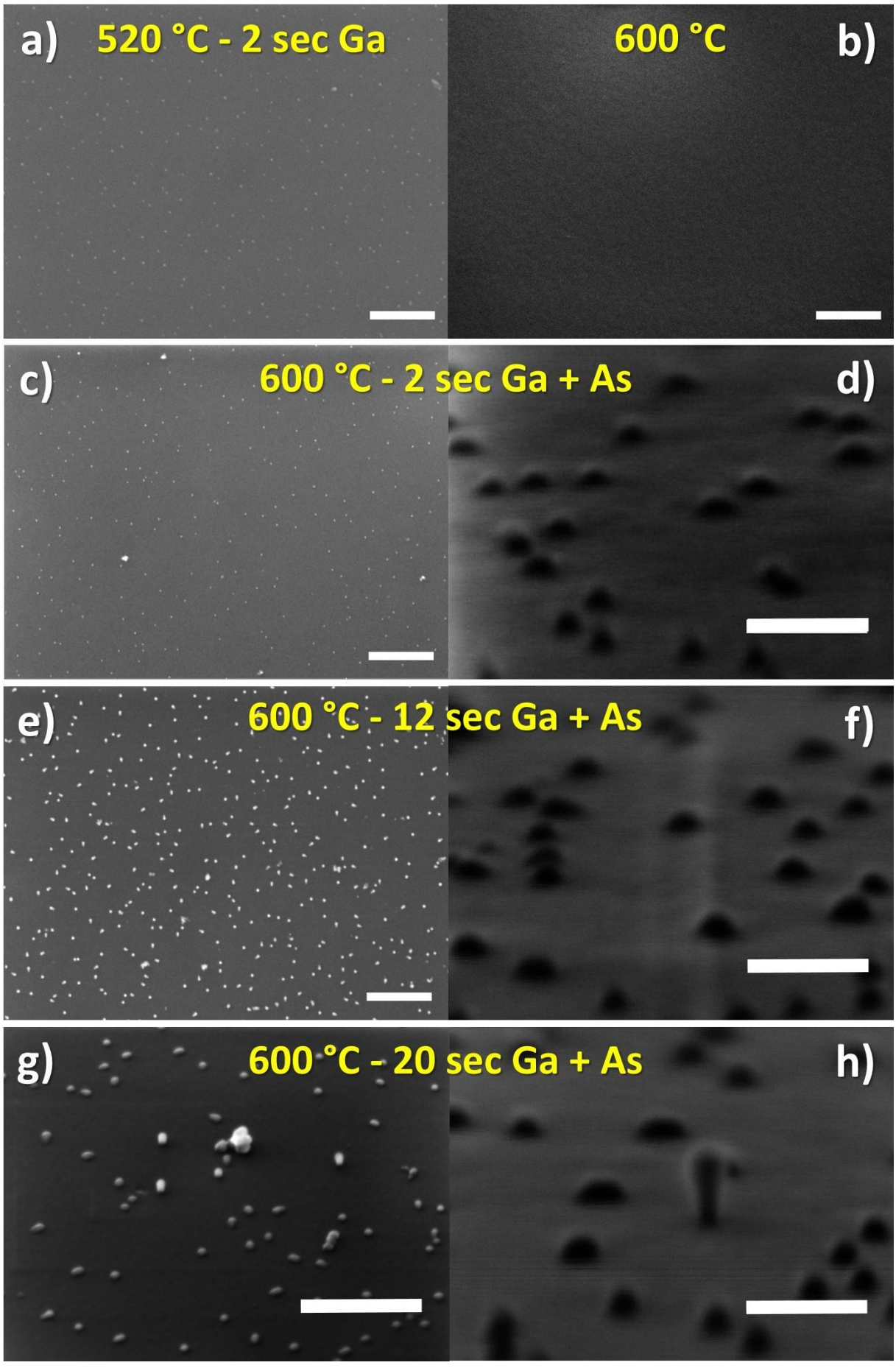
a) 520 °C - 2 sec Ga
600 °C
b)
c)
600 °C - 2 sec Ga + As
d)
e)
600 °C - 12 sec Ga + As
f)
g)
600 °C - 20 sec Ga + As
h)

Figure 3.7. SEM images showing all stages of the standard procedure as illustrated in Figure 3.5; (a) Top-view of Ga droplets obtained after pre-deposition at 520°C. (b) Top-view of Ga-free surface after the temperature increasing to T_{growth}=600°C. (c) Top-view and (d) cross-section 5° tilted view of Ga droplets re-formed after 2 sec exposition to Ga and As fluxes. (e) Top-view and (f) cross-section 5° tilted view after 12 sec exposition to Ga and As fluxes. (g) 45° tilted view and (h) cross-section 5° tiled view after 20 sec exposition to Ga and As fluxes. The values reported in yellow correspond to the temperature at which every step was performed. White scale bars corresponds to 500 nm in (a, b, c, e, g) and to 100 nm in (d, f, h).

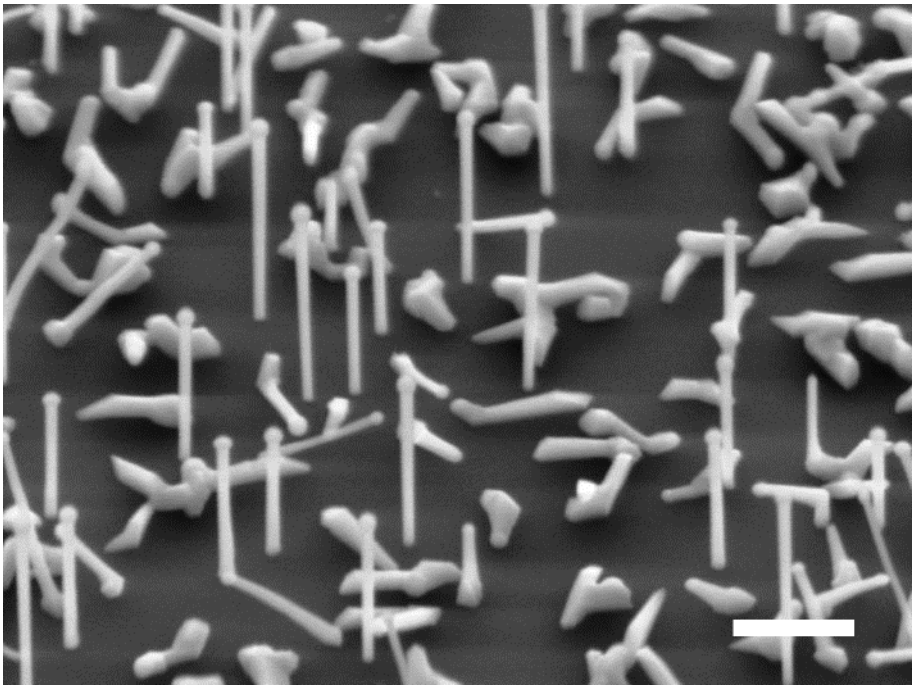

Figure 3.8. SEM images (45°-tilted) of GaAs NWs grown for 10 minutes with the standard procedure: the density of vertical NWs is equal to 1.4 NWs/μm^2. The white scale bar corresponds to 500 nm.

By comparing the results in Figure 3.7(h) and Figure 3.8 it can also be noticed that NWs grown in standard conditions for 10 min present a diameter ≈ 50 nm, whereas after 20 sec D is only ≈ 11 ± 4 nm: in order to explain this diameter increase we refer the reader to the following paragraph 3.4.

3.4 The impact of the Ga flux incidence angle

3.4.1 Introduction

At the beginning of this thesis work, the reactor employed (RIBER 32) was equipped with a Ga source in position Ga(7), i.e. with an incidence angle α = 9.3° between the incident flux of Ga and the direction normal to the substrate surface (the growth direction of vertical NWs). Observing that the NW growth results in this configuration were different (in particular concerning the axial growth rate) than those obtained with another reactor (RIBER C21) of our group, having α = 40° for the Ga cell (and for all cells), we decided to move the Ga source from Ga(7) to Ga(5) position. In this setting, α is equal to 27.9°, permitting to operate in a configuration "more similar" to that of the RIBER C21 reactor: that is why in this thesis are reported samples grown either with Ga(7) or Ga(5) source.

The comparison between the experimental results obtained using different Ga sources triggered our interest for the influence of the Ga flux incidence angle α on the NW growth. In particular, this was first noticed on preliminary results obtained by Guan Xin, at that time PhD student in our group. She already reported a significant difference in length between NWs obtained in growth conditions which were nominally the same in terms of T_{growth}, V and III fluxes, growth times and procedure steps, but whose Ga sources were different (Figure 3.9).[145]

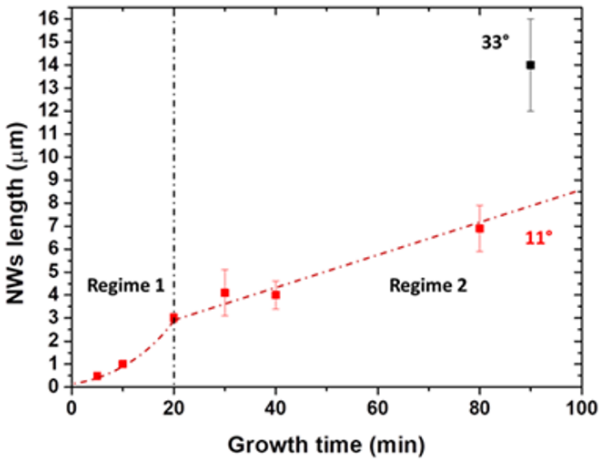

Figure 3.9. Graphic from Guan Xin's Ph. D thesis[145] reporting the length of GaAs NWs as a function of the growth time. It can be observed that Ga(7)As NWs (red) present two different growth regimes, whose switching point is at 20 min (NWs about 3 μm long), and that Ga(5)As NWs grown for 90 min (black spot) are clearly outliners of their curve, showing a noticeable higher length.

It was observed that GaAs NWs grown with Ga(7) (also known as Ga(7)As NWs) present two different growth regimes, depending on the growth time, and that their length was significantly lower than that one of GaAs NWs grown with Ga(5) (also known as Ga(5)As

NWs) for long growth times (80-90 min). Based on these results, we decided to investigate the role of the incidence angle α for the two cases of Ga(5) and Ga(7) sources.

The influence of the incidence angle α of the sources has been already taken into account by several groups to explain their own experimental results, although in quite different contexts than ours.[148–152]

In this regard, it is worth mentioning the work of Tchernycheva et al,[148] who studied the changes in shape of Au-assisted InAs NWs as a function of the growth duration, and observed a significant lateral growth only in the inferior part of NWs grown for longer times (at least ≈ 20 min in their growth conditions). This eventually leads to a bottle-neck morphology as illustrated in Figure 3.10. Based on these considerations and on previous models developed by Dubrovskii et al,[126,127] Tchernycheva et al developed a semi-empirical analytic model for the diffusion-controlled growth of NWs by VLS-MBE taking into account the incident angle of the element III flux to provide a qualitative description of the system . The model is based on the assumption that the variation of the volume per unit time for a NW with height H and droplet radius R_0 is equal to $\pi R_0^2(dH/dt)$, and if V denotes the nominal deposition rate (on the substrate), the NW growth is supplied by three contributions:

1- The direct impingement of atoms on the droplet:

$$V\pi R_0^2 \cos\alpha$$

2- The diffusion of adatoms from the substrate to the droplet (with l_0 the diffusion length on the substrate):

$$V\pi[(R_0 + l_0)^2 - R_0^2]\cos\alpha$$

3- The diffusion of adatoms from the lateral surface of the NW

$$V2R_0H(t)\sin\alpha$$

It follows that the relationship between the NW growth rate and α can be expressed with:

$$\pi R_0^2 \frac{dH}{dt} = V\pi(R_0 + l_0)^2 \cos\alpha + V2R_0\, H(t)\sin\alpha$$

This model, developed without considering the desorption of the adatoms, can explain the observed NW shape. When the NW length exceeds the adatom diffusion length on the lateral facets, only the adatoms arriving on the upper part of the NW will participate in the axial growth, whereas those in the bottom part will eventually be condensed on the facets and increase the NW diameter.

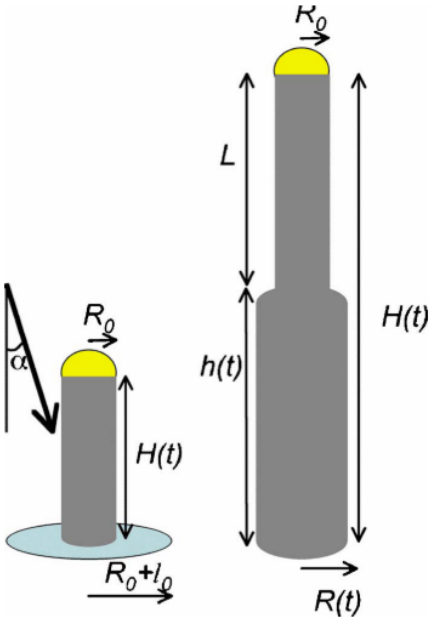

Figure 3.10. Illustration of the system considered by Tchernycheva et al.[148] Beyond a certain growth time the NWs develop bottle-neck morphology.

Another relevant work in this field is the study by Glas et al.[150] In this case, the authors developed a quantitative model of the self-assisted growth of III-V NWs, which considers only the As species and, contrary to the previous one, assumes a constant NW radius during the whole growth. The incidence angle α is introduced in order to explain why the NW growth rate varies almost linearly with the As flux. For this purpose, the authors consider the balance between the amount of Ga adatoms supplied to the droplet, either the one from direct flux (the only directional quantity, which strongly depends on α) or the one re-emitted from the environment,[153] and the quantity of As which is depleted either by the growth or by re-evaporation (Figure 3.11). Contrary to the case of III-group adatoms, no contributions from the diffusion of As adatoms on the NW facets are taken into account.

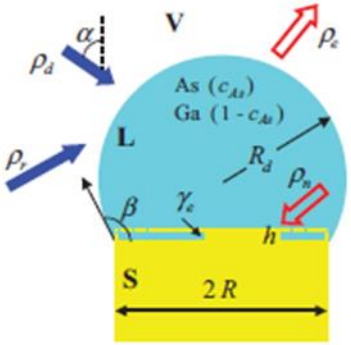

Figure 3.11. Illustration of the self-catalysed VLS growth of GaAs NWs from the model of Glas et al.[150] As current supplying and emptying the droplets are schematised respectively with empty blue and full red arrows.

Like many other experimental works,[45,102,140,154] and contrary to our case, results in Reference[150] are based on the assumption that the self-assisted growth of III-V NWs depends only on the flux of As, being independent from the Ga flux. This is due to the fact that all these authors start from the basic assumption that the group III flux is sufficient for the droplet to survive with a constant volume. As shown in the following paragraph, this is not always the case as a function of α, and it is precisely on the basis of this consideration that our experimental results can be explained.

3.4.2 Experimental results on axial (and radial) growth rate as a function of Ga flux incidence angle α

In order to obtain experimental evidence into this issue, we introduced one more Ga cell in position Ga(7) of our reactor so as to carry out a detailed and accurate study about the influence of the Ga flux incidence angle α on the NW length and morphology. With such a purpose, many samples were grown at nominally the same experimental conditions for several growth times (5, 10, 15, 20, 30, 40, 60 and 80 min), so as to obtained a vast and complete series of samples to be compared. In all cases the samples were grown with the standard procedure ($T_{pre\text{-}dep}$ ≈ 520 °C, T_{growth} ≈ 600-610 °C, F_{Ga} = 0.5 ML/sec, F_{As} = 1.15 ML/sec, $R(F_{As}/F_{Ga})$ = 2.3) either with Ga(5) or Ga(7) flux. In all cases we use Ga(5) source in order to perform the Ga pre-deposition, so as to be certain of reproducing also the same conditions in terms of Ga droplet size and density.

The results of this growth campaign are reported in the SEM images in Figure 3.12 and in the graphic in Figure 3.13. The difference between the two cases was confirmed: concerning the NW length, it can be noticed that while NWs grown for growth times shorter than 20 min present the same length, for growths longer than 20 min, Ga(5)As NWs are always significantly longer than their Ga(7)As counterpart. Moreover, it can be observed that the experimental points of Ga(5)As can be fitted by a linear regression. On the contrary, those for Ga(7)As lie on the same one for shorter growth times, whereas the points obtained with times longer than 20 min are fitted by a different linear regression. As a consequence, it is possible to conclude that the growth process undergoes two different regimes (named Regime 1 or R1 and Regime 2 or R2), thus confirming the preliminary results obtained by Guan Xin, although in our case a linear rather than super-linear trend is observed in Regime 1.[145] By interpolation of the red line fitting Ga(7)As with the black one for Ga(5)As it is possible to determine the values of growth time and NW length which mark the separation between the two regimes. These correspond to a growth time of about 17 min and a NW length of about 1.8 μm, as marked respectively by the vertical and horizontal dashed blue lines. The axial growth rate for Ga(5)As NWs is 1.9 nm/sec (≈ 7 ML/sec), whereas for Ga(7)As NWs it decreases from 1.9 nm/s in Regime 1 to 0.83 nm/sec (≈ 3 ML/sec) in Regime 2.

Furthermore, the SEM images show that the incidence angle α affects not only the NW size and morphology but also the droplet shape. In fact, whereas Ga(5)As NWs show a Ga droplet roughly constant in shape on their tip for all growth times, the droplets on the Ga(7)As NWs tend to decrease in size and sometime even disappear as the growth time increases, more specifically when the growth time is superior to 20 min.

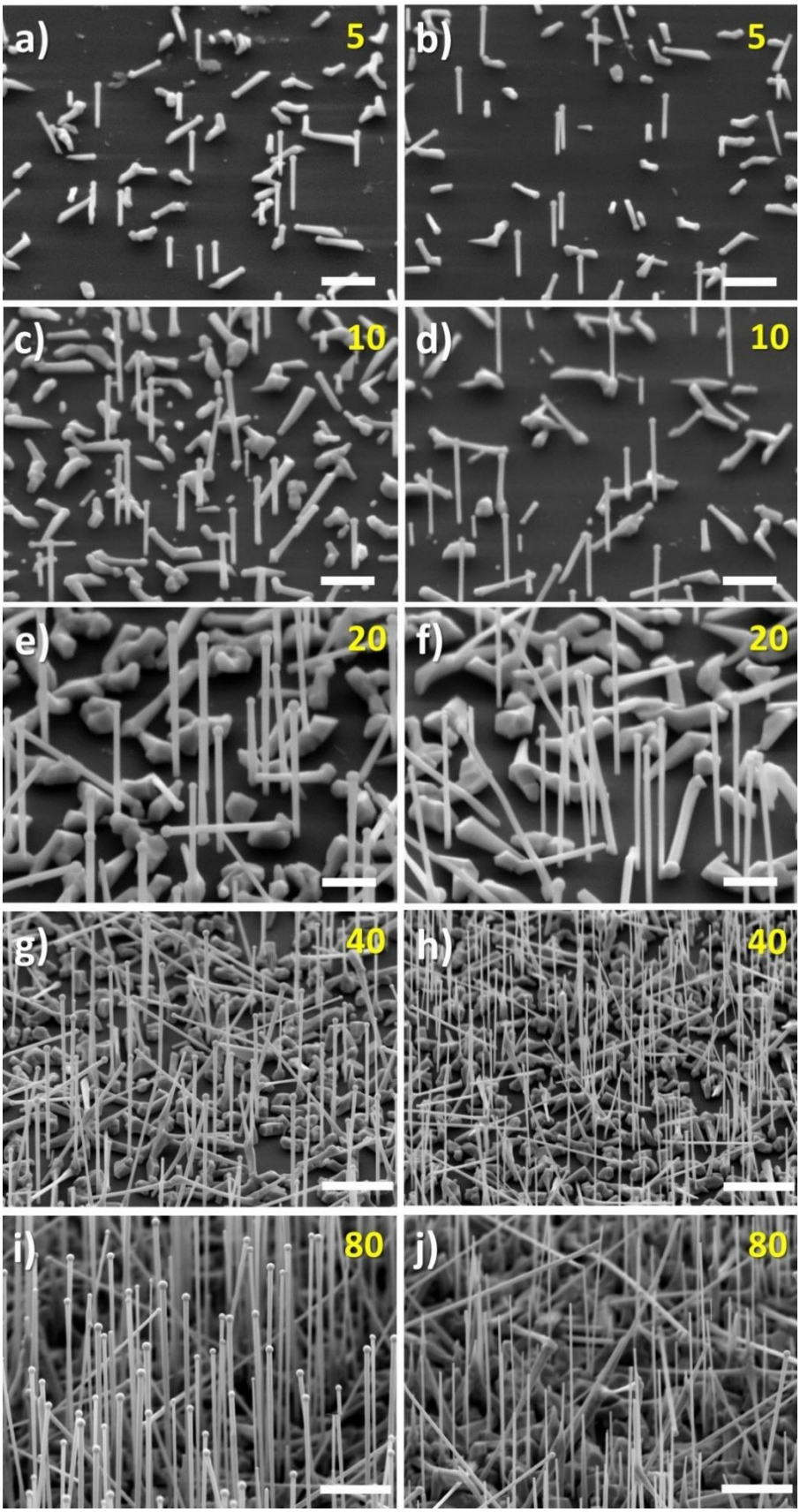

Figure 3.12. 45°-tilted SEM images of Ga(5)As NWs (a, c, e, g, i) and Ga(7)As NWs (b, d, f, h, j) as a function of the growth time (growth time in minutes indicated by yellow number). The white scale bars correspond to 500 nm in (a, b, c, d, e, f) and to 2 µm in (g, h, i, j).

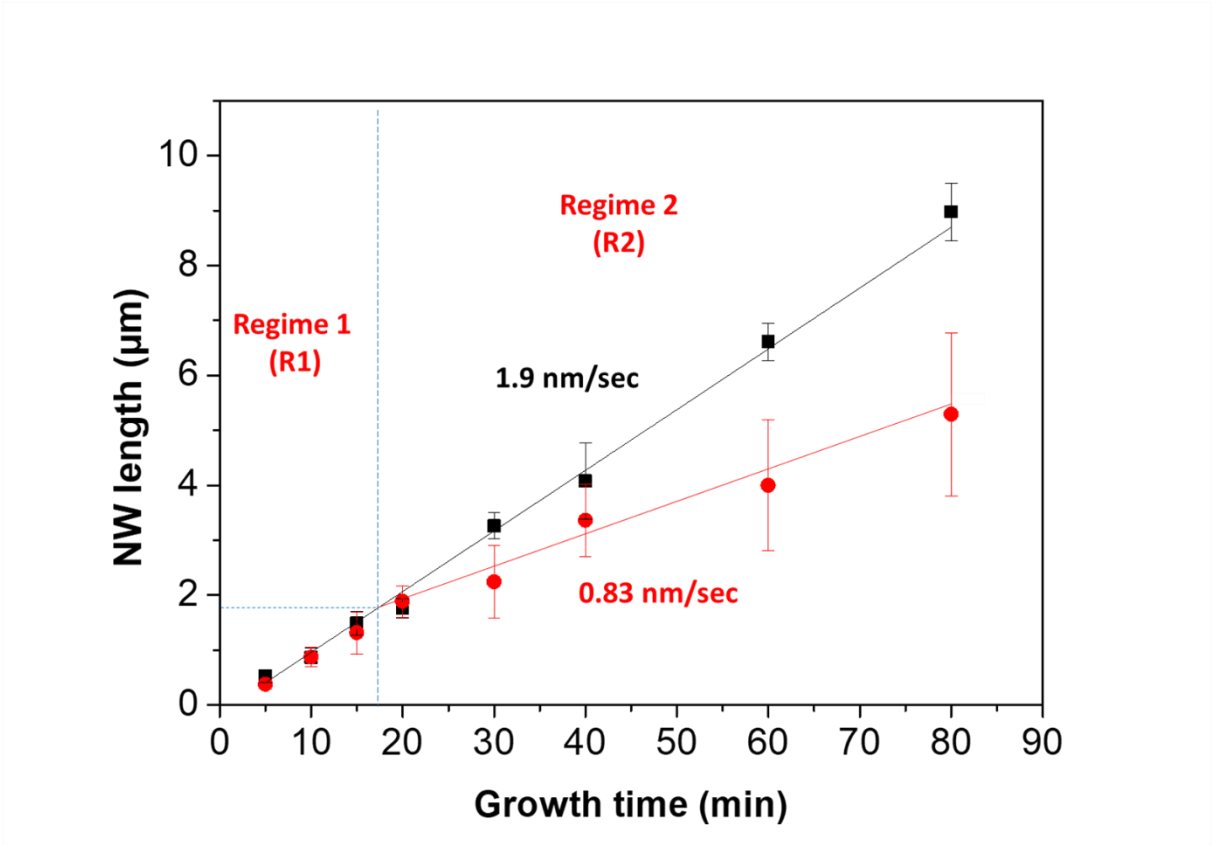

Figure 3.13. Length of Ga(5)As NWs (black) and Ga(7)As NWs (red) as a function of the growth time. The vertical dashed blue line mark the separation between the two growth regimes observed for Ga(7)As NWs, while the horizontal one shows the corresponding NW length.

Not only the length but also the diameter is affected by α, as illustrated in Figure 3.14; herein it can be noticed that the diameter of Ga(5)As NWs and Ga(7)As NWs increases linearly with the growth time but the Ga(7)As NW diameter increases much more slowly than those of the Ga(5)As NWs .

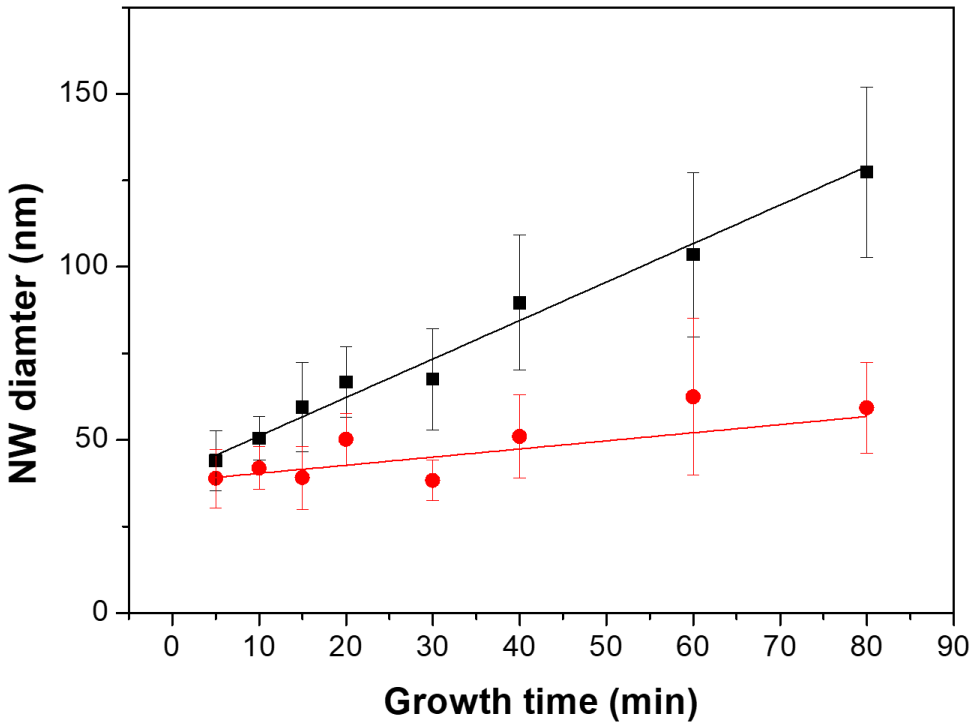

Figure 3.14. Diameter of Ga(5)As NWs (black) and Ga(7)As NWs (red) as a function of the growth time.

In order to determine whether linearity persists also for shorter growth times, we grew Ga(5)As NWs and Ga(7)As NWs also for 20 sec, 1 min and 3 min (Figure 3.15). Although these samples were grown with a higher ratio R(F_V/F_{III}) than the standard value of 2.3 (likely ≈ 3.1) because of a technical problem with the gauge that prevented an exact measurement of the As flux, we decided to compare them with the previous series of data of Figures 3.13 and 3.14. Graphics of the NW length and diameter as a function of the growth time are reported in Figure 3.16: black and red spots correspond to Ga(5)As and Ga(7)As growths respectively, while squares and triangles correspond respectively to R(F_V/F_{III}) of 2.3 and likely ≈ 3.1.

The difference in R(F_V/F_{III}) between shorter (≤ 3 min) and longer (≥ 5 min) growth times is not so significant in this particular analysis, since our purpose is to define a qualitative trend of the curves rather than a quantitative ones, therefore small discrepancies between the two cases can be still considered as acceptable. Observing the evolution of the NW length as a function of the growth time in Figure 3.14(a), it can be noticed that both Ga(5)As and Ga(7)As curves have a substantially linear trend.

On the contrary, it can be observed that the trends in the graphic of the diameter as a function of the growth time in Figure 3.16(b) are quite different, showing that the diameter increase rapidly for short growth times before passing to a linear regime for the longer ones.

These differences in diameter evolution are confirmed by the comparison of the SEM images of the two cases. Given the tapering coefficient:[140]

$$T_{\%} = \frac{(D_t - D_b)}{L} \cdot 100$$

with D_t and D_b diameter at the top and the bottom of the NW, respectively, $T_{\%}$ results equal to 4-6 % for shorter growth times, but only 0.5-1% for the longer ones. As a consequence, it is possible to say that for both Ga(5)As and Ga(7)As the NW diameter increases much faster in the first 5 min of growth rather than in longer times.

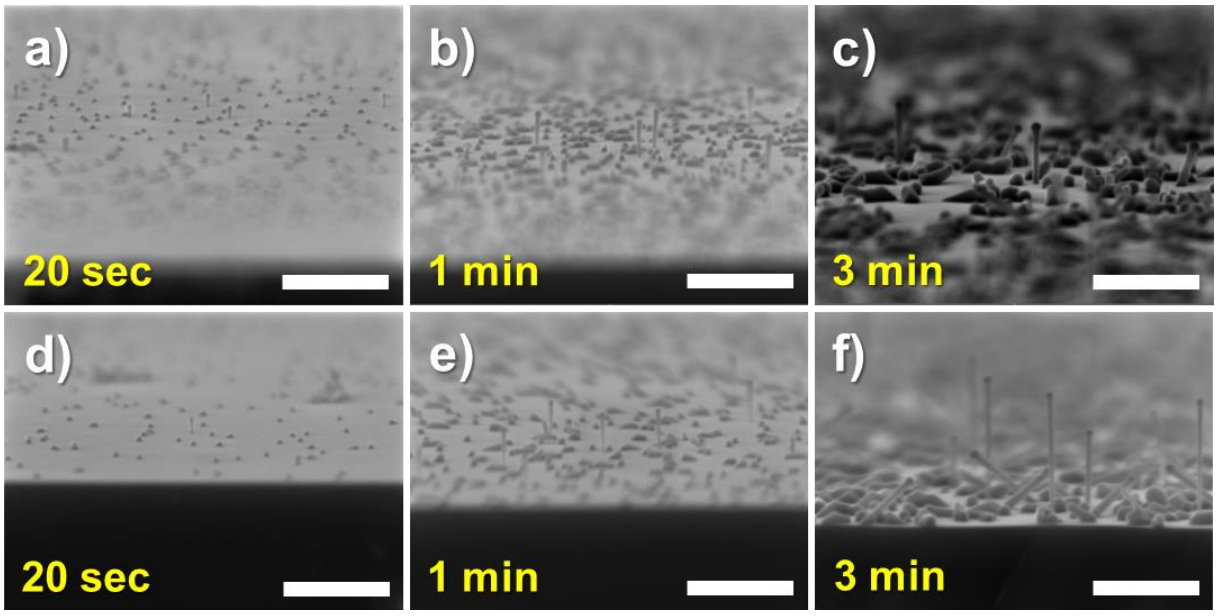

Figure 3.15. SEM images (5°-tilted cross section) of (a, b, c) Ga(5)As NWs and (d, e, f) Ga(7)As NWs grown for short times. The white scale bars correspond to 500 nm.

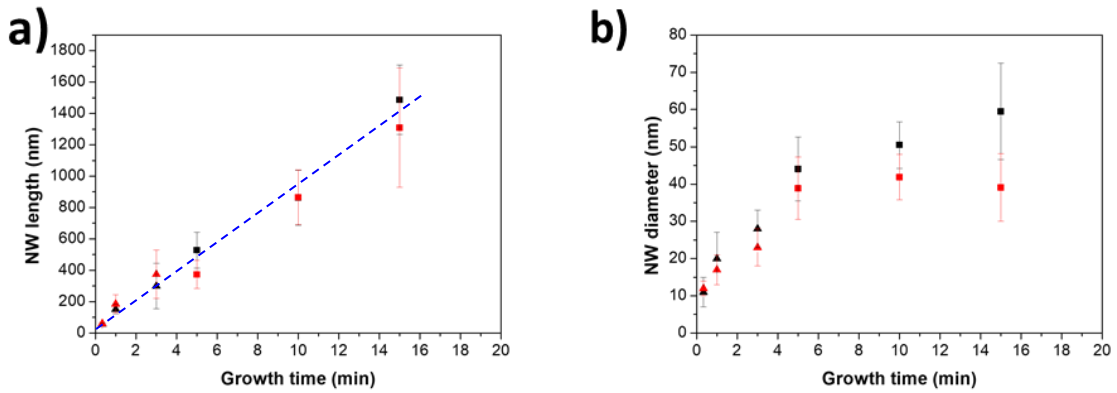

Figure 3.16. Graphics of: (a) the NW length and (b) diameter as a function of the growth time. Black and red curves correspond to Ga(5)As NWs and Ga(7)As NWs, respectively, whereas triangles and squares stand respectively for shorter time growths (≤ 3 min), (likely) realised with $R(F_V/F_{III}) \approx 3.1$, and for longer ones (≥ 5 min), performed with $R(F_V/F_{III}) = 2.3$.

Based on these results it can be concluded that, under the same experimental conditions, the incident angle α of the Ga flux plays a fundamental role in the NW growth. In order to analyse these results, we have used the model developed by Tchernycheva et al[2] to the case of self-assisted GaAs NW growth to evaluate: 1 the Ga flux and the related amount of Ga atoms which contribute to the filling of the Ga droplets as a function of the capture surface (and thus of α), and 2- the amount of Ga atoms involved in the growth of the GaAs NWs and thus contributing to the emptying of the Ga droplets.

3.4.3 The semi-empirical analytic model

As mentioned in the model of Tchernycheva et al,[148] the atoms coming from the Ga flux are collected by the Ga droplets via 1- direct impingement, 2- diffusion on the NW facets, 3- diffusion on the substrate. We remind the reader that in this model no desorption of Ga adatoms is considered. Generally speaking, given a certain surface of capture S_{capt}, the amount of atoms Q_{capt} collected per second and per unit of surface under a nominal flux having an incidence angle α with the NW growth direction, further denoted $F^{N\alpha}$ (cf. Figure 3.17), corresponds to:

$$Q_{capt} = S_{capt} F^{N\alpha}$$

and is expressed in ML nm^2 sec^{-1}.

Thus, we have to express and calculate: 1- the capture surfaces S_{capt} for these 3 cases as a function of α, and 2- the nominal flux $F^{N\alpha}$.

Concerning the nominal flux of Ga(5) and Ga(7) cells, they can be calculated from the Ga flux F_{sub}, measured on the surface S of the substrate taking into account the projected surface S' (cf. Figure 3.17) by:

$$F_{sub} = F^{N\alpha} \sin\theta = F^{N\alpha} \cos\alpha$$

As already mentioned in Chapter 2, F_{sub} can be expressed as the growth rate in ML/s, measured by RHEED, of a 2D GaAs layer.[154] Hence, in our particular case with F_{sub} = 0.5 ML/sec, it follows that the nominal fluxes $F^{N\alpha}$ of Ga(5) and Ga(7) cells are:

$$F^{N\alpha}_{Ga(5)} = \frac{0.5\ ML/sec}{\cos\alpha} = \frac{0.5\ ML/sec}{\cos 27.9°} = 0.57\ ML/sec$$

$$F^{N\alpha}_{Ga(7)} = \frac{0.5\ ML/sec}{\cos\alpha} = \frac{0.5\ ML/sec}{\cos 9.3°} = 0.51\ ML/sec$$

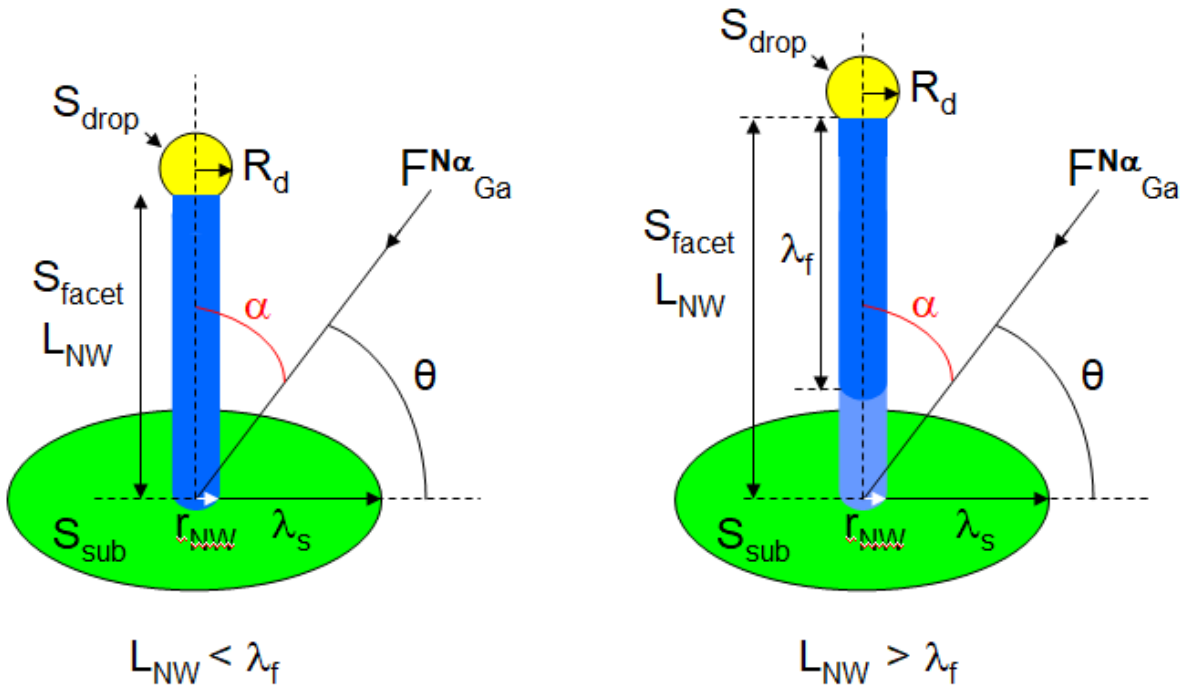

Figure 3.17. Schematics to define the different parameters used in the model.

<u>NB:</u> It can be noticed that, considering that the flux captured by the NW facet, F_{facet}, is equal to:

$$F_{facet} = F^{N\alpha} \sin \alpha$$

It results:

$$F_{facet} = \frac{F_{sub}}{\cos \alpha} \sin \alpha = F_{sub} \tan \alpha$$

To calculate Q_{capt}, as above mentioned, three different capture surfaces are to be considered: on the substrate (S_{sub}), on the NW facets (S_{facet}), and on the Ga droplet (S_{drop}), schematised in green, blue and yellow respectively, as reported in Figure 3.17.

These can be expressed as following:

For S_{sub}:

$$S_{sub} = [\pi(r_{NW} + \lambda_s)^2 - \pi {r_{NW}}^2] \cos \alpha$$

where λ_s is the diffusion length of the Ga adatoms on the substrate and r_{NW} the NW radius.

For S_{facet}, we have to consider two cases as a function of the NW length L_{NW}:

1- If $L_{NW} \leq \lambda_f$ the diffusion length on the NW facets:

$$S_{facet} = 2r_{NW}L_{NW}\sin\alpha$$

2- If $L_{NW} > \lambda_f$

$$S_{facet} = 2r_{NW}\lambda_f\sin\alpha$$

For S_{drop}, if we consider a semi-spherical droplet with a contact angle β equal to π/2, it is:[155]

$$S_{drop} = \frac{(1+cos\alpha)\pi {R_d}^2}{2}$$

where R_d is the droplet radius, which can be expressed as: $R_d = r_{NW}/\sin\beta$.

Note that, assuming a Ga droplet with a contact angle β = 135°, i.e. in the case where $\beta \geq \alpha + \pi/2$, S_{drop} becomes: [155]

$$S_{drop} = \pi {R_d}^2$$

thus being independent of α.

For the sake of simplicity, in this simple model we will consider a constant droplet volume during the NW growth.

The total surface of capture S_{capt} being the sum of each contribution, it is possible to notice that S_{capt} depends on L_{NW}. Accordingly, different phases can be identified in the growth as a function of L_{NW} (cf. Figure 3.18).

$S_{capt.}$ =	S_{sub}	+	S_{facet}	+	S_{drop}	
$S_{capt.}$ =	$[\pi(r_{NW}+\lambda_s)^2 - \pi r_{NW}^2]\cos\alpha$	+		+	πR_d^2	$L_{NW} = 0$
$S_{capt.}$ =	$[\pi(r_{NW}+\lambda_s)^2 - \pi r_{NW}^2]\cos\alpha$	+	$2r_{NW} L_{NW} \sin\alpha$	+	πR_d^2	L_{NW} [0-λ_f]
$S_{capt.}$ =		+	$2r_{NW} \lambda_f \sin\alpha$	+	πR_d^2	$L_{NW} > \lambda_f$

Figure 3.18. Expression of the capture surface depending on L_{NW}, with a droplet with β = 135°.

At the very beginning, when L_{NW} = 0, the only contribution to S_{capt} are S_{sub} and S_{drop}. Then, when L_{NW} is lower or equal to λ_f, S_{capt} includes also the contribution from the NW facets S_{facet}.

Subsequently, when $L_{NW} > \lambda_f$, S_{facet} is limited by λ_f. Note also that the Ga adatoms gathered from the substrate cannot reach anymore the Ga droplet, so that this contribution is suppressed.

Knowing that λ_s can be estimated around 100 nm[136,156,157] and that λ_f is about 1 µm,[158] it is thus possible to estimate the area of each surface of capture. The results of the calculations for the representative case of a NW with r_{NW} = 30 nm and a droplet with β=135°, are reported in Figure 3.19.

$S_{sub}^{Ga(5)}$ = 44420 nm²		$S_{drop}^{Ga(5)}$ = 5660 nm²	$L_{NW} = 0$
$S_{sub}^{Ga(7)}$ = 49610 nm²		$S_{drop}^{Ga(7)}$ = 5660 nm²	
$S_{sub}^{Ga(5)}$ = 44420 nm²	$S_{facet}^{Ga(5)}$ = 28080 nm²	$S_{drop}^{Ga(5)}$ = 5660 nm²	$L_{NW} = \lambda_f$
$S_{sub}^{Ga(7)}$ = 49610 nm²	$S_{facet}^{Ga(7)}$ = 9700 nm²	$S_{drop}^{Ga(7)}$ = 5660 nm²	
	$S_{facet}^{Ga(5)}$ = 28080 nm²	$S_{drop}^{Ga(5)}$ = 5660 nm²	$L_{NW} > \lambda_f$
	$S_{facet}^{Ga(7)}$ = 9700 nm²	$S_{drop}^{Ga(7)}$ = 5660 nm²	

Figure 3.19. Calculation of the capture surfaces (in nm²) depending on L_{NW}, in the case of a NW with r_{NW} = 30 nm and a droplet with β=135°.

In order to obtain the amount of Ga adatoms feeding the droplet, it is sufficient to multiply each term by the corresponding nominal flux (we remind the reader their values of $F^{N}\alpha_{Ga(5)}$ = 0.57 ML/sec and $F^{N}\alpha_{Ga(7)}$ = 0.51 ML/sec). These data, reported in Figure 3.20, denote a significant difference in terms of captured Ga atoms between the two Ga cells, in particular concerning S_{facet}.

Whereas for L_{NW} = 0, Q_{capt} is almost the same with both cells, a Ga(5)As NW gathers more Ga adatoms than its Ga(7)As counterpart as L_{NW} increases, i.e. when the contribution of S_{facet} becomes predominant (cf. Figure 3.20).

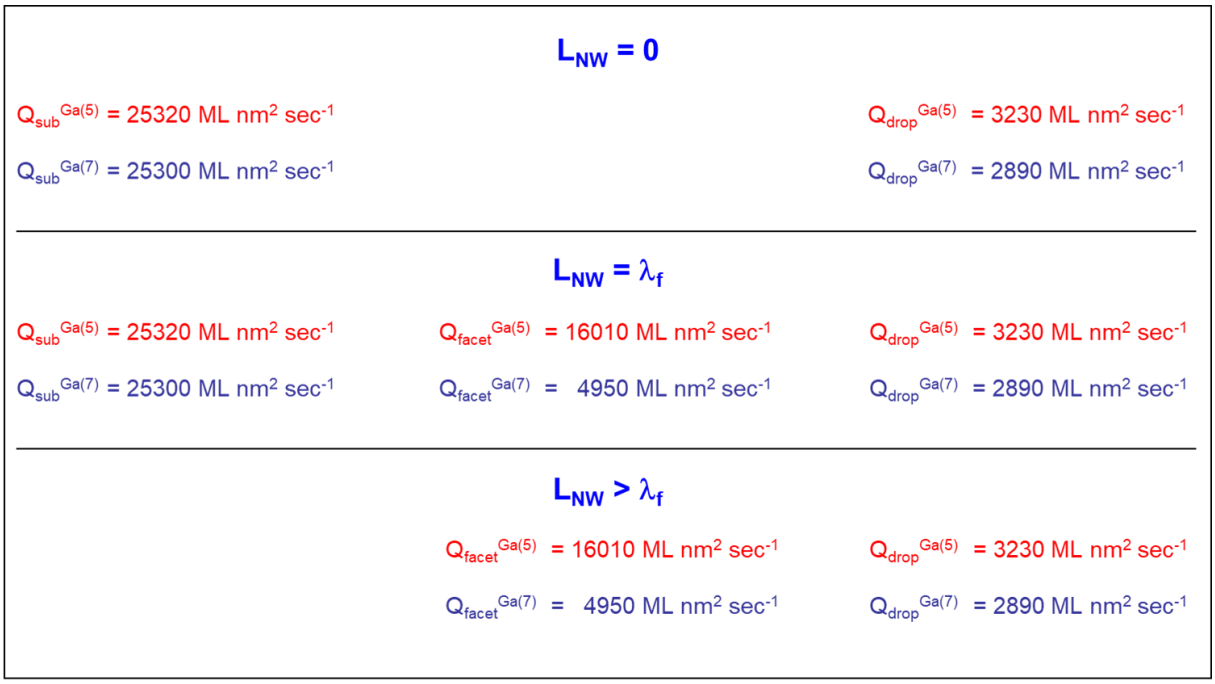

Figure 3.20. Calculation of the amount of Ga atoms collected by the Ga droplet (in ML nm^2 sec^{-1}) depending on L_{NW}, in the case of a NW with r_{NW} = 30 nm and a droplet with β=135°.

These results show the great difference in Ga atoms collected by the Ga droplet as a function of α, in particular when the NW length becomes greater than λ_f: 19240 ML nm^2 sec^{-1} with Ga(5) cell compared to 7840 ML nm^2 sec^{-1} with Ga(7) cell.

This difference may not be negligible if we compare the amount of collected Ga atoms with the amount of Ga atoms which are involved in the growth of the GaAs NWs and which contribute to the emptying of the Ga droplets.

If we consider a NW with r_{NW} = 30 nm with a typical axial growth rate of 1.9 nm/sec (measured in Regime 1) corresponding to about 6.7 ML/sec, the amount of Ga lost by the droplet Q_{lost} corresponds to:

$$Q_{lost} = 6.7 \text{ ML sec}^{-1} \cdot \pi 30^2 \text{ nm}^2 = 18940 \text{ ML nm}^2 \text{ sec}^{-1}$$

When we compare this value with those of $Q_{capt}^{Ga(5)}$ and $Q_{capt}^{Ga(7)}$, it is thus clear that once $L_{NW} > \lambda_f$, i.e. when there is no more Ga atom supply from S_{sub}, there will be a deficit of Ga atoms for Ga(7)As NW droplets, whereas the amount of collected Ga atoms is enough for supplying the Ga droplet in the case of Ga(5)As NWs (cf. Figure 3.21).

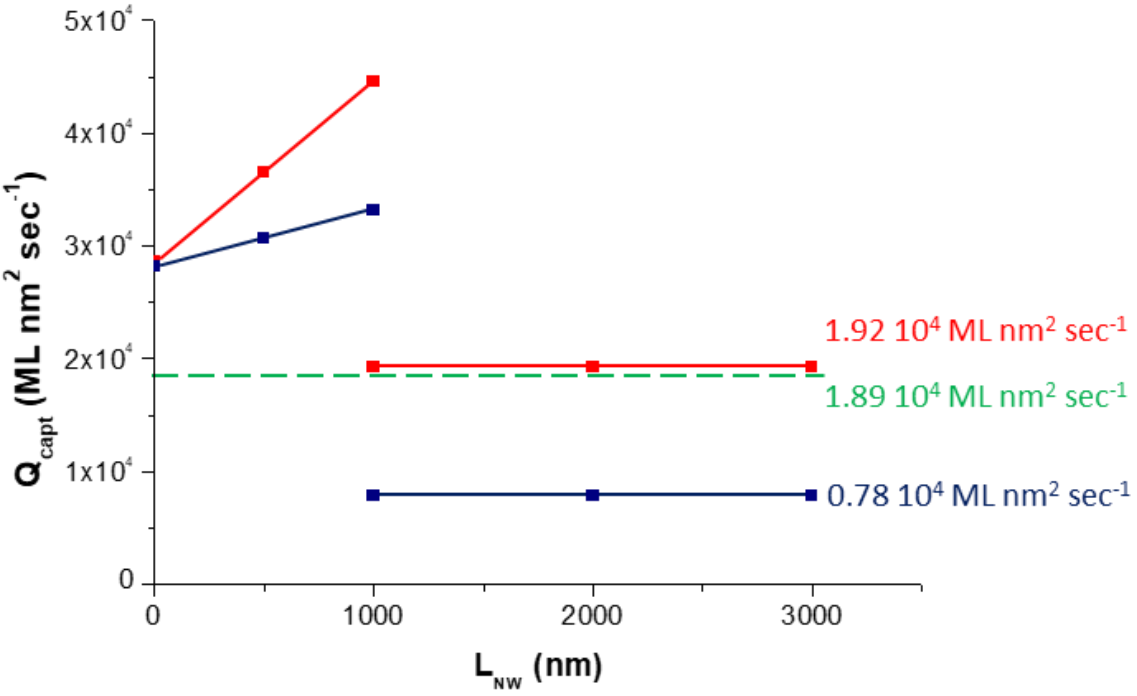

Figure 3.21. Quantity of Ga atoms captured per sec by the NWs as a function of their length for Ga(5) (red) and Ga(7) (blue) source. The green dashed line corresponds to the amount of Ga atoms lost by the droplet per sec during the NW growth.

Therefore, sources with a proper α (like Ga(5)) will be capable to supply enough Ga atoms to the NW droplet, whereas others (like Ga(7)) will not. In the latter case, the Ga droplet at the top of the NW will gradually decrease its volume, reducing progressively its contact angle (which explains why the droplets cannot be easily seen on Ga(7)As NWs grown for long times) and eventually disappearing, with the passage from a VLS to a VS growth regime.

This fact can explain not only the differences observed in terms of both length (cf. numerical simulations in Paragraph 3.4.4) and morphology between Ga(5)As and Ga(7)As NWs, but also those in diameter. In fact, if the quantity of Ga atoms provided to the droplet is larger than that one consumed, the Ga droplets will increase its volume, and so will the NW diameter.[140]

These considerations allows us to compute the minimum value needed to prevent the droplet consumption, in an operation of droplet engineering which can be adapted from case to case so as to potentially achieve better control on the NW size and morphology.

3.4.4 Numerical simulations

With a refinement of this semi-empirical model which takes into account the time-dependent shape and size of the droplet, numerical simulations were carried out in our

group by A. Danescu so as to evaluate the axial growth rate of the NWs as a function of Ga flux incidence angle α and therefore of the droplet volume and shape. It is now a matter of considering the capability of a Ga droplet to capture As atoms by direct impingement from the As flux. The objective of these numerical simulations is to evaluate, depending on α, the length of the NWs as a function of the growth time and to compare these values with the experimental results.

The implemented algorithm is based on a time-incremental procedure that:

1. Computes the amount of Ga atoms feeding the droplet either by direct impingement of the Ga-flux on the droplet surface or by adatom diffusion on the substrate and on the NW facets. This computation involves the geometry of the droplet and of the NW, the values of external fluxes and the diffusion lengths of Ga adatoms on the substrate and on the NW facets.

2. Computes the amount of As atoms feeding the droplet by direct flux.

3. Computes the fraction of Ga and As atoms available for the NW growth using the droplet geometry and the critical value of the As concentration in the droplet.

4. Updates on the NW length, droplet radius and contact (or wetting) angle.

The model is developed considering a constant NW radius and (like the one of Tchernycheva et al[148]) does not consider atom desorption.

The inputs for the algorithm are the initial values of the droplet radius (e.g. 30 nm), NW length (e.g. 10 nm), Ga and As fluxes of standard growth conditions, diffusion lengths (e.g. λ_{NW} = 1 µm on the NW facets and λ_S = 100 nm on the substrate, i.e. in good agreement with the values reported in the literature.[136,156–158]) and the critical As concentration in the droplet (e.g. 2.6 %). Note that, in a first approximation, the NW radius was considered constant and equal to 30 nm all along the growth. The numerical procedure predicts the evolutions with the growth time of the droplet radius and wetting angle, the capture surfaces for Ga and As atoms, to which we hypothesize the amount of Ga and As atoms which can be involved in the NW growth process is proportional, the As concentration in the droplet before the nucleation leading to the NW axial growth, and finally the NW length. Note that the capture surface for Ga atoms is the one which was calculated in the preliminary model presented in the previous section, but here it is obtained by taking into account the evolution of the droplet volume and shape during the NW growth (cf. Figure 3.22(f) below). Further details about the main concept of these calculations are reported in Annex 2.

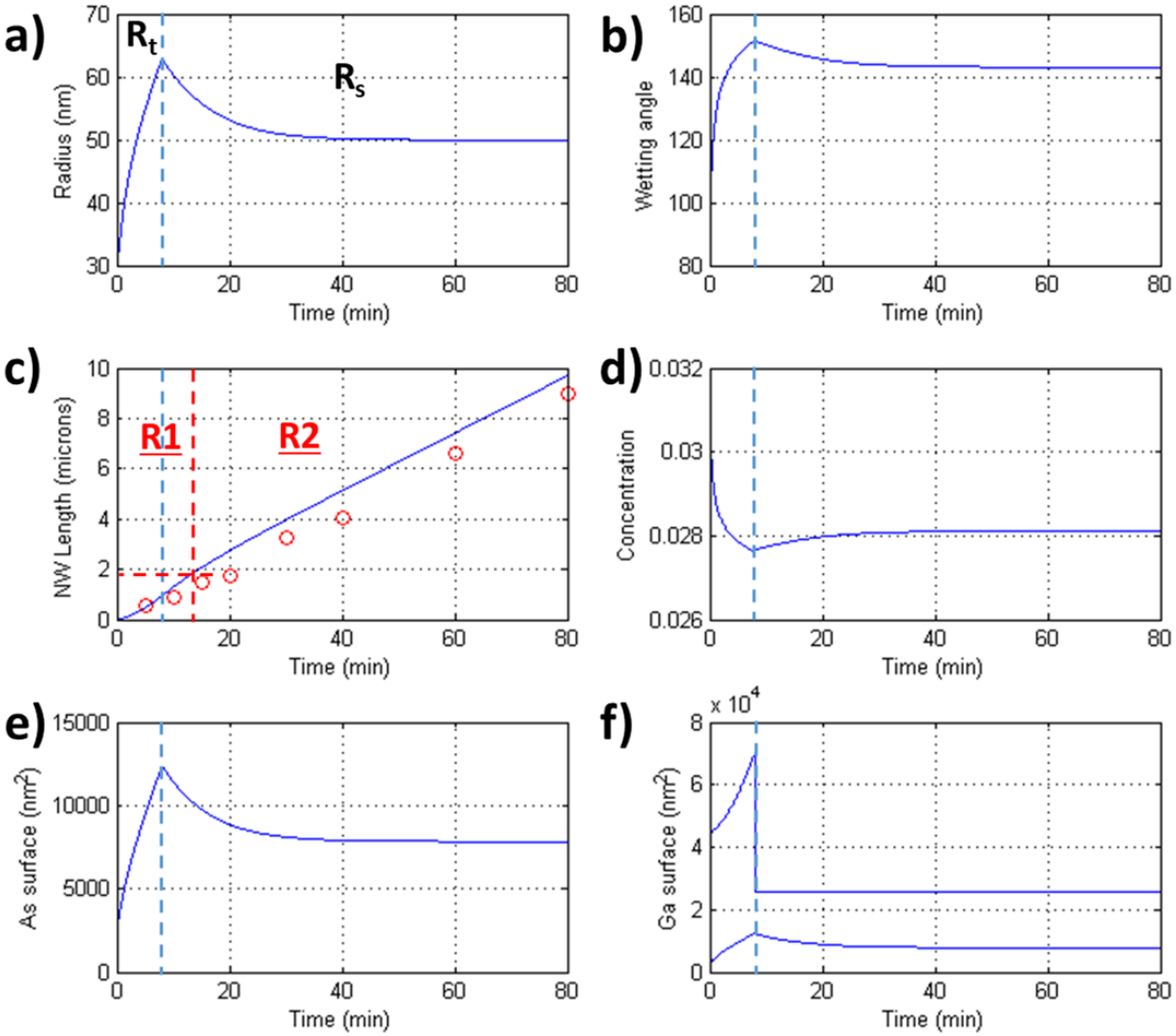

Figure 3.22. Simulation results (continuous blue curves) obtained for Ga(5) source, by using diffusion lengths λ_f = 918 nm and λ_s = 100 nm, (Δt = 0.5 sec and 9600 time steps). Evolution with growth time of: (a) droplet radius, (b) droplet contact (or wetting) angle, (c) NW length; the red circles correspond to the experimental points from Figure 3.13, (d) As concentration in the droplet before condensation, (e) droplet capture surface for As atoms and (f) capture surfaces for Ga atoms by diffusion on the substrate and on the NW facets (top curve), and by direct impingement on the droplet surface (bottom curve).

The results of the numerical simulations (with λ_f = 918 nm, see below why) are shown in Figure 3.22. From these results, it seems that the droplet evolves at growth time ≈ 8 min from a first regime, that we named “transitory regime”, R_t, where all the droplet parameters change, towards a second one, named “stationary regime”, R_s, with an asymptotic trend of the droplet parameters towards constants values, which are, as expected, dependent on the initial data. In this regime, the system parameters are such that an exact balance between the amount of Ga and As atoms feeding the droplet is achieved. It is interesting to mention that this stationary regime is "attractive", which means that slight variations of the

parameters still drive the system towards it. Similar results have already been obtained by simple models developed by Dubrovskii et al.[159] Concerning now the evolution of the NW length with growth time (Figure 3.22(c)), the simulation (blue line) displays two different growth regimes R1 and R2, with a regime transition at about 15 min (corresponding to NW length of about 1.8 µm). These two regimes are not observed on the curve obtained from the experimental points (red circles), where only one linear regime is observed.

It can be mentioned that in order to determine the slope of the Ga(5)As NW length evolution with the growth time in this stationary regime R_s, theoretical estimations lead to a value of the diffusion length of Ga adatoms on NW facets, λ_f = 918 nm. The evolutions of the droplet parameters and of the NW length were thus calculated assuming λ_f = 918 nm and λ_S = 100 nm (Figure 3.22). With these material parameters, even if the axial growth rate is correct in the R2 regime (cf. Figure 3.22(c)), we can observe that the values of the NW length in this regime are too high.

In order to improve the fitting and to achieve a higher correlation, simulations show that it is necessary to decrease the value of λ_S to 65 nm. In this case, it is possible to fit remarkably well the evolution of the NW length using the Ga(5) source, with a curve corresponding to a large linear regime (Figure 3.23(c)). The observation of only one regime, for experimental results (cf. Figure 3.13) and for simulation results, must be understood as being due to an equivalent axial growth rate slope for the R1 and R2 regimes. We remind the reader that, from the experimental curves (Figure 3.13), the axial growth rate for Ga(5)As NWs is always 1.9 nm/sec (≈ 7 ML/sec) whatever the NW length, whereas for Ga(7)As NWs it decreases to 0.83 nm/sec (≈ 3 ML/sec) after the transition from R1 to R2 regime corresponding to NW length of ≈ 1.8 µm.

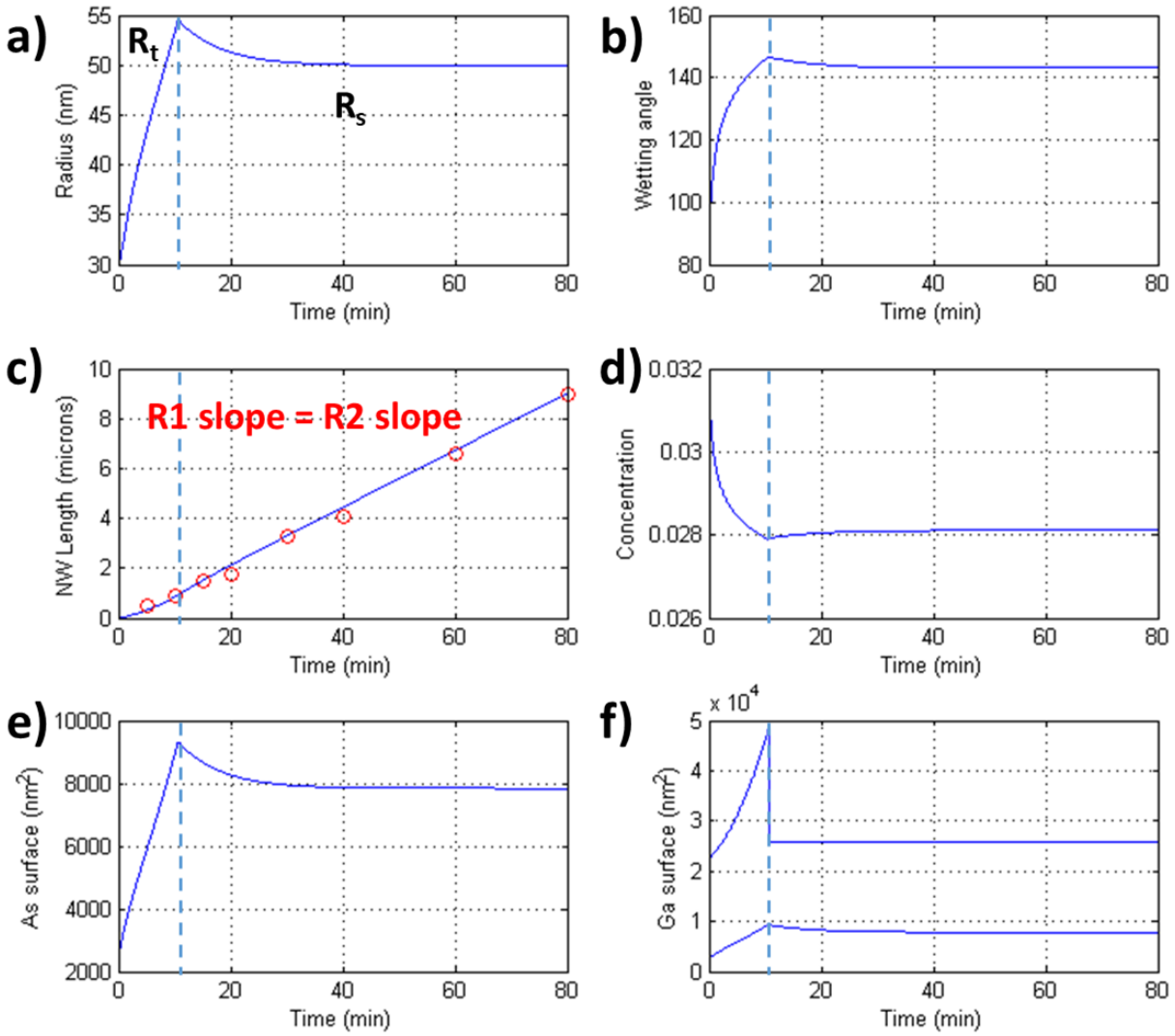

Figure 3.23. With λ_S = 65 nm, the experimental points from Figure 3.13 (red circle in (c)) for Ga(5) source are well fitted by the simulation results.

Using now the same material parameters, λ_{NW} = 918 nm and λ_S = 65 nm, with the Ga(7) source, the system evolution with the growth time is predicted as illustrated in Figure 3.24. For the NW length evolution (Figure 3.24(c) two regimes are highlighted with a transition from R1 to R2 at about 17 min (corresponding to NW length of about 1.5 µm), i.e. at a growth time equivalent to what it is observed on the experimental curve. However, while the main qualitative features of the experimental data are reproduced, it can be noticed that: 1- simulations lead to a critical NW length of ≈ 1.5 µm for the R1-R2 regime transition while experimental curve leads to a critical NW length of ≈ 1.8 µm, and 2- the NW length predicted in the stationary regime is lower than that one observed in the experiments. This shows that the model lacks some of the physical phenomena involved in the growth process, in particular the initial values of the droplet and NW radius, and the radius increase of the NW with growth time (cf. Figure 3.16(b)). Moreover, the asymptotic value of the wetting angle obtained in the numerical simulations for the NW growth with the Ga(5) source (Figure

3.23) is larger than commonly reported values. This is of course, a straightforward consequence of the assumption that the NW radius is constant.

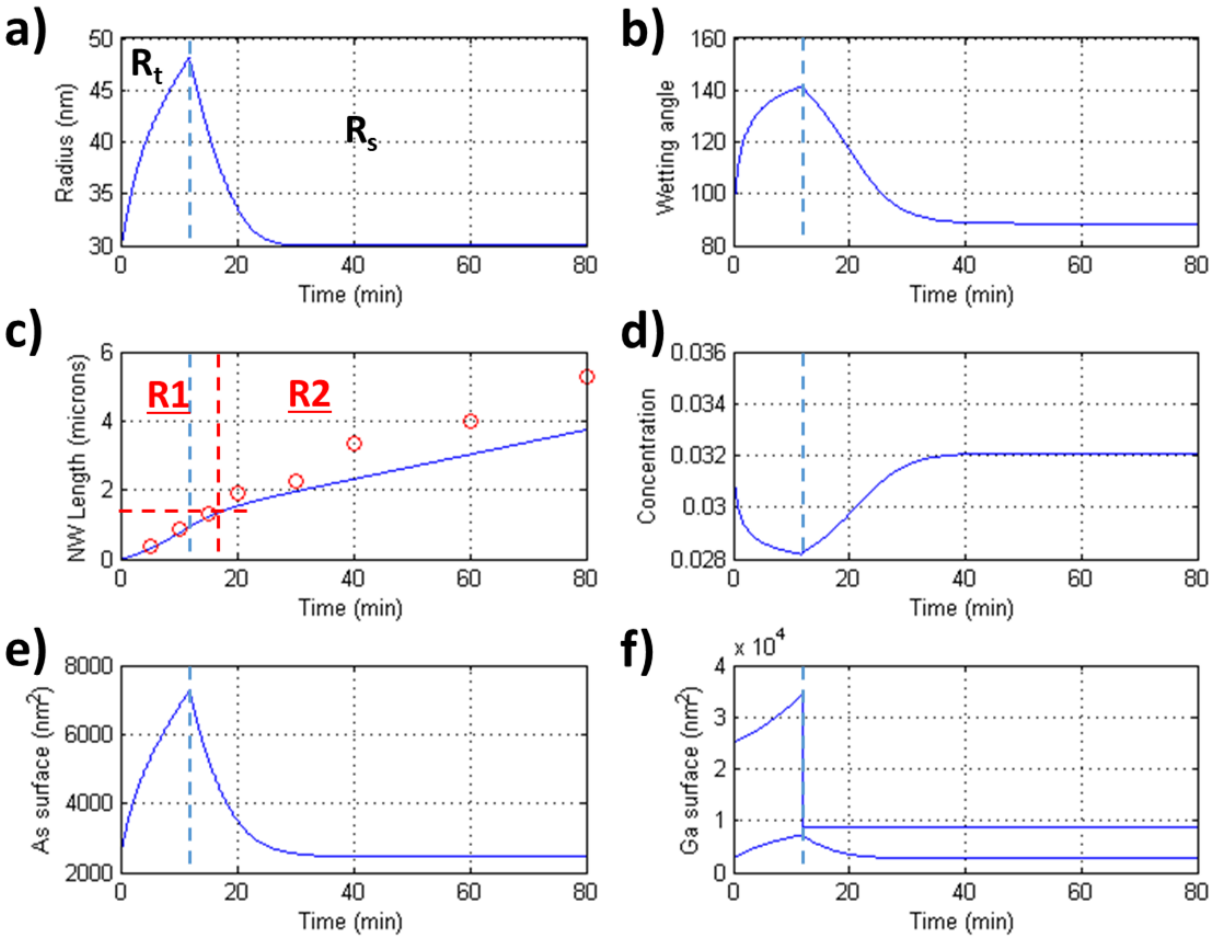

Figure 3.24. Simulation results (blue line) obtained for Ga(7) source, by using λ_f = 918 nm and λ_S = 65 nm. In (c), comparison of the NW length evolution with time and comparison with the experimental data (red circles).

A modified version of the model which accounts for all these considerations, as well as for the limitation of the wetting angle, leads to the results shown in Figure 3.25.

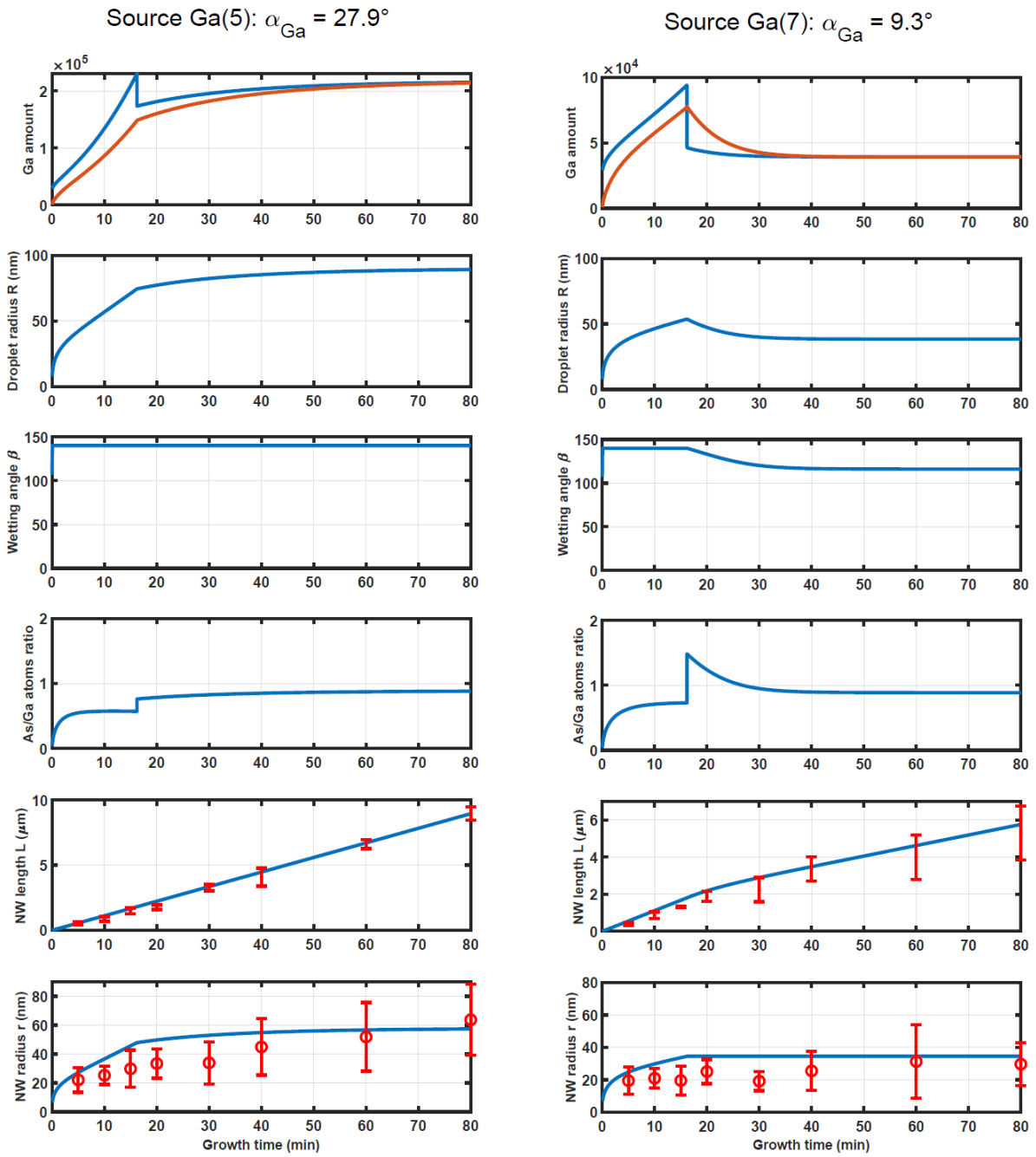

Figure 3.25. Numerical results (blue lines) obtained with the semi-empirical model for Ga(5) and Ga(7) sources. On the first line: the amount of Ga atoms supplying the droplet (in blue) and the amount of Ga atoms from the liquid droplet used for the NW growth (red), as a function of the growth time. On the next lines: droplet radius, wetting angle, the As/Ga atom ratio supplying the droplet, NW length (computed-blue; experimental-red) and the NW radius (computed-blue; experimental-red). Numerical parameters are identified by fitting only the Ga(5) experimental data (left column). Using the same model parameters, but for the Ga(7) source, we have obtained the numerical results (blue lines) in the right column, plotted together with the experimental data (red points and error bars).

Ultimately, we can state that our experimental results and their accordance with the simulations confirm the importance of the Ga flux incidence angle α in the self-assisted growth of GaAs NWs, as already claimed by other authors but not yet demonstrated with systematic experiments. Our model permits to link the evolution of the NW length during the growth with α by considering the Ga droplet feeding and, consequently, its changes of both volume and shape. In an indirect way, these play a significant influence on the capture surface of As atoms and, therefore, on the NW axial growth rate. In particular, we noticed that in the case of Ga(7), with a small incidence angle α, the balance of all Ga droplet supply mechanisms, and thus on its As atom capture surface, implies a critical length of about 1.8 µm (experimental value). Above this value, the droplet is no longer sufficiently supplied and stabilize to a smaller droplet radius of 30 nm (from simulation in Figure 3.24(a)) compared to the stabilized droplet radius of 50 nm (from simulation in Figure 3.23(a)) obtained with the Ga(5) source. The droplet features predicted by the simulations in the stationary regime are reported in Figure 3.26(a, b) for Ga(5) and Ga(7), respectively. In fact, we should notice that droplets with such shapes are correctly predicted by the results of the simulations on corresponding samples (Figure 3.26(c, d)).

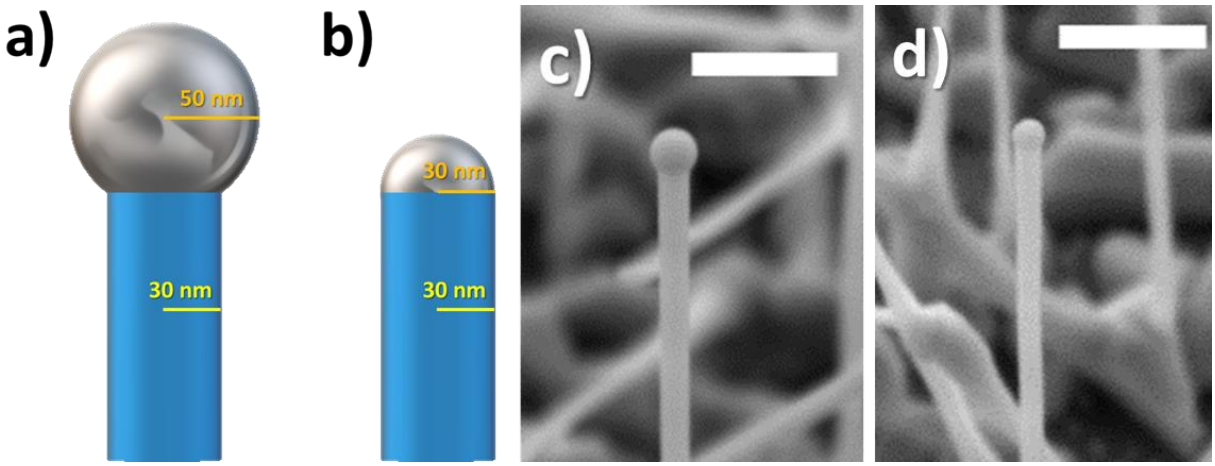

Figure 3.26. Schematics of the droplet shape and size in the stationary regime as predicted by the simulations for NWs with 30 nm radius in the case of: (a) Ga(5) and (b) Ga(7) sources. SEM images (45°-tilted) of corresponding: (c) Ga(5)As NWs and (d) Ga(7)As NWs; the white scale bars correspond to 500 nm.

This fact originates a second growth regime for Ga(7)As NWs longer than a critical length of about 1.8 µm, in which the growth mechanism is still VLS, but where the droplets tend to shrink, thus determining a capture surface for As and thus an axial growth rate which are lower than that one for their Ga(5)As counterparts.

Moreover, by observing the curves in Figure 3.23(d) and 3.24(d), it can be noticed that once in the stationary regime the As concentration in the droplet is slightly lower for Ga(5)

(2.8 %) than for Ga(7) (3.2 %). This fact suggests that the key parameter to determine the axial growth rate is not only the As concentration in the droplets but rather the overall amount of As atoms inside them. Considering that such a value is proportional to the capture surface of As atoms, which is equal to 8000 nm^2 for Ga(5) droplets (Figure 3.23(e)) and to 2400 nm^2 for Ga(7) droplets (Figure 3.24(e)), it follows the amount of As in the droplets, and consequently the NW axial growth rate, will be much higher in the former case.

3.4.5 Marker technique

Although improvements can still be made, especially to explain the results obtained with Ga(7)As NWs, the model proposed by our group seems already consistent with the results obtained in the series of Ga(5)As and Ga(7)As NWs. In order to study in detail the impact of α on the NW axial growth rate, we decided to investigate the growth kinetic of the GaAs NW with a marker technique, as previously reported by Galopin et al[152] and Ramdani et al.[153] The objective was to grow alternating sequences of Ga(5)As and Ga(7)As segments in the same NW, so as to be able to compare the effect of the incident angle on the axial growth rate of NW segments having the same diameter. To this end, thin $Al_xGa_{1-x}As$ markers were inserted periodically during the growth to delimit the different Ga(5)As and Ga(7)As segments, whose length was then evaluated by fine TEM measurements (Figure 3.27). Unless otherwise specified, all TEM measurements reported in this paragraph were recorded with zone axis [11-2] for detecting the compositional contrast.

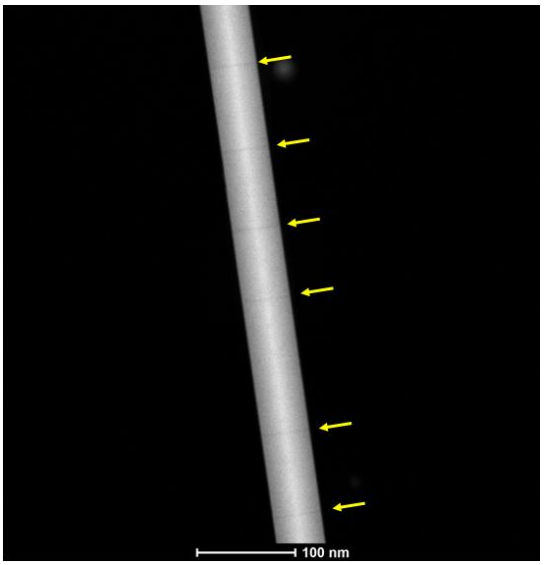

Figure 3.27: TEM image of a GaAs NWs with $Al_{0.5}Ga_{0.5}As$ markers (yellow arrows). These permit to measure the length of each segment as a function of its growth time. TEM imaging by G. Patriarche at C2N.

The HR-TEM image in Figure 3.27 shows that the employ of $Al_{0.5}Ga_{0.5}As$ markers is an effective method to distinguish the different segments. As a consequence, it is possible to measure accurately the length of each of them and to plot it as a function of their growth time.

The first growths in sequence were realised when not all the aspects and implications of our models had already been clarified, therefore it has proven necessary to prepare several samples so as to achieve the optimal growth conditions for our purposes. After a first sample of non-adapted sequences, a second one was realised as following: a Ga(5)As stem was grown for 20 min in standard conditions, then a first sequence of Ga(5)As segments grown for different times, and separated by $Al_{0.25}Ga_{0.75}As$ markers (1 sec growth time), was inserted. The sequence consisted in double segments deposited for 10, 15, 25, 35, 45 and 55 sec. Subsequently, a buffer segment of Ga(7)As was grown for 3 min before inserting a similar sequence of Ga(7)As segments. The growth was finally concluded with a final sequence consisting of two segments of Ga(5)As and Ga(7)As for 25 sec growth. A schematic of the structure is shown in the following Figure 3.28.

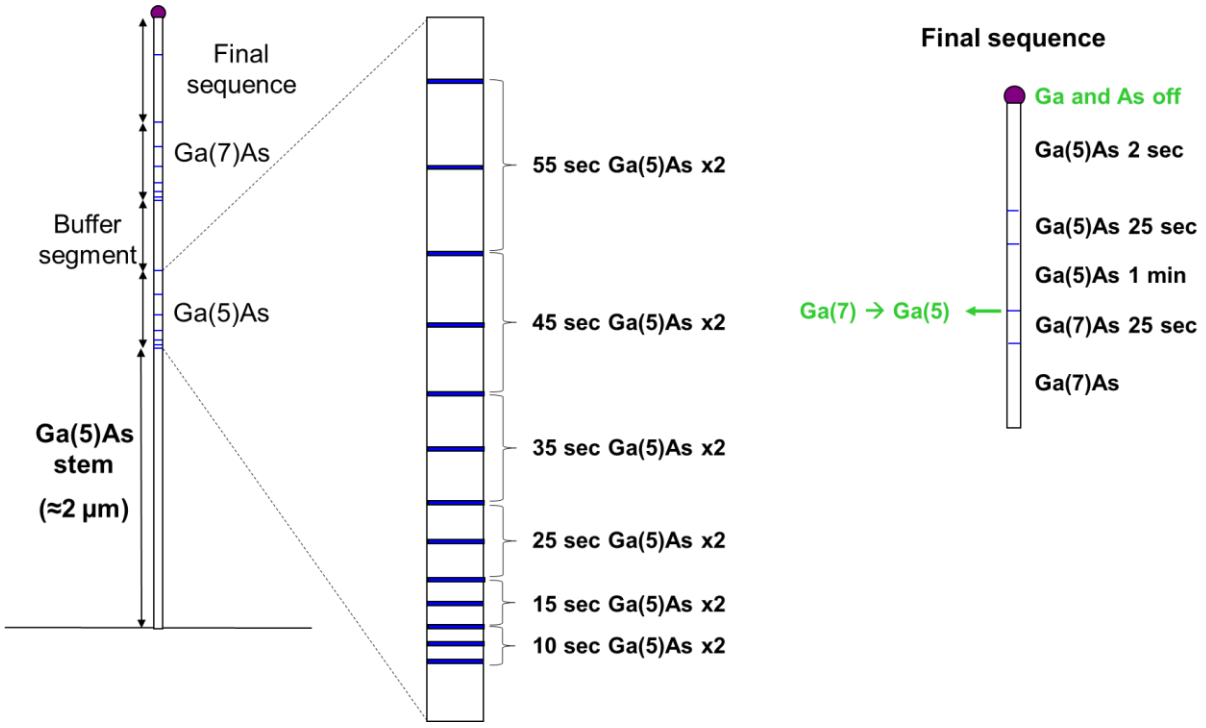

Figure 3.28. Schematics of the NWs grown with a Ga(5)As stem of 2 µm, a sequence of Ga(5)As segments, a sequence of Ga(7)As segments and a final sequence with Ga(7)As and Ga(5)As segments of 25 sec growth time each. The blue lines correspond to the $Al_{0.25}Ga_{0.75}As$ markers inserted to delimit each segment.

Observing the SEM and TEM images of this sample (Figure 3.29), it is possible to notice that the NWs show a reduced diameter on their tips or a reduced wetting angle of the droplet (cf. respectively yellow and red arrows in Figure 3.29(a)). From the TEM image in Figure 3.29(c), it is possible to see that this evolution occurs during the Ga(7) sequence and can thus be attributable to the partial consumption of the Ga droplet. Indeed, with the exposition to the Ga(7) flux, the droplet is not supplied enough with Ga, and for this reason it either reduces the diameter of the NW maintaining a similar wetting angle, or preserves the NW diameter while reducing the wetting angle.

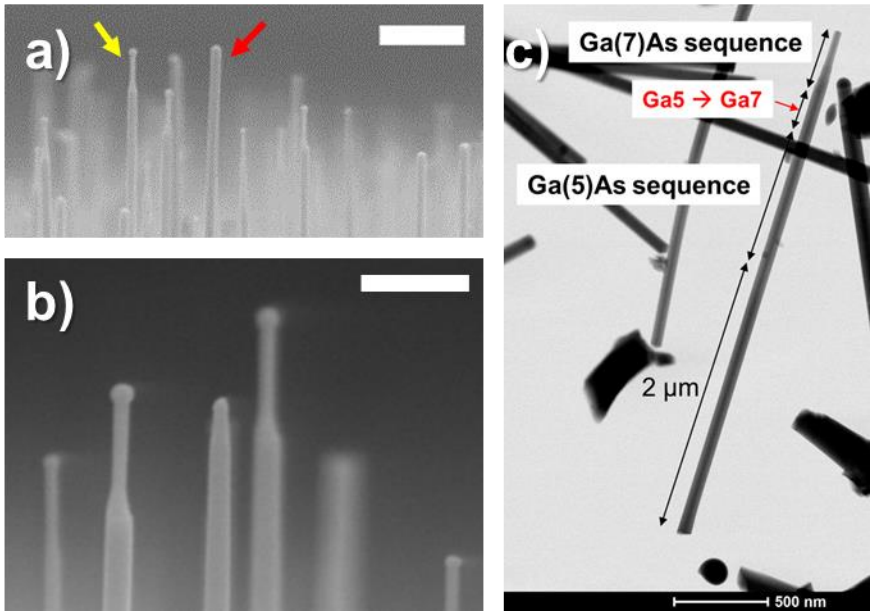

Figure 3.29. SEM images of NWs with alternate sequences of Ga(5)As and Ga(7)As segments (a, b). The yellow arrow in (a) shows a NW on which the diameter reduced while the contact angle of the droplet kept constant. The red arrow on the contrary shows the case of a NW with a constant diameter and a decreased wetting angle of the droplet. The white scale bars corresponds to (a) 1 µm and (b) 500 nm. (c) TEM image of one of this NWs: the stem, Ga(5) and Ga(7) sequences are reported.

Due to the long stem, it must be noticed that all sequences are situated above the critical length of 1.8 µm, beyond which the growth is in the R2 regime for Ga(7)As NWs. While the Ga(5) sequence is naturally not affected by this, the Ga(7) one might undergo a decrease in droplet volume and shape. Moreover, this decrease may be further enhanced by the fact that the addition of Al to realize the markers may have a detrimental effect on the droplet Ga alimentation, possibly causing the diffusion length of Ga adatoms to decrease (cf. our hypothesis in Chapter 4, Paragraph 4.2). This seems confirmed by the fact that the first $Al_{0.25}Ga_{0.75}As$ marker of the Ga(7)As sequence coincides with the beginning of the NW diameter decreasing (cf. Figure 3.30(c) below). As a consequence, NWs may show diameter shrinkage rather than diminution of droplet wetting angle at constant diameter. In this case,

it will not be possible to make a reliable comparison between the two sequences, having failed the aimed condition of a constant diameter.

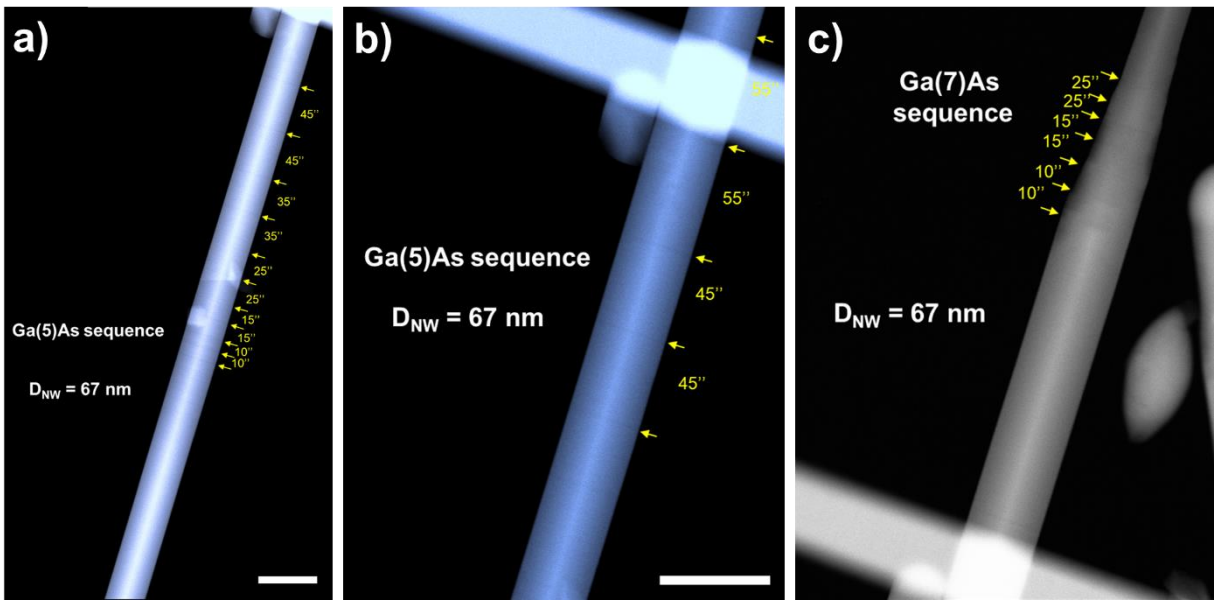

Figure 3.30. TEM images highlighting: (a, b) the Ga(5) sequence and (c) the Ga(7) sequence in the NW already illustrated in Figure D(c). The white scale bars correspond to 100 nm.

However, on those NWs where the Ga(7) sequence was (totally or partially) preserved from the droplet shrinkage, it is on the contrary possible to perform a comparison. This is the case of the NW reported in Figure 3.31, where shrinkage occurred only from the 45 sec Ga(7)As segment, so that it was possible to compare at least the first segments with their Ga(5)As counterparts.

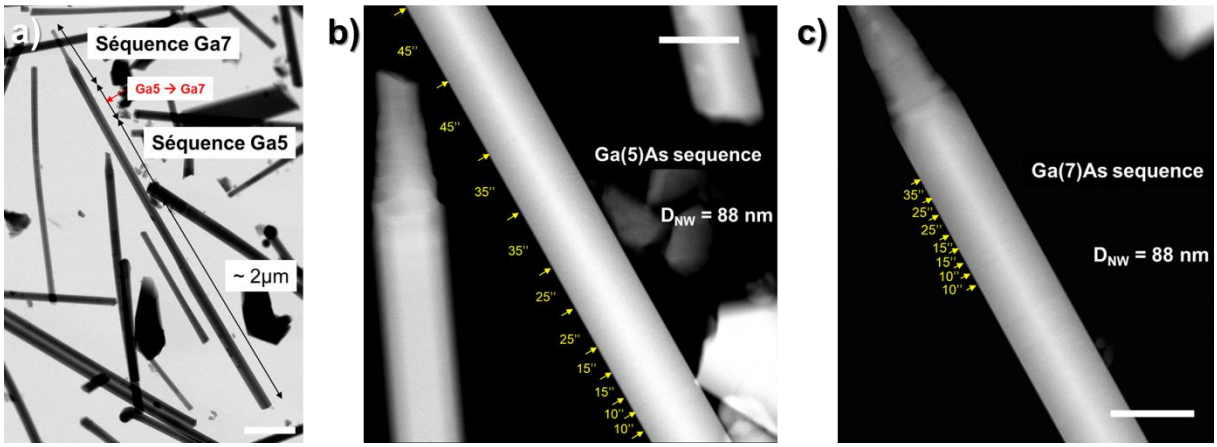

Figure 3.31. TEM images highlighting: (a) the analysed NW, (b) the Ga(5) sequence and (c) the Ga(7) sequence in the NW. In the latter case insertions up to 35 sec were not affected by droplet shrinkage. The white scale bars correspond to 100 nm.

Therefore, it was possible to obtain a first comparison of the axial growth rate through the graphic in Figure 3.32(a) for a NW with diameter equal to 88 nm, which displays the length of the segments as a function of their growth time. As expected, the axial growth rate is linear for both cases and much higher for the Ga(5) sequence than for the Ga(7) one. This is consistent with what is observed in Figure 3.13, the sequences being performed in a NW length greater than 1.8 µm, i.e. when the VLS growth had already passed to the R2 regime for Ga(7)As NWs.

Also, we reported on Figure 3.32(a) the evolution of the Ga(5)As segment length measured on NWs having different diameters. The evolution of the length of 35-sec Ga(5)As segments as a function of the NW diameter is reported in Figure 3.32(b). It can be observed that the trend for the axial growth rate is increasing with the NW diameter, and therefore with the droplet volume.

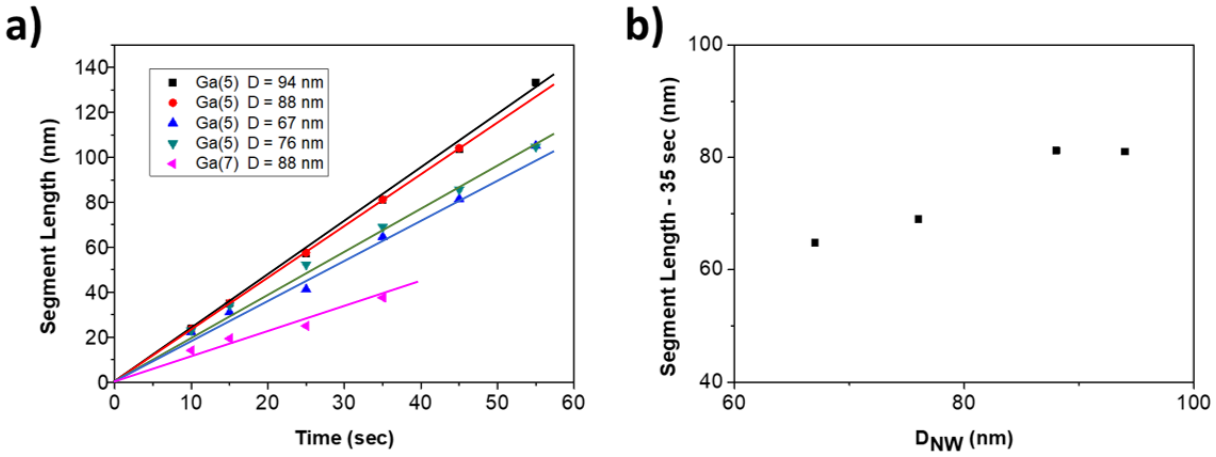

Figure 3.32: (a) Graphic reporting the length of Ga(5)As and Ga(7)As segments (grown above the critical length of 1.8 µm) as a function of their growth time. For Ga(5) sequence, the measurements were made on NWs with different diameters. (b) Graphic reporting the length of Ga(5)As segments grown for 35 sec from different NWs as a function of the NW diameter.

In order to realise sequences before the R2 regime for Ga(7)As growth, we firstly decided to reduce the stem length to 1.2 µm, and secondly to alternate the insertion of single Ga(5)As and Ga(7)As segments in the growing NWs, so as to prevent the accumulation of the effect of droplet shrinkage induced by the Ga(7) source and obtain an as-new Ga/GaAs interface at every source switch. Therefore, the NWs were grown as following: after 8 min growth of a Ga(5)As stem, alternated segments of Ga(5)As and Ga(7)As were grown for growth times of 10, 15, 25, 35, 45 and 55 sec. Each segment was delimited with $Al_{0.5}Ga_{0.5}As$ markers grown for 1 sec, and every segment was preceded by 30 sec growth of GaAs with the same source, so as to buffer the transient on the Ga fluxes caused by the cell closing and opening. The growth was concluded with a 2 min growth of Ga(5)As. A schematic of the structure is shown in Figure 3.33.

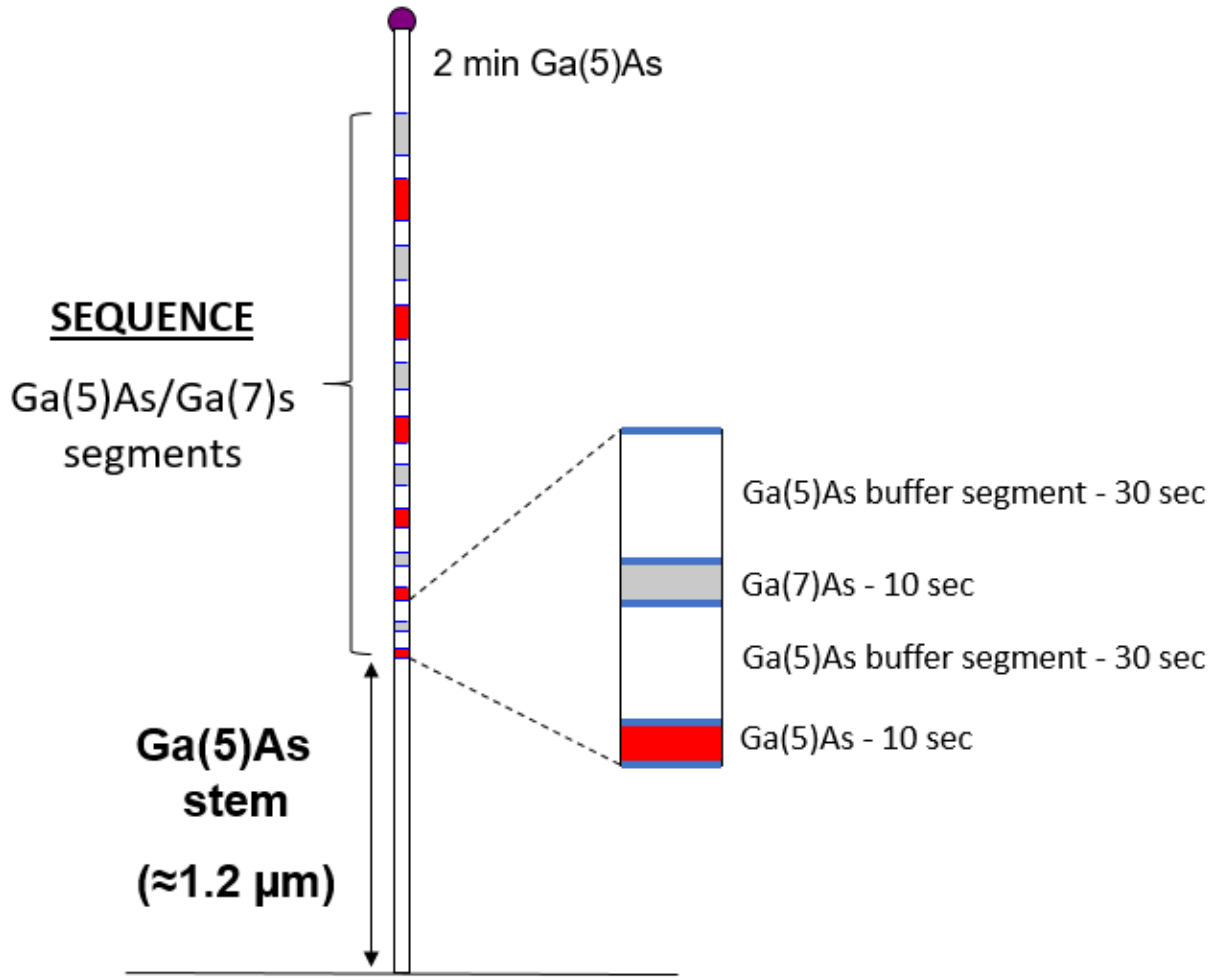

Figure 3.33: Schematics of the NWs grown with stem of 1.2 µm and alternated segments of Ga(5)As and Ga(7)As.

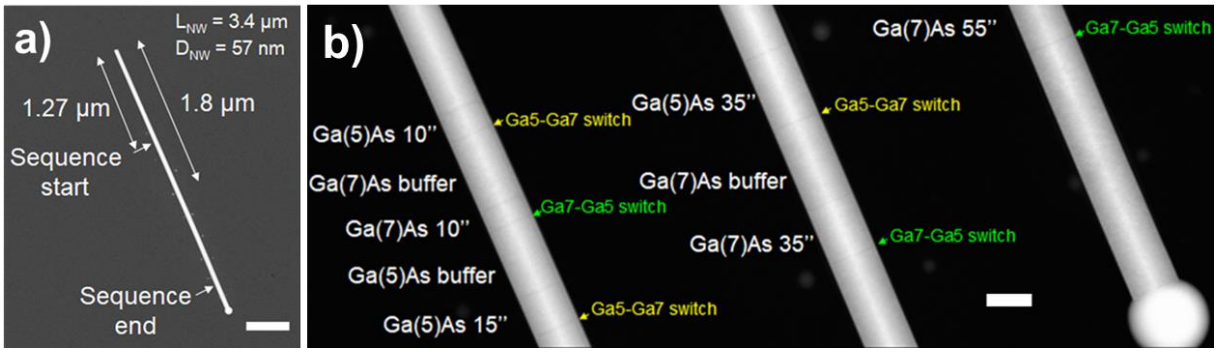

Figure 3.34. (a) TEM image of a GaAs NW showing the position of the sequence with alternated segments of Ga(5)As and Ga(7)As. (b) HR-TEM image of some Ga(5)As and Ga(7)As segments: the $Al_{0.5}Ga_{0.5}As$ markers delimiting each segment can be observed. The moments of the Ga flux switches are also indicated. The white scale bars correspond to (a) 500 and (b) 50 nm, respectively.

From the measurements realised on the NW shown in Figure 3.34, which can be considered as an exemplificative case, the length of the Ga(5)As and Ga(7)As segments can be reported as a function of their growth time (Figure 3.35(a)). It can be observed, once again, that the growth for Ga(5)As segments is faster than for Ga(7)As ones.

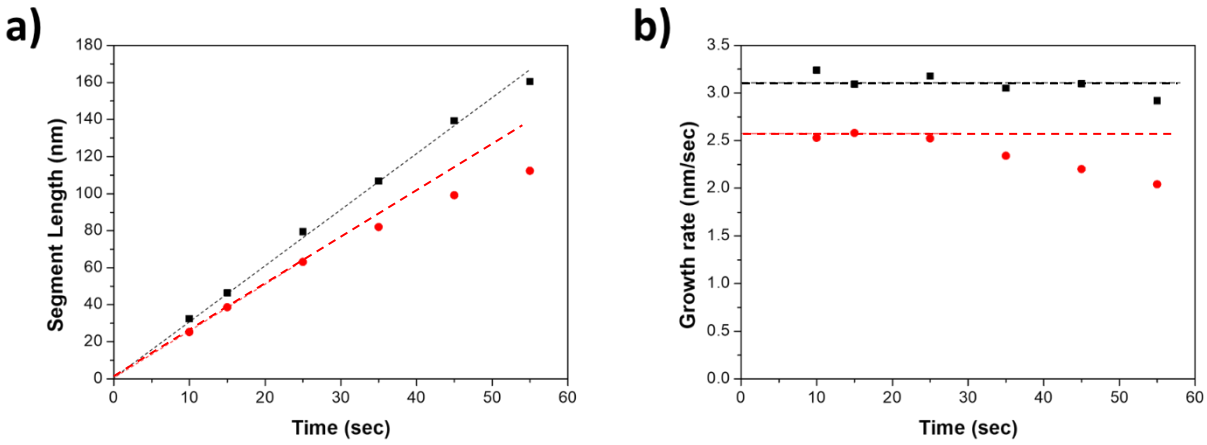

Figure 3.35. (a) Graphic reporting the length of Ga(5)As (black) and Ga(7)As (red) insertions in a single NW as function of the deposition time. (b) Growth rate of Ga(5)As (black) and Ga(7)As (red) segments as a function of their deposition time.

The axial growth rate is linear for all Ga(5)As segments, but only for the first points the Ga(7)As ones. Moreover, it is a little different and equal to 3.1 and 2.6 nm/sec, for Ga(5)As and Ga(7)As segments, respectively, considering only the first three points for Ga(7)As segments (Figure 3.35(b)). This can be explained considering that, although the sequences were started before achieving the critical length of 1.8 µm with Ga(7) source, they were realised when L_{NW} had already exceeded $\lambda_f \approx 1$ µm, i.e. in this particular moment at the beginning of the stationary regime (corresponding more or less to growth times of 12-25 min) when the decrease in droplet radius with the Ga(7) source is much higher than that with the Ga(5) one (cf. the slopes of the curves in Figure 3.24(a) and 3.23(a), respectively). As a consequence, the lower axial growth rate for Ga(7)As segments during this phase must be already due to this strong reduction of the droplet size. However, the little difference between the growth rates of Ga(5)As and Ga(7)As segments is detectable only with the marker technique in the case of segments grown in a NW with a constant diameter, whereas it is not observable in Figure 3.5 since it tends to disappear into the error margins of the experimental points.

TEM and HR-TEM images of a similar NW in length to that shown in Figure 3.34, were recorded with [1-10] zone axis (Figure 3.36). We observed that the NW stem and tip are pure, low-defected ZB, as expected with the growth conditions used, and that a high-volume droplet is present: these fact are consistent with the employ of Ga(5) as a source, which prevents the reduction of the droplet volume and of the wetting angle and, thus, favours the

ZB phase. However, between the stem and the NW tip, it can be seen faulted zones where a Wz phase can be identified in their center (marked with red crosses in Figure 3.36(a)). Because of the lack of a corresponding image from [11-2] zone axis, it is hard to associate such segments with a composition. However, given their number, their position, their increasing length and periodicity, we strongly believe that they correspond to the Ga(7)As segment positions. Such hypothesis is consistent with the fact that a reduction of the wetting angle caused by a lower Ga supply to the droplet with the Ga(7) source would tend to the formation of the Wz phase, as already predicted and observed.[134,137–139]

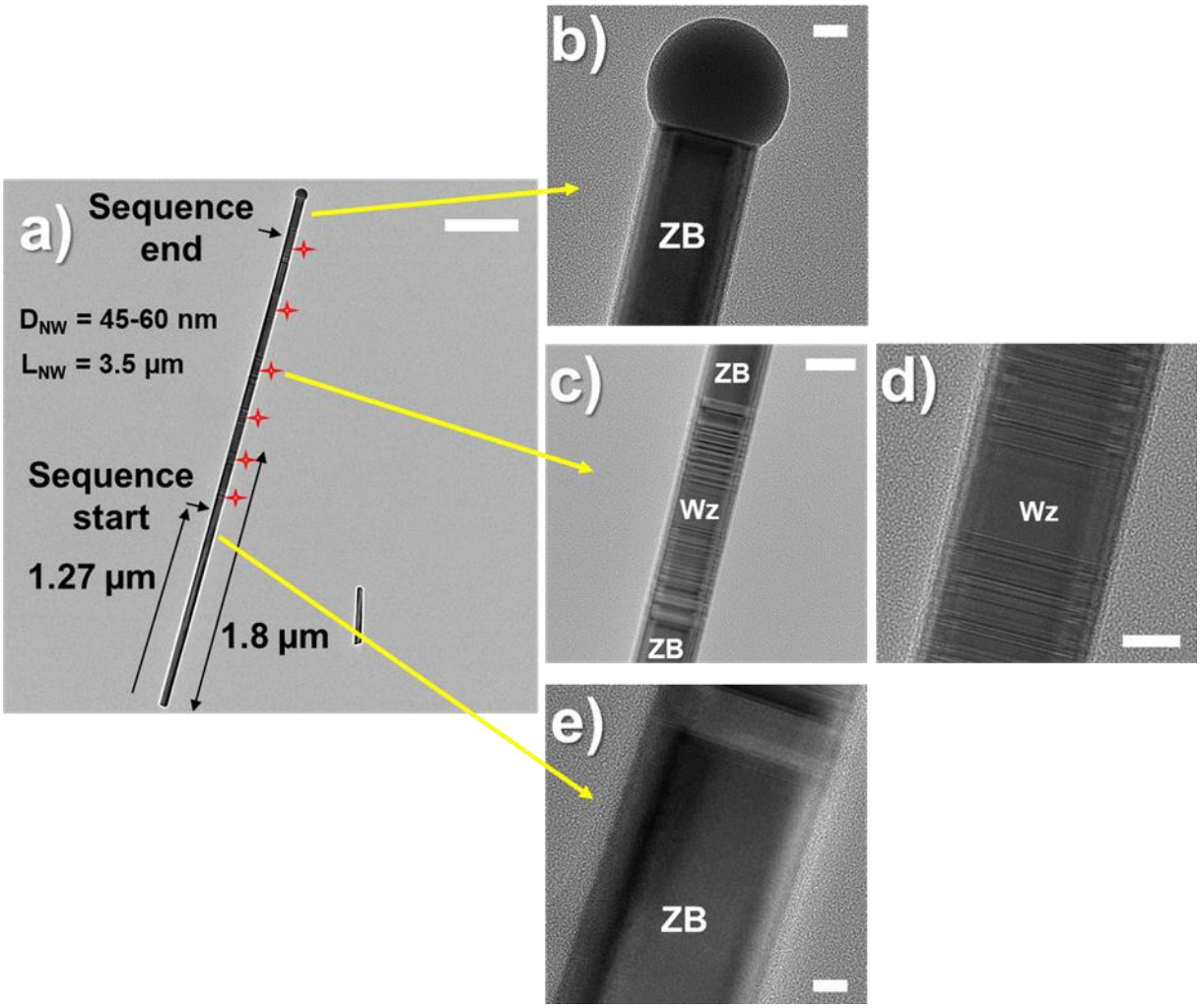

Figure 3.36. (a) TEM and (b-e) HR-TEM images of a similar NW like that one analysed in Figure 3.34, recorded with [1 -1 0] zone axis. (a) General view of the NW, with red crosses marking the faulted zones, attributable to Ga(7)As segments. (b) NW tip with Ga droplet; the crystal structure is pure ZB, (c, d) Highlights on a faulted zone with a Wz segment in the center. It can be identified as the 35 sec Ga(7)As segment. (e) Highlight on the Ga(5)As stem, having also a pure ZB structure. The white scale bars correspond to (a) 500, (b) 20, (c) 50, (d) 20 and (e) 10 nm.

3.5 Conclusion

In conclusion, from experimental and simulation results, it is demonstrated that the Ga flux incidence angle α has a strong influence on the amount of Ga atoms which can be captured by the droplets, leading to different droplet volumes, shapes and surfaces. It is also shown that the surface diffusion of Ga adatoms on Si substrates covered with a thin epi-ready oxide layer (1-2 nm-thick) has an important influence on the self-assisted growth of GaAs NWs, whereas Ga adatoms behave differently on patterned Si substrates covered with thicker SiO_2 masks (10-20 nm-thick), as firstly remarked by Krogstrup et al[136] and confirmed by Oeheler et al[160], as well as by our results (cf. Chapter 5). Indeed, when the supply of Ga adatoms from the diffusion on the epi-ready Si substrate stops (i.e. the NW length becomes greater than λ_f), it becomes possible to see a significant difference between the Ga(5) and Ga(7) cases, due to a smaller capture surface of Ga atoms by the NW facets for the Ga(7)As NWs compared to the Ga(5)As ones. Finally, it is also shown that the droplet volume and shape are one of the most important parameters for the self-assisted growth of GaAs NWs due to their influence on the As atom capture surface and thus on the amount of As atoms in the droplet, on which the axial growth rate depends.

4 The failure of AlGaAs axial growth and the synthesis of core/shell nanowires as a viable alternative

4.1 Introduction

In this chapter we report the results observed in the growth and characterization of NWs which were expected to constitute the building blocks of our TSC. Given the complexity, time and economic costs related to the fabrication of patterned substrates, we decided to developed good NW architectures with well-performing PV active regions on cheaper and more easily available substrates at first, before transferring the know-how on patterned substrates once acquired. For such a reason, these preliminary studies about the NW architecture were undertaken on epi-ready Si(111) substrates. All samples fabricated for these studies were grown on p-doped Si(111) substrates with a doping level in the $5 \cdot 10^{17}$-$2.5 \cdot 10^{18}$ cm^{-3} range.

According to the guiding principle of our work, this chapter can be divided into three main parts: the first concerning the attempts of growing AlGaAs NWs and their failures, the second regarding the growth of core/shell GaAs/AlGaAs NWs as a possible solution to overcome these failures, and the third one about the identification of a suitable material for the passivation shell.

4.2 The attempts to obtain AlGaAs axial growth

At the very beginning of HETONAN project we aimed to develop a top-cell constituted of $Al_{0.2}Ga_{0.8}As$ NWs, so as to provide the optimal band-gap of 1.7 eV to this sub-unit: in particular, we conceived the NWs as structures constituted of a Be-doped $Al_{0.2}Ga_{0.8}As$ core with intrinsic and Si-doped shells, thus obtaining a device based on radial p-i-n junctions. This fact implied the development of the Ga-assisted axial growth of $Al_{0.2}Ga_{0.8}As$ NWs, a task that immediately appeared arduous to accomplish, as suggested by the lack of bibliographic references. As a matter of fact, although the scientific literature reports some examples of AlGaAs NWs grown by MOVPE[161–163] and some examples of insertion of short AlGaAs segments in self-assisted GaAs NWs by MBE[153,164], to the best of our knowledge there is not any work attesting the Ga-assisted growth of AlGaAs NWs by MBE on Si substrates. The only examples so-far achieved of AlGaAs NWs grown by MBE consist in four articles by Wu,[165] Chen[166,167] and Barettin[168], reporting the Au-assisted growth of such structures on GaAs substrates. Despite these not very encouraging premises, we still thought it was worth trying to obtain Ga-assisted axial growth of $Al_{0.2}Ga_{0.8}As$ NWs, and we started therefore a series of

experiments to achieve this objective. In order to achieve a ternary alloy with the desired composition, all growths were performed adopting equivalent fluxes of 0.13 ML/sec for Al and of 0.5 ML/sec for Ga. The Ga source employed for all NW growths presented in this first study was the cell Ga(7), having an incident angle α = 9.3° to the sample normal.

Firstly, we try to obtain Ga-assisted $Al_{0.2}Ga_{0.8}As$ NWs on epi-ready Si(111): with such a purpose, we indeed pre-deposited 1 ML of Ga at 520 °C to form the droplets, then we deposited the ternary alloys at 600 °C for 10 minutes. The V/III flux ratio ($R(F_V/F_{III})$ in the following) adopted in this case was equal to 2.3 and 1.8 for GaAs and $Al_{0.2}Ga_{0.8}As$, respectively. This approach was totally unsuccessful, since all we could obtain was the formation of a rough 2D layer of material with some 3D crystals, as shown in the following Figure 4.1.

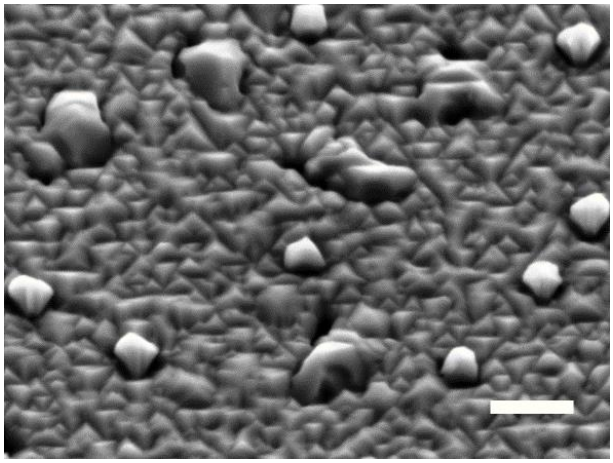

Figure 4.1. SEM image (45°-tilted) showing the failed attempt to obtain $Al_{0.2}Ga_{0.8}As$ NWs by depositing all precursors at 600 °C after Ga pre-deposition at 520 °C to form the catalyst droplets. The white scale bar corresponds to 500 nm.

Such a failure is attributable to the easy oxidation of Al adatoms in presence of silica, since the value of ΔH_R for the reaction

$$3\ SiO_2 + 4\ Al \rightarrow 2\ Al_2O_3 + 3\ Si$$

is about -808 kJ/mol (as calculated from the enthalpies of formation at 900 K reported in Reference[169]), thus making the Al oxidation favourable. This is confirmed by the XPS spectra in Figure 4.2, obtained after the deposition at 600°C of 2 MLs of Al with F_{Al} = 0.2 ML/s on an epi-ready Si wafer with about a 2 nm-thick native oxide layer (the sample was transferred from the MBE chamber to the XPS one in UHV). The Al2p core level main component is located at 75.7 eV, the Si2p core level at 99.4 eV being taken as binding-energy reference. This binding energy is between the value of 76.95 eV given for Al_2O_3 and the one of 72.6 eV for metallic Al,[170] thus suggesting the presence of a non-stoichiometric alumina or an aluminosilicate on the surface.

Concerning the Si2p signal, it can be noticed that the difference in energy between the peak of the bulky silicon (at 99.4 eV) and that one of the oxide (at 103.6 eV) is equal to to 4.2 eV, i.e. to the characteristic value for stoichiometric SiO_2, and with a peak intensity corresponding to a thickness estimated at 1-2 nm. Following Al deposition the oxide peak is still located at 103.6 eV, meaning that the composition of SiO_2 has not changed, but its intensity has become lower, thus denoting a thickness estimated at about 1 nm.

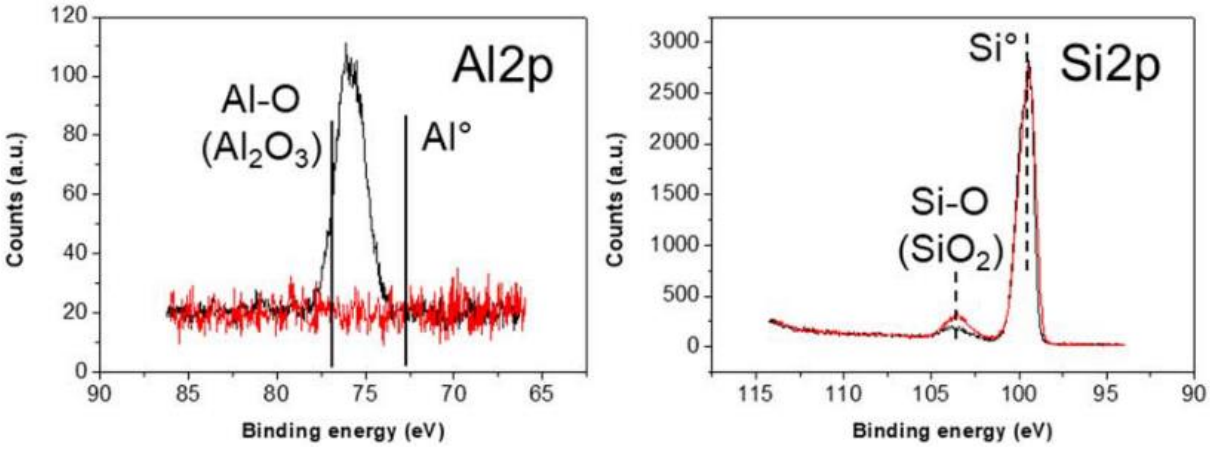

Figure 4.2. XPS spectrum of Al2p and Si2p before (red curve) and after (black curve) the deposition of Al (2 MLs) at 600°C on an epi-ready Si(111) substrate. The spectra were recorded at INL in collaboration with C. Botella.

Regarding the growths performed exposing the substrate to both Ga and Al fluxes from the very beginning, we tend therefore to think that the Al oxidation which can take place on the SiO_2 surface could inhibit the formation of the Ga droplets needed for the nucleation of the Ga-catalyzed NWs, thus leading to the deposition of bulk material as previously reported in Figure 4.1. On the other hand, as far as the growths with GaAs seeds are concerned, we might hypothesise that when the Al flux reaches the NW facets strongly lower the diffusion coefficient of Ga adatoms, thus determining the progressive consumption of the droplets and eventually leading to the suppression of the axial growth.

Based on these experimental evidences, we must conclude that all attempts to grow Ga-assisted $Al_{0.2}Ga_{0.8}As$ NWs on epi-ready Si proved to be unsuccessful. Since depositing both III-group precursors at the same time did not lead to any axial growth, we decided to adopt a different approach, i.e. to start the growth with GaAs only for a certain time before opening the Al flux. In this case a first series of samples was realised with a Ga pre-deposition temperature between 510 and 530 °C, and a growth temperature in the range of 590-600 °C. $R(F_V/F_{III})$ adopted in this case was equal to 5.7 and 4.5 for GaAs and $Al_{0.2}Ga_{0.8}As$, respectively, and all samples were realised so as to obtain a total growth time equal to 10 min, which is to say that the growth of GaAs NWs "seeds" for 30 sec, 1 and 3 min was followed by $Al_{0.2}Ga_{0.8}As$ (nominal) growth for 9 min and 30 sec, 9 and 7 min, respectively. The results concerning these samples are shown in Figure 4.3. It can be thus noticed that after 30 sec

only of GaAs seed deposition no NWs are visible on the sample, which appears as a very rough surface (Figure 4.3(a)). When GaAs seeds are deposited for 1 min, very short NWs start to appear from the rough layer (Figure 4.3(b)), whereas a seeding time of 3 min determines the presence of longer NWs, having density equal to ≈ 10 /μm^2, length equal to 300 ± 35 nm and diameter of 54 ± 4 nm (Figure 4.3(c)). Based on these data, two considerations can be expressed. Firstly, by observing Figure 4.3(b) and (c) it can be noticed that the NWs do not have any visible Ga droplet on their tips, suggesting that Ga droplets were totally consumed or at least significantly shrunken: this is a very important fact, since the NWs were not exposed to As flux only after the growth to consume the droplets, thus meaning that the droplet consumption occurred spontaneously during the NW growth. Secondly, since shorter GaAs seeding times correspond to longer AlGaAs depositions for an overall growth time of 10 min, the fact the NWs in Figure 4.3(c) may only appear longer than those ones in Figure 4.3(b), is only due to the fact that in the latter case more bulk material has been deposited around the NWs. As a consequence, we cannot exclude that the Ga droplets were spontaneously consumed and the axial growth suppressed when Al was introduced as precursor.

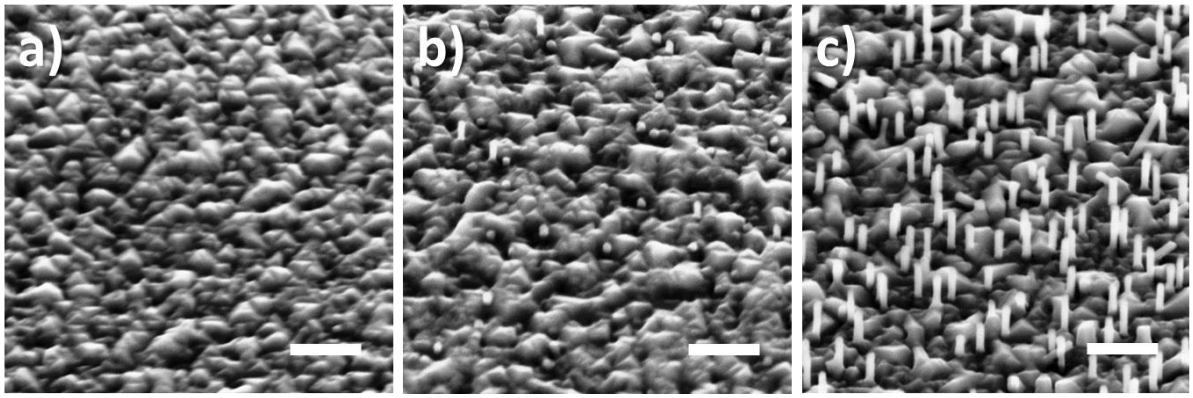

Figure 4.3. SEM images (45°-tilted) showing the growth of $Al_{0.2}Ga_{0.8}As$ (nominal) with GaAs seeds at $R(F_V/F_{III})$ = 5.7 (4.5). (a) NWs grown with 30 sec GaAs seeding time. (b) NWs grown with 1 min GaAs seeding time. (c) NWs grown with 3 min GaAs seeding time. The total growth time is equal to 10 min. In every image the white scale bar corresponds to 500 nm.

In order to further investigate the possibility of using GaAs seeds, we decided to prepare similar samples with lower As/Ga flux ratios and a higher GaAs seeding time. In this case, the Ga pre-deposition temperature was 530 °C, the growth one in the range of 610-625 °C and $R(F_V/F_{III})$ = 2.3 (1.8) or 1.4 (1.1). In any case, GaAs seeds were grown for 5 min, while the $Al_{0.2}Ga_{0.8}As$ (nominal) growth was performed for 10 min. It can be noticed in Figure 4.4 that the morphology of the structures depends on both V/III flux ratio and growth temperature. As a matter of fact, $R(F_V/F_{III})$ = 2.3 and T_{growth} = 610°C lead to longer NWs, as shown in Figure 4.4(a), with L = 700 ± 200 nm and D = 67 ± 8 nm (d = 0.9 /μm^2), whereas a higher T_{growth} = 625°C originates shorter NWs with L = 500 ± 100 nm and D = 72 ± 8 nm (d = 2.0 /μm^2), as

reported in Figure 4.4(b). This length decrease is probably due to the T_{growth} increase which enhances the desorption of As thus reducing the axial growth rate. The same tendency, but amplified, is observed for $R(F_V/F_{III})$ = 1.4 (Figure 4.4 (c)-(d)). In all cases no Ga droplets are present at the NW tips. Such results demonstrate that lowering the As/Ga flux ratio did not prevent spontaneous consumption of Ga droplets, thus suggesting that this phenomenon occurs independently from the amount of Ga and As supplied, being rather attributable to the introduction of Al flux into the NW growth.

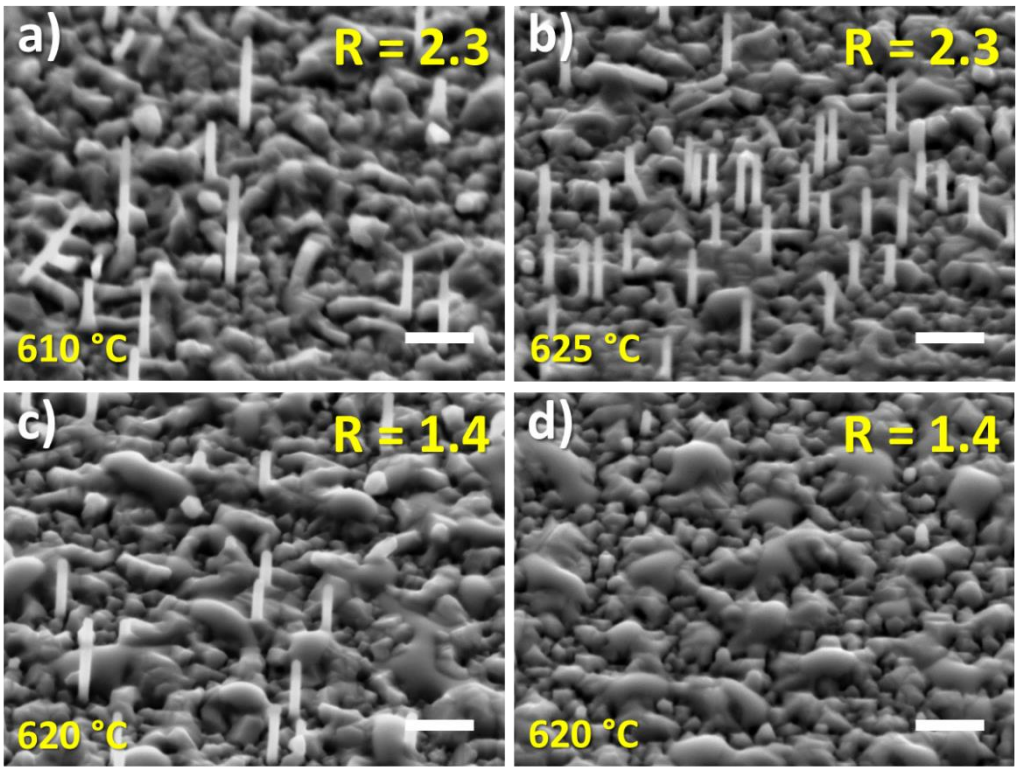

Figure 4.4. SEM images (45°-tilted) showing the growth of $Al_{0.2}Ga_{0.8}As$ (nominal) with GaAs seeds at different $R(F_V/F_{III})$ and T_{growth} (in yellow). In every image the white scale bar corresponds to 500 nm.

In order to investigate the structure and the chemical composition of such NWs grown with 5 min of GaAs seeding (Figure 4.4(a)), we have performed a TEM analysis on them (Figure 4.5). We observed that the droplets on the NW tips were completely or partially consumed, showing in this case a contact angle below 90°, thus confirming what observed by SEM. Moreover, the TEM analysis allowed collecting insights about the crystal structure of the NWs: it is thus possible to recognise three different zones in most of the NWs, i.e. a first ZB region (marked as L1 in Figure 4.5), a region many stacking faults leading to a ZB-WZ mixed phase (L2), and a final region where the ZB phase re-appears. According to Jacobsson's model[138], this NW structure could suggest a structure evolution with the droplet contact angle decrease when Al is added in the flux, as follow: the GaAs NWs start with a ZB phase (L1 region), as expected with the V/III flux ratio used, then stacking faults and WZ phase are formed when the droplets consume with the Al addition, leading to a contact

angle decreases below a critical value (L2 region), until the contact angle becomes too low and ZB phase forms again (L3 region).

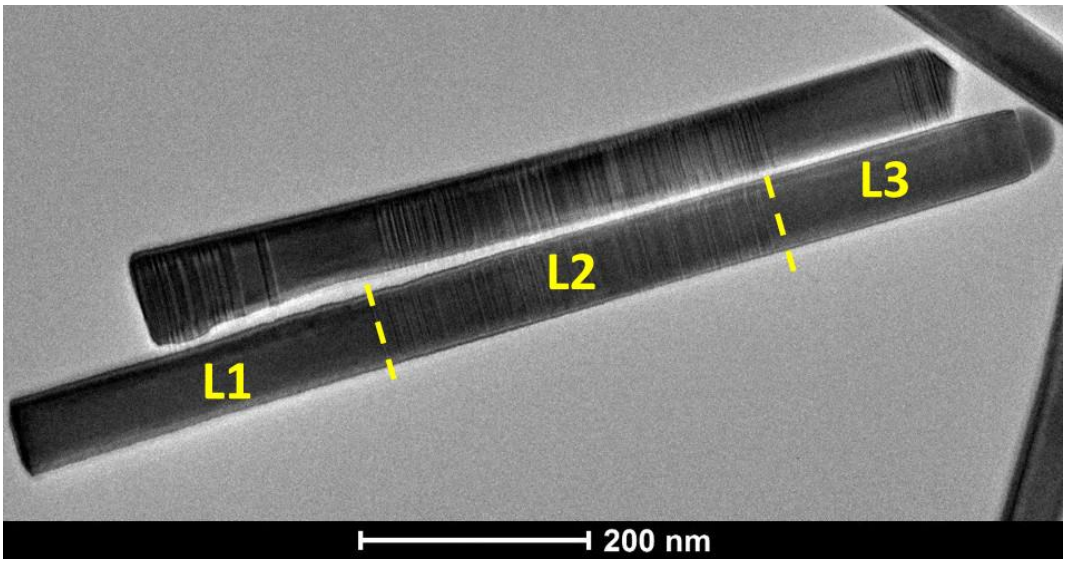

Figure 4.5. TEM image of NWs obtained with 5 min GaAs seeds and 10 min of $Al_{0.2}Ga_{0.8}As$ (nominal) growth with $R(F_V/F_{III}) = 2.3$ and $T_{growth} = 610$ °C (NWs from sample shown in Figure 4.3(a)).

In order to determine the composition of the NWs, an EDX analysis was performed on several NWs. The results shown in Figure 4.6 indicate that the ternary alloy has a very low Al composition, equal to 4 % in the core (yellow circle) and 12 % in the shell (yellow square). Such a result seems therefore to confirm a low diffusion of Al towards the Ga droplets, which would explain the low Al % measured in the core of the NWs. The consumption of the Ga droplet faster than usual also suggests that the Ga supply of this one is not optimal and that the Ga diffusion on the NW facets is probably also lowered by the Al addition.

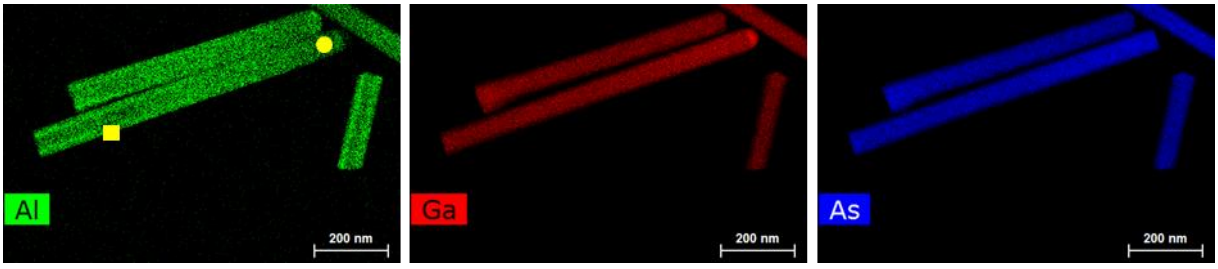

Figure 4.6. Al, Ga and As EDX maps for NWs obtained with 5 min GaAs seeds and 10 min of $Al_{0.2}Ga_{0.8}As$ (nominal) growth with $R(F_V/F_{III}) = 2.3$ and $T_{growth} = 610$ °C (NWs from sample shown in Figure 4.3(a)). The yellow circle and square correspond respectively to the area of the core and the shell where the composition was measured by EDX.

4.3 The growth of core/shell NWs on epi-ready Si

The failure of all our attempts to grow $Al_{0.2}Ga_{0.8}As$ NWs on Si forced us to reconsider the whole approach to the project. This approach, already exploited for other types of applications (refs),[171–176] consists in the growth of core/shell GaAs/AlGaAs NWs with a p-doped GaAs core and $Al_{0.2}Ga_{0.8}As$ shells in which the p-i-n junction is introduced, and protected by a "passivation" shell of higher band-gap material. A schematics of the tandem solar cell that is targeted is reported in the Figure 4.7.

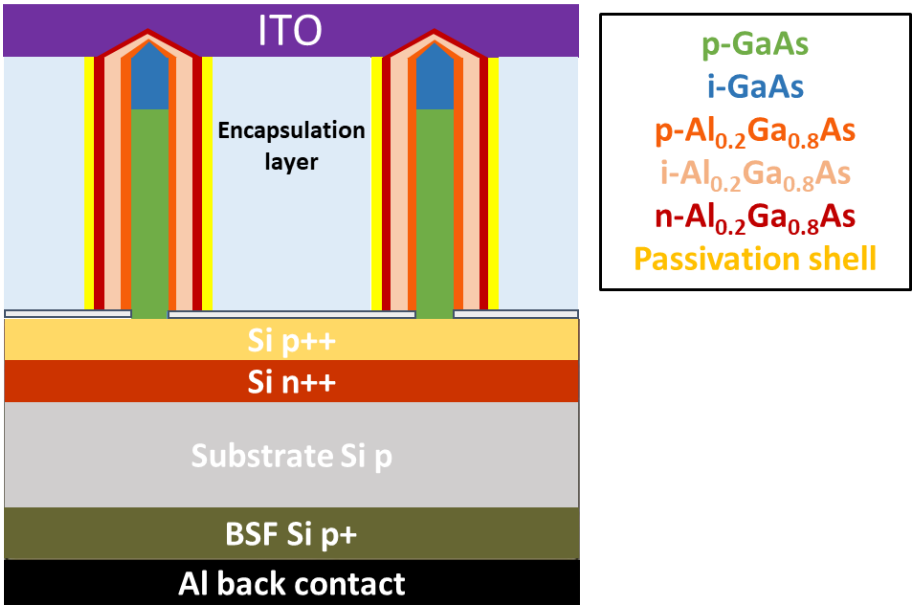

Figure 4.7. Schematics of the target structure of the tandem solar cell, in which the radial p-i-n junction is inserted in the $Al_{0.2}Ga_{0.8}As$ shell grown around the p-GaAs core of the NW top-cells.

As a consequence of this new approach, part of the work of this thesis was devoted to the development of the core/shell NWs. This can be summarized in a first study concerning the impact of the p-doping level on the NW core morphology, the consumption of the Ga droplets and the growth and characterization of p-GaAs core/n-GaAs shell NWs as a reference NW structure (a work reported in Reference[177]). The Ga source employed for this first study was the cell Ga(7) with α = 9.3°. Then, a second study concerning the growth and characterization of p-GaAs core/$Al_{0.2}Ga_{0.8}As$ shell NWs with p-i-n junction inside $Al_{0.2}Ga_{0.8}As$ (a work reported in Reference[178]. The Ga source employed for this second study was the cell Ga(5) with α = 27.9°.

4.3.1 Influence of p-doping on the NW core morphology

According the configuration we chose for our core/shell NWs, the GaAs core should be positively doped with Be. However, this fact raises a problem, since it is well known that excessive Be-doping of GaAs during the axial growth may heavily affect the morphology of the NWs.[179] In order to calibrate our dopant flux for preventing morphological defects, two samples of p.n core/shell GaAs NWs were realised: after growing the Be-doped core for 20 min with the standard procedure and F_{Ga} = 0.5 ML/sec, F_{As} = 2.3 ML/sec (corresponding to $R(F_V/F_{III})$ = 4.6), the Ga droplets were consumed under As flux (F_{As} = 2.3 ML/sec) for 4 min at T_{growth}, and the samples were cooled to 460 °C under the same As flux. After that, the n-GaAs shell was deposited for 23 min with the same Ga and As fluxes and a Si flux as dopant corresponding to a nominal doping concentration (i.e. the doping level in 2D GaAs layers grown with the same growth rate of 0.5 ML/sec) of $1.13 \cdot 10^{19}$ cm^{-3}. This was followed by a 5 min n-$Al_{0.2}Ga_{0.8}As$ passivation shell, obtained with the same parameter plus a flux of Al equal to 0.13 ML/sec, and by a final n-GaAs shell grown for 2 min. The growth conditions were the same for both samples except for the Be flux employed to dope the core: a lightly doped one corresponding to a nominal value of $5 \cdot 10^{18}$ cm^{-3}, and a five times heavier one nominally equal to $2.5 \cdot 10^{19}$ cm^{-3}. Based on the data reported in the literature, the doping level in the p-GaAs core is expected to be equivalent to the nominal value.[90,180] SEM images of the samples are reported in Figure 4.8(a) and (b), respectively, It is clear that the variations in doping level have a dramatic effect on the NW morphology. In the case of the heavily doped one, the NWs appear as hockey-stick-shaped: such kind of effect was already observed by Hilse et al[179] and Zhang et al,[180] and explained as a consequence of a surface energy imbalance caused by the increase in Be concentration inside the droplets. This effect eventually modifies the surface energies causing the Ga droplet to displace from the NW tip to its edge, thus originating this morphology.[180] On the contrary, this does not happen with $5 \cdot 10^{18}$ cm^{-3} doping level, thus originating straight NWs.

Therefore, a p-core doping level of $5 \cdot 10^{18}$ cm^{-3} appears as a suitable value for our purpose.

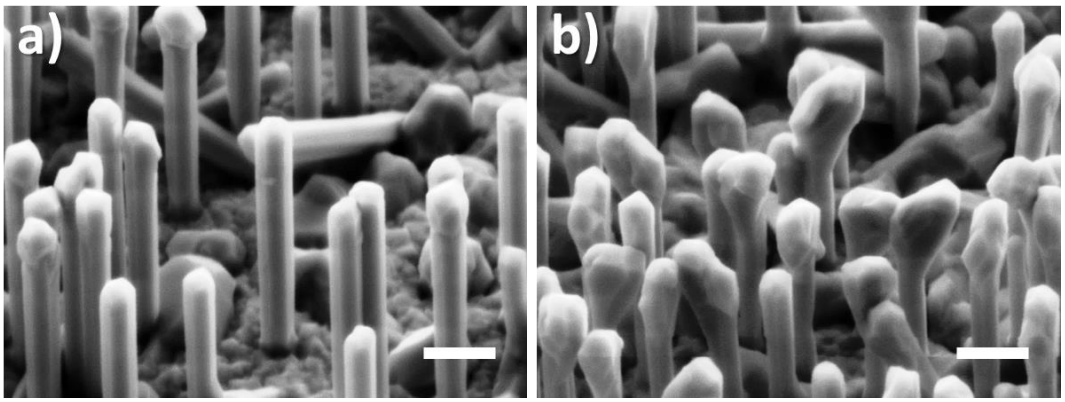

Figure 4.8. SEM images of p-n core/shell GaAs NWs with core p-dopant concentration of: (a) $5 \cdot 10^{18}$ cm^{-3} and (b) $2.5 \cdot 10^{19}$ cm^{-3}. The white scale bar corresponds to 500 nm.

4.3.2 Consumption of the Ga droplet

When growing Ga-assisted core/shell NWs, an important part of the procedure consists in the consumption of the Ga droplet after the core growth, performed by exposing the NWs to a flux of As only. Since the shell growth process enhances the presence of morphological defects on the top of the NWs, it is very important to develop a protocol of consumption giving an appropriate shape to the NWs. In particular, when it comes to the synthesis of core/shell NWs for PV applications, it is very important to identify a procedure which determines NWs with well-shaped tips, ideally flat, so as to eventually achieve a better top contact with ITO.[90] Fur such a reason, we committed to obtaining NWs with a flat-tip morphology and carried out a brief study of the Ga droplet consumption. This was performed on two different samples, which underwent the same standard NW growth procedure reported in chapter 3. After 10 min growth, the Ga flux was stopped and the droplet consumption was effected in both cases by exposing the specimens to F_{As} = 4.05 ML/sec for 4 min, with the only difference that on the first sample (Figure 4.9(a)) it was performed at the same temperature employed during the NW growth (T_{growth} ≈ 600°C), whereas on the second one (Figure 4.9(b)) it was carried out after stopping the heating so as to let the sample cool down quickly (the temperature dropping to about 350 °C). As shown in Figure 4.9, it can be noticed that the difference in treatment leads to different morphologies of the NW tips. In particular, the NWs whose droplets were consumed at T_{growth} tend to present either a rounded tip or a tapered bottle-necked one. On the contrary, the NWs in which the droplet consumption was carried out while cooling the sample appear as much flatter on their top. These procedures permits therefore to control the shape of the NW tip, a useful tool especially when it comes to the growth of core/shell NWs, which allows to obtain either conical (Figure 4.9 (c)) or flat shaped tip (Figure 4.9(d)), as shown more in detail in Paragraph 4.3.3 and 4.3.4.

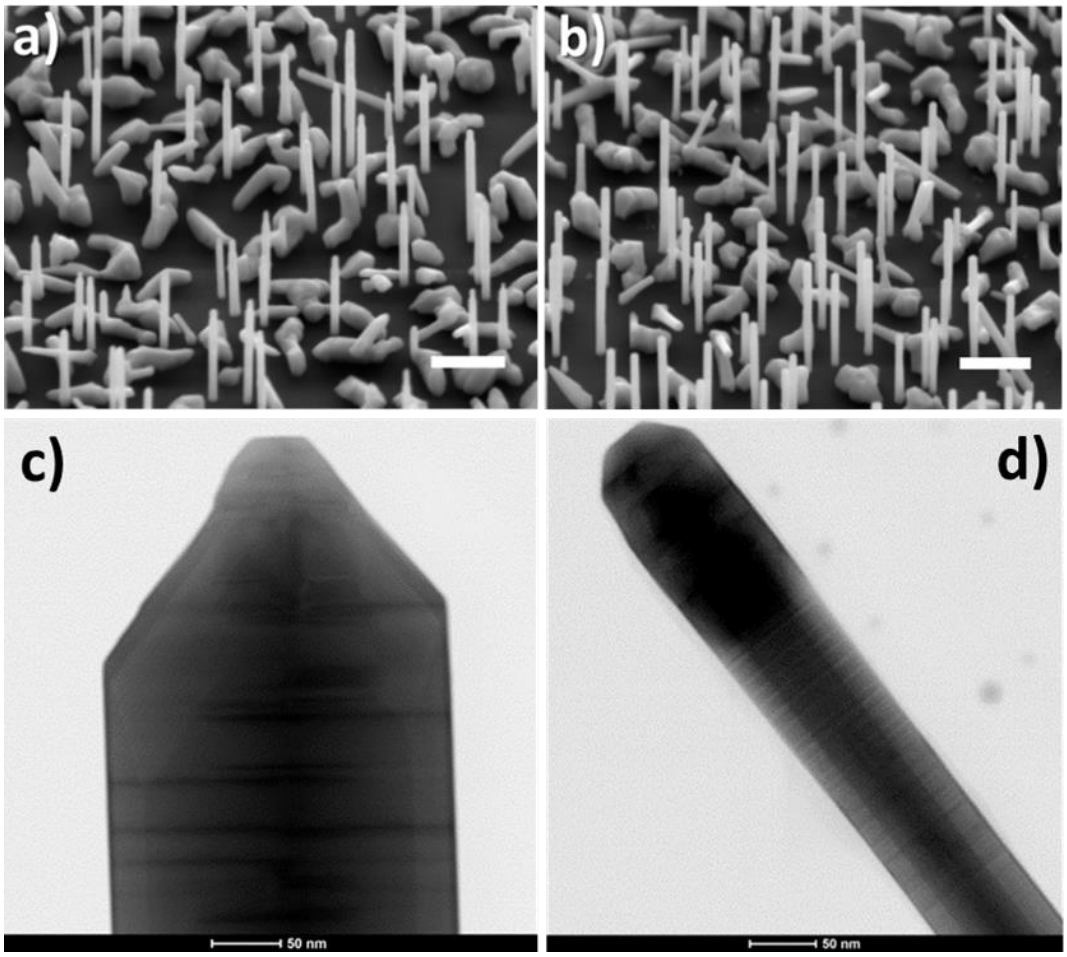

Figure 4.9. SEM images of GaAs NWs grown for 10 min with the standard procedure. The Ga droplets were consumed: (a) at T_{growth} and (b) while cooling fast. The white scale bars correspond to 500 nm. Bright field TEM image of (c) a p-GaAs/p-GaAs core/shell NW whose droplet was consumed at T_{growth} and (d) a p-GaAs/p.i.n.-$Al_{0.2}Ga_{0.8}As$ core/shell NW whose droplet was consumed by dropping the temperature to 350 °C. These two images come from the sample reported in Paragraph 4.3.3 and 4.3.4, respectively.

As a consequence, the Ga droplet consumption treatment performed with F_{As} = 4.05 ML/sec and fast decreasing temperature appears as the most suitable to realise core/shell NWs for the development of our TSC.

4.3.3 p-n junction in core/shell GaAs NWs: growth and characterization

As above-mentioned, the new design of the PV device requires a radial p-n junction in $Al_{0.2}Ga_{0.8}As$ shells grown on a p-GaAs core. However, in order to proceed step by step in the research and to provide a comparison, we committed to introducing the radial p-n junction in GaAs NWs before continuing with AlGaAs-based shell NWs.

4.3.3.1 Growth of the p-n core/shell GaAs NWs

Many samples were realised with this radial p-n GaAs NW configuration. We remind the reader that the Ga source employed in this study was the cell Ga(7) with α = 9.3°. After pre-depositing 1 ML of Ga at 520 °C at 0.5 ML/sec to form the droplets, the temperature was increased to 610 °C at 7 °C/min. Subsequently, the sample was exposed to fluxes of Ga, As and Be, so as to obtained p-doped GaAs NWs, which were grown for 10 min with As and Ga fluxes corresponding to 2.85 and 0.5 ML/sec, respectively ($R(F_V/F_{III})$= 5.7). In order to grow the shells, the Ga droplets at the top of the NWs were then consumed by exposition to the As flux only (without dopants), while decreasing the temperature to 460 °C ("cooling fast" procedure). The radial p-n junction was obtained by growing a Si-doped GaAs shell around the core at 460 °C for 10 min, still with $R(F_V/F_{III})$ = 5.7. The need for such a low shell growth temperature (T_{shell}) and for such a relatively high R is due to the fact that Si is meant to n-dope the GaAs NWs with {110} facets, a task which can be better performed minimizing the amphoteric behaviour of Si by using T_{shell} below 490 °C and $R(F_V/F_{III})$ > 4.5, as reported by Dimakis et al[181]. Subsequently, a second Si-doped shell of $Al_{0.5}Ga_{0.5}As$ (nominal) was grown for 10 min with $R(F_V/F_{III})$ = 5.7 plus a nominal Al flux equal to 0.5 ML/sec (corresponding to a $R(F_V/F_{III})$ = 2.85), as passivation shell in order to prevent carrier recombinations at the GaAs surface of the PV-active region.[182] The growth was then concluded with a further thin GaAs shell deposited for 3 min, so as to prevent the oxidation of Al.[183] Throughout all the procedure, the sample was rotated at 3 rpm. As far as the dopants are concerned, the Be and Si cell temperatures employed (760°C and 1020°C, respectively) corresponded to a nominal doping concentration of $5 \cdot 10^{18}$ cm^{-3} and $1.13 \cdot 10^{19}$ cm^{-3}, respectively, for a 2D GaAs layer growth rate equal to 0.5 ML/s.

Figure 4.10(a) illustrates a schematics of the as-obtained NWs, while an SEM image of the NWs is reported in Figure 4.10(b): the NW density is equal to 6.6/μm^{-2}), and the NWs have good morphological properties, with lengths of 1.1 ± 0.2 µm and diameters of 85 ± 5 nm. Considering that the diameter of core-only NWs grown in the same conditions is equal to 40 ± 3 nm, we can estimate the thicknesses of the n-GaAs, n-$Al_xGa_{1-x}As$ and final n-GaAs shells to be about 7 nm, 14 nm and 2 nm, respectively.

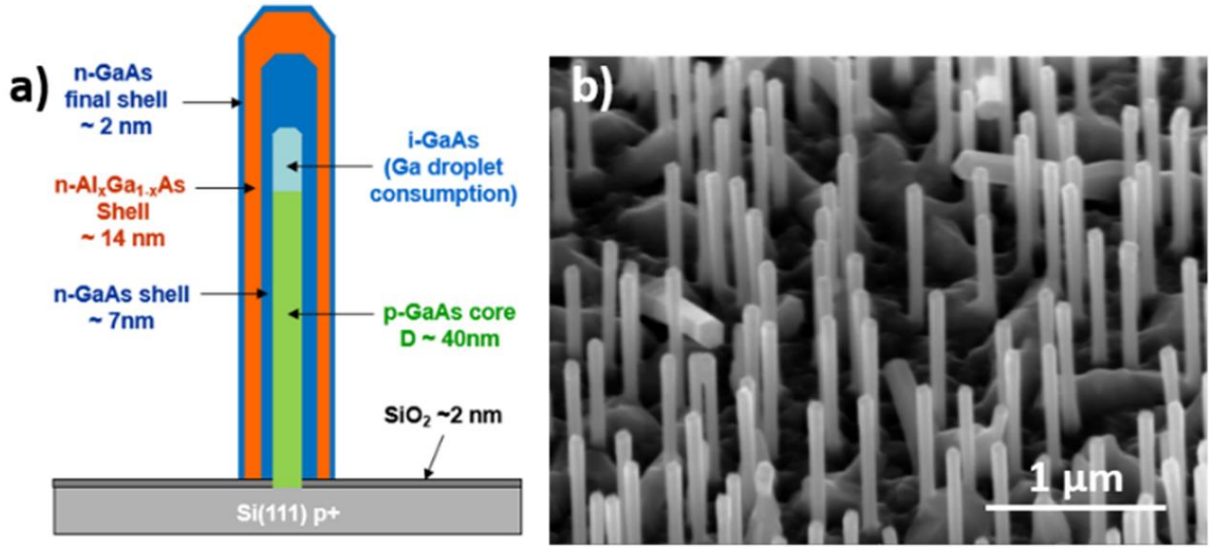

Figure 4.10. a) Schematic of the p-n core/shell GaAs NW structure (profile deduced from the following TEM observations). b) SEM image of the NWs (45°-tilted).

Concerning the doping level and as above-mentioned the p-core doping level can be assumed equivalent to the nominal one and thus equal to 5 ·10^{18} cm^{-3}. Unlike the core case, the doping level of the shell cannot be assumed equivalent to the nominal value, but should be corrected by the actual growth rate and by tan α, with α = 28.9° for the Si cell, following the equation:[181]

$$[\mathrm{Si}] = [\mathrm{Si}]_{\mathrm{planar}}\left(GR_{planar}/GR_{radial}\right)(\tan\alpha/\pi)$$

The factor π takes into account the effect of the substrate rotation during the shell growth, given that Si adatoms are considered immobile on the NW side-walls for the growth temperatures used here.[181]

The shell growth rates (GR_{radial}) can be calculated knowing the shell thickness and deposition times and result equal to 0.04, 0.08 and 0.04 ML/sec for n-GaAs, n-$Al_xGa_{1-x}As$ and n-GaAs shell respectively. Taking into account tan α/π, thus we have evaluated a n doping level of 2.5 ·10^{19} cm^{-3}, 1.25 ·10^{19} cm^{-3} and 2.5 ·10^{19} cm^{-3}, respectively.

4.3.3.2 Structural characterization

Figure 4.11 shows HAADF-STEM images of a typical NW whose length is equal to about 1.25 µm and diameter to 90 nm. While imaging along [1-10] zone axis (Figure 4.11(a, b)) points out the crystal structure of the NW, showing the presence of defects and of different phases, the micrographs taken with [11-2] zone axis (Figure 4.11(c,d)) denote the compositional contrast in the structure. Therefore, by combining the information obtained

with both type of images it is possible to recognize five different zones along the NW, corresponding to as many different growth stages (Figure 4.11(d)): the first one (715 nm long, marked with a red arrow) coincides with the VLS growth of the p-GaAs core and presents a Zinc-Blende (ZB) structure with some stacking faults (twins). These are likely due to the relatively high As/Ga flux ratio employed for growing the core. The succeeding zone (210 nm long) is the sequence grown during the Ga droplet consumption, with a first ZB segment with a high density of stacking faults, then a second segment with a Wurtzite (Wz) structure, as already observed by other groups.[133,137,141,184] Then, it can be seen again three highly stacking-faulted ZB zones formed at the tip of the NW during the radial growth of the n-GaAs and n-$Al_{0.5}Ga_{0.5}As$/n-GaAs shells, with lengths equal to 180, 95 and 27 nm, respectively, which provide a substantial contribution to the overall length of the NW. We can note that the shell thickness strongly depends on the plane orientation: as a matter of fact, the thickness of the shells grown on the {111} top facets is bigger than the thickness measured on the {110} lateral facets, since the latter ones are less exposed to the III element flux.

Further information about the composition of the shells were collected by EDX analysis of the NW as shown in Figure 4.11(e). In particular, the ternary alloy is revealed to have an actual composition between $Al0._{52}Ga_{0.48}As$ and $Al_{0.57}Ga_{0.43}As$ depending on the zone, in any case very close to the target value of $Al_{0.5}Ga_{0.5}As$. Finally, the HAADF-STEM image also gives information about the thickness of the different shells. As measured from Figure 4.11(d) inset, the $Al_{0.5}Ga_{0.5}As$ and GaAs passivation shells are 15 nm- and 1.8 nm-thick, respectively. Considering that the growth rate for $Al_{0.5}Ga_{0.5}As$ was twice the one adopted for n-GaAs, it is therefore possible to assume that the thickness of the n-GaAs shell around the core is 7.5 nm. These values are very close to the ones expected from SEM estimation, and considering that the overall diameter of the p-GaAs core plus the n-GaAs shell is 55 nm, they are also consistent with the assumption of a p-GaAs core diameter of 40 nm.

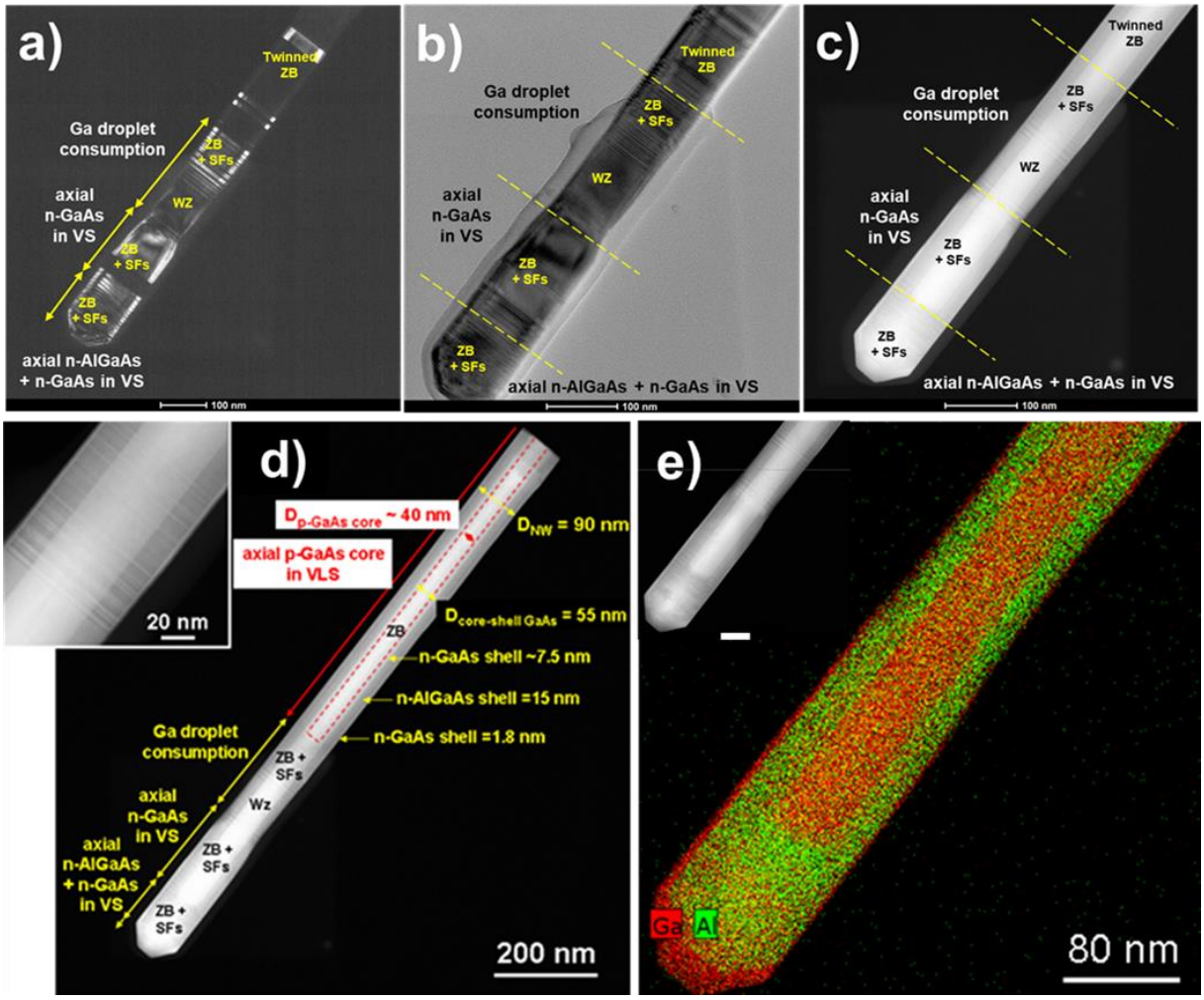

Figure 4.11. (a) HAADF-STEM image (with [1-10] zone axis) of a representative p-n core: shell GaAs NW with $Al_{0.5}Ga_{0.5}As$/GaAs passivation shells: the crystal structure is clearly visible. (b) Higher magnification of the previous image. (c) The same image taken with [11-2] zone axis: such orientation highlights the compositional contrast. (d) HAADF-STEM image (with [11-2] zone axis) of the whole NW. Inset: higher magnified image showing the thickness of $Al_{0.5}Ga_{0.5}As$ and GaAs final shells, and the composition inhomogeneity in the $Al_{0.5}Ga_{0.5}As$ shell caused by the presence of stacking-faults. (e) EDX mapping of Al and Ga. Inset: the corresponding HAADF-STEM image (with [11-2] zone axis); the scale bar corresponds to 50 nm.

4.3.3.3 Optical characterization

The optical characterization of p-n core/shell GaAs NWs was carried out by PL spectroscopy. The analysis was performed at 13 K with a 532 nm continuous wave diode-pumped solid-state laser (excitation power equal to 70 mW) and with a nitrogen cooled silicon CCD detector coupled to a monochromator. The optical characterization of NWs presented in this thesis has been realized by N. Chauvin at INL-INSA.

The PL spectrum reported in Figure 4.12(a) presents two peaks: one at 1.37 eV, attributable to GaAs, and one at 1.67 eV, originated from the $Al_{0.5}Ga_{0.5}As$ shell. Two hypothesis could explain the observation of the GaAs peak at 1.37 eV, i.e. 0.14 eV below the usual band gap of undoped ZB GaAs at cryogenic temperature (1.51 eV).[185] By comparing PL spectra recorded using different excitation powers we can see a strong blue-shifted of the low energy peak as the power is increased (Figure 4.12(b)). This behaviour is usually interpreted as a signature of carrier separation or state filling. As a first hypothesis, the emission is related to the p-doped GaAs core and to the ZB/Wz mixed structure (due to the presence of stacking faults) of the NWs. The low energy emission would be the consequence of the mixed structure and Be doping levels which can both induce potential fluctuations in the GaAs material along and perpendicularly to the NW axis. To support this hypothesis, we can mention that PL emission below 1.3 eV has already been reported for Si-doped GaAs NWs where the amphoteric behaviour of the Si dopant increases the potential fluctuations.[186] The second hypothesis is related to a band bending along the radial axis as a consequence of the p-n GaAs junction. The electrons are localized at the n-doped GaAs/$Al_{0.5}Ga_{0.5}As$ interface whereas the holes are in the p-doped GaAs core. To support this hypothesis, we can mention that such a band bending has already been observed for GaAs/ $Al_{0.5}Ga_{0.5}As$ core-shell NWs even in the case of an undoped heterostructure.[187]

In the case of the $Al_{0.5}Ga_{0.5}As$ peak, the PL emission is likely caused by donor-acceptor transitions or localized states induced by compositional inhomogeneity inside the $Al_{0.5}Ga_{0.5}As$ shell as observed on the magnified TEM image with [11-2] zone axis (cf. inset of Figure 4.11(d)), and as already mentioned by several groups.[188,189]

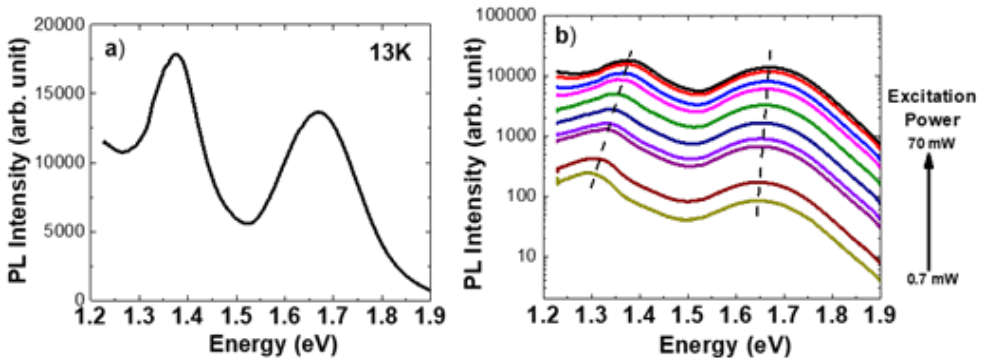

Figure 4.12. (a) PL spectrum of p-n core/shell GaAs NWs with $Al_{0.5}Ga_{0.5}As$/GaAs passivation shells at T = 13 K, with an excitation power P =70 mW. (b) PL spectra at 13 K as a function of the excitation power from 0.7 to 70 mW.

4.3.3.4 EBIC characterization

In order to further characterize the optoelectronic properties of the NWs, and especially their p-n junction as PV-active region, EBIC (Electron Beam Induced Current) measurements were performed on 16 single NWs from different areas of the sample, so as to constitute a statistical measure as representative as possible. EBIC measurements were carried out by V. Piazza and M. Tchernycheva at C2N; cf. Annex 1 for the experimental set-up. The results reported below are thus considered to be characteristic for the vast majority of the NW population, being representative for 87 % of the investigated cases. Therefore, the following results, even if based on individual cases rather than on arrays, are meant to be illustrative for the standard properties of the NW population of this sample.

The following Figure 4.13 shows the results of I-V and EBIC characterizations of an individual p-n core/shell GaAs NW contacted at its top by a nanomanipulator. It is possible to observe that the I-V curves (Figure 4.13(a)) present diodic behaviour also without external excitation, with opening voltage from 0.75 to 0.9 V and leakage current below the sensitivity of the instrument in the voltage range. When expose to the electrons the NW originates a current, detectable both under zero and reverse bias, of 0.54 pA (Figure 4.13(b)), which only weakly depends on the reverse bias. In the forward regime on the contrary the I-V curve shows V_{OC} of 0.36 ± 0.04 V, while its increased slope indicates a decrease of the series resistance. Although this particular NW shows fill factor FF equal to 32 %, the average values calculated on the statistically representative NW population is about 40 %.

Even if not representative of which could be the actual PV efficiency of these structures, being obtained with e-beam and not by exposition to light, these results are still very significant and positive, since they demonstrate that the p-n junctions are electrically active and capable to separate the generated carriers.

Figure 4.13(c, d, e) reports scanning electron micrographs and the related EBIC maps recorded with different external bias. With a negative bias (Figure 4.13(c)) the p-n junction induces a significant negative current (black contrast), which is consistent with the I-V curve in Figure 4.13(a). However, an induced current originated by the p-n junction is observable also without bias (Figure 4.13(b)), although the signal-to-noise ratio is much lower in this case, thus indicating the presence of a variable series resistance, e.g. due to the Schottky contact between the NW and the manipulator tip. The effect of this Schottky junction is more visible in Figure 4.13(e), where the signal from the NW disappears under forward bias, displaying only a positive signal (white contrast) at the NW/tip interface.

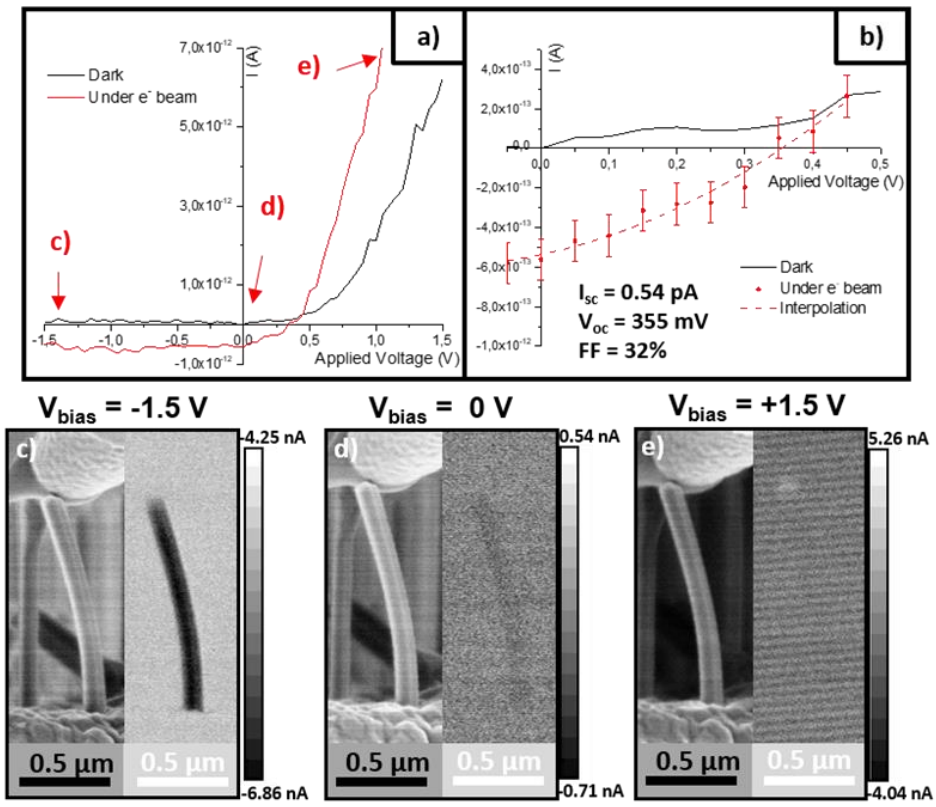

Figure 4.13. (a) I-V curves of a single NW in the dark (black) and under electron beam exposure (red): the red letters indicate the bias conditions as adopted in the EBIC maps reported in (c), (d) and (e). (b) Zoom on the origin of the I-V curve showing the interpolation of the experimental data acquired under electron irradiation. (c), (d), (e) SEM images and corresponding EBIC maps at V_{bias}= -1.5, 0 and +1.5V, respectively.

The generated current and its homogeneity or inhomogeneity along the NW length can be illustrated through EBIC profiling, as reported in Figure 4.14. This permits to identify three regions corresponding to three different regimes. In the top one (Region I), the collected current increases towards the NW base indicating a diffusive transport regime, which is consistent with the presence of an axial p-n junction formed due to the shell coverage of the NW top.

As far as Region II is concerned, which presents a mixed diffusion and drift transport, the EBIC profile shows that carriers can be efficiently collected also here despite the high density of stacking faults observed by TEM. This implying the absence of significant carrier losses, and considering the thickness of Region II, it follows that the diffusive axial transport can occur over a distance of 100 nm. Such a result is extremely significant, because based on the fact that stacking faults are perpendicular to the NW axis, it seems reasonable to assume that the diffusion length in the radial direction is higher than in the axial one. As a

consequence, since the NW radius is around 45 nm, it seems possible to assume that an efficient collection of carriers occurs all over the entire NW diameter.

Region III, corresponding approximately to the total length of the NW core and of the consumed droplet as measured by TEM, is the zone where carriers drift to the junction and showing a very homogeneous current which is maintained stable also in proximity of the interface with the substrate (green dashed oval). Since the current would decrease in presence of defects, it should be concluded that a good quality interface connects the p-GaAs core with the Si(111) substrate. The results observed along Region III testify the possibility of achieving homogeneous collection of carriers on a large surface, this cylindrical junction area being 38 times higher than the NW footprint.

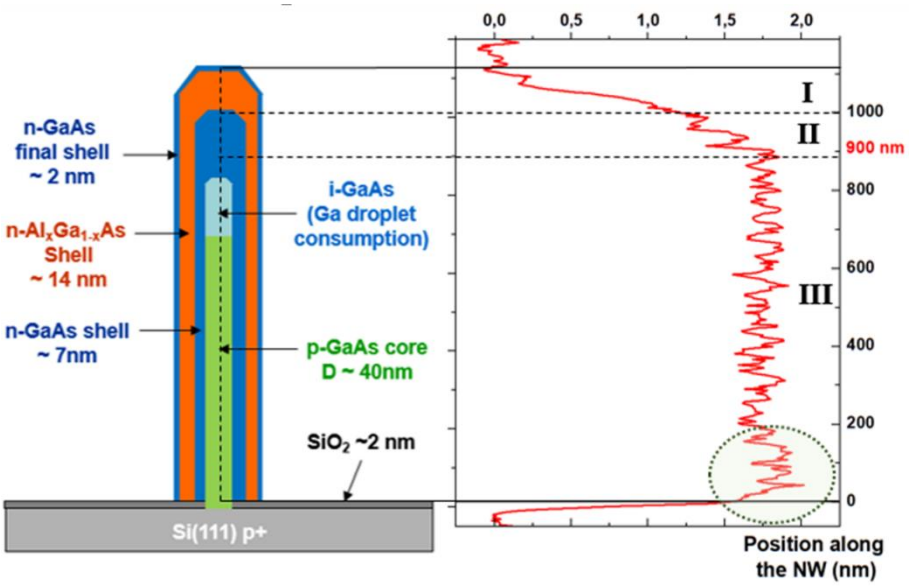

Figure 4.14. Comparison between the EBIC profile along the NW axis at -1.5V bias and the structure of the NW. The green dotted circle indicates the induced current recorded at the interface between the GaAs core/shell junction and the SiO_2 layer. Dotted lines are used to define the three transport regimes (I: diffusive transport; II: mixed diffusion and drift transport; III: carrier drift to the junction).

To conclude on these preliminary results obtained on p-n core/shell GaAs NWs, I-V measurements and EBIC mapping of single NWs have shown the absence of the leakage current under reverse bias. The homogenous collection of carriers from the entire core length leads to an estimation of the junction area about 38 times higher than the NW footprint. Both results are a further demonstration of the potentialities of the radial p-n junction for applications in photovoltaic devices.

4.3.4 p-i-n junction in the $Al_{0.2}Ga_{0.8}As$ shell: growth and characterization

After the preliminary study on p-n core/shell GaAs NWs, we approached the structure intended to function as the PV active region in our top-cell by fabricating and characterising NWs with the p-i-n junction in a $Al_{0.2}Ga_{0.8}As$ shell grown around a p-GaAs core. The substrate employed and the procedure adopted is similar to that one already reported in paragraph 4.3.1 to fabricate p-n core/shell NWs. We remind the reader that the Ga source employed for this second study was the cell Ga(5) with α = 27.9°.

Be-doped GaAs cores were then grown for 20 min with F_{Ga} = 0.5 ML/sec and F_{As} = 1.15 ML/sec, corresponding to $R(F_V/F_{III})$ = 2.3. After the core growth, the Ga droplets were consumed by exposition to the As flux only (F_{As} = 4.05 ML/sec) at 600 °C for 4 min. The temperature was subsequently reduced to 460 °C under the same As flux, so as to prevent As desorption from the NWs. Afterwards, the radial p-i-n junction was fabricated at 460 °C by growing Be-doped, intrinsic and Si-doped $Al_{0.2}Ga_{0.8}As$ shells, followed by two more Si-doped passivation shells of $Al_{0.5}Ga_{0.5}As$ and GaAs. All shells were grown with F_{Ga} = 0.5 ML/sec and F_{As} = 4.05 ML/sec, corresponding to $R(F_V/F_{III})$ = 8.1. In the case of $Al_{0.2}Ga_{0.8}As$ and $Al_{0.5}Ga_{0.5}As$, F_{Al} = 0.13 and 0.5 ML/sec were also adopted (originating an overall As/III ratio of 6.4 and 4.05, respectively). Also in this case the fluxes of Si and Be dopants adopted corresponded to a nominal concentration of $5 \cdot 10^{18}$ cm^{-3} and $1.13 \cdot 10^{19}$ cm^{-3}, respectively, for a 2D GaAs layer growth rate equal to 0.5 ML/sec.

Two different samples were realised under these conditions with different shell growth times: these are reported in Table 4.1. The so-called Sample A underwent TEM and PL analyses, whereas the Sample B was processed for I-V and EBIC characterization of NWs. A schematic of their structure is reported in Figure 4.15.

Shell	Sample A Growth time (Thickness)	Sample B Growth time (Thickness)
p-$Al_{0.2}Ga_{0.8}As$	5 min (16 nm)	10 min (32 nm)
i-$Al_{0.2}Ga_{0.8}As$	10 min (32 nm)	10 min (32 nm)
n-$Al_{0.2}Ga_{0.8}As$	5 min (16 nm)	10 min (32 nm)
n-$Al_{0.5}Ga_{0.5}As$	5 min (23 nm)	2 min (9 nm)
n-GaAs	2 min (4 nm)	2 min (4 nm)

Table 4.1. Growth time and corresponding thickness for the shells of samples A and B.

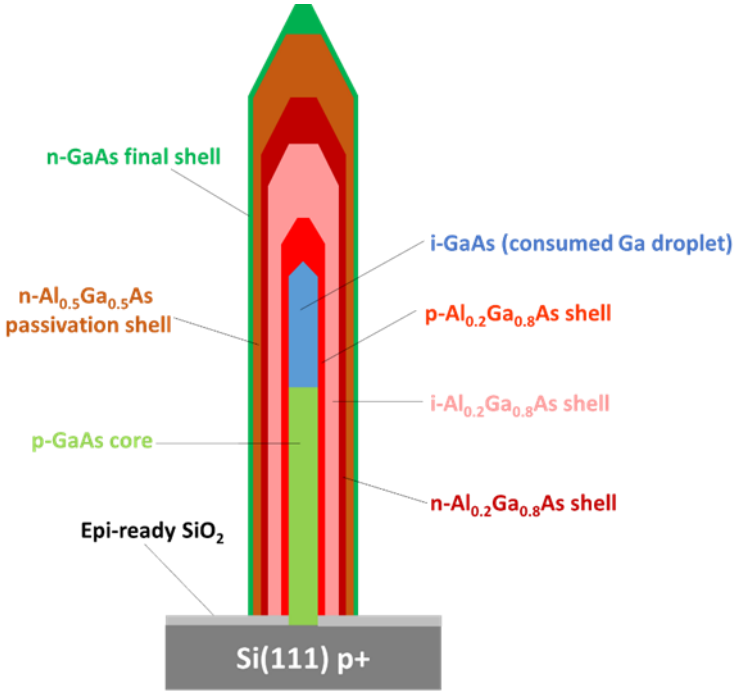

Figure 4.15. Schematic of the GaAs/AlGaAs NWs, consisting in a p-doped GaAs core with a p-i-n $Al_{0.2}Ga_{0.8}As$ shell and a final $Al_{0.5}Ga_{0.5}As$/GaAs passivation shell. Profiles and lengths of the different parts of the NW are deduced from the TEM analysis.

Once again, the doping level in the p-core can be assumed as equivalent to the nominal one (5.10^{18} cm^{-3}). Concerning the shell doping, knowing the shell thickness and the growth times and considering tan α for Be and Si cells (with α = 58° and 28.9°, respectively) we can evaluate the doping level in the shells. Since the deposition rates result equal to 0.19, 0.19, 0.27 and 0.12 ML/sec for p-$Al_{0.2}Ga_{0.8}As$, n-$Al_{0.2}Ga_{0.8}As$, n-$Al_{0.5}Ga_{0.5}As$ and n-GaAs shell respectively, the related doping concentration result to be about $6.7{\cdot}10^{18}$ cm^{-3}, $5.2{\cdot}10^{18}$ cm^{-3}, $3.7{\cdot}10^{18}$ cm^{-3} and $8.4{\cdot}10^{18}$ cm^{-3}, respectively. Moreover, it should be considered that, despite the fact that i-$Al_{0.2}Ga_{0.8}As$ shell is nominally intrinsic, some kind of very light doping effects may still occur in practice as background n-doping, as remarked by LaPierre.[106] Although

assessing the extent of such an effect is difficult, we can still assume a background n-doping level around $5 \cdot 10^{16}$ cm^{-3}, as reported in the above-mentioned work.

Figure 4.16(a) shows a SEM image of the p-GaAs/p.i.n-$Al_{0.2}Ga_{0.8}As$ core/shell NWs from Sample A. The growth leads to a density of about 1.5 NW/μm^2 and to average values of length and diameter equal to 2.8 ± 0.4 µm and 270 ± 30 nm, respectively. Since the diameter of the core should be equal to the one of GaAs NWs grown in the same conditions, which is typically about 70 nm, the thickness of all the shells can be estimated at about 100 nm.

Figure 4.16(b) shows a two-wave dark field TEM image (with [1-10] zone axis) of a NW from sample A having a diameter of 250 nm, consistent with the average value of 270 ± 30 nm. It is possible to distinguish three different zones: the first long L1 zone, about 2.1 µm in length, consists of a pure ZB crystal structure with a low density of twins, consistent with the low V/III flux ratio adopted during the growth.[133] On the contrary, the zone labelled as L2, about 260 nm in length, contains a high number of stacking faults (marked as SFs) followed by a Wz segment; this L2 zone is characteristic of the growth stop and of the Ga droplet consumption under As flux and put in evidence for a GaAs NW in Figure 4.16(c). The last L3 zone originates from the vapour-solid (VS) growth of material occurring after the consumption of Ga droplets. Here many stacking faults are present as well, and the significant length of this zone (≈ 500 nm) attests that the axial growth continued substantially in absence of a liquid Ga droplet via VS mechanism.

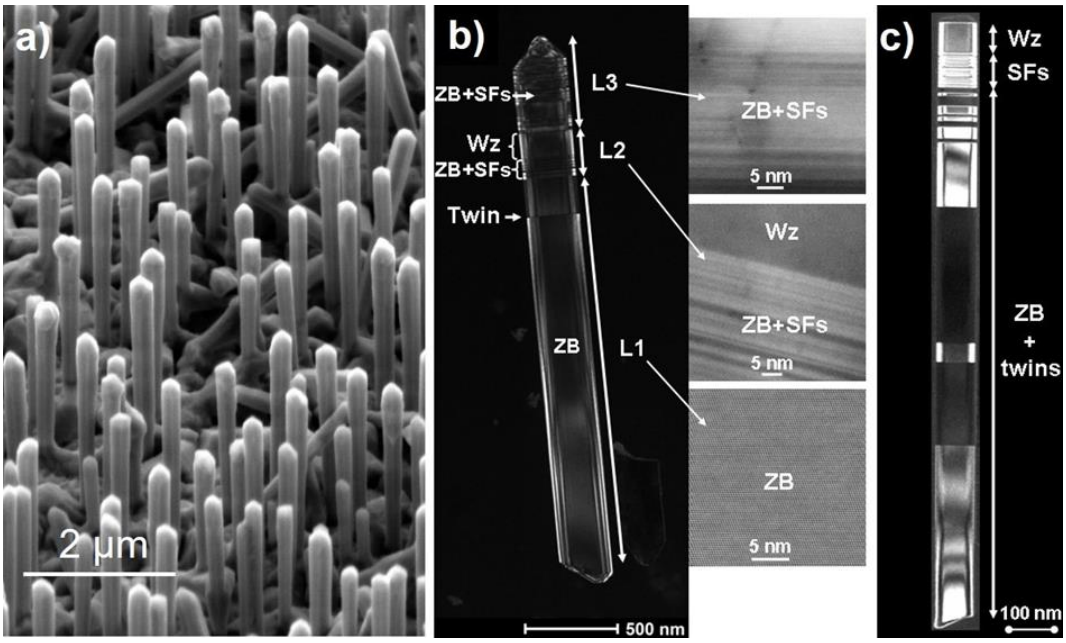

Figure 4.16. (a) SEM image of Sample A. (b) Two-wave dark field TEM image of a NW from Sample A. Insets are HRTEM images (with [1-10] zone axis) of the L1, L2 and L3 zones. (c) Two-wave dark field TEM image of a GaAs NW grown in the same conditions.

The stacking faults in L3 zone are also clearly visible in the HAADF-TEM image (with [11-2] zone axis) of Figure 4.17(a), which also highlights the presence of the $Al_{0.5}Ga_{0.5}As$ shell, marked by the dashed black line, and of the final GaAs shell. The thickness of the $Al_{0.5}Ga_{0.5}As$ and GaAs lateral shells can be measured and they result to be 23 nm and 4 nm, respectively. As far as $Al_{0.5}Ga_{0.5}As$ is concerned, it is possible to notice that its thickness strongly depends on the plane orientation: as a matter of fact, the thickness of $Al_{0.5}Ga_{0.5}As$ grown on the {111} top facets (≈ 60 nm) is bigger than the 23 nm-thickness measured on the {110} lateral facets, since the latter ones are less exposed to the III element flux. This datum is another evidence for the fact that the VS mechanism has an important impact on the axial growth of the NWs after the consumption of the Ga droplets. Moreover, the clear separation between the {111} top facet and {110} lateral facet observable in the $Al_{0.5}Ga_{0.5}As$ shell allows drawing a line of demarcation between the {111} and {110} grown layers (dashed yellow line in Figure 4.17(a)). Thus, although we cannot distinguish visually the two facets in the core and the inner shells, it is still possible to extrapolate where the boundary between the two layers is located inside the NW (cf. Figure 4.18).

The presence of the $Al_{0.5}Ga_{0.5}As$ passivation shell is further proved by EDX mapping, whose results for Ga and Al are exposed in Figure 4.17(b) and (c), respectively. The analysis showed that the actual composition of the passivation shell is between $Al_{0.51}Ga_{0.49}As$ and $Al_{0.56}Ga_{0.44}As$, i.e. very close to the target value.

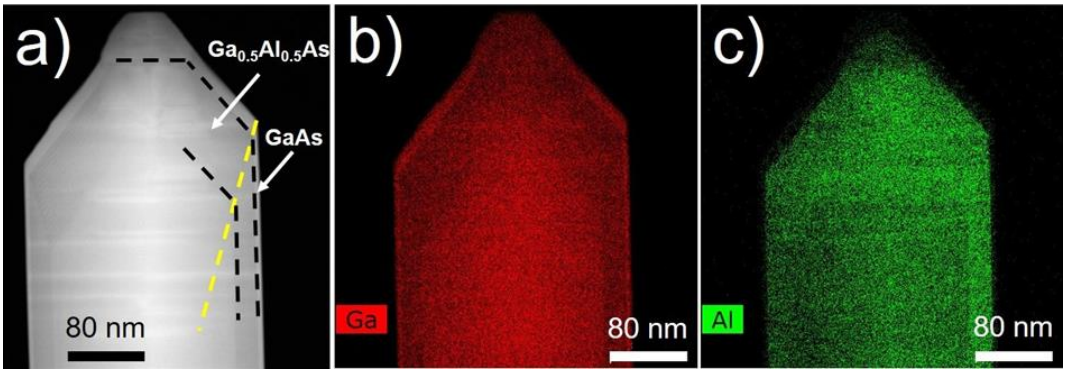

Figure 4.17. (a) HAADF-TEM image of the NW tip ([11-2] zone axis). The black dashed lines delimit the $Al_{0.5}Ga_{0.5}As$ passivation shell, while the yellow one shows the boundary between the {111} and {110} grown layers. (b) EDX map of Ga. (c) EDX map of Al.

The considerations mentioned above can be summarized in Figure 4.18, reporting the core/shell profile of the NW: by knowing the value of the core diameter from a reference sample (about 70 nm) and the thickness of $Al_{0.5}Ga_{0.5}As$ and GaAs passivation shells, it is possible to estimate those of $Al_{0.2}Ga_{0.8}As$ shells, which are about 16 nm for the p- and n-doped shells and about 32 nm for the intrinsic one. Consequently, it can be deduced that the radial growth rate of $Al_{0.2}Ga_{0.8}As$ is approximately 0.53 Å/s in these growth conditions. Moreover, by considering the length of the L2 zone grown during the consumption of the Ga

droplet, it is possible to notice how, according to our approximation, the boundary between the {110} and the {111} grown layers (dashed yellow line) well ends at the NW top after the consumption of the Ga droplet, i.e. between the L2 and L3 zones. It is worth to notice that the deduction of shell thickness from TEM profile of p-i-n junction NWs has been already effected in the remarkable work of Boulanger et al.[90]

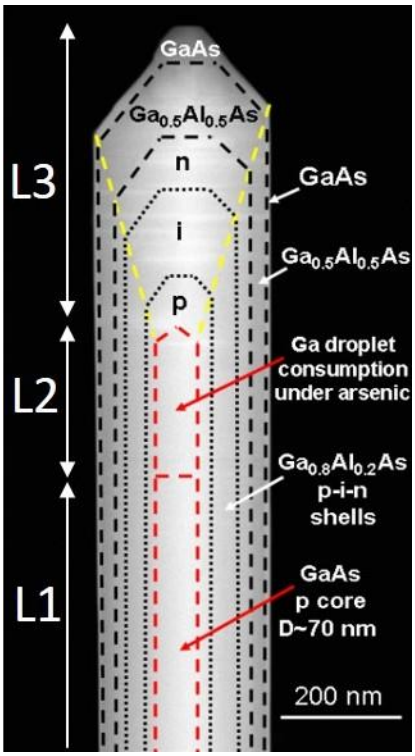

Figure 4.18. Schematic structure of the core/shell GaAs/AlGaAs NW as deduced from TEM and EDX analyses. The thicknesses of the $Al_{0.5}Ga_{0.5}As$ and GaAs passivation shells are deduced from HAADF-TEM image (with [11-2] zone axis). The thicknesses of $Al_{0.2}Ga_{0.8}As$ p-i-n shells are estimated based on the adopted growth times and on the fact that the diameter of the GaAs core is about 70 nm.

As far as the optoelectronic characterization is concerned, PL analysis was performed on Sample A at 13 K with a 532 nm continuous wave diode-pumped solid-state laser (excitation power equal to 60 mW) and with a nitrogen cooled silicon CCD detector coupled to a monochromator.

The PL spectrum in Figure 4.19(a) shows two different peaks: a first broad and weak one in the 1.6-1.7 eV range, and a second one at 1.48 eV, i.e. below the low temperature band gap of undoped ZB GaAs which is 1.51 eV,[185]. The emission at higher energy is related to the AlGaAs shells, and the peak broadening can be explained by the presence of numerous localized states originated in the AlGaAs shell by the alloy fluctuations.[190] The emission at 1.48 eV could be explained considering different phenomena, such as a type II emission due to a ZB/Wz mixture,[185,191,192] an emission involving conduction band-acceptor and/or donor-acceptor transitions,[193] a band-to-band emission in a doped material and a band bending at

the GaAs/AlGaAs interface.[187] However, type II emission, donor-acceptor transitions and band bending cause blue-shifts with increasing excitation power, which is not observed in the case of our sample (Figure 4.19(b)). Therefore, it can be assumed that the peak at 1.48 eV is rather related to conduction band-acceptor transitions or to a band gap narrowing effect as a consequence of the p-doping of the GaAs core.

A weak emission below the main emission peak at 1.48 eV is also observed for all excitation powers. This can be explained considering that ZB/Wz mixture in undoped GaAs NWs can induce an emission below the band gap at cryogenic temperature,[185,191,192] a phenomenon which can also by caused in undoped ZB GaAs NWs by the presence of twins.[194] Therefore, knowing from the TEM study that our NWs present a polytypic ZB/Wz structure in the upper part and a low density of twins in the lower part, tend to think that the observed low energy peak can be explained by this polytipism and the presence of twins.

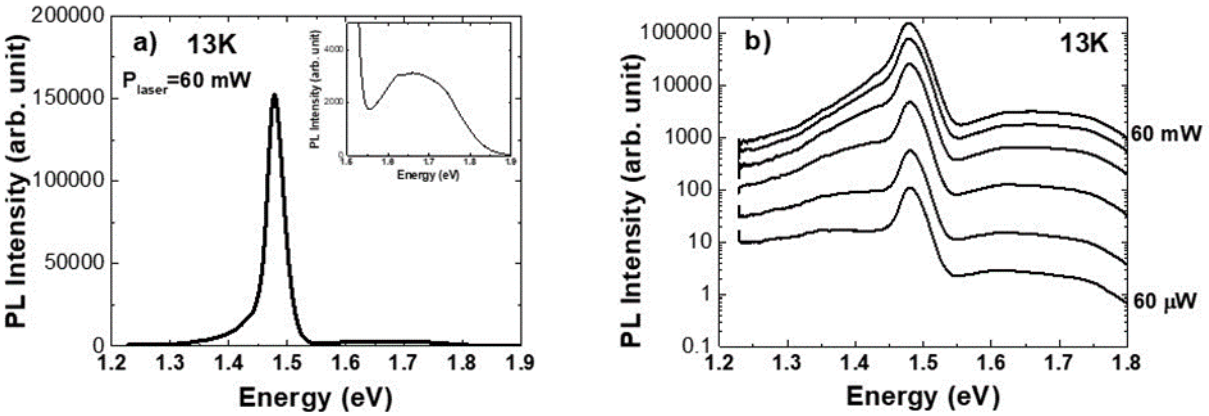

Figure 4.19. (a) PL spectrum of sample A at 13 K. The inset is a close up view of the peak related to the AlGaAs shells. (b) PL spectra of sample A as a function of the excitation power.

The NWs grown on Sample B have d = 2.7 NW/μm^2, L = 2.2 ± 0.3 μm and D = 280 ± 30 nm. EBIC characterization was performed on single NWs of Sample B employing the same experimental setup and conditions already described for p-n core/shell GaAs NWs. The results of this analysis are reported in Figure 4.20, where the data collected on a statistically representative NW are shown. The NWs grown on Sample B have d = 2.7 NW/μm^2, L = 2.2 ± 0.3 μm and D = 280 ± 30 nm.

It can be noticed that the NWs show a strong response to the electron beam irradiation, since it is possible to map the induced current over the whole length of the NWs even with zero bias (Figure 4.20(b)). Moreover, the current results extremely uniform along 83 % of the NW length, as demonstrated by the EBIC axial profile in Figure 4.20(c), thus suggesting the presence of a conformal radial p-i-n junction. When a reverse bias is applied the electric field across the junction is increased, thus enhancing also the induced current. This is quantified in Figure 4.20(c), where EBIC current results higher than in the previous case although less

uniform, with a slight increase (< 10 % variation) towards the top. This can be ascribed to a higher electrical resistance of the shell with respect to the core, since the profile variation over the length is influenced by the ratio between the resistance of the core and that one of the shell.[195] Finally, the application of a forward bias flattens the p-i-n junction making its signal disappear, as shown in Figure 4.20(b), while a current of opposite sign (black contrast) is visible at the top of the NW. This is likely caused by the rectifying Schottky contact at the NW/tip interface, and put in evidence in Figure 4.20(c), where no current is observed along the NW but a negative peak from the Schottky diode at 150 nm from the contact.

Figure 4.20(d) shows the related I-V curve. Like p-n GaAs NWs, also these NWs present diodic behaviour with very low leakage current (up to -2 V), thus confirming the good electrical quality of the radial p-i-n junction.

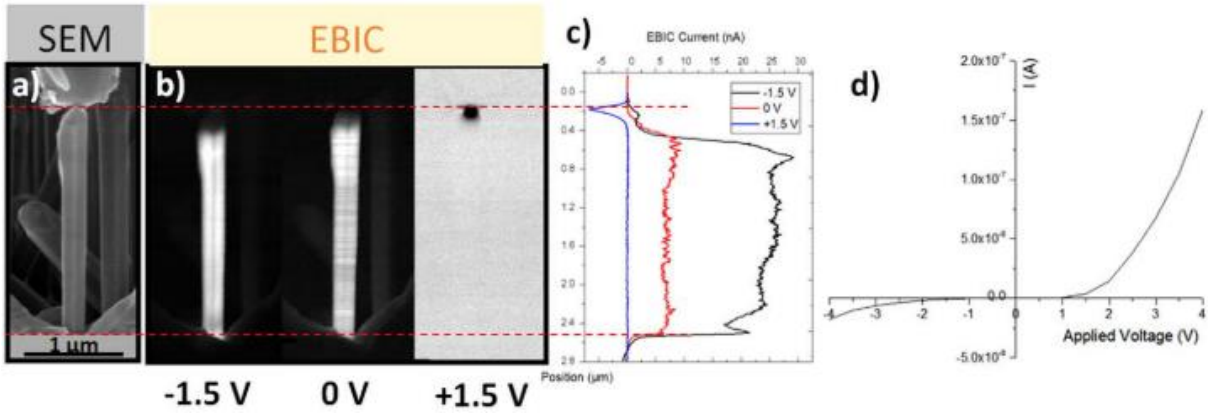

Figure 4.20. (a) SEM image and (b) EBIC maps under -1.5 V, 0 V and +1.5 V external bias on a single NW. (c) EBIC axial profiles under -1.5 V, 0 V and +1.5 V external bias. (d) Single NW I-V curve measured in dark condition.

Ultimately, these results indicate an efficient and uniform charge separation in the p-i-n junction of p-GaAs/p.i.n-$Al_{0.2}Ga_{0.8}As$ core/shell NWs. Therefore, such structures can be considered as potentially well-performing building blocks of our top-cell.

4.4 The passivation shell of core/shell NWs

In Chapter 1 we stress many times the importance of providing the NWs with a good passivation shell, and in the previous paragraph 4.3 we explain the reasons which made us adopt an $Al_{0.5}Ga_{0.5}As$/GaAs passivation shell. However, when it comes to the fabrication of a NW-based solar cell, the performance alone is not the only yardstick for the practical use of a material, another one being the compatibility with the other components of the device and with the overall fabrication process.

For this reason, the adoption of an $Al_{0.5}Ga_{0.5}As$/GaAs passivation shell introduces a problem: although such a structure preserves very well the inner regions of the NWs from oxidation and prevents surface states, it is also incompatible with the intended manufacturing process. As a matter of fact, if we aim to develop a top-cell like the one reported in Figure 4.7, after encapsulating the NWs it is necessary to remove that part of the passivation shell which emerges from the encapsulation layer, so as to deposit TCO on the exposed p-i-n junction and eventually contact the NW at their top. The problem of $Al_{0.5}Ga_{0.5}As$/GaAs consists in the fact that, to best of our knowledge, it does not exist any etching procedure capable to provide selectivity between this one and the PV active $Al_{0.2}Ga_{0.8}As$ shell, so that any attempt of etch would inevitably jeopardize the p-i-n junction on the exposed areas.

In order to overcome this problem, we considered two different passivating materials as possible substitutes of $Al_{0.5}Ga_{0.5}As$/GaAs, i.e. $Al_{0.5}In_{0.5}P$ and $Ga_{0.5}In_{0.5}P$, having band gap at 300 K equal to 1.85 and 2.30 eV, respectively. These were taken into account as feasible alternatives for different reasons: firstly, it is possible to perform selective etch in HCl solution of III-phosphides from III-arsenides,[196] thus preserving the latter ones. Secondly, their band gap is higher than that one of the $Al_{0.2}Ga_{0.8}As$ PV active region, thus reducing the impact on the photogeneration process. Moreover, although etch selectivity and high band gap are provided also by GaP and AlP, the ternary alloys in question are easier to integrate because of the lower lattice mismatch, since the lattice parameter of $Al_{0.5}In_{0.5}P$ and $Ga_{0.5}In_{0.5}P$ is close to that one of $Al_{0.2}Ga_{0.8}As$,[197] contrary to AlP and GaP (whose lattice parameter is 0.546 and 0.545 nm, respectively).

For such reasons, we prepared a series of three samples consisting in NWs with a GaAs core on which an $Al_{0.5}Ga_{0.5}As$/GaAs, $Al_{0.5}In_{0.5}P$ or $Ga_{0.5}In_{0.5}P$ shell was deposited. These NWs were subsequently characterized by PL spectroscopy in order to determine which compound is the most suitable to replace $Al_{0.5}Ga_{0.5}As$/GaAs. In all cases the GaAs cores were grown for 20 min following the standard procedure. Once formed the cores, the Ga droplets were consumed under As flux only (F_{As} = 4.05 ML/sec) at 610 °C for 4 min. Subsequently, the temperature was decreased and stabilized at 460 °C under the same As flux, so as to prevents its desorption. After that, the shells were grown. The first sample was prepared with 3 min of $Al_{0.5}Ga_{0.5}As$ and 2 min of GaAs growths, with F_{Ga} = 0.5 ML/sec, F_{Al} = 0.5 ML/sec and F_{As} = 4.05 ML/sec, corresponding to $R(F_V/F_{III})$ = 8.1 (and to an overall V/III flux ratio equal to 4.05 in the case of $Al_{0.5}Ga_{0.5}As$). The second one was coated with $Al_{0.5}In_{0.5}P$ for 3 min, with F_{Al} = 0.5 ML/sec, F_{In} = 0.5 ML/sec and F_{P2} = 4.2 ML/sec (both F_{In} and F_{P2} are expressed as equivalent growth rates of a 2D layer of InP on an InP(001) substrate). Similarly, the third one was made in $Ga_{0.5}In_{0.5}P$ under the same conditions but F_{Al}, in this case replaced by F_{Ga} = 0.5 ML/sec. In order to provide a reference for PL analysis, a sample of 20 min GaAs NWs was also prepared. Throughout the whole growth the samples were rotated at 6 rpm and the only source of Ga employed for this study was the cell Ga(5); no dopant was introduced into the structures.

SEM images of these samples are shown in Figure 4.21, whereas the values of NW diameter, length and density are reported in Table 4.2.

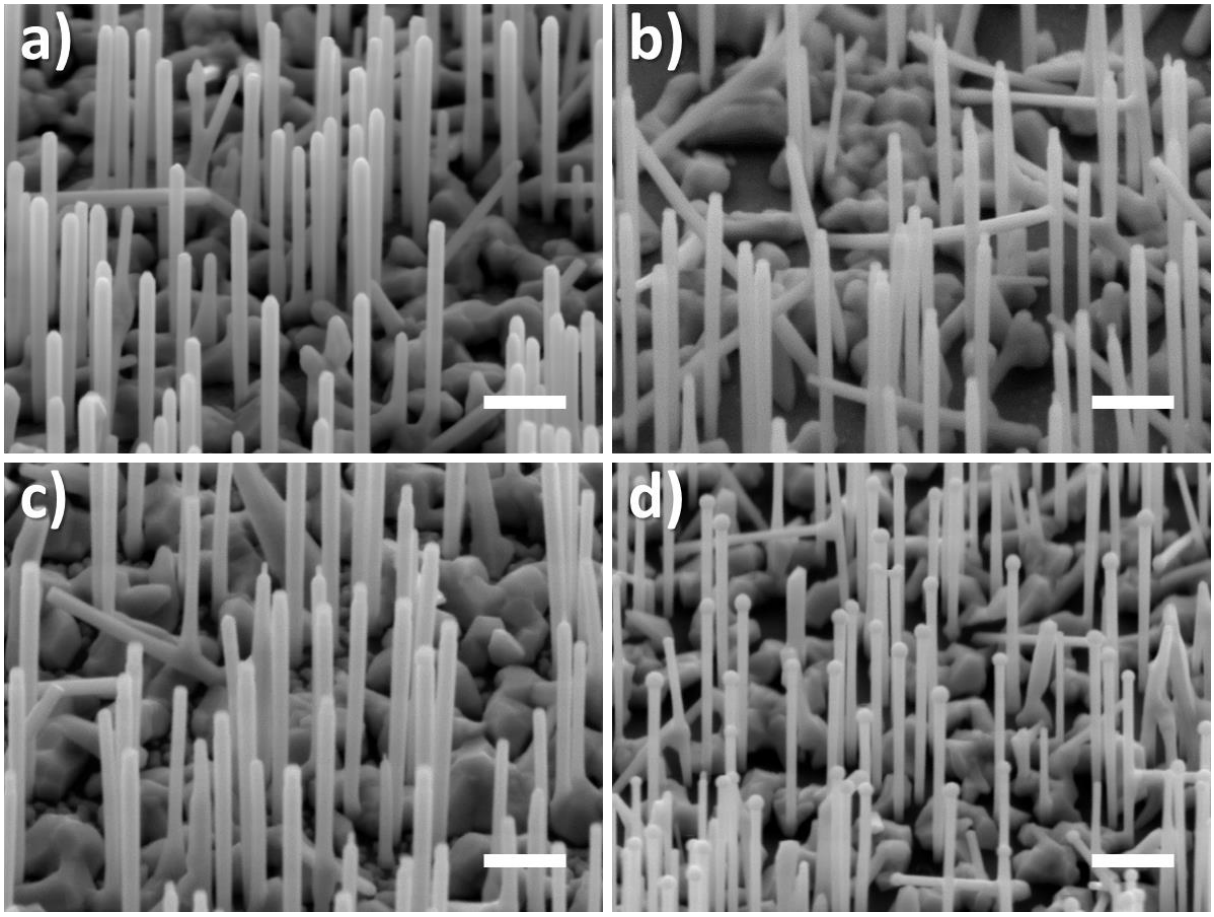

Figure 4.21. SEM images of 20 min GaAs NWs with (a) $Al_{0.5}Ga_{0.5}As$/GaAs, (b) $Al_{0.5}In_{0.5}P$, (c) $Ga_{0.5}In_{0.5}P$, and (d) without passivation shell (unconsumed droplets). The white scale bar corresponds to 500 nm.

Sample	d [NWs/μm^2]	L [μm]	D [nm]
GaAs/$Al_{0.5}Ga_{0.5}As$/GaAs	4.4	1.7 ± 0.1	97 ± 9
GaAs/$Al_{0.5}In_{0.5}P$	2.2	1.9 ± 0.2	88 ± 8
GaAs/$Ga_{0.5}In_{0.5}P$	1.8	1.8 ± 0.2	106 ± 12
GaAs	4.4	1.4 ± 0.1	62 ± 6

Table 4.2. Density, length and diameter for GaAs NWs with and without a passivation shell.

PL measurements were performed on the samples at 12 K with a 532 nm continuous wave diode-pumped solid-state laser with 70 mW power, and with a nitrogen cooled silicon CCD detector coupled to a monochromator. Time-resolved PL measurements were also carried out at 12 K with a pulsed laser source having wavelength equal to 515 nm, power of 40 mW (corresponding to about 2.4 μJ/cm^2 per pulse) and period of 52 Mhz.

A comparison of the PL spectra of the different samples normalized by the NW density is reported in Figure 4.22(a). It can be noticed the positive effect of the passivation shell on the PL peak, which become narrower and much more intense than that one of the non-passivated NWs. Concerning the GaAs/$Al_{0.5}Ga_{0.5}As$/GaAs NWs, the main peak at 1.504 eV can be attributable to undoped ZB GaAs, the expected value being 1.51 eV. A shoulder is also present at 1.487 eV which could be also explained considering a ZB/Wz mixture in the NWs : this is likely caused by twin defects or by the presence of stacking faults with ZB/Wz type II homojunction where the Ga droplet was consumed. It is noteworthy that corresponding peak and shoulder are observed also in the spectrum of the non-passivated NWs, thus confirming that these signals are due to GaAs only and not induced by the passivation shells.

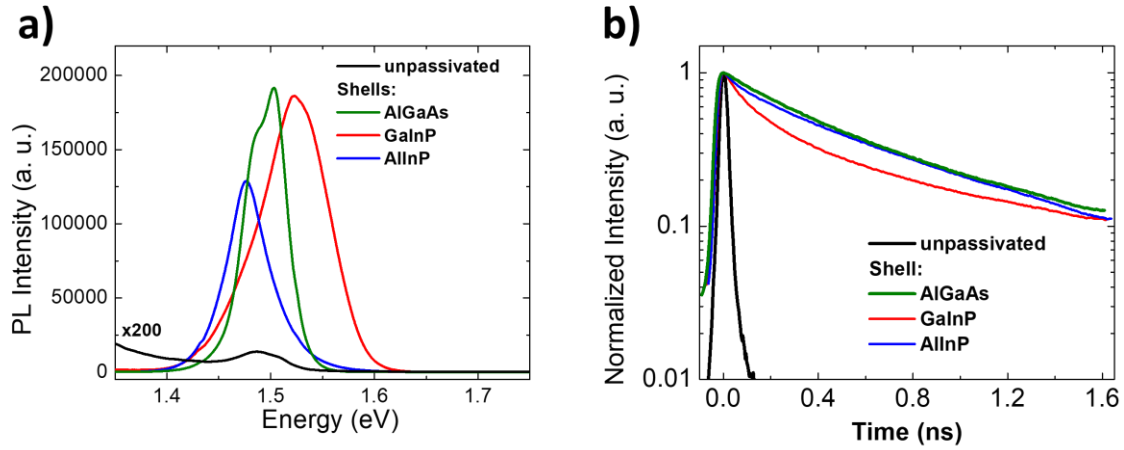

Figure 4.22. (a) PL spectra normalized for the NW density, and (b) normalized time-resolved PL spectra of passivated and non-passivated GaAs NWs.

Regarding the $Al_{0.5}In_{0.5}P$-passivated NWs, the intense peak observed at 1.476 eV undergoes thus a red-shift if compared to the NWs passivated with $Al_{0.5}Ga_{0.5}As$/GaAs. The red-shifts can be associated to a compressive strain in the shell and a tensile one in the core,[198] occurring when the shell has a bigger lattice parameter than the core (such a type of tensile strain evidently cannot occur in $Al_{0.5}Ga_{0.5}As$, its lattice parameter being equal to that one of GaAs). The observed red-shift is thus what is expected since the lattice parameter of $Al_{0.5}In_{0.5}P$ is slightly larger than that one of $Al_{0.5}Ga_{0.5}As$ (GaAs/$Al_xIn_{1-x}P$ mismatch is zero when x = 0.532).[197]

Contrary to what is observed with the $Al_{0.5}In_{0.5}P$ shell, the peak of GaAs/$Ga_{0.5}In_{0.5}P$ NWs is blue-shifted compared to the NWs passivated with $Al_{0.5}Ga_{0.5}As$/GaAs. However, in this case that cannot be associated to a tensile strain in the shell and a compressive one in the core, since $Ga_xIn_{1-x}P$ is matched with GaAs when x = 0.516.[197] As a consequence, in order to explain such experimental result, we should conclude that the composition of the passivation shell does not correspond to the nominal one of $Ga_{0.5}In_{0.5}P$, on the contrary having probably a composition $Ga_xIn_{1-x}P$ with x > 0.516. Another characteristic of the peak is

its broadness (about 77 meV), compared to that one for the signal of GaAs/$Al_{0.5}In_{0.5}P$ NWs (about 48 meV), which is likely induced by a higher compositional fluctuation in $Ga_{0.5}In_{0.5}P$ than in $Al_{0.5}In_{0.5}P$. This increase of the linewidth could also be a consequence of the strain which will induce a small heavy hole – light hole energy splitting.

In order to better evaluate the optoelectronic properties of the passivation shell, time-resolved PL measurements were also made to compare results obtained on passivated and non-passivated NWs (Figure 4.22(b)). The effect of the passivation is clearly visible, since the carrier lifetime increases significantly in presence of the passivation shell, thus indicating a strong reduction of the non-radiative recombination phenomena at the GaAs core surface. The carrier life-times in $Al_{0.5}In_{0.5}P$/GaAs and $Ga_{0.5}In_{0.5}P$/GaAs NWs are comparable to that one of the $Al_{0.5}Ga_{0.5}As$/GaAs NWs, (especially in the case of $Al_{0.5}In_{0.5}P$), suggesting that the carriers undergo the same dynamics in all the passivated NWs. In any case the decay curve is not mono-exponential, meaning that several decay processes are involved, such as exciton emission, type II emission and carrier relaxation from ZB to Wz.

Ultimately we can conclude that $Al_{0.5}In_{0.5}P$ and $Ga_{0.5}In_{0.5}P$ shells have similar behaviour, the time-resolved spectrum of the former being only slightly better than the latter. But, considering the possible presence of compositional inhomogeneities in the $Ga_{0.5}In_{0.5}P$ shell, which can originate unfortunate band curving, we have come to the conclusion that for our purpose it is $Al_{0.5}In_{0.5}P$ which can provide optimal passivation. This is also consistent with the previous work of Boulanger et al,[90] who employed $Al_{0.5}In_{0.5}P$ as passivation shell in a solar cell based on GaAs NWs with p-i-n radial junction.

4.5 Conclusion

In summary, we initially tried to grow $Al_{0.2}Ga_{0.8}As$ NWs on Si via self-assisted VLS mechanism, either by direct growth or with GaAs "seeds", but all our efforts failed, likely due to the interaction of Al with the substrate and the NW facets, which seems to inhibit the formation of Ga droplet (case of direct growth) or to cause the droplet consumption by reducing the diffusion coefficient of Ga adatoms (case of GaAs "seeds").

For this reason we opted for the alternative solution of inserting the PV-active p-i-n junction in a $Al_{0.2}Ga_{0.8}As$ shell grown around the p-GaAs core. Therefore, we investigated the effect of the doping level of Be on the core, observing that a heavy doping level ($2.5 \cdot 10^{-19}$ cm^{-3}) may affect the NW morphology, whereas a lighter one ($5 \cdot 10^{-18}$ cm^{-3}) seems suitable for our purpose.

Subsequently, we committed to growing and characterizing p-GaAs/p.i.n-GaAs core/shell NWs, and the EBIC analyses performed on them revealed their good diodic behaviour, a characteristic which makes them good candidates for a PV device. After that, similar growth were performed to obtain p-GaAs/p.i.n-$Al_{0.2}Ga_{0.8}As$ core/shell NWs, i.e. the type of structures expected to be the building blocks of the targeted TSC. Also in this case, the EBIC analyses gave a good response, confirming the potentialities of top-cell based on these NWs.

Ultimately, we performed a PL study on GaAs NWs with different passivation shells: taking into account the need for a material which is both well performing and compatible with the fabrication process, we came to the conclusion that a passivation shell of $Al_{0.5}In_{0.5}P$ is the most appropriate for our purpose.

5 The growth of self-assisted nanowires on patterned substrates

5.1 Introduction

After developing the procedure to obtain optimized core/shell NWs on epi-ready Si substrates, we directed our efforts to transfer the acquired know-how to the synthesis of similar structures on patterned substrates.

The main issue in this case was to achieve a high-enough percentage of vertical NWs, since non-vertical structures would be detrimental for the efficiency of the solar cell. For this reason, a large part of our experimental work on patterned substrates was directed to this end, although other important issues have also been addressed, such as the study of the dynamics of Ga pre-deposition, and the impact of the SiO_2 mask and fabrication process.

In order to expose systematically our work of research concerning this topic this chapter is subdivided into four sections. The first one presents the results of optical and electrical simulations performed by A. Kaminski's group at IMEP-LAHC in the frame of HETONAN ANR project to identify the optimal parameters of the NW network. The experimental results obtained by our group are described from the second part, which concerns the study of the Ga pre-deposition on patterned substrates realised at C2N. The third one treats the growth of NWs on the same type of patterned substrates, especially focusing on the optimization process undertaken to obtain high vertical yields and on the growth of core/shell NWs. This section offers insight into the factors which can have an influence on the vertical NW yield. The fourth section regards the growth of GaAs NWs on patterned substrates prepared at INL.

The results concerning the simulations exposed in Paragraph 5.2 have already been published by our partners of Anne Kaminski's group in an article by Maryasin et al,[199] therefore we refer to the reading of this paper for more details. Otherwise, a large part of the experimental data collected by our group about Ga pre-deposition and GaAs NW growth on patterned substrates, as included in Paragraphs 5.3 and 5.4, have already been reported in Reference[178].

5.2 Optimization of substrate and NW array parameters through simulations

Our partner at IMEP-LAHC performed coupled opto-electrical simulations so as to evaluate the effects of the geometrical parameters and define the optimal array configuration and NW geometry to develop a TSC. As simulations were performed, it had not yet been understood that it was not possible to obtain axial growth of $Al_{0.2}Ga_{0.8}As$, therefore the calculations were carried out assuming structures made of this alloy. Moreover, although calculations were performed assuming square arrays of NWs instead of the hexagonal ones later employed for the growth (cf. Paragraphs 5.3 and 5.4), we consider the differences between the two configurations as negligible. Optical simulations were run with Rigorous Coupled Wave Analyser (RCWA) solver. Their results were later coupled with those of the electrical ones, performed with the numerical Sentaurus TCAD. As a matter of fact, RCWA allows optimizing the light absorption over the geometrical parameters of a NW array, whereas Sentaurus TCAD permits to study complex architectures and to optimize the charge transport and carrier collection by considering also the effect of auxiliary layers and eventually modelling the device based on optical simulations.

The main concept at the basis of RCWA optical simulations is to vary the parameters of array period (p) (also named pitch), NW diameter (D) and length (generally indicated as L, but referred to as H only in this section to use the notation of Maryasin et al[199]) so as to fully exploit the resonant light trapping nature of NWs and eventually maximize light absorption. The basic strategy of the adopted approach has been already described elsewhere by Kaminski's group,[200] while the investigated system and the parameters employed for these calculations are summarized in Figure 5.1 and Table 5.1, respectively.

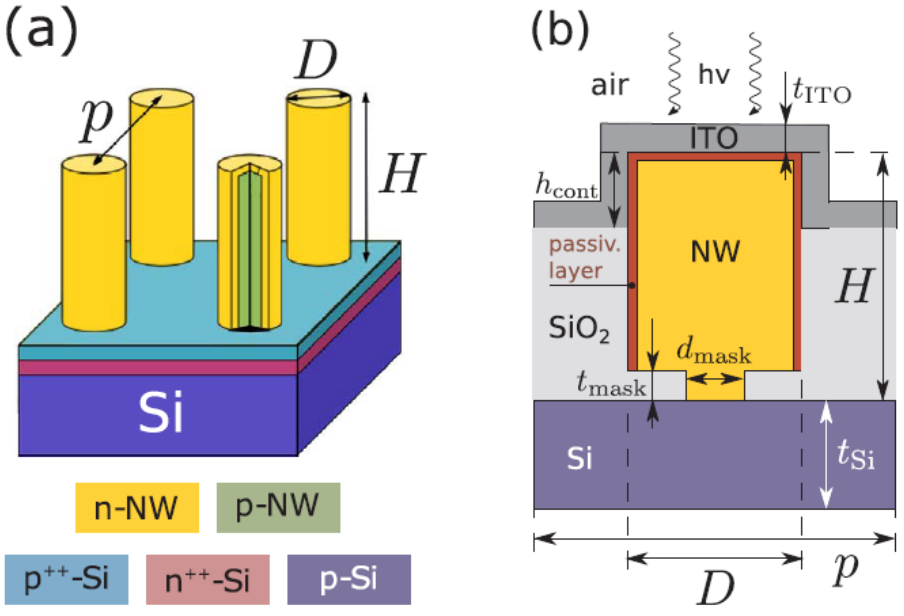

Figure 5.1. Schematics (a) of a square array of p-n core/shell AlGaAs NWs on Si and (b) of a single NW with geometrical parameters of the TSC in question.[199]

Parameter	Description	Value
		0.9 μm – 2.4 μm
H	Height of the nanowire	1.5 μm
		150 nm – 850 nm
p	Nanowire array pitch size	550 nm
		30 nm – 765 nm
D	Diameter of the nanowire	330 nm
t_{Si}	Si subcell thickness	200 μm
t_{ITO}	Thickness of the ITO layer	100 nm
t_{pass}	Thickness of the passivation layer	5 nm
h_{cont}	Vertical extent of top contact	300 nm
t_{mask}	Thickness of the SiO_2 mask	10 nm
d_{mask}	Hole diameter in the SiO_2 mask	50 nm

Table 5.1. Geometrical parameters adopted for RCWA simulations. For H, p, D, it is reported not only the considered range of values but also the optimal ones.[199]

H, p and the filling ratio D/p have been varied to increase the photogenerated current in the NW array. The spectral absorption is firstly calculated for each set of parameters, then integrated with ASTM AM1.5G solar radiation density spectrum I(λ) so as to provide the photocurrent density.

$$J_{NW/Si} = \frac{q}{hc}\int_{300\ nm}^{1100\ nm} A(\lambda)_{NW/Si}\, I(\lambda)\lambda d\lambda$$

where q is the elementary charge, h the Planck's constant, c the light speed, A the absorptance, I the ASTM AM1.5G spectrum and λ the wavelength.

Figure 5.2(a) shows the photogenerated current as a function of p and D/p for H = 1.5 μm, this corresponding to the optimal value of NW length. The dashed grey curves show as an example the response of NWs having D of 150 and 330 nm. The vertical grey dashed line separates two regions with different behaviour: for D/p < 0.5, the photogenerated current increases strongly with the filling factor, whereas with D/p > 0.5, the current tends to saturate with a broad maximum (the graphic in question displays two maxima for J = 18 mA/cm^2 marked with grey spot). Figure 5.2(b) shows the difference in photogenerated current between the top and bottom sub-cells; the grey full line marks the profile of perfect current matching, where the difference is zero. The best matching is achieved for D ≈ 330 nm and p ≈ 550 nm, so that these parameters can be assumed as the optimal ones, corresponding to a photogenerated current of 17.8 mA/cm^2 in the top cell and of 17.6 mA/cm^2 in the bottom one (the corresponding point is marked by a grey star in Figure 5.2(a)).

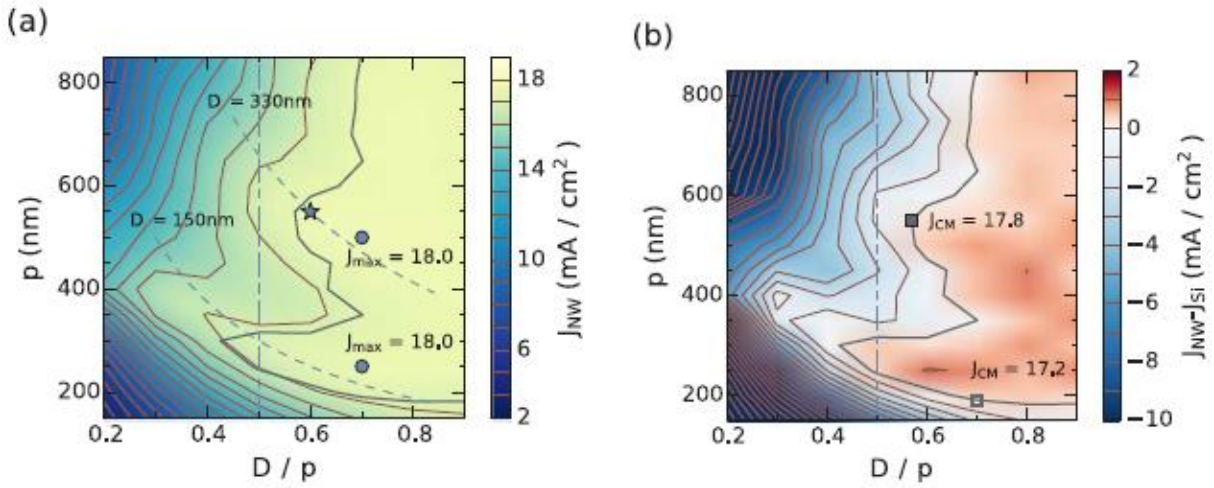

Figure 5.2. (a) Photogenerated current of the top cell J_{NW} as a function of p and D/p. (b) Photocurrent difference between top and bottom sub-cells.

As above mentioned, these results are obtained with H = 1.5 µm; indeed, the graphic of the current density as a function of the NW length for D = 330 nm and p = 550 nm displayed in Figure 5.3 shows an increasing trend with H, since longer NWs are capable to absorb more red photons. It can be also observed that the photocurrent matching J_{CM} saturates for H around 1.5 µm: for such a reason, this value has been considered as the optimal NW length for our TSC.

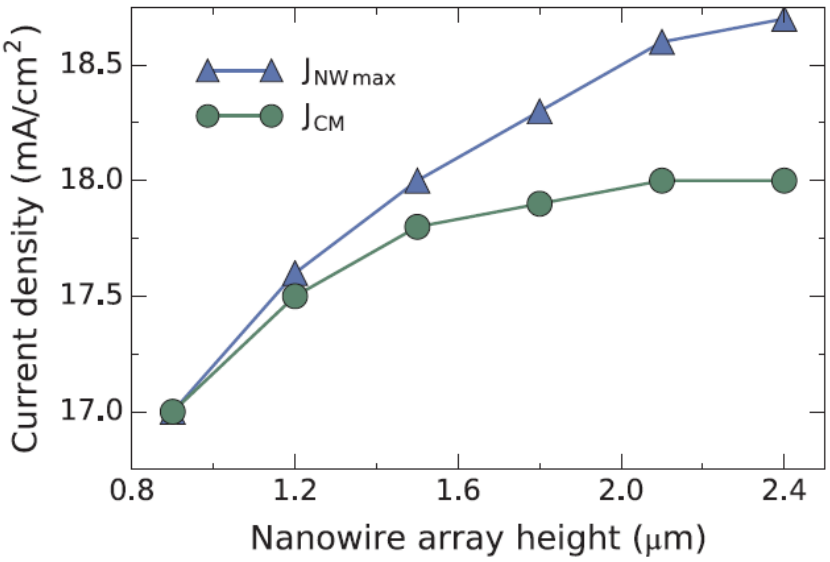

Figure 5.3. Photogenerated current in the top cell (blue) and overall current matching of the TSC (green) as a function of NW length H, for D = 330 nm and p = 550 nm.

The optimization of the single NW configuration through electrical simulation is performed by optimizing the carrier collection, i.e. taking into account the geometry and the

electronic parameters of the system (Figure 5.4), as well as the recombination mechanisms which are expected to occur in the structure. Continuity and Poisson's equations are thus solved assuming p = 550 nm, D = 330 nm, H = 1.5 µm and considering four types of recombination phenomena: surface, Shockley-Read-Hall (SRH), radiative and Auger recombinations. The parameters adopted in the electrical simulations are reported in Table 5.2.

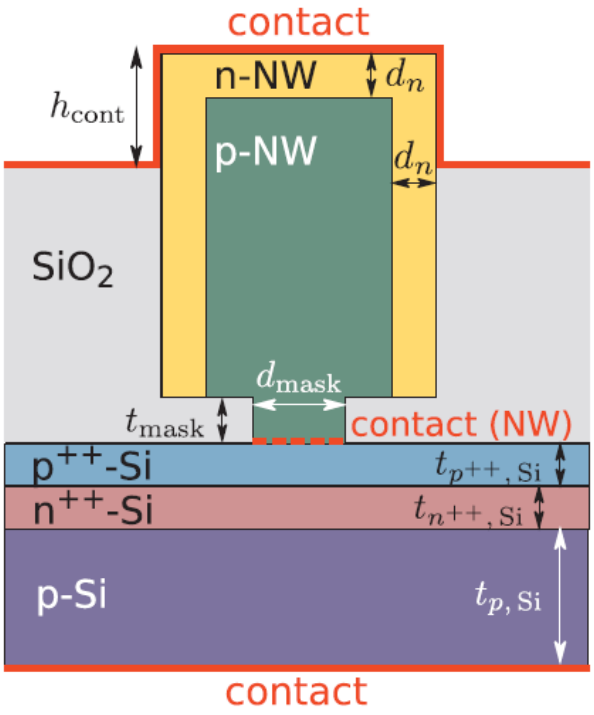

Figure 5.4. Cross-section schematics of the TSC reporting the geometrical parameters of the system.[199]

Parameter	Description	Value
d_n	Axial and radial shell thickness	15–50 nm 20 nm
r_p	Core radius	280–315 nm 310 nm
$N = N_n = N_p$	Nanowire donor and acceptor doping concentration	1×10^{17} cm^{-3}–1×10^{19} cm^{-3} 5×10^{18} cm^{-3}
μ_n	Electron mobility in the nanowire	1500 cm^2/(V s)–4500 cm^2/(V s)
μ_p	Hole mobility in the nanowire	100 cm^2/(V s)–280 cm^2/(V s)
v_{th}	Thermal velocity of carriers	1×10^7 cm/s
$\tau = \tau_n = \tau_p$	SRH recombination lifetime	1 ns
$S = S_n = S_p$	Surface recombination velocity	1×10^4 cm/s
$\sigma_n = \sigma_p$	Carrier capture cross-section of trap states	1×10^{-15} cm^2
$N_{\mathrm{TA}} = N_{\mathrm{TD}}$	Density of surface trap states	1×10^{12} cm^{-2}
C_{rad}	Radiative recombination coefficient	1.8×10^{-10} cm^3/s
C_{Aug}	Electron and hole Auger recombination coefficients	1×10^{-30} cm^6/s
$t_{p^{++},\mathrm{St}}$	Thickness of the tunnel junction layer	15 nm
$t_{n^{++},\mathrm{St}}$	Donor layer thickness of the silicon bottom cell	15 nm
$t_{p,\mathrm{St}}$	Acceptor layer thickness of the silicon bottom cell	199.97 µm
$N_{p^{++},\mathrm{St}}$	Donor doping concentration in the tunnel junction	1×10^{20} cm^{-3}
$N_{n^{++},\mathrm{St}}$	Acceptor doping concentration in silicon	1×10^{20} cm^{-3}
$N_{p,\mathrm{St}}$	Donor doping concentration in silicon	5×10^{16} cm^{-3}

Table 5.2. Parameters used in the electrical simulations.[199]

As already mentioned in Chapter 1, one of the drawbacks of radial junctions consists in the fact that geometry and doping level must be chosen very carefully, so as to prevent core or shell depletion.[201,202] Therefore, one of the purpose of the simulations was to perform an optimization of the radial junction by varying both the thickness of the emitter and the doping level: this was done assuming the doping level of the p-core always equal to that one of the n-shell. The graphic in Figure 5.5 shows the efficiency of the top cell as a function of the shell thickness and doping concentration. It can be noticed that higher efficiencies are achieved with heavier n-doping, since charge accumulations and band bending present on the NW surface can cause a complete depletion of the shell if this is too thin, with an increase of SRH recombinations.[201] A possible solution to this problem may consist in adopting a thicker and/or more heavily doped junction, or alternatively in decreasing the doping level of the core,[201] although the latter approach presents the risk of a complete depletion of the core, especially in the case of NWs with smaller radius.

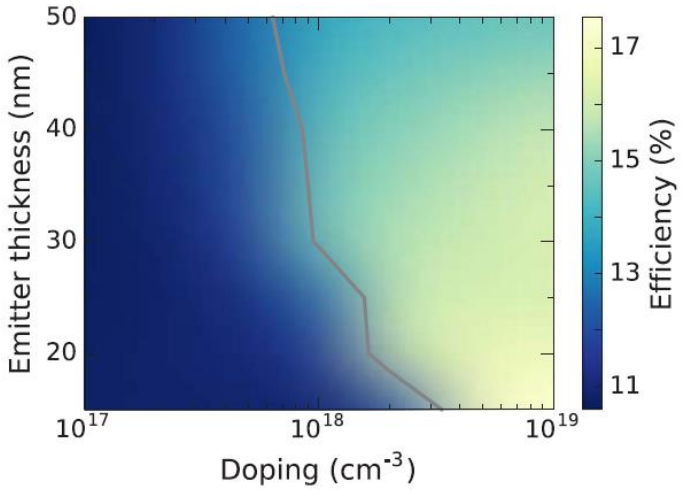

Figure 5.5. Conversion efficiency as a function of the shell thickness and doping concentration.

The electric simulations eventually permitted to determine the overall efficiency of the TSC (parameters concerning the bottom cell and the tunnel junction are also reported in Table 5.2). The as-obtained J-V curves for the two sub-cells and the TSC are shown in Figure 5.6. It can be noticed that according the calculations, V_{OC} of TSC should be almost the sum of those of the sub-cells, with a small loss due to the tunnel junction and to the slightly low current in the top cell. V_{OC} is thus found to be equal to 1.85 V, J_{SC} to 17.1 mA/cm^2 and FF to 0.87, while the efficiency of the TSC results 27.6 %. Such a value is consistent with the realistic efficiency estimations by Bu et al[109] and Wang et al[110] already mentioned in Chapter 1.

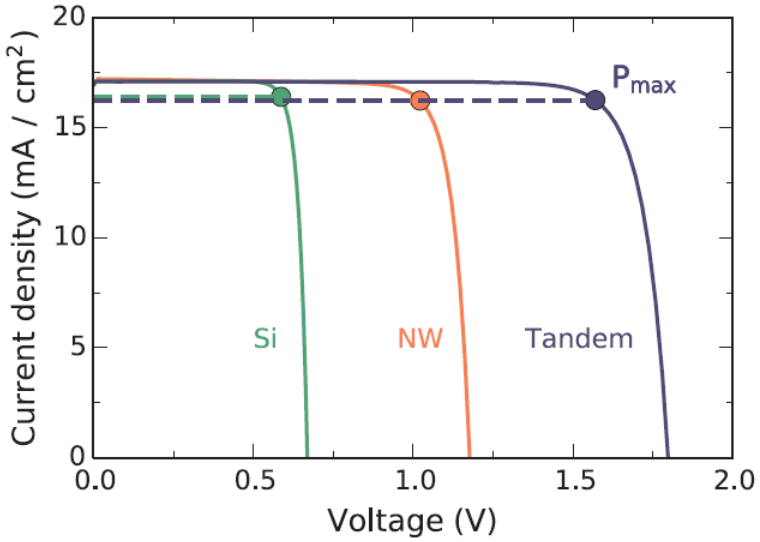

Figure 5.6. J-V curves for bottom cell, top cell and optimized TSC.

Ultimately, it should be noted that the electrical simulations showed no variation of the TSC performance for hole diameters (marked as d_{mask} in Figure 5.4) in the 50-200 nm range. Therefore, we can conclude that the optimal structures for the development of our TSC consists in an ordered array of holes with diameter equal to 50 nm and pitch of 550 nm, where to grow NWs having diameter of 330 nm and length equal to 1.5 µm.

5.3 The pre-deposition of Ga droplets on patterned Si substrates prepared at C2N

In order to achieve ordered arrays of vertical self-assisted GaAs/AlGaAs core/shell NWs and to reduce the growth of parasitic structures, it is necessary to deposit Ga droplets selectively, i.e. only in the holes of the mask. Therefore, outlining the correct pre-deposition protocol is a propaedeutic step to the growth of ordered arrays. In this case, experiments were carried out on Si(111) substrates with SiO_2 patterned mask prepared by electron-beam lithography (EBL). These were fabricated by A. Cattoni at C2N as following.

The patterned substrates came from B-doped (0.02-0.06 Ω·cm) 2-inches Si(111) wafers. These were cleaned following the procedure reported by Madiomanana et al,[203] based on repeated steps of plasma oxygen and HF etching in order to trap and remove all the non-volatile contaminants formed on the Si(111) surface. A 20-30 nm-thick SiO_2 layer was then deposited on the wafers by PECVD and patterned by EBL at 100 keV (with an instrument Vistec EBPG5000+) using positive-tone PMMA resist (495PMMA A - solids: 2% in Anisole). The pattern design was subsequently transferred into the SiO_2 mask by anisotropic reactive

ion etching (RIE) with SF_6/CHF_3 gasses. A thin layer of SiO_2 (4-5 nm) was intentionally conserved at the bottom of the holes, so as to prevent possible damages to the Si(111) surface by the RIE.

Each wafer was patterned so as to provide 9 chips of 1 cm x 1 cm (Figure 5.7) and to study the influence of hole diameter and pitch on the vertical NW yield. In every chip there was a first zone with 20 µm x 20 µm patterned areas with hexagonal arrays of circular holes realised by exposition to the electron beam. These patterned areas differed from one another because of the pitch (300, 400 and 500 nm) and the nominal hole diameter (from 20 to 80 nm - column 1 to 7) adopted, for a total of 21 different areas on each chip. Below this zone it was introduced a second one with 1 mm x 1 mm patterned areas (4 with p = 500 nm and 4 with p = 1µm) with circular holes realised with exposition to the electron beam with a single shot (dose from 18000 to 31000 mC/cm^2). Every chip was separated from the others by UV-laser cutting.

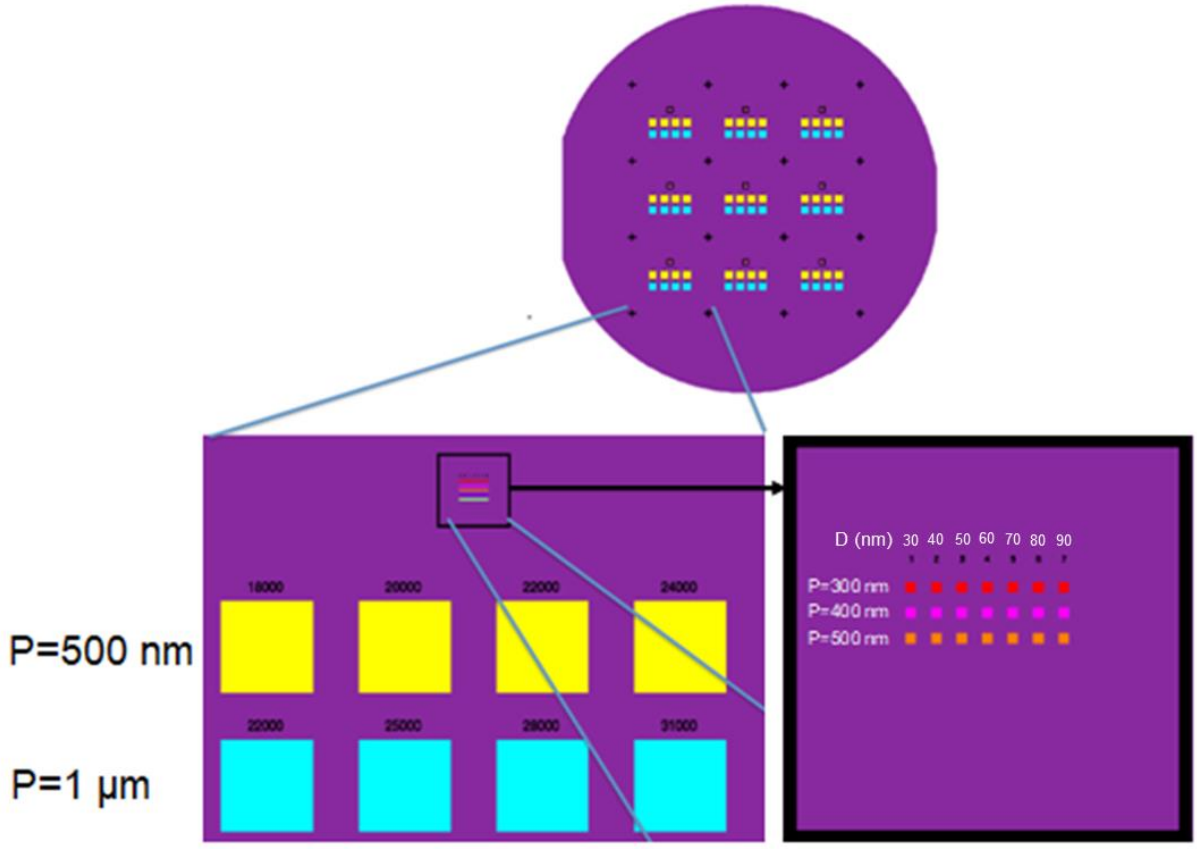

Figure 5.7. Design of the patterned mask prepared by our partners at C2N.

Since a decade, many experimental works concerning the growth of GaAs (or related ternary alloys) NWs on patterned Si substrates have been conducted to define optimal procedures and maximize the vertical NW yield.[75,139,210–213,141,159,204–209] In our work, this was carried out on patterned SiO_2/Si substrates after a chemical pre-treatment in a 1% HF

solution: as a matter of fact, the silicon oxide at the bottom of the holes in the silica mask prevents the selective deposition of Ga impeding the VLS growth, so that it is necessary to remove it to obtain the self-assisted VLS growth of the NWs. The etching time must be well calibrated in order to achieve the proper value of final thickness for the silica mask, given that this is a parameter which strongly affects the NW verticality.[205] The etching isotropy is another reason to control and reduce as much as possible the timing of this step since the size of the patterned holes might reach a critical value beyond which it is difficult to obtain vertical NWs.

Based on these considerations, the applied chemical pre-treatment consisted in etching the patterned substrate for 25 sec in a 1% HF solution, then rinsing it in de-ionized water for 20 sec, this causing a reduction of the SiO_2 layer thickness from 25 to 19 nm. Ga pre-deposition (108 MLs) was performed at 600°C on as-treated substrates with F_{Ga} = 0.5 ML/sec. It must be noticed that all NW growths on patterned substrates have been carried out employing the Ga(5) cell (α = 27.9°) as source.

This procedure provided excellent results in terms of selectivity, as illustrated in Figure 5.7, because all holes are filled with a single Ga droplet regardless their diameter and pitch (the only exception consists in those ones with nominal diameter of 20 nm, which were probably not transferred during the EBL because of the too small size), and because the deposition does not occur outside holes, thus reducing significantly the risk of parasitic NW growth.

It was also noticed that the diameter of the droplets, yet depending on that one of the holes, is independent from the value of the pitch, being almost the same in holes of the same size on pitches from 300 to 500 nm (Figure 5.8). This is as an evidence for the fact that, with a Ga flux alone (without any As flux), there is not any Ga adatom surface diffusion effect contributing to the size of the droplets, which is determined only by the amount of Ga arriving directly on the holes.

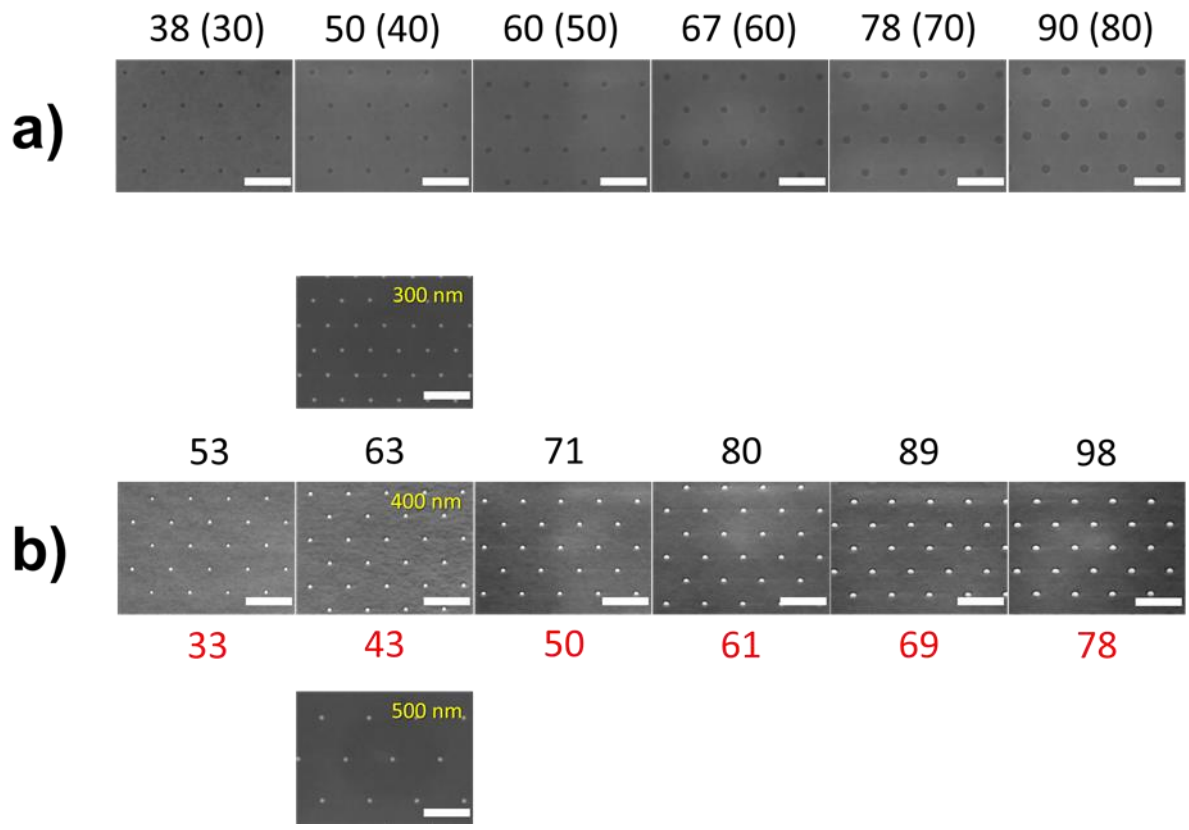

Figure 5.8. (a) SEM images of hole networks after the HF treatment and related values of the hole diameter (at the top) in nm (nominal diameter in brackets) (b) SEM images of the corresponding holes after the Ga deposition (108 MLs) and related values of the hole diameter (at the top) in nm (black) and of the Ga droplet diameter (red) in nm. The white scale bar in each image stands for 500 nm. The images here reported correspond to patterned areas with a 400 nm pitch, but analogous results in term of droplet diameter were observed also for 300 and 500 nm pitches (here reported as an example for nominal hole diameter of 40 nm), thus suggesting that the size of the droplet depends only on the Ga direct impingement and not on the diffusion of Ga adatoms.

In Figure 5.9, the average values of the hole diameters (at the top) before and after the Ga deposition are also reported. The most important consideration that can be made observing these data is that the hole top diameter increased significantly during the Ga deposition. Since the substrate was previously treated with 1% HF solution in both cases, the enlargement must be attributed to the action of Ga itself. A visible example of this phenomenon is reported in Figure 5.9, showing two holes patterned with the same nominal diameter of 60 nm after HF treatment (increase from 60 to 67 nm) and Ga deposition. It is thus possible to observe that the hole top diameter increased from 67 to 80 nm due to the Ga deposition, with a Ga droplet which is 61 nm in diameter.

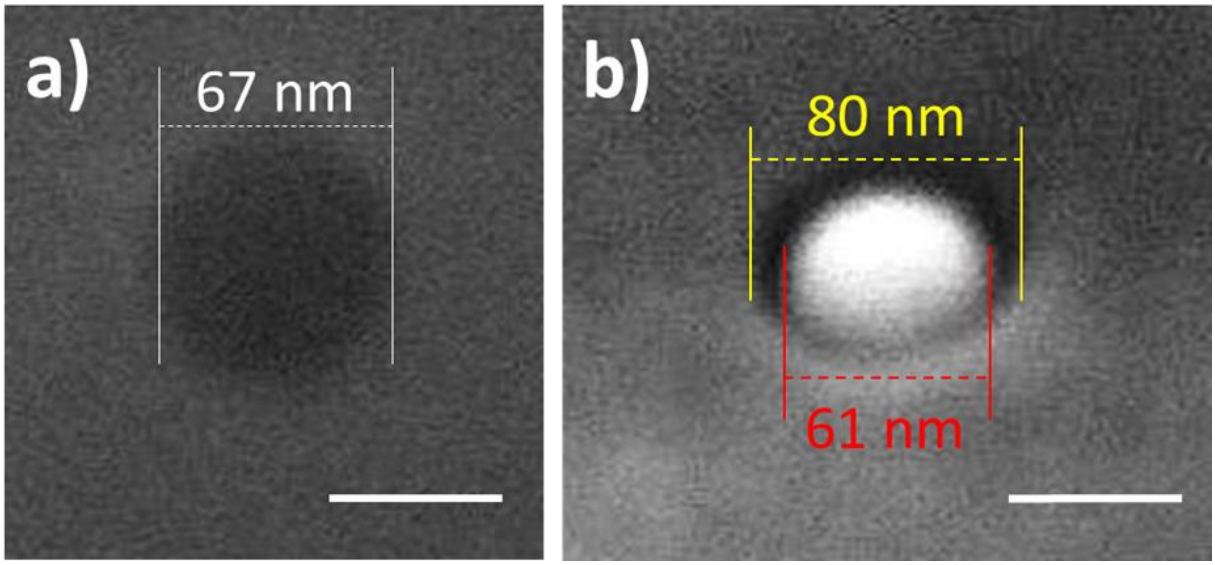

Figure 5.9. SEM images of holes patterned with the same nominal diameter: (a) after the 1% HF treatment (top view), and (b) after Ga deposition (45° tilted). In both cases the white scale bar corresponds to 50 nm.

Although these results may suggest that the SiO_2 mask was etched by the Ga flux, ellipsometric measurements proved that the overall thickness of SiO_2 is unchanged after the Ga deposition, so that it can be concluded that only the hole walls were involved in the etching process.

Starting from the SEM images it is also possible to calculate the approximate volume of holes after the Ga deposition and of the related Ga droplets. For the hole volume, we have therefore to take into account the profile of the hole as revealed by TEM imaging performed on thin lamellae prepared by Focused Ion Beam (FIB) on a sample were GaAs NWs had been grown (Figure 5.10). The FIB procedure was performed at INL by S. Brottet.

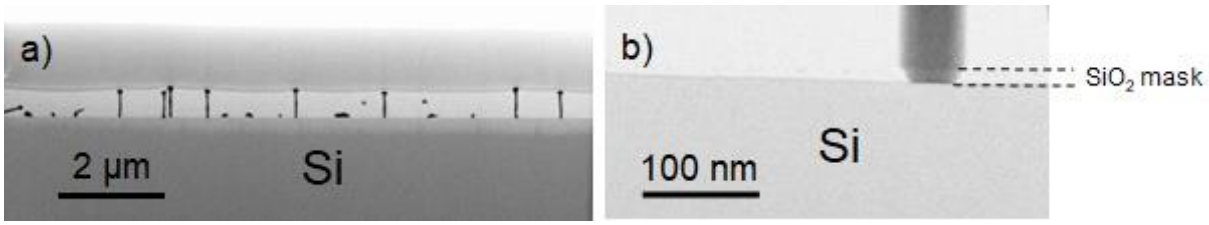

Figure 5.10: TEM images of a thin lamella prepared by FIB including a row of self-assisted GaAs NWs grown on a patterned substrate.

TEM images like the one shown as an example in Figure 5.11(a) shows that the shape of the holes corresponds to a truncated cone with an average angle α equal to 62°, and consequently their volumes were calculated adopting this geometry. This allows estimating

the diameter of the hole at the bottom for each case knowing the one at the top from SEM measurements. Given a hole depth equal to 19 nm, the hole volumes can be obtained. The volume and the height of the Ga droplets were instead calculated assuming them as spherical caps with a diameter equal to the one measured by SEM and a contact angle ϑ for liquid Ga on a crystalline Si surface equal to 50°.[147]

The results of the diameter measurements or calculations of the Ga droplets and of the top and the bottom of the holes are reported in Table 5.3, as well as the hole volume and the droplet volume and height for each related case. By comparing the bottom diameters after the 1% HF treatment only and after the Ga deposition with the nominal values of the untreated holes and considering the related errors, it can be stated that the three series of values are *de facto* equivalent. Considering that after the RIE etching the holes are cylindrical, these results suggest that neither the HF etch nor the Ga deposition step increases the diameter of the hole bottoms and that the etching of the SiO_2 during the 1% HF treatment and the reduction of SiO_2 by Ga only occur on the SiO_2 walls, as schematized in Figure 5.11(b): as a consequence, the bottom diameter can be considered always constant and approximated to the nominal one, and the same consideration can be made therefore for the Ga capture surface.

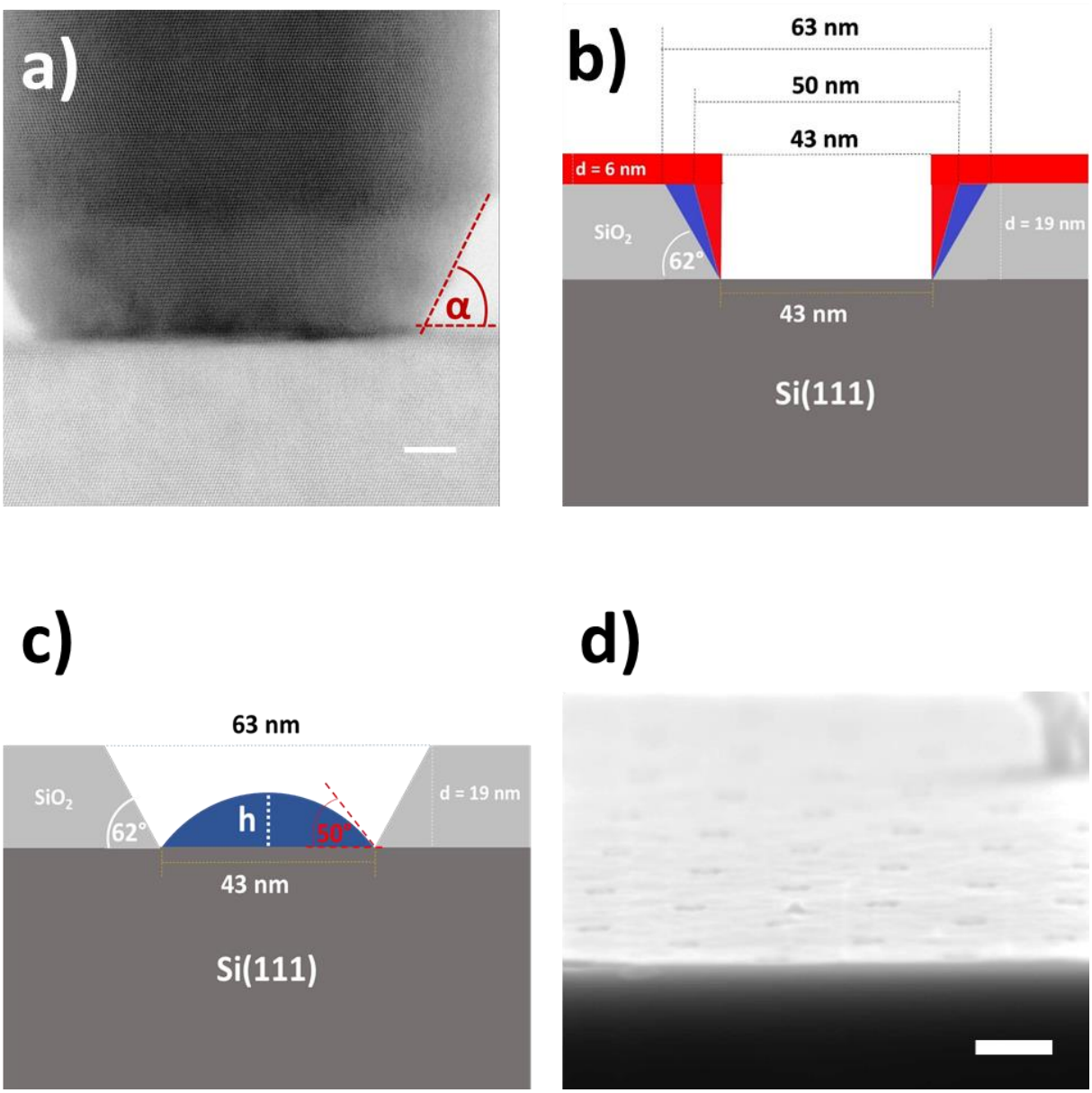

Figure 5.11. (a) TEM image of a FIB-prepared thin lamella showing a NW grown inside a patterned hole in SiO_2; it is possible to observe the truncated conical shape of the hole, with the angle α marked in red. The white scale bar corresponds to 5 nm. (b) Schematics of the hole enlargement caused by 1% HF etching (red) and Ga deposition (blue) in a hole whose top and bottom diameter before any treatment corresponds, as an example, to the nominal value of 40 nm (measured value: 43 nm); the final angle α of the hole is 62°. (c) Schematics of a Ga droplet deposited in a hole whose top and bottom diameters are, as an example, equal to 63 and 43 nm, respectively, after the Ga deposition; the angle α is equal to 62°, the contact angle θ is equal to 50° and the height of the droplet is estimated at 9.6 ± 1 nm. The hole depth is equal to 19 nm (SiO_2 thickness after the 1% HF treatment). (d) SEM image at grazing angle (5°) showing patterned holes after the deposition of 108 MLs Ga: as expected, no Ga droplet peeps through the holes, which is consistent with the hypothesis of a wetting angle at Ga/Si interface around 50°. The white scale bar corresponds to 200 nm.

Nominal diameter of the holes (as patterned) [nm]	Hole diameter at the top after HF treatment (measured) [nm]	Hole diameter at the top after Ga deposition (measured) [nm]	Hole diameter at the bottom after Ga deposition (calculated based on the TEM image) [nm]	Hole volume after Ga deposition V_h (calculated) [nm^3]	Ga droplet diameter D_d (measured) [nm]	Ga droplet height h_d (calculated based on a contact angle = 50°) [nm]	Ga droplet volume V_d (calculated based on measured droplet diameter) [nm^3]	Ga volume coming from atomic flux V_f (calculated) [nm^3]
30	38 ± 3	53 ± 3	33 ± 3	28000 ± 3900	34 ± 2	7.9 ± 1	3900 ± 600	11000 ± 2000
40	50 ± 3	63 ± 3	43 ± 3	42300 ± 4700	41 ± 2	9.6 ± 1	6800 ± 700	18700 ± 2600
50	60 ± 3	71 ± 3	51 ± 3	55800 ± 5400	51 ± 1	11.9 ± 1	13000 ± 1100	26300 ± 3100
60	67 ± 2	80 ± 3	60 ± 3	73400 ± 6500	61 ± 2	14.0 ± 1	21900 ± 2100	36300 ± 3500
70	78 ± 3	89 ± 2	69 ± 2	93400 ± 6200	69 ± 2	16.1 ± 1	32300 ± 2700	48100 ± 2800
80	90 ± 2	98 ± 3	78 ± 3	115800 ± 8000	76 ± 2	17.7 ± 1	43100 ± 3900	61400 ± 4700

Table 5.3. Hole diameter and volume (measured or calculated) and corresponding diameter and volume of Ga droplets (measured or calculated) for patterned area with pitch equal to 350 nm. Experimental data from Figure 5.7.

Similarly, it can be observed that the values of the Ga droplet diameters and those of the hole bottoms are equal in their margins of error: this fact suggests that the Ga droplets tend to cover entirely the available Si surface at the bottom of the hole, thus adopting a configuration, as schematized in Figure 5.11(c), where the droplet do not wet the silica. Since the difference in diameter between the Ga droplets and the related holes at their top is always about 20 nm, it can be concluded that this is the common configuration for any hole diameter here reported, providing the Ga amount is sufficient to cover entirely the hole bottom.

It can be also noticed that, based on these calculations, the height of the droplets is always lower than the depth of the corresponding holes. This result is consistent with SEM images of the patterned areas collected at grazing angles (Figure 5.11(d)), showing that, for

this amount of Ga and in this range of hole diameters, the Ga droplet height do not exceed the hole height.

In order to evaluate the Ga volume V_f coming from the Ga atomic flux which can be intercepted by the hole, we assumed a capture surface corresponding to the one at the bottom of the hole, as above mentioned. Based on this consideration and adopting a procedure previously used by Plissard et al. in 2011,[205] the corresponding volume of Ga to which every hole was exposed was finally estimated (Table 5.3). This can be calculated with the formula:

$$n_h = \Gamma T_d D_{Ga} S$$

where n_h is the amount of Ga adatoms evaporated in the hole, Γ is the growth rate (ML sec^{-1}), T_d is the duration of the deposition step (sec), D_{Ga} is the density of adsorption sites (sites ML^{-1} nm^{-2}) and S is the hole surface (nm^2).

It is noteworthy that these calculated volumes always exceed those ones of the Ga droplets V_d, thus suggesting that not all the Ga arriving on the holes contributes to the formation of the droplets, part of it being desorbed at such temperatures. A possible interpretation to explain such results is that part of the Ga coming from the atomic flux desorbs because in such conditions the droplets might be in an equilibrium state with a contact angle ϑ = 50°, and therefore they would tend to maintain this stable configuration rather than changing their shape and increasing their size.

In particular, considering ΔVol the difference between the volume V_f of the Ga coming on the capture surface from the atomic flux and the volume V_d of the droplets, it can be noticed that plotting ΔVol as a function of the droplet radius R_d, on which the droplet perimeter depends, a linear relationship is obtained (Figure 5.12(a)). On the contrary, plotting ΔVol as a function of the droplet surface clearly does not show any linear behaviour (Figure 5.12(b)). This fact suggests therefore that the excess of Ga is desorbed from the perimeter of the droplet and not from its surface. As schematized in Figure 5.12(c), a Ga atom desorption process taking place on the silica flanks at the droplet perimeter droplet can be advanced to account for the measured droplet volumes.

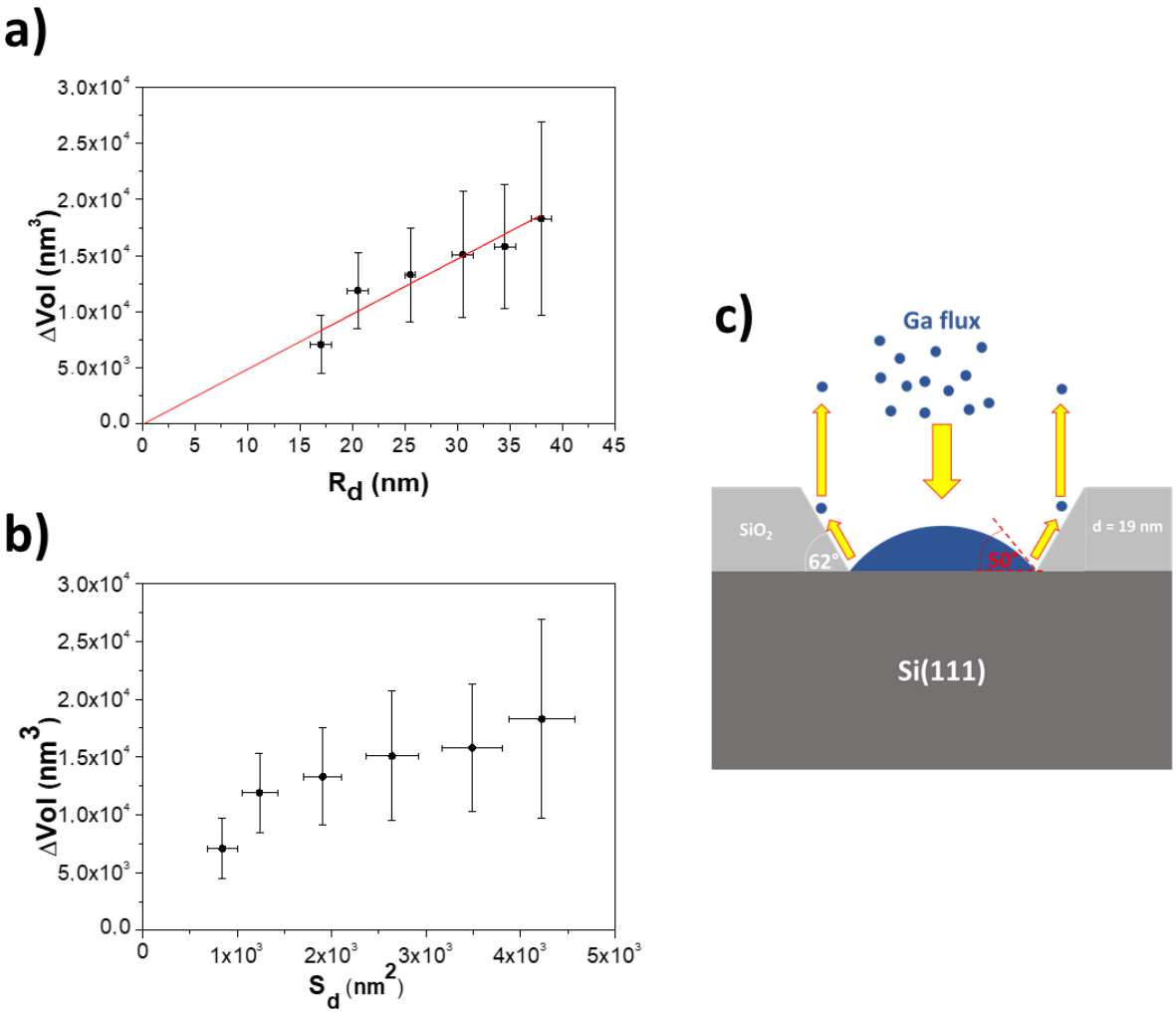

Figure 5.12. Evolution of ΔVol as a function of (a) the droplet radius (relative to its perimeter) and (b) the droplet surface. (c) Schematics of the proposed mechanism for the Ga desorption; once the droplet reaches an equilibrium configuration, it tends to keep it by desorbing the excess of Ga from its perimeter.

The above-reported experimental data show that the Si(111) substrates covered with EBL-patterned SiO_2 mask as prepared at C2N ensure a total selectivity for Ga deposition in the holes. This study allowed us to describe how the Ga droplets are placed inside the holes, and to link the size and shape of the holes with those ones of the Ga droplets. In particular, having found out that the diameter of the droplets coincides with that one of the hole bottom and that the hole have conical shape, constitutes an important information about the system configuration at the beginning of the growth. This will certainly be helpful to develop hypotheses to identify the factors and mechanisms leading to high vertical yields (cf. Paragraphs 5.4 and 5.5).

5.4 The growth of NWs on patterned substrates prepared at C2N

In this section, we will finally address the growth of ordered arrays of NWs on patterned substrates prepared at C2N. As previously mentioned, in order for the photovoltaic cells to function properly, it is crucial to obtain a high rate of vertical GaAs NWs, minimizing the presence of both parasitic crystallites and inclined structures. In particular, we assumed a vertical rate of about 90 % as a good enough target for proceeding with the development of PV devices. Such an objective was eventually fulfilled, although the development of an efficient and reproducible protocol, based on the use of a thermal pre-treatment, was a difficult step which cost us a lot of effort. The details concerning this study are reported in the Paragraph 5.4.1.

Once achieved this goal, we committed to employing the acquired know-how to synthesize ordered arrays of PV active core/shell NWs, with the prospect of using these same samples in the future manufacture of photovoltaic cells. The results of the growth of these core/shell NWs, as well as the characterization of their radial junction by EBIC, are reported in the Paragraphs 5.4.2 and 5.4.3.

5.4.1 The quest for a high vertical yield: the importance of the thermal pre-treatment

Having obtained promising results with the protocol adopted for the Ga pre-deposition, we decided to adopt this procedure in the growth of GaAs NWs. Therefore, we adopted the same type of substrate and procedure described in Paragraph 5.3, firstly cleaning the bottom of the holes with 1% HF solution for 20 sec, then pre-depositing 108 MLs of Ga at the rate of 0.5 ML/sec at temperatures in the 600-615°C range, and finally growing the NWs for 10 min with F_{Ga} = 0.5 ML/sec and F_{As} = 1.15 ML/sec ($R(F_{As}/F_{Ga})$ = 2.3) at the same temperature.

The results obtained initially proved to be contradictory: although a couple of samples provided high vertical yields (up to ≈75 %) in some patterned areas (Figure 5.13(a)), the rest of the specimens (prepared with such a procedure both as GaAs and as GaAs/$Al_{0.2}Ga_{0.8}As$ core/shell NWs) presented a much lower rate of vertical NWs, reaching a maximum of 30-40 % (Figure 5.13(b)). This fact could not be associated either with a chronological effect, since the few high yield samples were alternated with the vast majority of low-yield samples, or to an influence of the substrates, since this behaviour was observed on samples coming from different Si wafers.

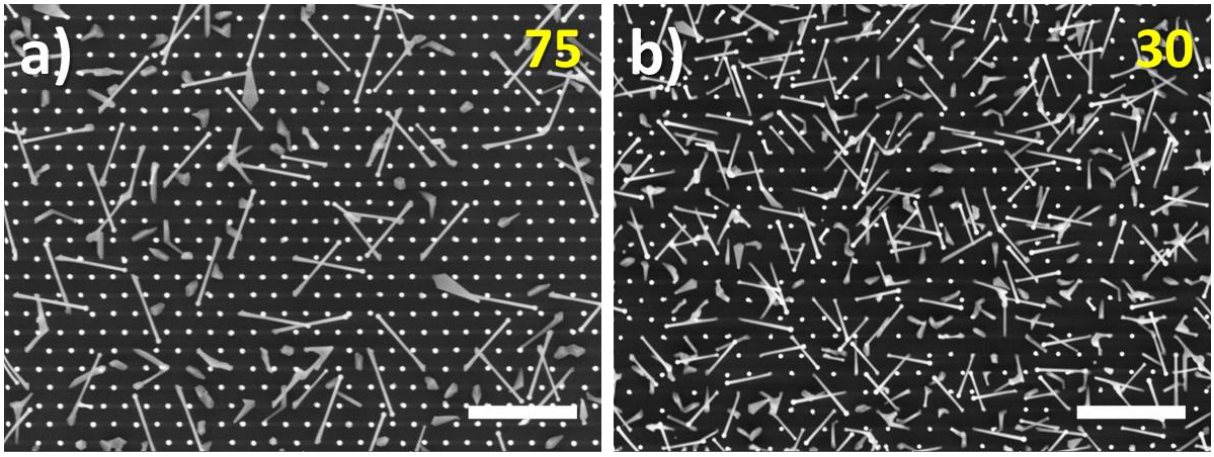

Figure 5.13. (a, b) SEM images (top view) of GaAs NWs taken from different samples on equivalent patterned area with pitch equal to 400 nm and nominal hole diameter of 40 nm. The white scale bar corresponds to 500 nm. Despite the procedure for growing the NWs was the same in both cases, the percentages of vertical structures (in yellow) differ by 2.5 times.

We then performed a statistic study on a sample which provided high vertical yields (Figure 5.14). We observed that whatever the pitch, the highest vertical yields are reached for nominal diameters in the 40-50 nm range, as reported in Figure 5.15. The graphic shows also that there is no significant dependence of the vertical yield for pitches ranging from 300 nm to 500 nm: this is consistent with the results already observed for the Ga droplets which, as above-mentioned, showed homogeneous diameters despite the different pitches.

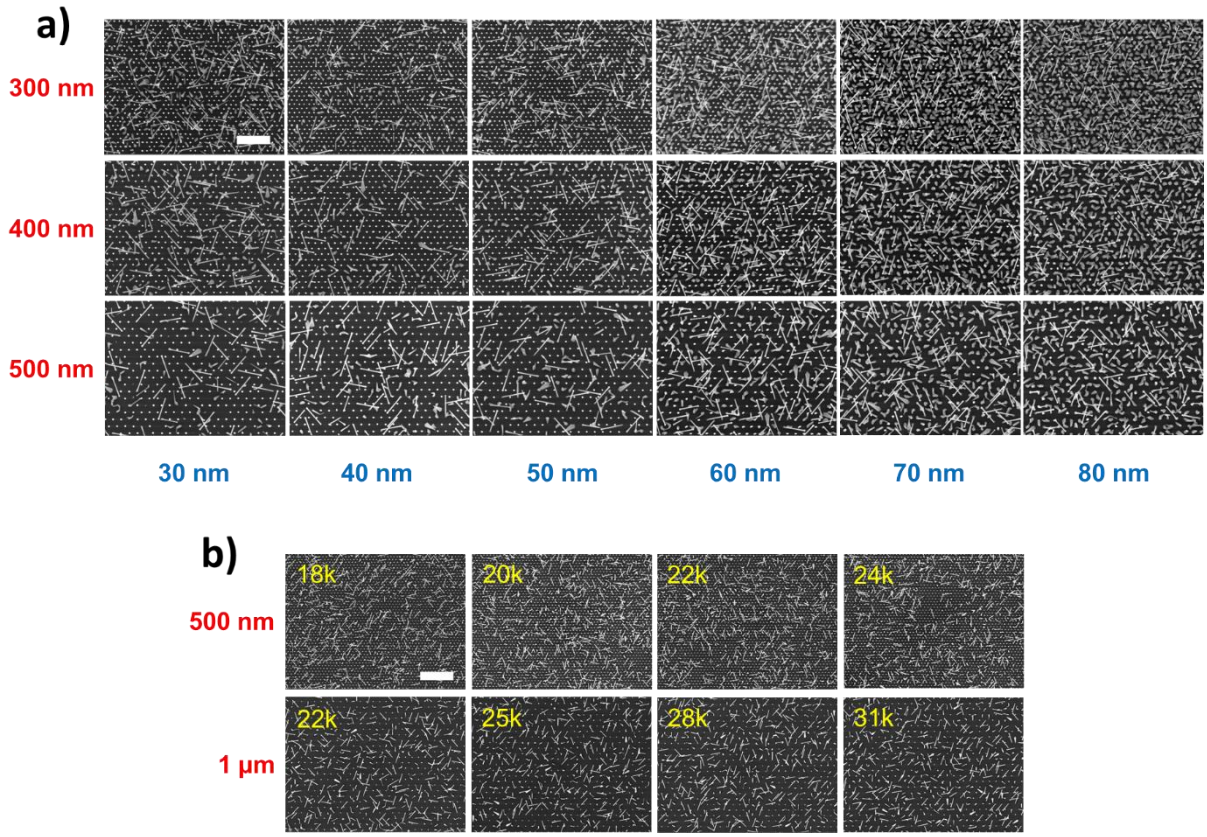

Figure 5.14: SEM images (top view) of a sample with high vertical yield from (a) multi-exposure and (b) single-exposure patterned areas. The red values corresponds to the pitch, the blue ones to the nominal hole diameter and the yellow ones to the exposure dose. The white scale bars correspond to 2 µm.

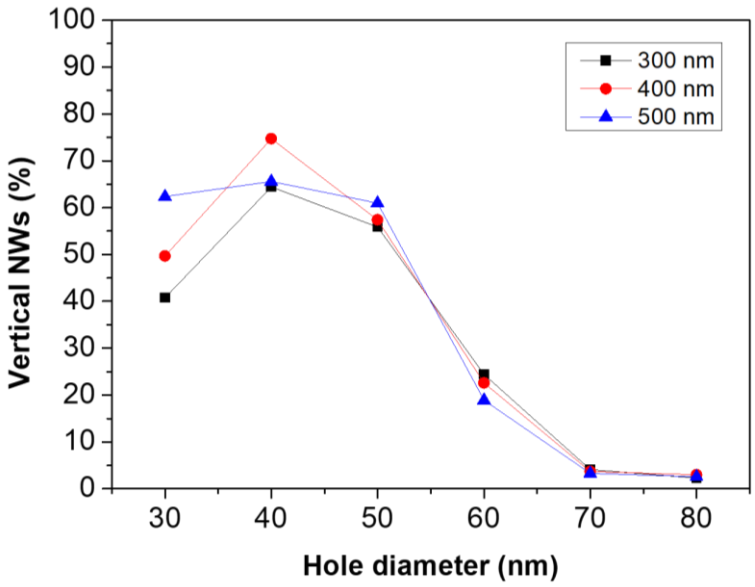

Figure 5.15. Percentage of vertical NWs as a function of the nominal hole diameter and pitch for a sample with high vertical yields (SiO_2 thickness equal to 19 nm; 108 MLs of Ga).

Based on these results, we advanced the hypothesis that the gap in vertical rates between different substrates may be caused by some differences in the shape of the holes. Therefore, we prepared thin lamellae by FIB including a single row of vertical and non-vertical NWs. In order to determine the crystal structure of the NWs, it is necessary to observe the NWs along the zone axis [110]. After the orientation of the (1-10) faceted NWs (typical faceting for self-assisted GaAs NWs having a ZB structure), the lamellae were realized along an orientation perpendicular to a <110> direction, as shown in Figure 5.16. Such procedure was performed at INL in collaboration with S. Brottet.

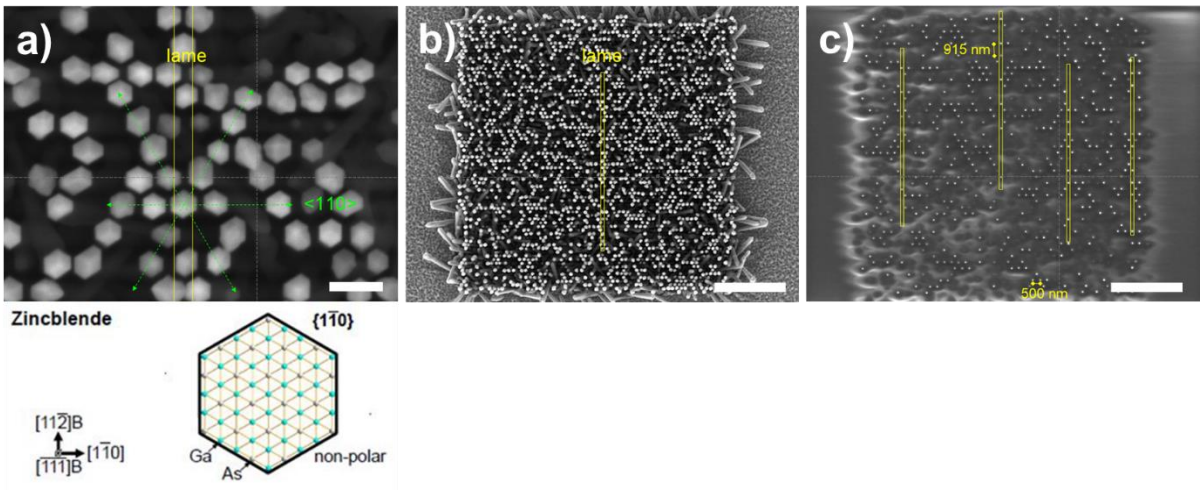

Figure 5.16. SEM images (top view) of GaAs/$Al_{0.2}Ga_{0.8}As$ core/shell NWs grown on 20 x 20 μm^2 patterned areas. Lamellae (marked in yellow) were realised by FIB to be perpendicular to a <110> direction (cf. schematics[214] below (a)) so as to provide a TEM observation with [110] zone axis. The white scale bars correspond to (a) 1 µm and (b, c) 5 µm.

The row reported in lamellae included both vertical and non-vertical NWs (Figure 5.17(a)): the TEM images collected over them (Figure 5.17(b, c)) showed that there was no visible difference between the two cases in terms of hole shape, the α hole angle being equal to about 62°, the average value measured on a large number of holes (cf. Paragraph 5.3, Figure 5.11).

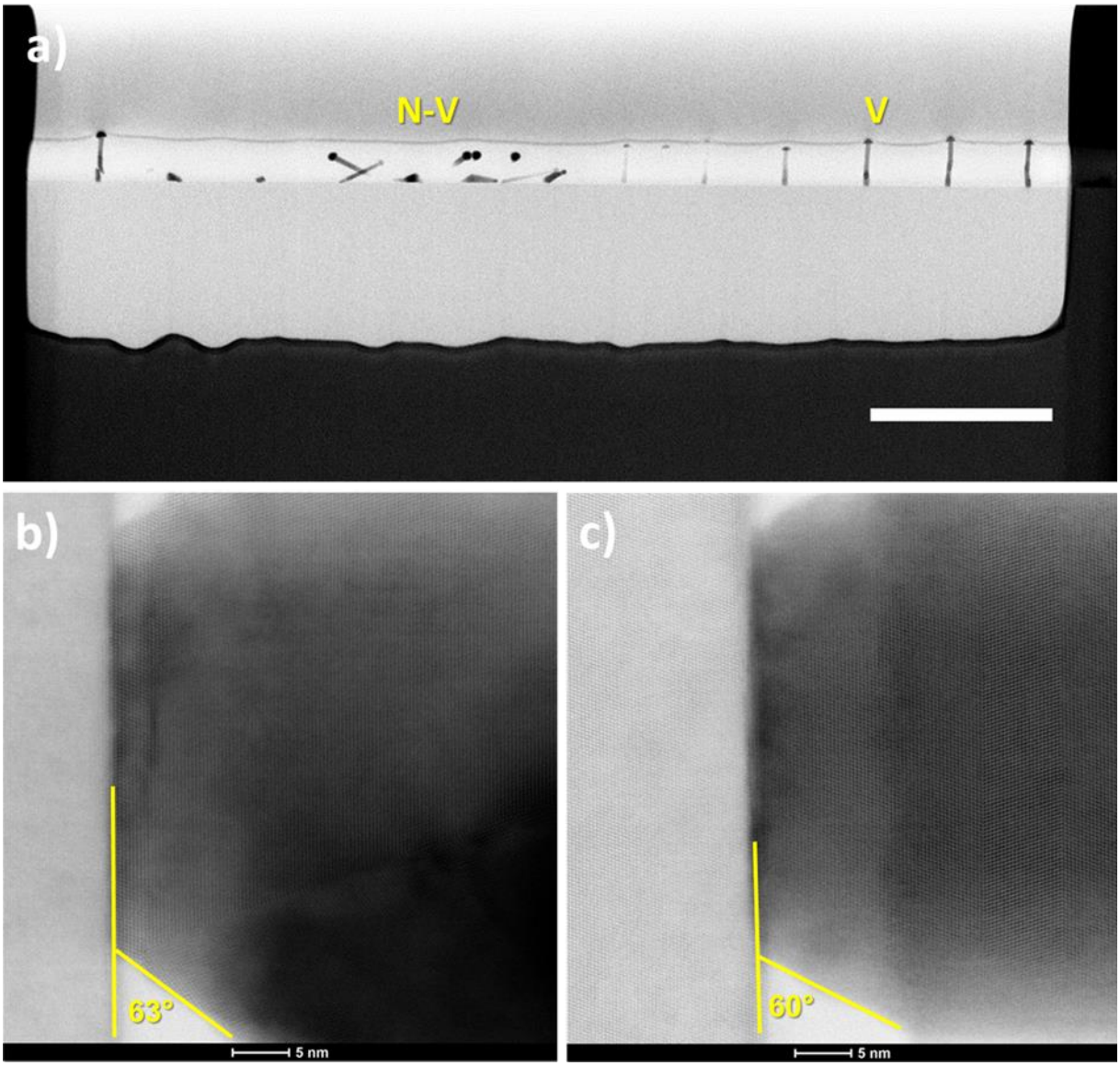

Figure 5.17. (a) TEM image of a thin lamella containing a NW row with non-vertical and vertical NWs removed from the patterned area of the sample by FIB. The white scale bar corresponds to 2 µm. TEM images of the NW bottom of: (b) a non-vertical NW (marked as N-V in (a)), and (c) a vertical NW (marked as V in (a)). No significant differences in shape or geometry can be observed.

In a remarkable study, Tomioka et al[215] related the orientation of InAs NWs grown on Si(111) by MOCVD to the polarity of the NWs, in particular suggesting that NWs with As-polarity would grow vertically, while their In-polarity counterpart would be tilted. Based on these considerations, we decided to characterize the polarity of the NWs to verify any link between this parameter and the verticality. The results of this analysis are reported in Figure 5.18. We observed that in our case all NWs, either vertical (Figure 5.18(a)) or not (Figure 5.18(b)) have As-polarity at the beginning of the growth, with Ga-polarity which can be possibly caused by non-horizontal twin defects (Figure 5.18(c)). As a consequence, it must be

concluded that in our case there is no correlation between verticality and As-polarity, which can at most be regarded as a necessary yet not sufficient condition to obtain vertical NWs.

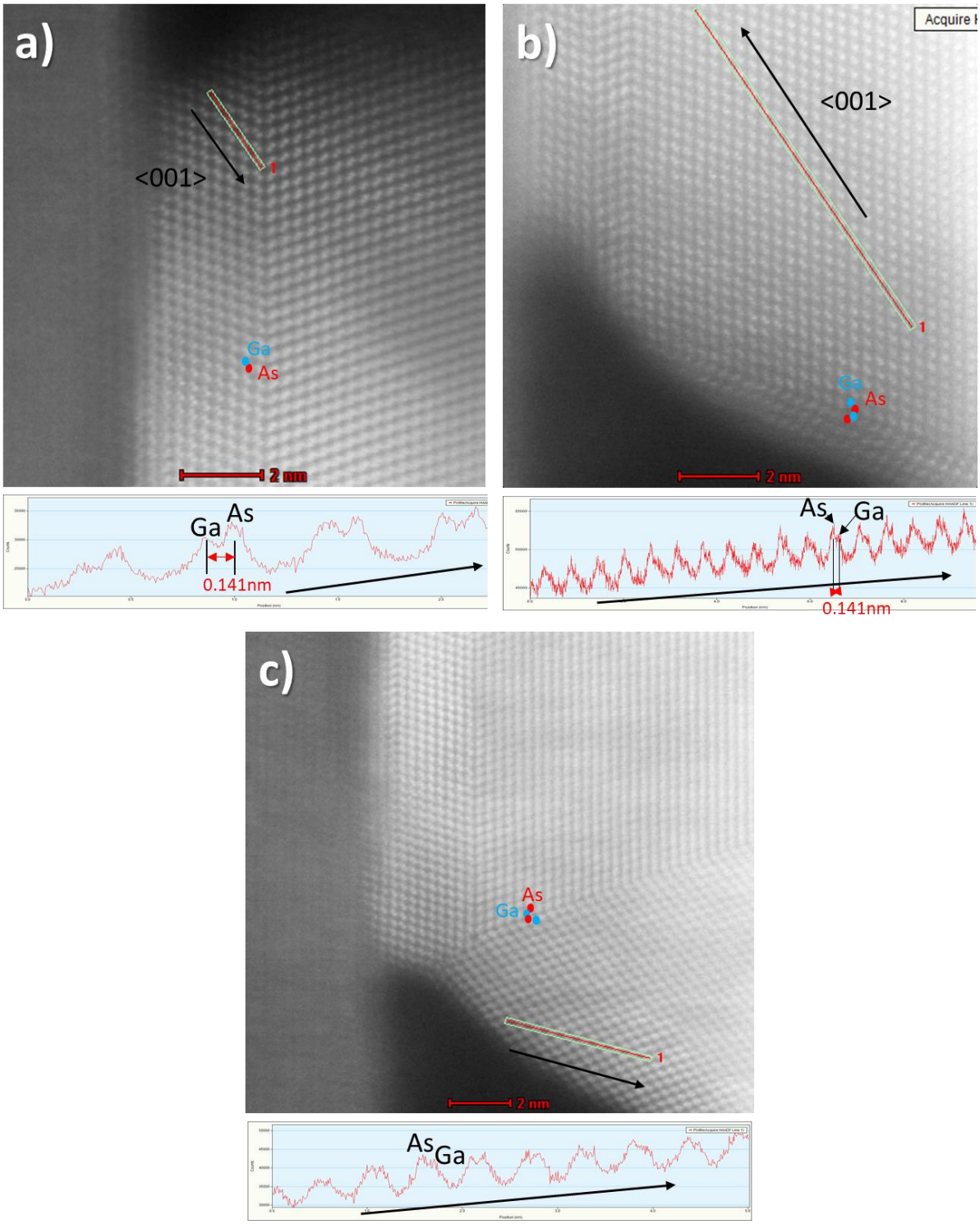

Figure 5.18. HR-TEM images of (a) vertical and (b, c) non-vertical GaAs NWs from FIB-prepared lamellae, and related diagrams of the contrast as a function of the position, which provide the NW polarity. All NWs have an As-polarity. In the case (c), the polarity switches from As to Ga after the formation of a non-horizontal twinning defect.

The solution to the problem of verticality came after many vain efforts and failed attempts to reproduce systematically the high vertical yields. Finally, we found out that the only difference between the couple of samples which provided a high vertical yield and the rest of the samples consisted in the fact that, in the previous case, the T_{growth} of the recipe was corrected shortly before starting the pre-deposition of Ga, since the real temperature as measured by the pyrometer resulted 15 °C higher than expected (625 °C instead of 610 °C). After realising that, we started to believe that heating the substrate to a temperature T_{th} higher (+15°C) than T_{growth} and decreasing it a few minutes before the Ga pre-deposition may have acted as a sort of thermal pre-treatment, which may have influenced the system in the right way to achieve higher vertical yields.

In order to verify such hypothesis, we decided to repeat the growths in the same experimental conditions either with (Figure 5.19) or without a thermal pre-treatment at T_{th} = 15°C above T_{growth}.

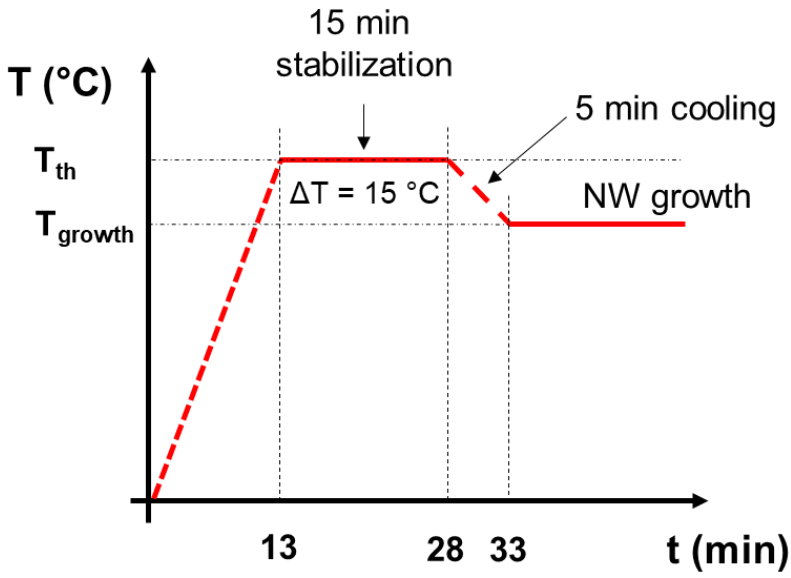

Figure 5.19. Synopsis of the procedure adopted for sample grown with a thermal pre-treatment and a cooling time equal to 5 min.

These experiments were carried out on patterned samples prepared at C2N with the above-mentioned procedure, but with a pattern design consisting of a hexagonal array of holes with pitch equal to 500 nm and nominal diameter of 50 nm, prepared by single exposition with a dose of 20000 μC/cm^2. Such values were chosen both for the high vertical yields observed with this parameter, as above-mentioned, and because close to the optimal parameters calculated by Maryasin et al[199] at Anne Kaminski's group already reported in Paragraph 5.2.

Moreover, in order to go further in the development of PV devices, these new substrates were prepared by patterning a much larger area than in the previous cases, corresponding to a surface of 0.9 x 0.9 cm^2. Eventually, in order to verify the possible influence of the thermal pre-treatment on the vertical yield, we kept all parameters constant except the thermal ones, as above-mentioned. Therefore, three different samples coming from the same patterned wafer were prepared: the first one at T_{growth} = 600 °C without thermal pre-treatment, the second at T_{growth} = 615 °C without thermal pre-treatment, and the third one at T_{growth} = 600 °C after 5 min of thermal pre-treatment at 615 °C plus sudden cooling and thermal stabilization at 600 °C in 5 more min. Since our hypothesis assumed an influence of the thermal pre-treatment alone rather than of the overall temperature at which the growth is performed, we expected to achieve a low vertical yield for both samples grown without thermal pre-treatment, and a high one on the thermally pre-treated sample. Our expectations were not disappointed: as a matter of fact, the two samples realised without thermal pre-treatment (Figure 5.20(a, b, c, d)) present vertical yield from 13 to 22 %, whereas the sample prepared with the thermal pre-treatment shows a vertical rate from 73 to 86 %, depending on the zone (Figure 5.20(e, f)).

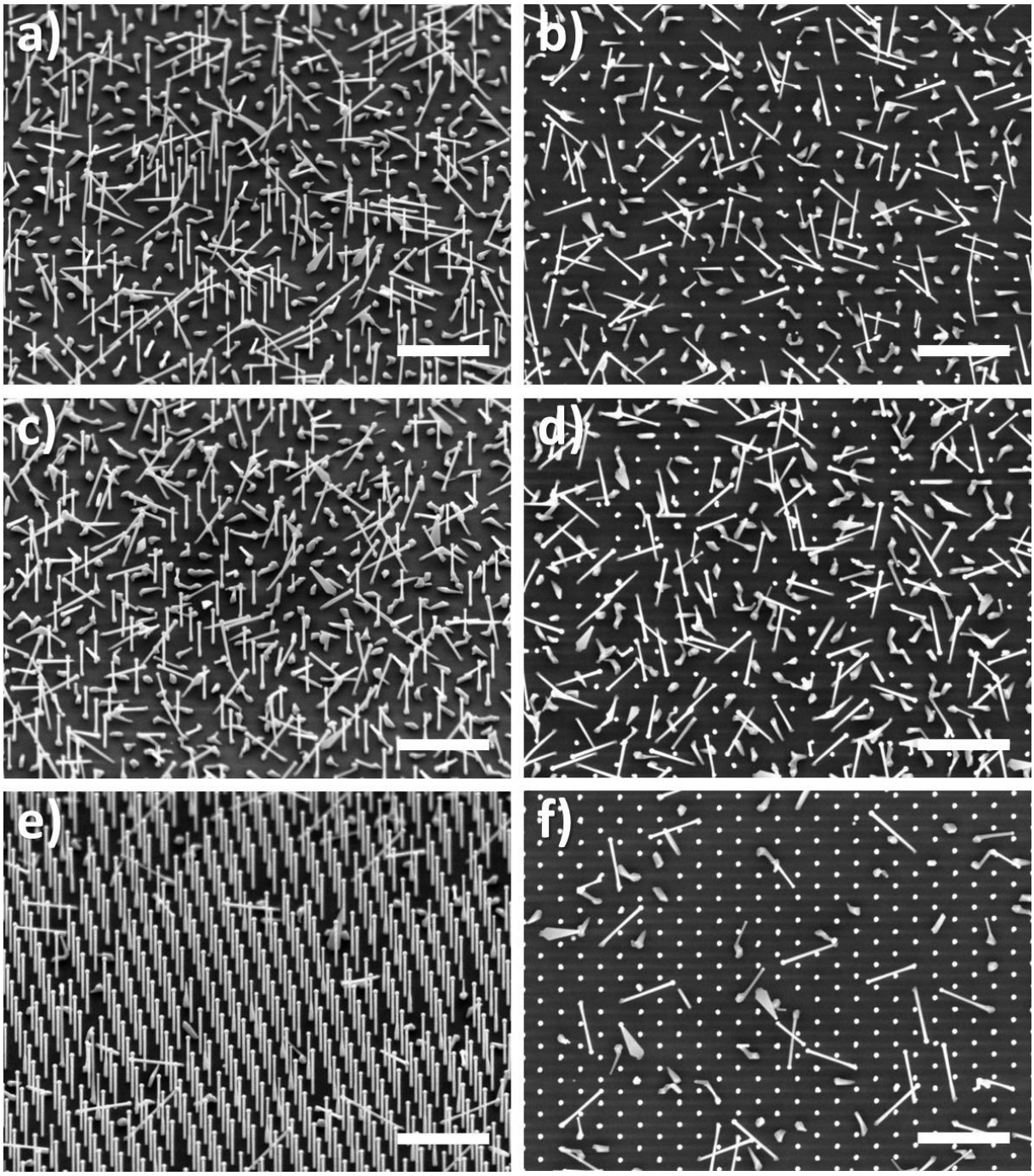

Figure 5.20. 45°-tilted (a, c, e) and top view (b, d, f) SEM images of NWs grown on 0.9 x 0.9 cm^2 hexagonal array with pitch equal to 500 nm and hole diameter of 50 nm. (a, b) Growth performed at 600 °C without thermal pre-treatment (vertical yield 13-22 %). (c, d) Growth performed at 615 °C without thermal pre-treatment (vertical yield 14-22 %). (e, f) Growth performed at 600 °C after thermal pre-treatment at 615 °C (vertical yield 73-86 %). The white scale bars correspond to 2 µm.

Considering that similar results for the three procedures were reproduced on chips from different wafers prepared at C2N, as well as on patterned substrates prepared at INL (cf. paragraph 5.5.2), the correlation between thermal pre-treatment and high vertical yield is neither accidental nor due to other hidden factors, e.g. related to the nature of the single wafer used or to the quality of the SiO_2 deposited. Moreover, it should be noticed that the

high verticality so achieved can be attributed to the only influence of the thermal pre-treatment rather than to the value itself of sample temperature, since growths carried out at lower temperatures (with thermal pre-treatment at 560 °C before growth at 545 °C) provided similar results. Therefore we can state that, in our MBE reactor, the thermal pre-treatment is actually a key-step for obtaining a high percentage of vertical NWs on this kind of patterned substrates.

5.4.2 Growth and characterization of core/shell NWs

Once realised that the pre-treatment was necessary for high vertical yields, we introduced this step in the growth procedure of core/shell NWs. Aiming to obtain fully-optimized structures, so as to eventually employ them in the fabrication of solar cells, we grew p-GaAs NWs with p-i-n $Al_{0.2}Ga_{0.8}As$ PV-active shell and $Al_{0.5}In_{0.5}P$ passivation shell.

Our purpose in this case was to match and possibly break the record of verticality previously obtained with the growth of NWs on pre-treated substrates (≈ 75 %), overcoming the previous vertical rates obtained for GaAs/$Al_{0.2}Ga_{0.8}As$ core/shell NWs grown without pre-treatment, the highest ones being ≈ 40 % (Figure 5.21).

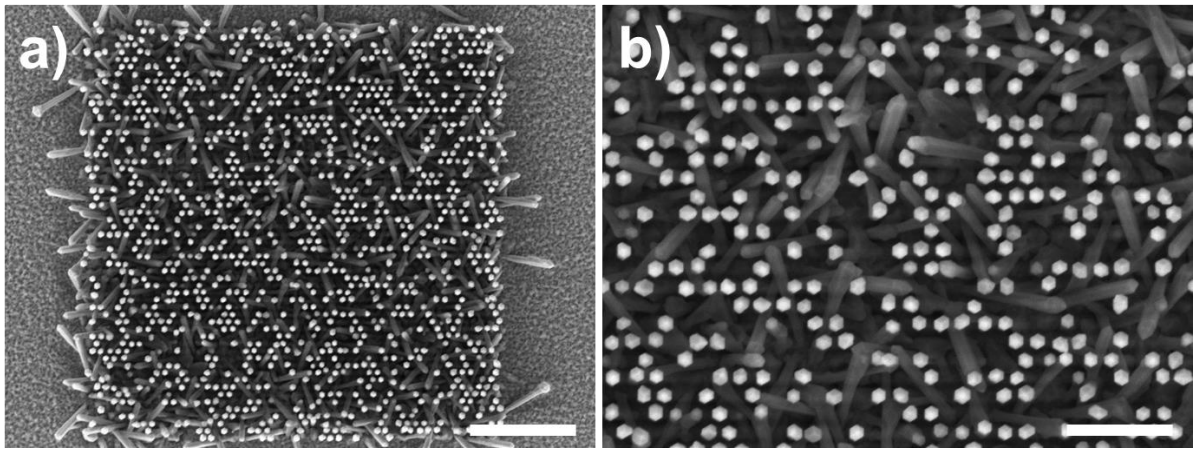

Figure 5.21. SEM images (top view) of GaAs/$Al_{0.2}Ga_{0.8}As$ core/shell NWs with pitch of 400 nm and nominal hole diameter equal to 40 nm grown without thermal pre-treatment; their vertical yield (≈ 40 %) is the highest one obtained without pre-treatment. The white scale bars correspond to (a) 5 and (b) 2 μm.

Also in this case, the thermal pre-treatment has a dramatic effect, the vertical yield of GaAs/$Al_{0.2}Ga_{0.8}As$ core/shell NWs passing from ≈ 40 % to more than 80 % (Figure 5.22).

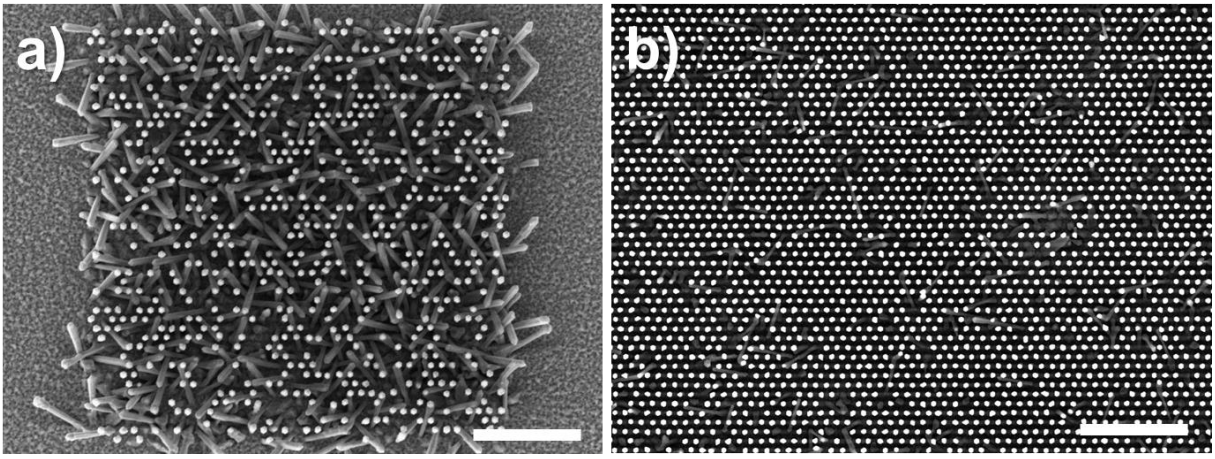

Figure 5.22. SEM images (top view) of GaAs/$Al_{0.2}Ga_{0.8}As$ core/shell NWs grown (a) without thermal pre-treatment on a 20 x 20 μm^2 patterned area (pitch and hole diameter of 400 nm and 40 nm, respectively) and (b) with thermal pre-treatment on a 0.9 x 0.9 cm^2 patterned area (pitch and hole diameter of 500 nm and 50 nm, respectively). The white scale bars correspond to 5 µm.

In Figure 5.23, SEM images shown a representative result obtained for core/shell NWs realised with a thermal pre-treatment at 625 °C during 15 min before reducing and stabilizing the temperature at 610 °C in 5 min. Typically, a vertical yield from 83 to 87 % is obtained depending on the zone, a value which is not only high but also uniform over the relatively broad area of 0.9 x 0.9 cm^2. The NW diameter results equal to 260 ± 18 nm, lower than the expected value of 330 nm.

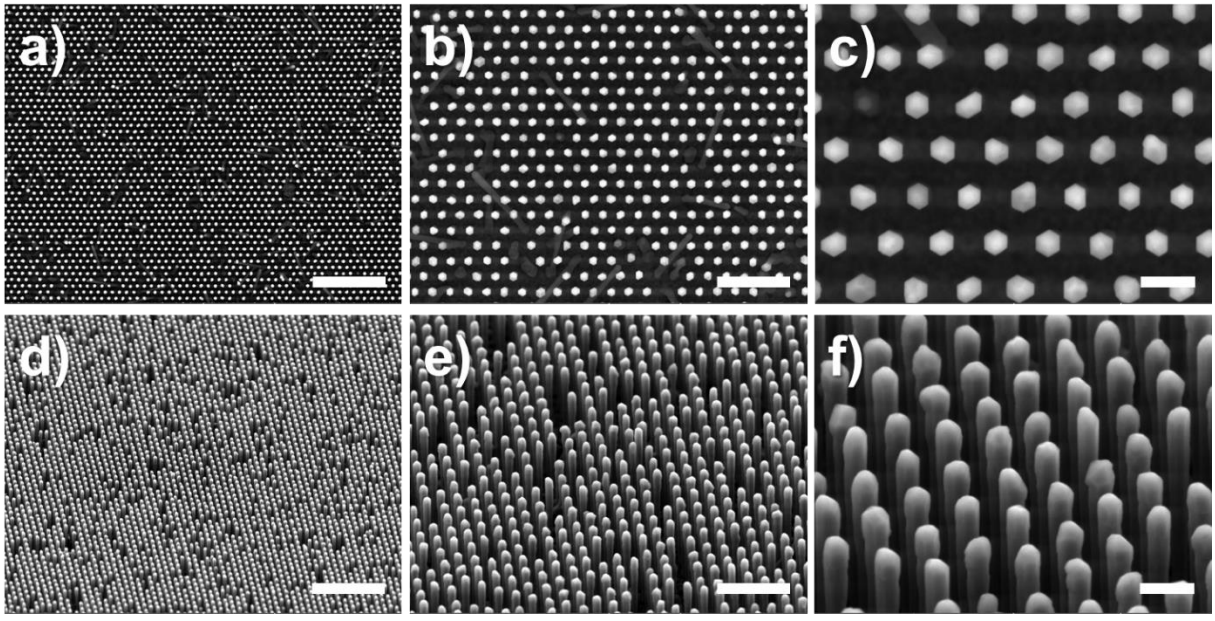

Figure 5.23. (a) Top view (a, b, c) and 45°-tilted (d, e, f) SEM images of p-GaAs/p-i-n $Al_{0.2}Ga_{0.8}As$ core/shell NWs grown on patterned Si substrates with thermal pre-treatment. The white scale bar corresponds to 5 µm (a, d), 2 µm (b, e) and 500 nm (c, f).

Other experiments confirmed these results, providing high vertical yields in the 80-90 % range, as a proof that the protocol including the thermal pre-treatment leads to reproducible results. Ultimately, thanks to this procedure we have been able to develop a protocol which allows to achieve high yields of vertical NWs on large-area patterns realised by EBL through single exposures and having pitch close to the optimal values.

5.4.3 EBIC characterization of core/shell NWs

In order to investigate the optoelectronic properties of individual NW, EBIC and I-V measurements were performed on analogous p-GaAs/p.i.n-$Al_{0.2}Ga_{0.8}As$ core/shell NWs with n-doped $Al_{0.5}Ga_{0.5}As$/GaAs passivation shells.

The analyses were performed on the same sample reported in Figure 5.22(a), which was realised when the thermal pre-treatment had not yet been introduced in the procedure, and thus presents a relatively low verticality yield (10-40 %, depending on the zone). However, it is precisely this characteristic that makes it a good candidate for EBIC analysis, since the lower the density of vertical NWs, the easier it is to contact them with the tungsten tip.

Figures 5.24(a, b) show the SEM image and the corresponding EBIC map for a NW contacted on the top. Similarly to the case of the core/shell NWs grown on epi-ready Si substrates reported in Chapter 4, an induced current is observed over the entire NW length under zero external bias. The collected current is increased under revers bias of -1.5 V, whereas under a forward bias of +1.5 V the signal from the p-i-n junction disappears and a signal from a Schottky contact is revealed at the NW top.

We have further analysed the impact of the contact position on the charge collection. The tungsten tip was moved and a NW was contacted on a lateral facet. We note that a strong force should be applied to establish a reliable lateral contact and a NW can be easily broken during this contacting procedure. For this reason, Figures 5.24(a, b) and (c, d) show results obtained for two different NWs coming from the same patterned substrates. Figures 5.24(a, b) display the SEM image and the corresponding EBIC maps obtained for a NW contacted on the top, while Figures 5.24(c, d) are obtained for a NW contacted at the middle of a lateral facet. Under zero and reverse bias, a uniform EBIC signal is found over the entire NW length. This shows that the contact position does not impact the carrier collection. Under forward bias, a signal characteristic of a Schottky diode is revealed around the contact point.

Current-voltage characteristics were compared for two NWs contacted on the top and on a lateral facet, respectively, as presented in Figure 5.24(e). For both NWs with different contact positions, the I-V curves present a diodic behaviour. However, for the NW contacted on the top, the slope of the curve is steeper in the forward bias indicating a lower series resistance. The knee diode voltage is ≈1.0 V for the top contact, whereas it decreases to 0.6 V for the NW contacted on the lateral facet. We suppose that these modifications are not

inherent to the NW, but are related to the variation of the tip-to-NW contact. For both NWs contacted at different positions, the reverse leakage current is very low thus confirming the behaviour already observed for the NWs grown on epi-ready Si substrates. The difference in the leakage current may arise from NW-to-NW variability, although it may also be ascribed to some modifications/degradations induced by lateral bending.

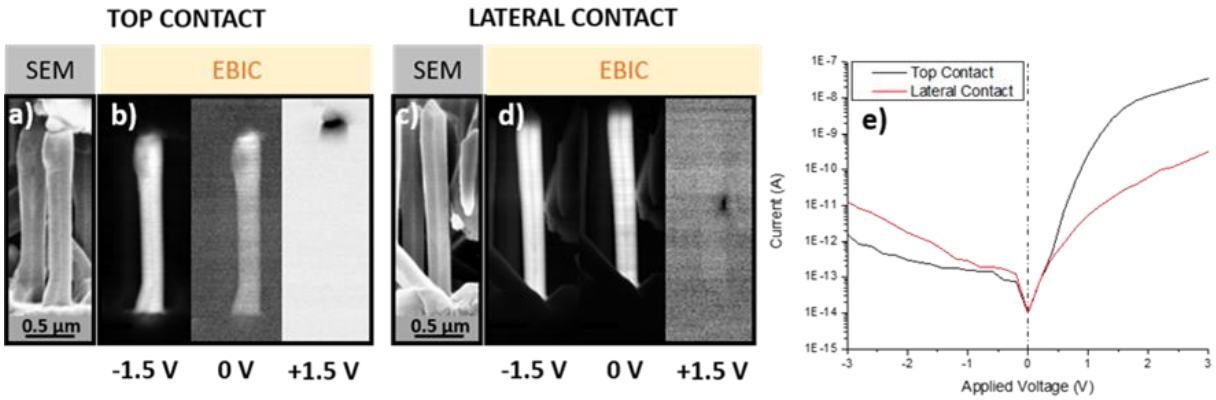

Figure 5.24. (a) SEM image and (b) EBIC maps under -1.5 V, 0 V and +1.5 V external bias, for a NW contacted on the top. (c) and (d) same as (a) and (b) for a NW contacted on a lateral facet. (e) Semi-log I-V curves for a NW contacted on the top and on a lateral facet.

Ultimately, the NWs grown with this protocol on patterned substrates also appear as promising building-block for a PV device, just as their counterparts on epi-ready Si substrates previously dealt with in Chapter 4, and their suitability for the intended purpose seems all the more confirmed by the high vertical yield and uniformity achieved on patterned substrates.

5.5 The growth of NWs on patterned substrates prepared at INL

As above mentioned, the results shown so far were obtained on patterned substrates prepared by our partners at C2N. However, one of the goal of the work in our group was also to develop an independent know-how of patterning, not only to be capable of working autonomously but also to verify the robustness of our growth protocol (and especially of the thermal pre-treatment) on different substrates.

For such purpose, we also prepared Si(111) substrates with a SiO_2 mask. Since patterning large surfaces is expensive and time consuming, and considering that these samples were meant to be employed mainly in preliminary studies for better investigating the mechanisms at the origin of the high vertical yield, in this case the ordered arrays were limited only to

small patterned areas. As a consequence, these samples could not be employed in the fabrication of PV devices, notwithstanding the experiments carried out on them have helped to clarify the factors which influence the vertical rate.

The guidelines of our work in this regard were basically of two orders: the study of the impact of the absence or presence of the native oxide on the Si substrates before the SiO_2 mask deposition, and the investigation of the influence of the cooling rate during the step of thermal pre-treatment. These two topics are addressed respectively in paragraph 5.5.1 and 5.5.2.

5.5.1 The impact of the epi-ready oxide etching before the SiO_2 mask deposition, on the NW verticality

INL patterned substrates were realised from B-doped (0.02-0.06 Ω cm) Si(111) wafers. The overall procedure included a first deposition of SiO_2 (20-30 nm) by Electron Cyclotron Resonance (ECR) PECVD (performed in our laboratory by P. Regreny), followed by EBL patterning (performed at CIME Nanotech in Grenoble by C. Chevalier) to transfer the mask. The mask design in this case consists of a series of 20 small patterned areas of different size (about 15 x 15 or 20 x 20 μm^2 each) with different nominal hole diameters and pitches, as shown in Figure 5.25.

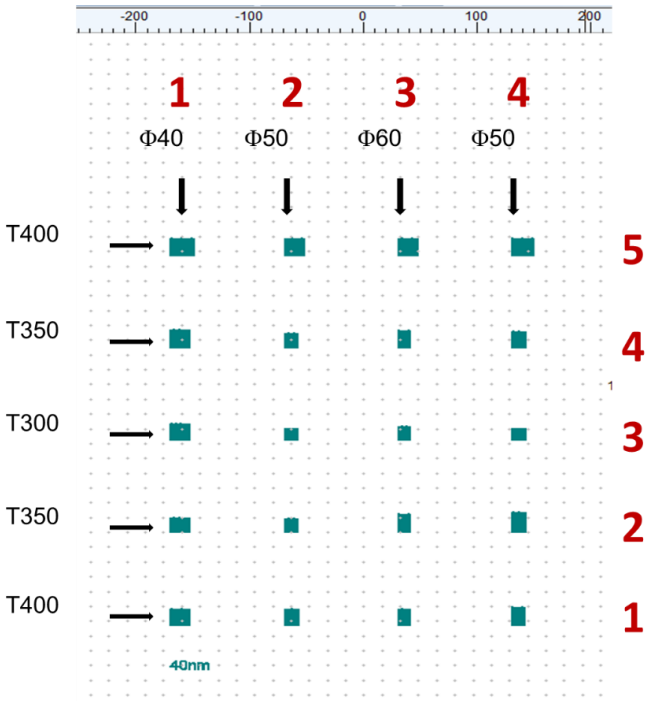

Figure 5.25. Schematics of the mask design adopted to fabricate the INL patterned substrates. The value of T at the left of each line indicates the related pitch expressed in nm, whereas the value of Φ at the top of each column corresponds to the nominal hole diameter, also expressed in nm.

Also in this case, before the growth of GaAs NWs, the Si(111) substrates were treated in 1% HF solution for 25 sec and degassed at 200 °C in UHV before introduction inside the reactor. The NW growth protocol is also the same as the one already adopted on C2N substrates (deposition at 610 °C of 108 MLs of Ga at 0.5 ML/sec and growth of GaAs NWs for 10 min at the same temperature with standard conditions).

The first experiments on this type of substrates were performed without thermal pre-treatment, because at that time we had not yet realized the importance of this procedure to obtain high vertical yields. These samples were grown on Si substrates on which SiO_2 had been deposited by ECR-PECVD directly on the epi-ready Si surface (without any HF etching of the epi-ready oxide surface layer), and the results in terms of verticality were rather poor, with vertical yield only about 30 %. Based on an article by Tan et al,[212] we decided to repeat the growth on samples undergone the same patterning procedure, plus a wet etch in HF solution immediately before the ECR-PECVD deposition of SiO_2, so as to eliminate the epi-ready oxide (this being a step also adopted by our partners at C2N in their standard patterning procedure) and deposit the SiO_2 mask on the bare Si surface. These substrates eventually lead to about twice higher vertical yields (≈60 %) than in the case of a direct SiO_2 mask deposition on the epi-ready Si surface, thus confirming what already reported in the literature and demonstrating that the removal of the epi-ready oxide layer before the mask deposition is not a negligible step to obtain high vertical yields.

5.5.2 The impact of the cooling rate in the thermal pre-treatment

The development of the patterning know-how at INL has meant a greater availability of samples, and thus the possibility to go deeper into the mechanisms which ensure that the thermal pre-treatment provides high vertical yields. This leads us to formulate some hypothesis which, although still far from being a definitive explanation, can at least constitute a starting point for the understanding of the phenomenon in question.

The clue which triggered our reflection came from the experimental results performed on C2N patterned substrates. When illustrating Figure 5.20 in Paragraph 5.4.1 we already mentioned the fact that the high vertical yield was due to the temperature gap between pre-treatment and growth and not to the absolute T_{growth}, since samples grown at 600 and 615 °C without pre-treatment both showed low vertical yields. This particular fact caught our attention: how to explain that the behaviour of the system depends on a temperature gap in its thermal history rather than on its absolute temperature?

Our hypothesis is based on the consideration that in the system in question there are two components with very different physical characteristics i.e. Si and SiO_2. Since it is widely known that the thermal properties of semiconductors differ significantly from those of their corresponding oxide, it does not seem unrealistic assuming that Si and SiO_2 might also have a different response to the heating-and-cooling steps of thermal pre-treatment. In

particular, we came up with the idea that one of the components might keep hotter than the other for a certain time after the cooling phase, determining therefore the presence of a thermal gradient, and that this fact might somehow exert a positive influence on the NW growth and/or nucleation, thus leading to high vertical yields.

Theoretically speaking, despite the thin thickness of the mask and the narrow temperature gap between the temperatures of pre-treatment and growth (≈15 °C), the preservation of a difference in temperature between Si and SiO_2 is possible. As a matter of fact, if we express the heat equation in the following form:

$$\frac{\delta\vartheta}{\delta t} = \frac{k}{\rho c}\left(\frac{\delta^2\vartheta}{\delta x^2} + \frac{\delta^2\vartheta}{\delta y^2} + \frac{\delta^2\vartheta}{\delta z^2}\right)$$

(with ϑ absolute temperature, t time, k thermal conductivity, ρ volumetric mass, c specific heat, and x, y, z the dimensions of the considered component) the system could show a difference in temperature between Si and SiO_2 while cooling, i.e. different $\delta\vartheta/\delta t$ for each material, if for example the two compounds have different k/ρc terms. As a consequence, we should take into consideration the values of ρ, c, and k for Si and SiO_2 in order to verify whether such an assumption is justified.

In this regard, knowing that ρ is equal to 2329 and 2170-2650 kg m^{-3} for Si and SiO_2 respectively,[216,217] it can be concluded that there is not a significant difference between the two materials in terms of volumetric mass.

As far as the specific heat is concerned, the main problem is the lack of data regarding the values of this parameter at high temperatures. Nevertheless we found out that c of Si and SiO_2 at room temperature correspond to 712 and 680-730 J kg^{-1} K^{-1}, respectively.[216,217] Since the two values are almost the same, if we assume that no significant deviation in the ratio between them occurs when the temperature is increased up to 615 °C, it seems reasonable to think that there will not be significant differences between the specific heat of the two materials at the conditions of growth.

Regarding the thermal conductivity, to the best of our knowledge there are no available data concerning k of SiO_2 at 600 °C. However, if we refer to the work of Yamane et al[218], who measured this properties for layers of SiO_2 with different thickness at room conditions, we can see that the thermal conductivity decreases dramatically as the thickness is reduced, passing from about 1.4 W m^{-1} K^{-1} for bulk SiO_2 to about 0.55 W m^{-1} K^{-1} for 25 nm-thick SiO_2 layers. It is therefore reasonable to assume that for our 20 nm-thick SiO_2 mask, the value of thermal conductivity could be very similar. On the contrary, considering that our Si samples are 1 cm x 1 cm large and about 0.3 µm thick, we can assume that their thermal conductivity corresponds to that of bulk Si, i.e. about 160 W m^{-1} K^{-1} at room temperature.[219] Therefore, the difference in thermal conductivity between Si and SiO_2 at room temperature is as big as four orders of magnitude, thus determining a not negligible difference between the k/ρc terms of Si and SiO_2. As a consequence, assuming that such a ratio between the thermal

conductivities of the two materials is maintained also at the NW growth temperature (around 600°C), the hypothesis of a difference in temperature between Si and SiO_2 after thermal pre-treatment is not precluded (in particular with SiO_2 maintaining a higher temperature than Si).

In such case, if the difference in temperature between mask and substrate is the factor which determines a higher verticality, we would expect the cooling time to play an important influence on the vertical yield, because the more we wait and the lower the temperature gap between SiO_2 and Si should become, thus causing a lower verticality. In order to verify this hypothesis, we decided to perform the growth on three different samples (grown on substrates patterned after etching the epi-ready oxide) adopting the same experimental conditions as in Figure 5.19, i.e. heating up to 625 °C and stabilization for 15 min, cooling and growth at 610 °C with standard parameters after the deposition of 108 MLs Ga at 0.5 ML/sec, but with cooling time equal to 2, 5 and 10 min. The purpose was to compare these results with those obtained for the growth performed in the same conditions but without thermal pre-treatment.

SEM images of the four samples in question are shown in Figure 5.26 and the evolution of the vertical yield with the cooling time $t_{cooling}$ is reported in Figure 5.27. Our expectation was to observe the lowest vertical yield for the sample without thermal pre-treatment, a similar or higher verticality for the one cooled in 10 min (depending on whether this time is enough or not to still conserve some significant difference in temperature between Si and SiO_2), a still higher vertical rate for 5 min cooling and the highest one in the 2 min case, where the difference in temperature is supposed to be the highest.

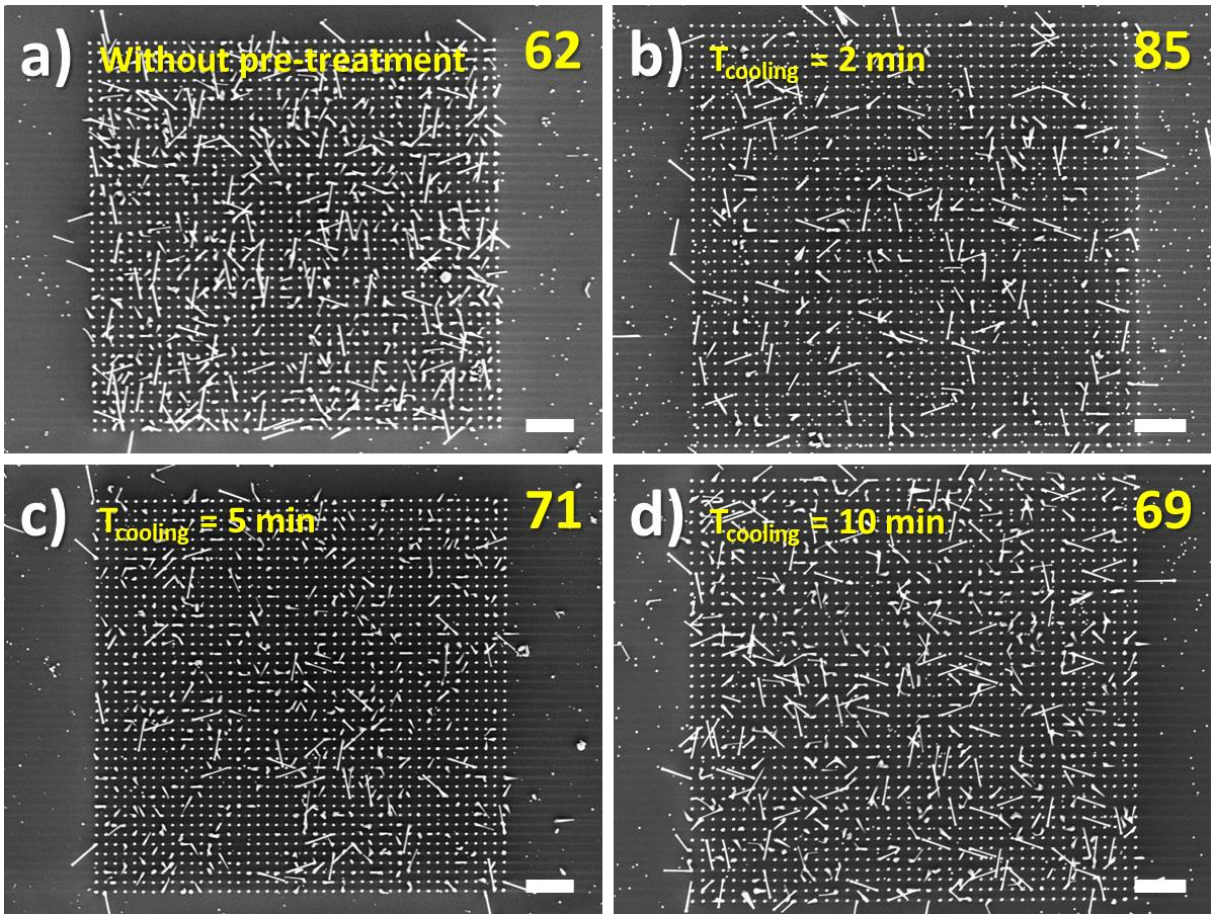

Figure 5.26. SEM images of GaAs NWs grown on INL patterned substrates: (a) without thermal pre-treatment, and with thermal pre-treatment and $t_{cooling}$ equal to (b) 2 min, (c) 5 min and (d) 10 min. All images came from patterned area corresponding to line 1 and column one, as marked in Figure 5.16. The percentage of vertical NWs is reported in yellow for each case. The white scale bars correspond to 2 µm.

It can thus be noticed that our expectations are entirely confirmed: the sample which was not pre-treated gives the lowest vertical yield, with values almost equal to or slightly lower than the sample pre-treated with 10 min cooling; the sample cooled in 5 min provides higher vertical yields than the previous cases, but as expected it is the sample undergone 2 min cooling which shows the highest verticality, in a range which is about 75-85 % depending on the patterned zone.

In terms of vertical yield, the results achieved with 2 min cooling is not as good as those one observed on C2N patterned substrates, but still very promising, especially because it includes some margins of improvement, for example by producing a cleaner Si/SiO_2 interface thanks to the procedure of Madiomanana et al,[203] which as above-mentioned is habitually employed by our partners at C2N but which had not been yet introduced at INL when these patterned substrates were fabricated. Also, we might still be able to increase the verticality by further reducing the cooling time.

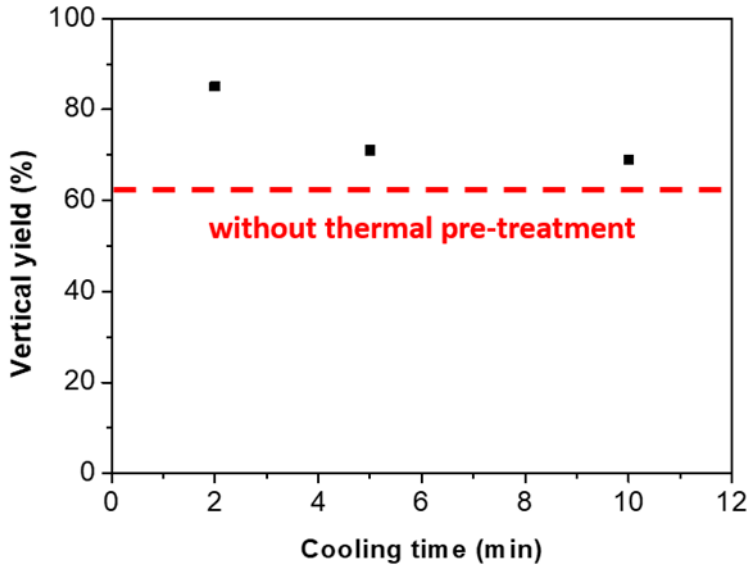

Figure 5.27. Vertical NW yield as a function of the cooling time. The red dashed line corresponds to the yield obtained without thermal pre-treatment (62 %).

Ultimately, the agreement between our previsions and these experimental data is encouraging and gives us hope that we have found the right track to explain what the role of the thermal pre-treatment actually consists of. Of course, these results constitute only a preliminary study and our hypothesis to explain the phenomenon are still assumptions which should be validated. As a matter of fact, we still have to verify our assumption that the thermal conductivities of the two materials, as well as that their specific heats, maintain at 610 °C the same relationship observed at room temperature. Also, we should still define for which physical effect a possible difference in temperature between Si and SiO_2 may induce a high vertical yield. Nevertheless, we think that the hypothesis formulated so far may provide a proper starting point, and we hope to be able to solve the problem with our future research in this regard, involving further computational simulations to be carried out at INL by A. Danescu.

5.6 Conclusion

In this chapter we have treated the growth of Ga-assisted NWs on patterned substrates. The preliminary step before the NW growth consisted in the optimization of the cell parameters through numerical simulations by our partners at IMEP-LAHC. The simulations revealed that the most proper parameters for our purpose are a pitch of 550 nm and a NW diameter and length of 330 nm and 1.5 µm, respectively, which can theoretically provide a photoconversion efficiency up to 27.6 % with V_{OC} = 1.85 V, J_{SC} = 17.1 mA/cm^2 and FF = 0.87.

Subsequently, we focused our efforts on the growth of vertical NWs on patterned substrates. For such a purpose, we began our study from the pre-deposition of Ga to form ordered arrays of droplets, and the procedure adopted provided excellent results in terms of selectivity and uniformity. By comparing the volume of the droplets with the amount of Ga deposited into the holes, we tend to believe that part of the Ga desorbs from the droplets so as to let them in an equilibrium state with a contact angle ϑ = 50°.

Having obtained satisfactory results with Ga pre-deposition, we then committed to achieve regular arrays of, firstly, GaAs NWs, and secondly, p-GaAs/p.i.n-$Al_{0.2}Ga_{0.8}As$ core/shell NWs with high vertical yields on patterned substrates provided by C2N. This task was eventually fulfilled thanks to a procedure including a thermal pre-treatment at temperature 15°C higher than that one for the Ga deposition and NW growth (for example, at 625 °C for a NW growth at 610 °C). Despite the short time of the pre-treatment and the narrow difference in temperature, this step has proved to be of crucial importance, leading to verticality rate up to 90 % over 0.9 x 0.9 cm^2 patterned areas. The as-grown p-GaAs/p.i.n-$Al_{0.2}Ga_{0.8}As$ core/shell NWs were characterized by EBIC: the results have shown that these NWs are potential building blocks for a TSC, thus confirming the performances already observed in Chapter 4 on their counterparts grown on epi-ready Si substrates.

After that, we aimed to reproduce these results on patterned substrates prepared at INL, both to develop our own know-how and to test the reproducibility of our procedure: these series of experiments have shown that the cooling time after the thermal pre-treatment is a very important factor, since the faster is the cooling, the higher is the vertical yield. For the moment, we are inclined to attribute this effect to a possible difference in temperature between the Si substrate and the SiO_2 mask, which may persist after the thermal pre-treatment, during the formation of the Ga droplets and the NW nucleation. However, further analyses are necessary to verify our hypothesis.

6 The fabrication of nanowires-based PV cells: preliminary results

6.1 Introduction

Although the work of this thesis focuses mainly on the MBE growth and characterization of NWs, it was also addressed to develop a proper fabrication protocol so as to achieve well performing NW-based PV cells. In this chapter we present therefore some preliminary results concerning such topic. The first section of this chapter summarizes schematically the work flow that should finally allow us to fabricate the targeted TSC. The second section is devoted to the experimental procedure employed to prepare the Si substrate for the bottom cell of the TSC. Subsequently, we present our study about the top cell manufacturing by following two main guidelines: the encapsulation and the top-contacting of NWs. The third section reports our preliminary study of NW encapsulation by hydrogen silsesquioxane (HSQ), the reason of its failure, the proposed alternative with benzocyclobutene (BCB) and the removal of the BCB in excess by reactive ion etching (RIE) to expose the NW tips. Then, the fourth section assesses the top contact issues, and shows the results obtained with the deposition of ITO on the NWs.

6.2 Development of the TSC architecture

The complete process of TSC fabrication can be summarized in the following sequence:

Si substrate is (111) oriented and p-type doped with B (1-5 Ω·cm)	Substrate Si p

Thermal diffusion "Lydop" from $POCl_3$ source (25 min at 840 °C)	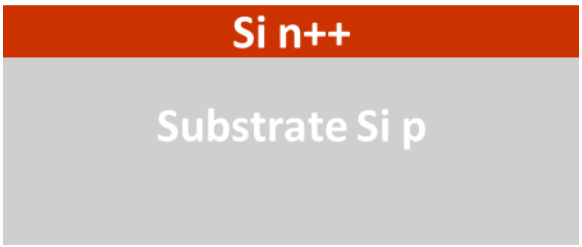
Back Surface Field formation by P-RTD with Boron SOD (30 sec at 1000°C)	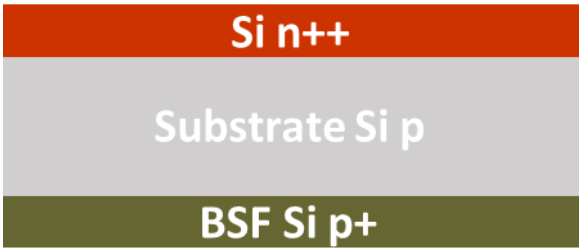
Tunnel junction formation by using P-RTD with Boron SOD (cf. Paragraph 6.4)	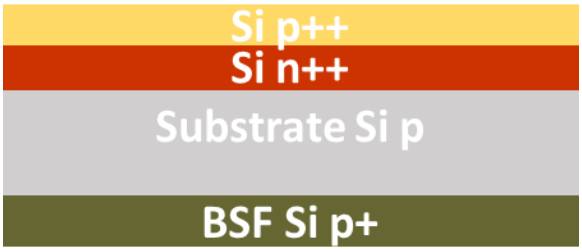
SiO_2 deposition by PECVD at C2N and mask patterning by EBL (cf. Chapter 5, Paragraph 5.3 and 5.4)	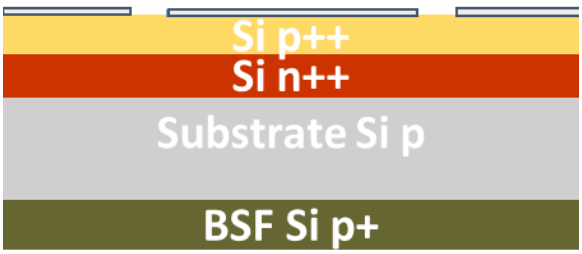

<u>NW growth</u>: **p-GaAs core** **Ga droplet consumption (i-GaAs)** **p-$Al_{0.2}Ga_{0.8}As$ shell** **i-$Al_{0.2}Ga_{0.8}As$ shell** **n-$Al_{0.2}Ga_{0.8}As$ shell** **$Al_{0.5}In_{0.5}P$ Passivation layer**	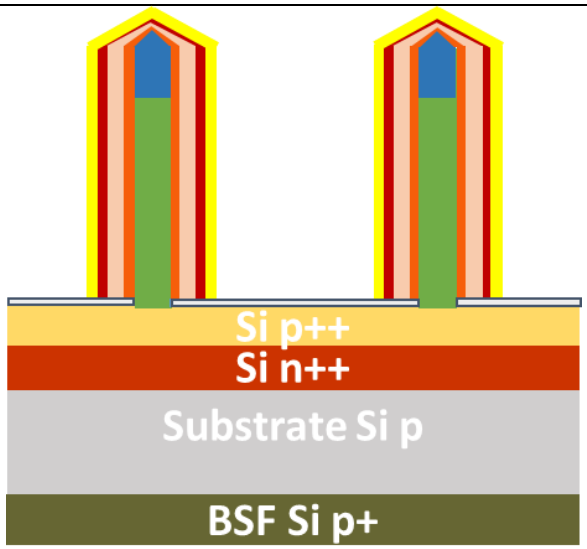
Encapsulation of NWs with BCB	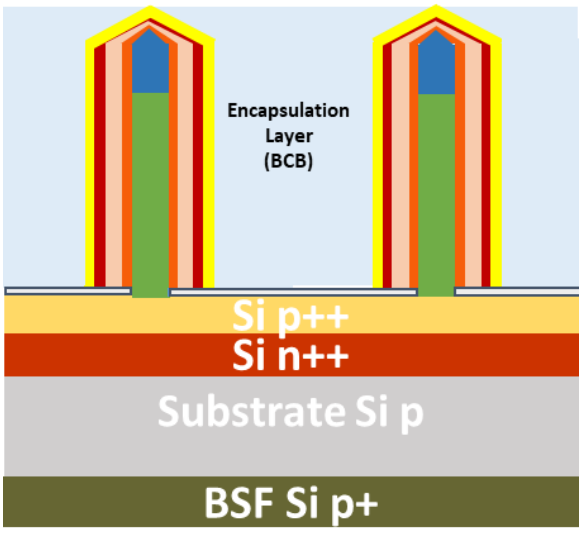
RIE to eliminate BCB in excess and expose NW tips	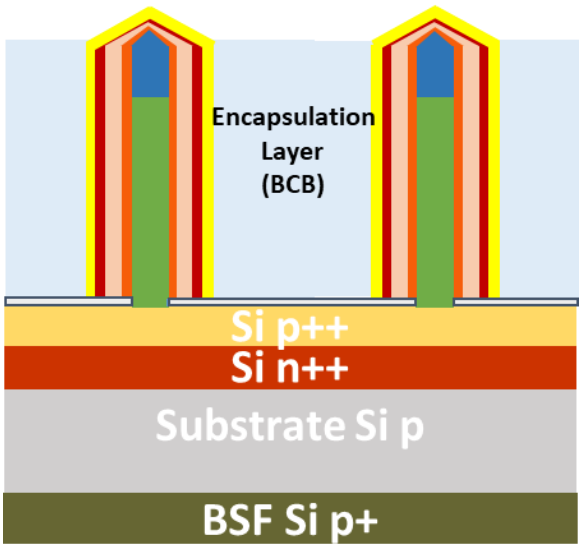

Etching of $Al_{0.5}In_{0.5}P$ passivation layer with HCl to expose the top of the PV-active region	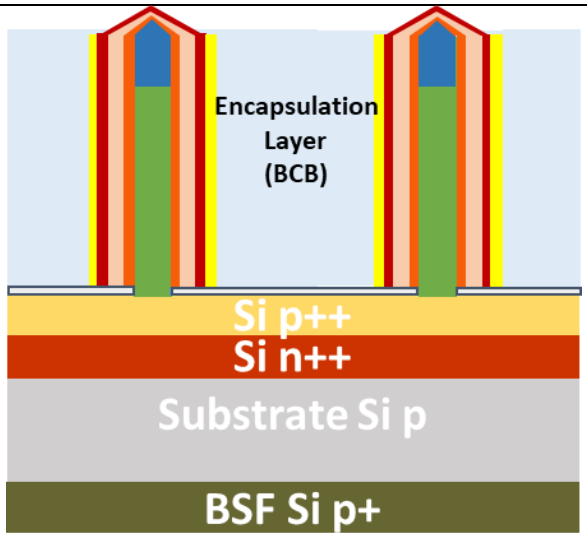
Deposition of ITO by sputtering to contact the NW top	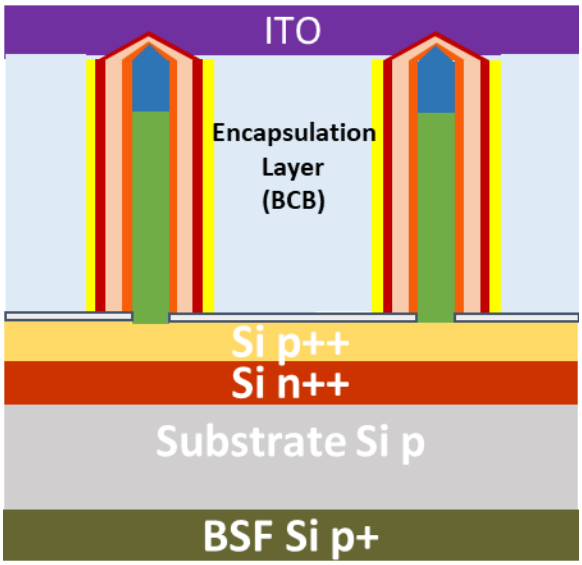
Deposition of back and front Al contacts + Contacts annealing	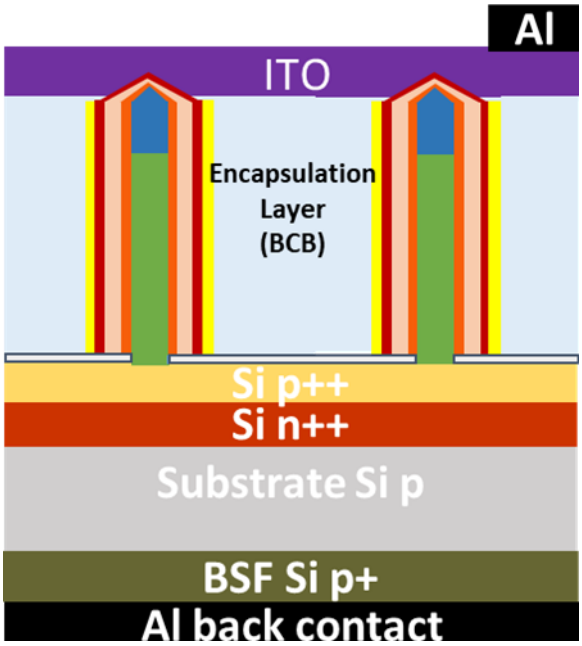

Whereas the issues concerning the NW growth for the top cell have already been treated in the previous chapters, here below we will expose the rest of the operations necessary to obtain a TSC, i.e. the fabrication of the Si bottom cell, the NW encapsulation and finally their top contacting.

6.3 Fabrication of the Si bottom cell

All the results presented so far in this thesis, concerning the growth and encapsulation of NWs, might be employed in the fabrication of NWs-based PV cell regardless of the number of junctions in the device. However, in order to obtain a NWs-based TSC, it is necessary to develop also a proper Si bottom cell. Therefore, in this section we will show some preliminary results in this sense, and conclude by summarizing the whole TSC manufacturing process we will adopt in the light of the skills acquired during this work and of the experimental results reported in this and in the previous chapters.

Our 2-terminal TSC requires an electrical coupling between the 2 sub-cells without preventing transmission of infrared light to the Si bottom cell. This contact should not be affected by thermal budget of the top cell fabrication process (610°C during 20-30 min under UHV). Therefore the Esaki tunnel junction consisting of two highly doped and very thin n-type and p-type regions was selected in the frame of the HETONAN project. This tunnel diode is implemented within the Si bottom cell. In such a diode, the electrons move from the degenerated n-type region to the degenerated p-type region via tunneling process, enabling electrical coupling with minimal parasitic absorption. INL developed a low-cost technique combining spin-on dopant (SOD) sources and rapid thermal annealing (RTA) to realize 2 successive diffusion of p- and n-type dopants (or vice versa). Also, as the standard n^{++}-doped emitter of the Si solar cell has doping level higher than 10^{20} cm^{-3} near the surface, it is possible to use only one additional B diffusion to realize an efficient structure. The main difficulty is to achieve very high doping concentrations with very sharp doping transitions considering the compensation of the two dopants inherent to this method.

Spin-on dopants (SOD) containing B cannot be deposited directly on the n^{++}-doped emitter because, after annealing, this can generate a residual layer of boron silicide at the wafer surface, which is difficult to remove as it is insoluble in HF solution. To avoid this problem, we use proximity rapid thermal diffusion (P-RTD).[220] The dopant source consists in the SOD layer, which is deposited on a Si wafer used as support; this is stacked in proximity to the Si target wafer, from which it is separated by 300 µm thick Si spacers, as shown on Figure 6.1. When heating under N_2, the dopants go across the short space from the source wafer to the target wafer and diffuse through the silicon; this method allows also a better control of the junction depth.

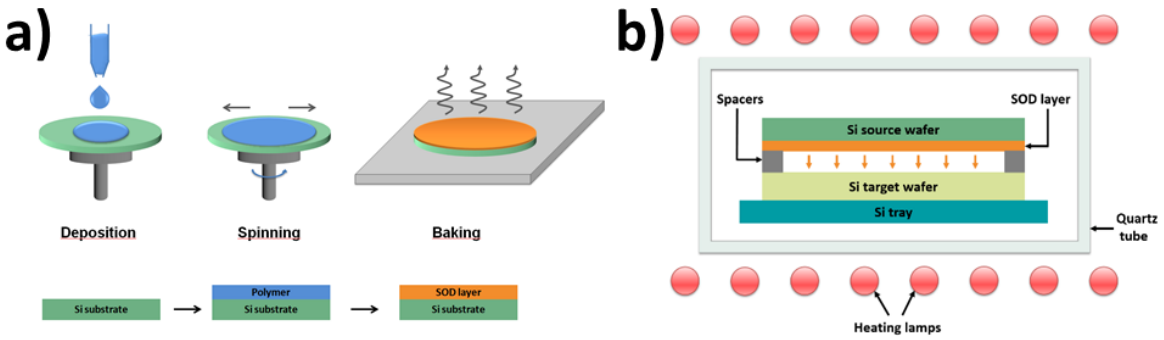

Figure 6.1. Experimental set-up of (a) SOD and (b) P-RTD.

Source wafers were cleaned by using 5% HF solution followed by a 15 min treatment in H_2SO_4/H_2O_2 solution, so as to form a chemical oxide on the Si surface to improve the stability of the SOD, which is deposited in the next step. Emulsitone Borofilm 100, the SOD source, was spun onto the source wafers at 3000 rpm during 30 sec. Subsequently, the wafers were baked at 200°C in air for 10 min. The P-RTD was then performed under dry air flow at atmospheric pressure in an ADDAX RTA furnace. The temperature peak adopted was in the 980-1020°C range with a 50-100°C/s heating ramp.[221]

In a P-RTD processes the diffusion relies heavily on the temperature and on the diffusion time to which the wafer is subject at the peak temperature; in particular, if the temperature is too high or the time is too long, the concentration profile runs the risk to be not abrupt, therefore not leading to a shallow junction. On the contrary, if the temperature is too low, the concentration of dopants might not be high enough to have a good tunnel junction. Moreover, the combination of two subsequent processes lets the second dopant compensate the first one in the proximity of the surface.

The resulting doping profiles are measured by means of electrochemical capacitance-voltage (ECV - WEP-CVP21). Unlike SIMS measurements which give total concentration, the ECV profile represents the concentration of only electrically active dopants within Si, thus giving an accurate measurement of the junction depth.[222] During measurements, Si is slowly etched with a standard 0.1M NH_4HF_2 solution.

The ECV profiles before and after B thermal diffusion are reported in Figure 6.2. Figure 6.2(a) displays the graphic of the carrier concentration as a function of the depth for the original n^{++}-doped emitter (P doped obtained by standard $POCl_3$ thermal diffusion at 840 °C). Figure 6.2(b) shows the equivalent graphic for the resulting profiles of both p and n type regions of the tunnel junction. It can be noticed that both regions are degenerated with an active dopant concentrations above $10 \cdot^{20}$ cm^{-3}, the carrier concentration being about $2 \cdot 10^{20}$ cm^{-3} (p-type) and about $1.2 \cdot 10^{20}$ cm^{-3} (n-type). Besides, it can be observed that the p-type region is very shallow (50 nm), and that a depletion region of only 3 nm is expected. All these characteristics are suitable to form a high-quality tunnel junction.

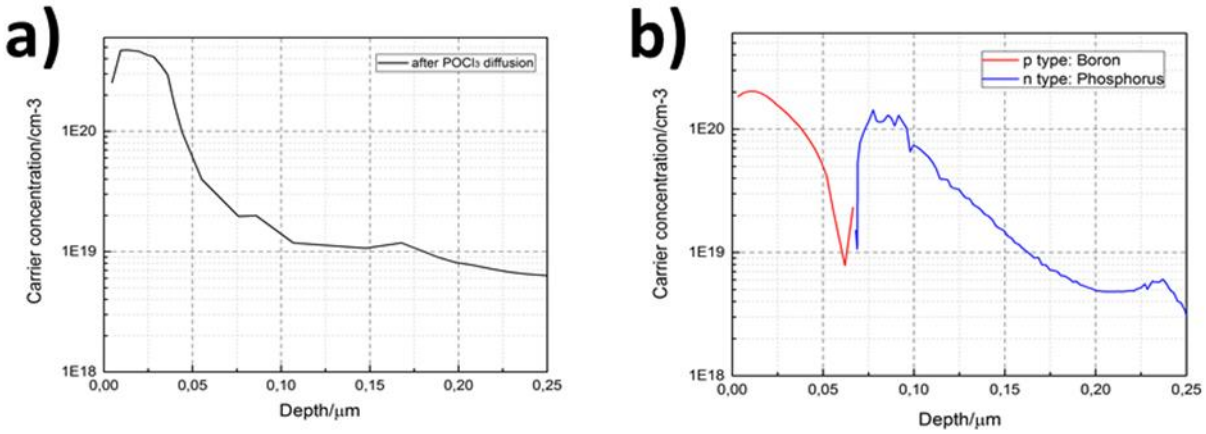

Figure 6.2. Carrier concentrations as a function of the depth for (a) the original phosphorus n^{++}-doped emitter and (b) for a sample with tunnel junction.

In order to simulate the thermal budget of the GaAs/$Al_{0.2}Ga_{0.8}As$ core/shell NWs epitaxy process, we tested two samples with shallow P- and B-doped structures at 610°C during 30 min under UHV. We did not observe any modification of the profiles for the B-doped structure, while in the P-doped one only a slight decrease in concentration was found near the surface, probably due to exo-diffusion. Since in our real structures the P-doped region will not be near the surface, we can assume that the top cell fabrication process will not affect the behavior of the tunnel diode.

After the implementation of the tunnel structure, the samples were sent to C2N for the deposition and patterning of the SiO_2 mask.

6.4 Preliminary results on NW encapsulation

The idea of encapsulating the NWs with HSQ came from the know-how already acquired by our group on this compound.

In order to provide mechanical stability to the cell, NWs must be properly embedded in a transparent encapsulation layer. This can be realized by spin-coating, depositing a droplet of precursor on the substrate where NWs were grown and subjecting the sample to rotation so as to spread the precursor uniformly over the surface. Adjusting the parameters of acceleration, rotation speed and time allows gaining control on the overall thickness of the encapsulating layer. Spin-coaters generally consist of rotating chucks located into a basin where samples are placed and fixed thanks to a vacuum pump. Since rotational acceleration and speed can vary up to several thousand rounds per minute (rpm), the final thickness of the encapsulating layer obtained with a single drop of precursor on a sample with smooth

surfaces can vary around several hundreds of nm. In the presence of NWs, on the contrary, the thickness obtained with a single drop of precursor increases with the diameter and density of the NWs, usually being between 0.5 and 2 µm, and changes in these two parameters can have dramatic consequences on the final layer thickness.

We therefore started a series of experiments of encapsulation and etch using as sacrificial patterned samples those ones which had provided low vertical rates, the growth protocol not including yet thermal pre-treatment at that time. Generally speaking, when it comes to the deposition and curing of HSQ on small surfaces as in the case of our 1 cm x 1 cm samples, the procedure consists in the deposition of only one droplet of liquid precursor, followed by spin coating and bake; in particular, the function of the bake is to thermally anneal HSQ so as to convert it into SiO_2, i.e. the final encapsulation material. The first attempts were carried out on two samples (A and B) treated with the parameters reported in Table 6.1, performing the bake in air on a hot plate for a short time (1 min); the procedure was performed twice on sample B, so as to compensate the high spin coating acceleration and speed for obtaining a thicker encapsulation layer.

Sample	Spin coating speed (rpm)	Acceleration (rpm/sec)	Spin coating time (sec)	Baking temperature (°C)	Baking time (sec)
A	1500	1500	60	300	60
B	3000	3000	60	300	60

Table 6.1. HSQ spin coating and baking parameters employed for the first series of samples.

SEM images of samples A and B after HSQ deposition are reported in Figure 6.3(a, b), respectively. In both cases the NW tips emerge from the HSQ layer: considering that the NW length are 1.4 ± 0.1 µm and 2.2 ± 0.1 µm, respectively, based on the length of the emerging part of the NWs, the HSQ thickness can be estimated around 1.1 and 1.5 µm, respectively. It can be noticed that in the case of sample A some cracks are already present on the surface of the encapsulation layer (Figure 6.3(a)), whereas in the case of sample B a dark/bright contrast is observable on the surface, thus suggesting the presence of density inhomogeneities. After the deposition, the sample A was treated with 1% HF solution for 40 sec so as to reduce the thickness of the layer and remove the silica from the NW tips (Figure 6.3(c)). It can be noticed that such a treatment has a dramatic effect on the encapsulation layer, originating holes around the NWs. In order to prevent this effect, sample B was exposed to a lower etching time of 7 sec in 1% HF (Figure 6.3(d)): yet smaller than in the previous case, the holes are still present around the NWs. Moreover, it can be also noticed that a 7 sec etch is not enough to remove all the materials from the NWs, some residues being still present on their tips.

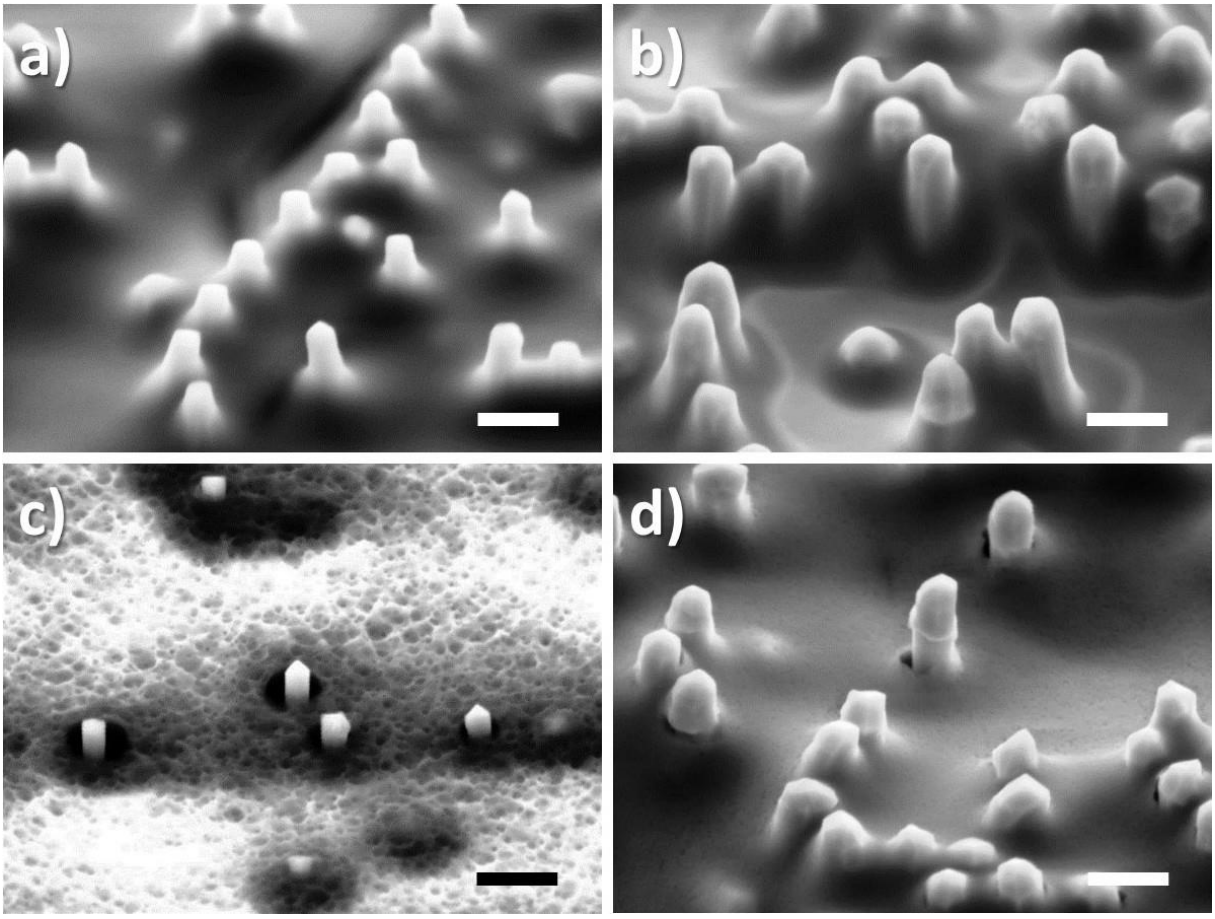

Figure 6.3. 45°-tilted SEM images of (a) sample A after HSQ deposition and bake, (b) sample B after HSQ deposition and bake, (c) sample A after 40 sec etch in 1% HF solution, (d) sample B after 7 sec etch. The scale bars correspond to 500 nm.

The presence of holes around the NWs after etching shows that the curing procedure of the encapsulating material was not effective enough. In order to compensate for this failure, a second series of three samples was prepared with a different procedure; this consists of HSQ deposition performed with the same spin coating parameters already employed for sample A, plus 20 min baking at 150 °C on hot plate in air, 60 min more baking at 350 °C, and eventually either 75 sec Rapid Thermal Annealing (RTA) in N_2 atmosphere at 600 °C (sample C) or 60 min at 500 °C (sample D) or 60 min annealing at 600 °C, also in N_2 atmosphere (sample E). SEM images of these samples after deposition and baking are reported in Figure 6.4(a, b, c), respectively. It can thus be noticed that, contrary to the two other samples, sample E already shows cracks in the encapsulating layer, likely because of the severe baking procedure adopted; for such a reason, sample E was not further investigated, whereas sample C and D were etched in 1% HF for 10 sec each so as to verify whether the formation of holes around the NWs could be prevented.

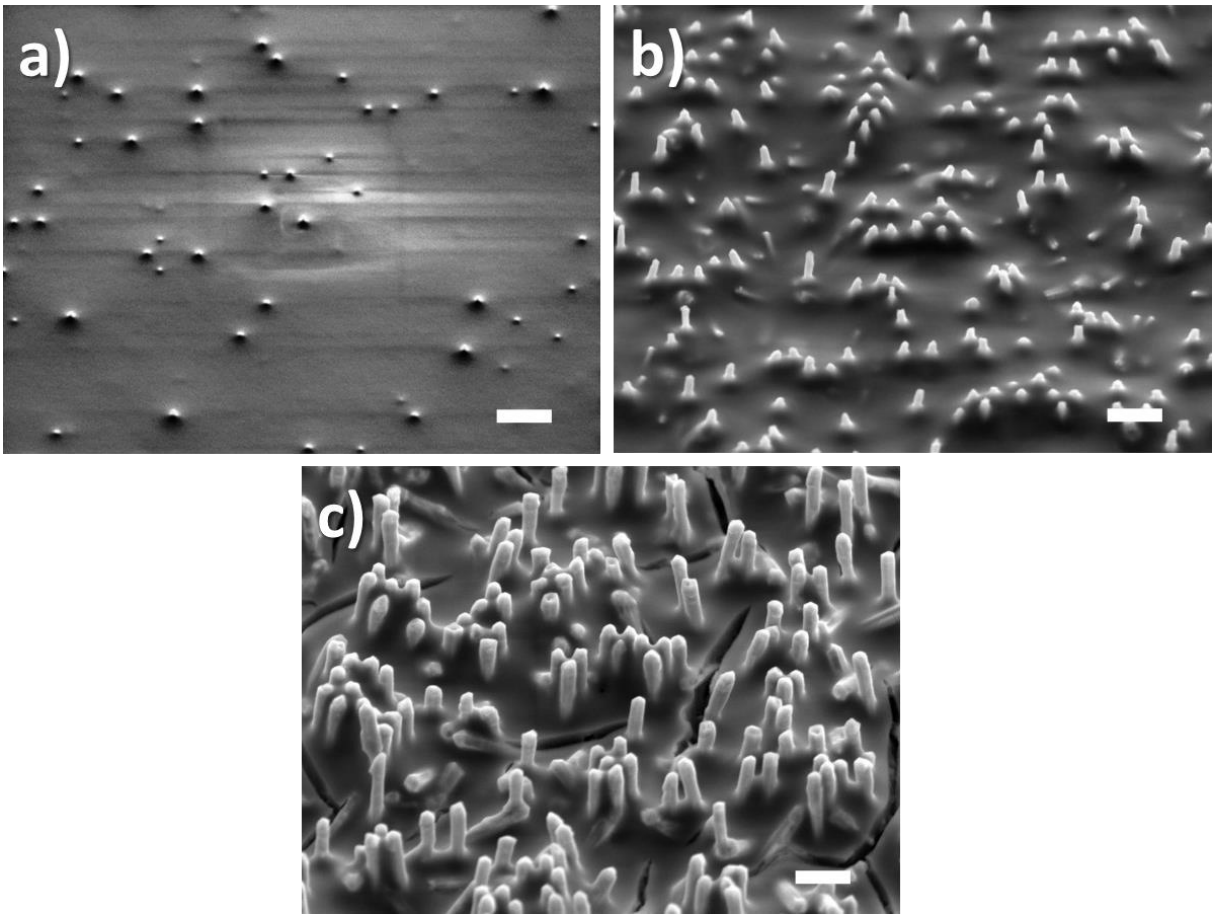

Figure 6.4. 45°-tilted SEM images of the samples C (a), D (b) and E (c) after HSQ deposition and baking. The white scale bars correspond to 1 µm.

SEM images of sample C and D after 10 sec 1% HF etch are reported in Figure 6.5: it is evident that despite the harder baking conditions, a uniform etch of the encapsulating layer could not be achieved. As a matter of fact, in the case of sample C, holes preferentially formed around the NWs, whereas on sample D large part of the silica has been etched. However, this is not the only drawback of this procedure: in fact, it seems that silica was etched preferentially from the layer but not from the NWs, since in both cases some NWs still present silica on their profile (marked with red arrows). Moreover, such a treatment also changed the morphology of some NWs, now appearing as crooked (marked in yellow), whereas before HSQ deposition all NWs, either vertical or tilted, were always straight.

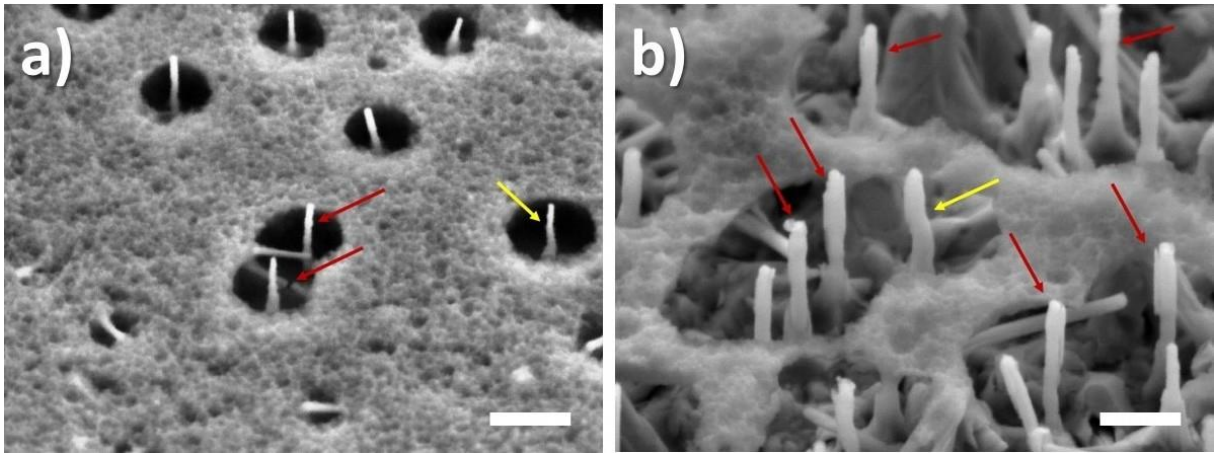

Figure 6.5. 45°-tilted SEM images of (a) sample C and (b) sample D, after 10 sec etch in 1% HF solution. The white scale bars corresponds to 500 nm.

This change of shape is likely attributed to the strain induced by silica on the NWs as a result of a too severe thermal annealing: indeed, it was already observed that in the case of NWs on thin lamellae (cf. Chapter 5, Paragraph 5.3) the strain originating in HSQ encapsulation layer could extend to the NWs and eventually fracture them (Figure 6.6).

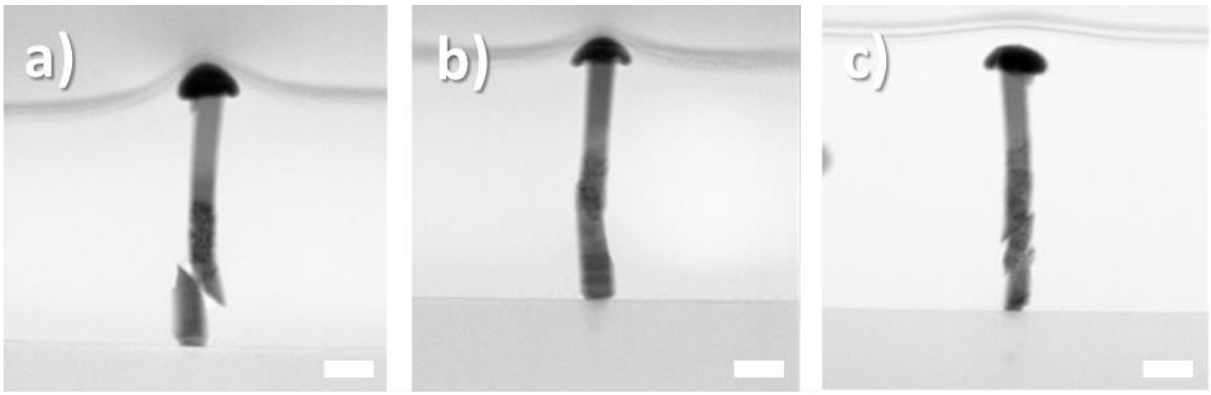

Figure 6.6: TEM images on thin lamellae of HSQ-encapsulated NWs (cf. Chapter 5, Paragraph 5.3). The white scale bars correspond to 100 nm.

Following these results, we decided to prepare one more sample F adopting the same procedure for C, D, E, although in this case only 20 min baking at 150 °C on hot plate in air plus 60 more min at 350 °C were performed. Subsequently, sample F was treated with 1% HF for different times to monitor the course of the etching: results are reported in Figure 6.7. As it can be seen, NWs were completely covered after HSQ deposition; after 5 sec etching some tips begin to appear, however after 20 sec silica is already over-etched and holes form around the NWs.

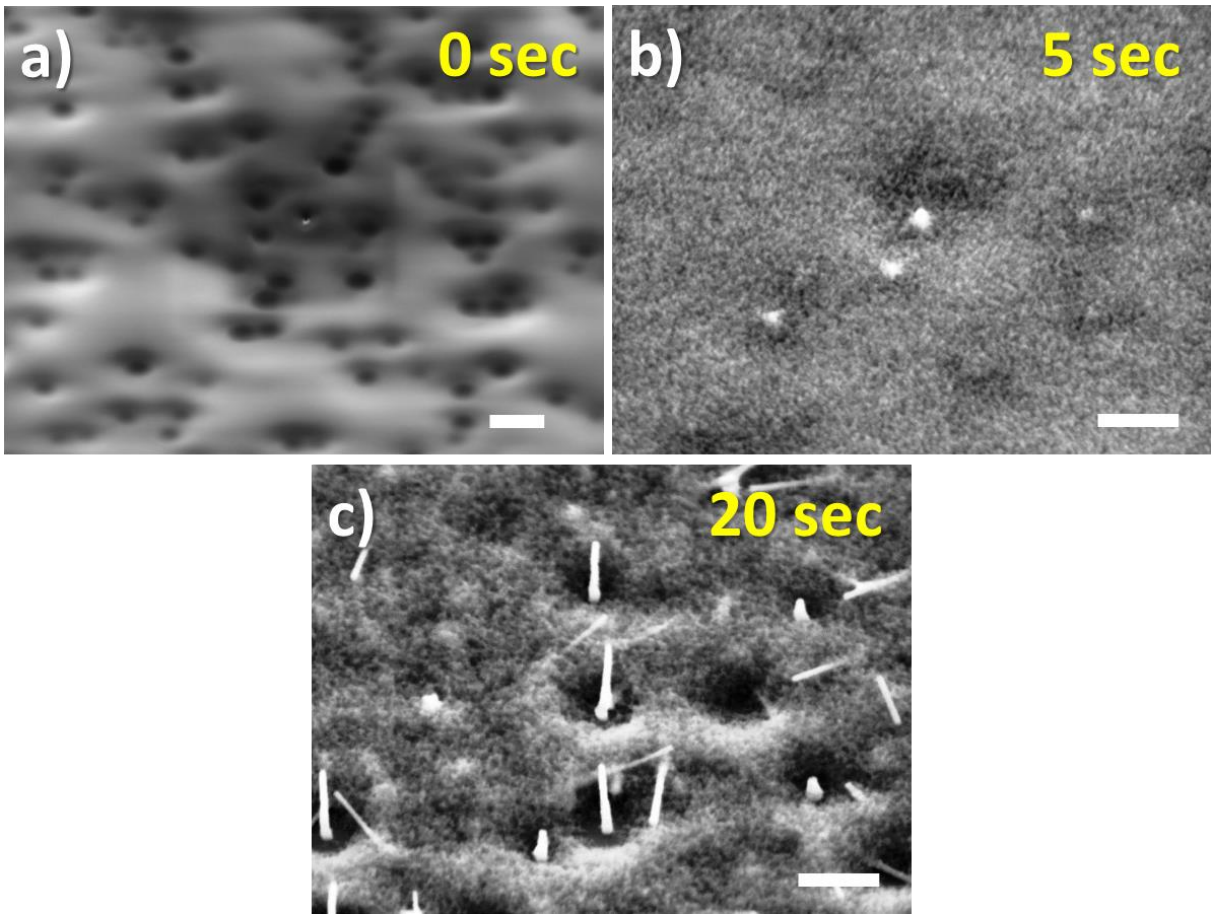

Figure 6.7. 45°-tilted SEM images of (a) sample F after HSQ deposition and baking, (b) after 5 sec etch in 1% HF solution and (c) after 20 sec etch. The yellow values in each image corresponds to the etching time. The white scale bars correspond to 1 µm in (a) and to 500 nm in (b, c).

Following this latest failure we have come to the conclusion that HSQ is not a good encapsulating material for our purpose. As a consequence, we decided to replace it by benzocyclobutene (BCB), which acts as a stable, transparent encapsulating material without damaging the NWs. For these reasons, it has already been widely employed in the fabrication of PV devices based on ordered arrays of NWs:[76,78,82,86,87,90–92,223] the optimisation of BCB deposition, baking and etching has already been undertaken in our group and is still in progress. A spin coating procedure based on the deposition of BCB and spinning at 10000 rpm for 77 sec with acceleration of 1000 rpm/sec was adopted. This was followed by a thermal curing procedure consisting of a first soft bake in air at 100 °C for 90 sec, followed by a second bake in N_2 atmosphere where the sample was gradually heat up to 250 °C and kept at this temperature for one hour. The results of such a procedure on patterned substrates with high vertical yield (80-90%) of GaAs/$Al_{0.2}Ga_{0.8}As$ core/shell NWs are reported in Figure 6.8(a); the encapsulation layer shows a quite uniform thickness, is crack-free even after the thermal treatment at 250 °C and exposes only the very tips of the NWs.

In order to remove the BCB in excess from the NW tips and to expose them sufficiently for the contact procedure, this sample was then treated by RIE for 30 sec (with 20 sscm O_2, 5 sscm SF_6, pressure = 100 mTorr and RF power = 50 W). The results of this treatment are reported in Figure 6.8(b): it can be noticed that all BCB were removed from the tips of the NWs, which are now partially exposed for a length of 300 ± 38 nm. Considering such value as sufficient for our purpose, we decided to introduce this etching procedure in the final fabrication process.

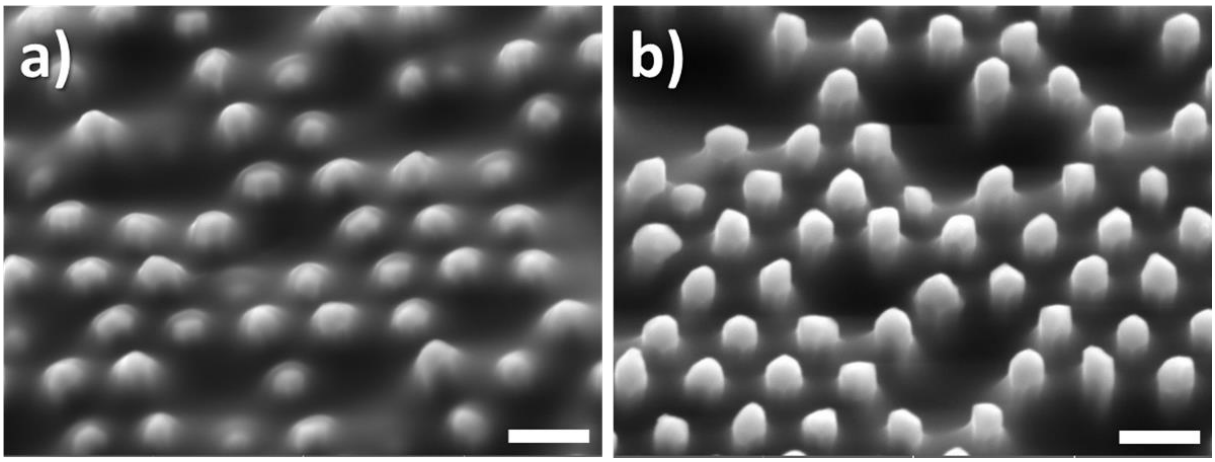

Figure 6.8. SEM image (45°-tilted) of (a) GaAs/$Al_{0.2}Ga_{0.8}$As core/shell NWs encapsulated with a BCB layer after baking at 250 °C, and (b) the same sample after 30 sec of RIE. The white scale bars correspond to 500 nm.

All HSQ and BCB depositions and RIE treatments here reported were carried out at INL by X. Li. We consider such results very encouraging and expect them to be a good starting point for the further development of our PV device.

6.5 ITO deposition on NWs by sputtering

As already mentioned, in order to provide an electrical contact to the top sub-cell after encapsulation, it is necessary to locally remove the passivation shell and deposit ITO on the exposed PV-active region. A preliminary study was carried out in this regard to verify the response of the NWs to sputtering deposition.

Sputtering deposition is a physical vapour deposition (PVD) technique largely adopted to form thin layers of materials on substrates. The process is performed thanks to a plasma, whose ions are electrically accelerated towards a source material (also called target) so as to cause the emission of ions, atoms or molecular fragments: these eventually deposit on the surface of the sample forming the thin layer in question.

One of the plasma precursors most widely employed is Ar, or mixes of Ar and other gases. The most basic sputter deposition techniques is surely the direct current (DC) sputtering; here the gas pressure in the deposition chamber usually ranges from 1 to 100 mTorr, while a voltage from 2 to 5 kV is applied between the target (cathode) and the substrate (anode), so as to direct the ions towards the first one (Figure 6.9). When plasma/target collisions occur, the sputtering of target atoms is the result of a momentum transfer process involving the first atomic layers. About 95 % of the incident energy is retained by the target as heat (making cooling necessary) while about 5 % of it is carried off by the expelled atoms, with energy between 5 and 100 eV. These pass through the plasma before deposition, where they may collide with ions, electrons and precursor atoms either causing back-side chemical reactions, or being ionized or just loosing part of their energy which will eventually be reduced to 1-10 eV. Nevertheless, part of them will finally reach the substrate and deposit on it. The species eventually impinging on the substrate surface are not only target atoms and ions, but also electrons and plasma precursor atoms, which may be incorporated in the layer, especially when high pressures of precursors are employed: hence, the use of chemical inert Ar to obtain plasma.

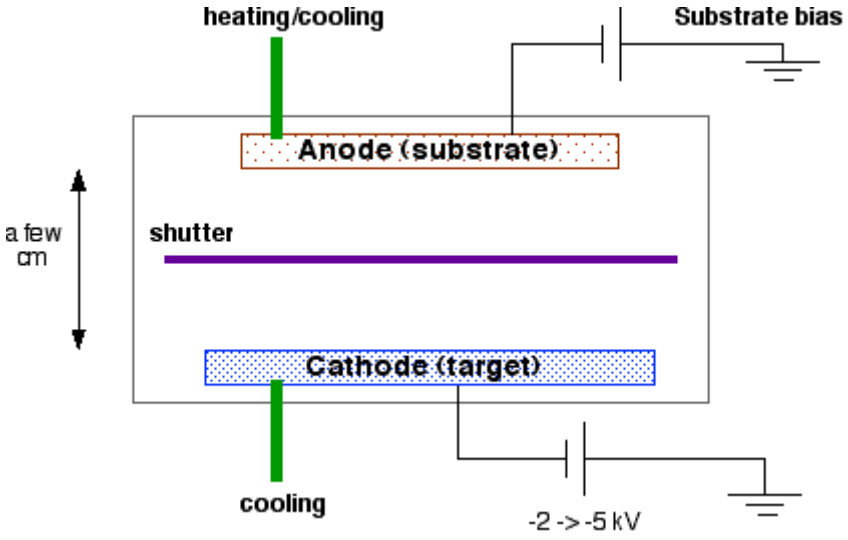

Figure 6.9. Schematics of a DC sputtering setup.

The final composition of a deposited layer results very similar to that one of the alloy in the target: this characteristic distinguishes sputtering from evaporation, thus making the first technique generally preferred to the second one.

The principle of DC sputtering has been above summarized: other sputtering techniques largely adopted in the fabrication of thin films are radio frequency (RF) sputtering and magnetron sputtering. RF sputtering is usually employed to overcome the limitations caused to DC sputtering by targets of insulating materials, where positive ions tends to accumulate on the target surface thus preventing other collisions: in order to prevent this problem, the voltage between anode and cathode can be alternated so as to eliminate the excess of

positive charges on the target. Magnetron sputtering on the contrary is a different approach which does not define the voltage set between anode and cathode; in fact it can be used either in DC or RF mode. In this case, electric and magnetic fields are used to trap electrons near the cathode in order to increase the probability of ionizing the precursors, so that it is possible to achieve higher sputter rate at lower pressures, thus increasing the overall efficiency of the process.

The depositions performed during this thesis were carried out at INL under the supervision of R. Mazurczyk with an AC450 sputter by Alliance Concept.

Preliminary depositions were performed on two different kind of structures: GaAs NWs grown for 10 min with standard procedure (Figure 6.10(a)) and GaAs/$Al_{0.2}Ga_{0.8}As$/GaAs core/shell NWs, obtained growing the core for 10 min with standard procedure, consuming the Ga droplet under As flux (f_{As} = 4.05 ML/sec) in 4 min while cooling to 460 °C, and finally depositing $Al_{0.2}Ga_{0.8}As$ (with F_{Al} = 0.13 ML/sec) and GaAs at the same temperature for 20 and 10 min respectively (Figure 6.10(b)).

ITO deposition was performed on these two samples by magnetron sputtering at room temperature, for a nominal layer thickness equal to 250 nm. After the deposition, the samples were baked at 250 °C for 30 min under N_2 flow. SEM images of the NWs after the deposition are reported in Figure 6.10(c, d). It can be observed that in both cases a conformal coating was achieved, this fact being encouraging since it introduces the possibility of forming a uniform contact layer for the top cell on the NW tips. Table 6.2 reports a comparison of the size parameters of NWs before and after the deposition; it can be noticed that, although the nominal thickness of the deposited ITO is 250 nm, the diameter of the structures increased only by 115 nm for GaAs NWs and by 148 nm for the core/shell ones, whereas their length increased by 0.3 and 0.6 µm, respectively, thus showing a higher deposition rate along the axial direction.

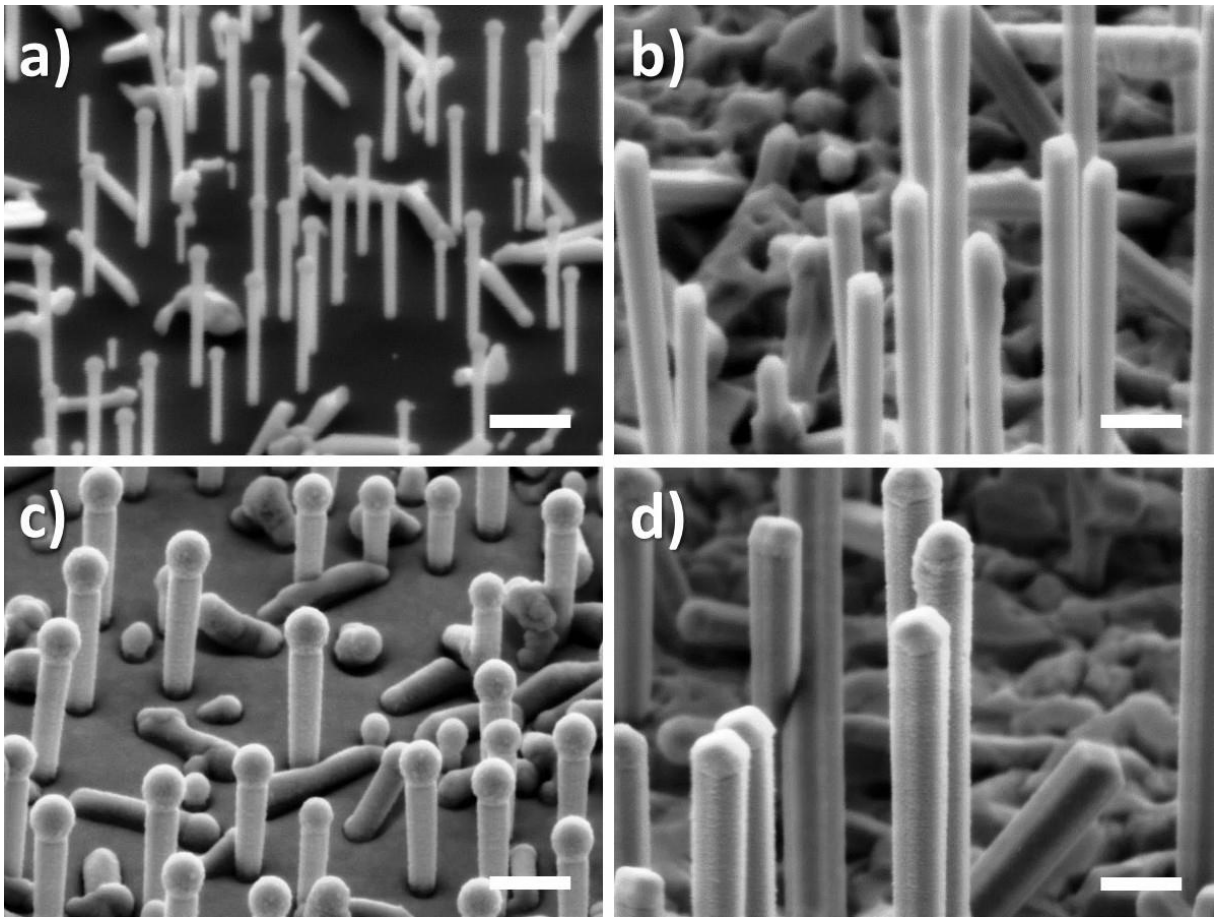

Figure 6.10. 45°-tilted SEM images of (a) GaAs NWs and (b) core/shell NWs before ITO deposition, and of (c) GaAs NWs and (d) core/shell NWs after ITO deposition by magnetron sputtering and thermal annealing at 250 °C under N_2 flow for 30 min. The white scale bars correspond to 500 nm.

Sample	Diameter before ITO (nm)	Diameter after ITO (nm)	Length before ITO (µm)	Length after ITO (µm)
GaAs NWs	73 ± 9	188 ± 18	1.0 ± 0.2	1.3 ± 0.2
GaAs/$Al_{0.2}Ga_{0.8}As$/GaAs NWs	210 ± 17	358 ± 28	4.1 ± 1.5	4.7 ± 1.2

Table 6.2. Diameter and length of GaAs NWs and GaAs/$Al_{0.2}Ga_{0.8}As$/GaAs core/shell NWs before and after ITO deposition by magnetron sputtering and thermal annealing at 250 °C under N2 flow for 30 min.

In the case of these samples, ITO was deposited directly on the NW surface. Nevertheless, it is well known that depositing a thin film of metal on the structure before the transparent conductive oxide can significantly enhance the electrical conductivity at the interface, thus forming a good ohmic contact at the top. The benefits of such a procedure were firstly demonstrated by Patkar et al with the deposition of Ag and Ti/Au on doped GaAs layers[224] and by Zhang et al with the deposition of In on GaAs NWs,[225] then eventually adopted by

Mariani et al[92] and Boulanger et al[90] for the fabrication of NWs-based PV devices. In order to verify whether we can adopt the same technique to improve the ohmic contact of our NWs, four-probe measurements were carried out on two samples constituted of a semi-insulating GaAs substrates on which 1 µm of n-GaAs ($8 \cdot 10^{18}$ cm^{-3}) and 225 nm of ITO were deposited and annealed in the same conditions reported for the NWs. In one case, an additional thin layer of In (25 nm) was also inserted between n-GaAs and ITO, thus determining conditions that are similar to those ones employed by Zhang et al (25 nm In, 500 nm ITO)[225] and by Boulanger et al (25 nm In, 250 nm ITO).[90] The electrical measurements showed a significant reduction of the sheet resistance thanks to the In thin film, the values decreasing from 16 to 6 Ω/□. For this reason we decided to employ this technique to contact our encapsulated NWs, also considering that such an approach should not affect significantly the light absorption from them.[90,225] Therefore, after 25 sec of wet etching in 10 % HCl solution to remove the $Al_{0.5}In_{0.5}P$ passivation shell and expose the n-AlGaAs shell, we deposited 25 nm of In by evaporator on the BCB-encapsulated NWs already reported in Figure 6.8(b). Subsequently, 100 nm of ITO were sputtered on the sample (optimal value according to the simulations reported in Chapter 5, Paragraph 5.2), which was then annealed at 250 °C under N_2 for 4 min, following Boulanger's procedure.[90] The result of such a treatment is illustrated in Figure 6.11. Contrary to what obtained with the deposition of ITO directly on the NWs shown in Figure 6.10 (c, d), in this case, ITO is extremely granular. This can be likely attributed to the In layer, which was deposited by evaporator, whereas its sputtered counterpart would be more uniform.[90] Considering that, we have no chance in our laboratory to deposit In by sputtering, and that such a granular ITO would affect the optoelectronic properties of the cell, we eventually decided to adopt only ITO as top contact of the NWs in the final process. Since the sheet resistance for this material only is quite low (16 Ω/□), this should not decrease the performances of our device.

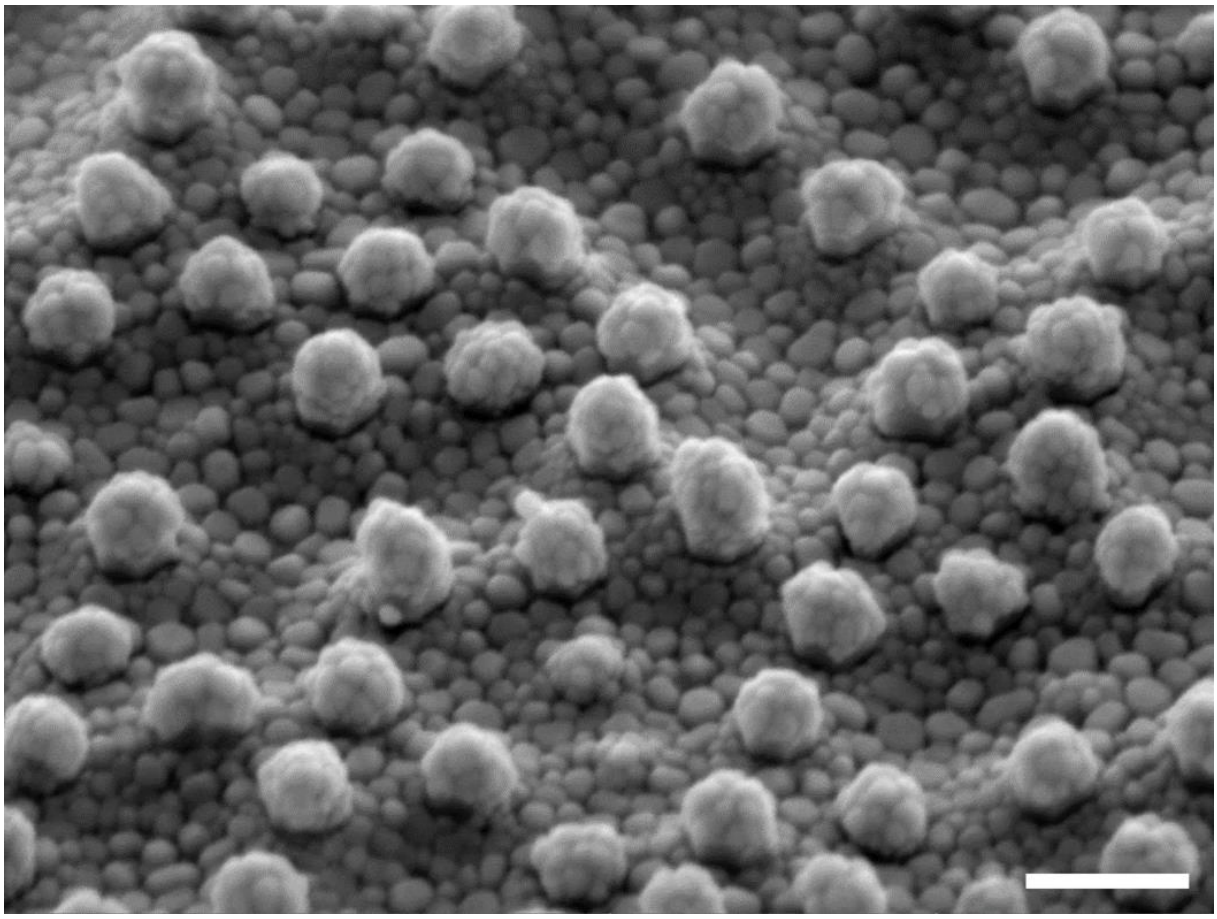

Figure 6.11. SEM image (45°-tilted) of the sample with BCB-encapsulated NWs (already shown in Figure 6.8(b)) after the deposition of 25 nm In by evaporator, 100 nm of ITO by sputtering, and after 4 min of thermal annealing at 250 °C under N_2. The white scale bar corresponds to 500 nm.

6.6 Conclusion

In this chapter we faced the issues of developing the process to fabricate our TSC after the NW growth.

Regarding the fabrication of the Si bottom cell, we developed a protocol based on SOD and P-RTD to obtain substrate with a tunnel junction on the surface. As shown by ECV analyses, the doping profile results to be resisting to the NW growth temperature and time.

Concerning the NW encapsulation, we ascertained that HSQ is not a suitable material due to the presence of post-baking cracks and strong strains, which eventually damage the NWs. For this reason we adopted BCB as encapsulation material, obtaining good preliminary results.

Promising preliminary results were collected also in the case of the NW top contacting, with conformal depositions of ITO obtained by sputtering. Moreover, 4-probe measurements showed good conductivity in both cases of ITO and In-ITO thin films: the latter ones in particular showed very low sheet resistances. However, due to the granular aspect of the ITO films deposited on evaporator-deposited In/NWs, which eventually will affect the performances of the cells, only the ITO deposition by sputtering directly on the NWs will be introduced in the final process.

Ultimately, based on the results reported in this chapter and in the previous ones, we can say that we are now close to the realization of the targeted TSC.

Conclusion

In this PhD thesis we addressed the issue of the use of NWs to obtain monolithical integration of III-V semiconductors on Si and develop a III-V NWs-based Tandem Solar Cell. We have focused on the MBE growth on Si substrates of self-assisted p-i-n core/shell $Al_{0.2}Ga_{0.8}As$-based heterostructured NWs. In order to achieve such an objective, we have devoted a great effort to optimise the NW growth for obtaining high vertical NW yieds on patterned Si(111) substrates. First results have been also obtained on the cell manufacturing process.

Regarding NWs, we initially focused our attention on the self-assisted growth of GaAs NWs on epi-ready Si(111) substrates as a propaedeutic step towards the development of our structures. We have firstly verifyied the effects of the growth temperature and of the Ga pre-deposition on the NW growth and defined an optimal protocol. Then, we committed to analysing the impact of the incidence angle of the Ga flux with the normal direction to the substrate, on the NW growth kinetic, taking advantage of the fact that our reactor is provided with two Ga cells with different incidence angles. The results put in evidence how different incidence angles may have dramatic effects on the NW growth, influencing heavily the droplet shape and thus the NW length and diameter, as a function of the growth time. In order to better understand the physical phenomena behind the experimental results, a model was developed and numerical simulations were performed by A. Danescu from our group. These highlighted that the growth kinetic and morphology of the NWs may strongly depend on the incidence angle of the Ga flux insofar as the amount of Ga atoms supplying the Ga droplets can change their volume and shape. This modifies the capture surface of As and, consequently, the axial growth rate. Such a result is quite significant, since it introduces the possibility of achieving higher control on the droplet size and shape, and consequently on the NW dimensions, only by the way of the incidence angle of the Ga flux. This capacity is potentially useful for the fine tuning of NW morphology and crystalline structure.

Once optimized and carefully analysed the growth of self-assisted GaAs NWs, we committed to transfer our know-how to the growth of self-assisted $Al_{0.2}Ga_{0.8}As$ NWs. However, all our attempts in this sense failed, either by direct or by “GaAs-seeded” growth. This failure is likely attributable to two reasons: 1- in the case of direct growth, to the oxidation of Al on the SiO_2 surface, which probably inhibits the Ga diffusion on the substrate and thus the Ga alimentation of the Ga droplets necessary to assist the VLS growth, 2- in the case of “seeded” growth, to the formation of $Al_xGa_{1-x}As$ on the NW facets which, in the same way, may reduce the diffusion of Ga adatoms causing progressive shrinkage (and eventually consumption) of droplets. In order to overcome these drawbacks, we proposed an alternative configuration consisting of starting the NW growth with a p-GaAs core before the active p.i.n-$Al_{0.2}Ga_{0.8}As$ shell. After studying the impact of the p-doping level in the GaAs core

and of the droplet consumption on the NW morphology, we firstly grow p-n GaAs core/shell NWs on epi-ready Si substrates. Their structural, optoelectronic and electronic properties were investigated by TEM, PL and EBIC, respectively. In particular, the EBIC analysis (performed at C2N) showed a good diodic behaviour from the NWs with a homogeneous collection of carriers on their entire length, characteristics which make these NWs potential building blocks of a PV device.

Reassured by these positive results, we continued our research focusing on the ultimate NW structure for our TSC, i.e. p-GaAs/p.i.n.-$Al_{0.2}Ga_{0.8}As$ core/shell NWs also grown, in a first step, on epi-ready Si substrates. These core/shell NWs were also characterized by TEM, PL and EBIC: the latter one provided important results for us, confirming the good response of the p-i-n junction, similar to what is already observed for the p-n GaAs core/shell NWs. Subsequently, we focused our attention to define the optimal passivation shell for these NWs; based on a PL study, we came to the conclusion that an $Al_{0.5}In_{0.5}P$ passivation shell is the most suitable with the cell fabrication process.

Once optimized the protocol to obtain the core/shell NWs on epi-ready Si, we aimed to transfer the acquired know-how onto patterned Si substrates, so as to finally achieve ordered arrays of p-GaAs/p.i.n.-$Al_{0.2}Ga_{0.8}As$ core/shell NWs as PV-active structures of the top cell. After a preliminary study of the selective deposition of Ga droplets, we performed many growths on patterned substrates (prepared at C2N according to the optimal parameters defined by the simulations carried out at IMEP-LAHC) to achieve high vertical yields of NWs. After many failures we eventually developed a growth procedure, whose key-step consists in a thermal pre-treatment right before the Ga deposition and NW growth, leading to high vertical yields of NWs (80-90 %). The reproducibility and effectiveness of this procedure were demonstrated on different substrates both for GaAs NWs and p-GaAs/p.i.n.-$Al_{0.2}Ga_{0.8}As$ core/shell NWs. The latter ones were also characterized by EBIC, providing once again a positive response which confirms their potential in the fabrication of tandem solar cells. Subsequently, we committed to the growth of NWs on patterned substrates realised by our group at INL, both to develop our own know-how in this field and to investigate the reasons for which the thermal pre-treatment induces high vertical yields. Ultimately, we advanced the hypothesis that the verticality might be induced by a possible temperature gradient between the Si substrate and the SiO_2 mask persisting after the thermal pre-treatment. However, it is not yet clear to us how this gradient would assist the growth of vertical NWs. For this reason, we are planning to continue the research in this sense so as to provide valuable hypotheses for explaining such results.

Finally, we dedicated part of our effort to the solar cell fabrication process as well. After trying to encapsulate the NWs with inorganic compound HSQ and ascertaining the failures of this approach due to the high strain induced by this compound on the NWs during the annealing, we came to the conclusion that the polymer resine BCB is a more suitable compound for this purpose. In fact, the preliminary results achieved with this compound are

quite encouraging and suggest that the encapsulation task is almost fulfilled. Positive results were achieved also for the etching of the AlInP passivation shell from the NW tips and for the ITO deposition by sputtering, which are necessary steps to contact the NWs. In this case, the deposited layers resulted morphologically uniform, while 4-probe measurements performed on thin films of ITO and In-ITO showed the possibility to achieve good conductivity. Ultimately, we also developed a protocol (based on SOD and P-RTD) to obtain Si wafers including temperature resistant tunnel junctions: these kinds of substrates are very important to our purpose, being expected to form the bottom cell of our TSC.

In conclusion, we can say that in the course of this thesis we developed the necessary know-how to fabricate a TSC. All the building blocks are ready, and with the acquired ensemble of skills and knowledges, the next step is to integrate all of them towards the fabrication of a prototype. Based on the progress of the work, it can be expected to achieve the realization of the TSC over the very next months, as targeted as part of the HETONAN project.

References

(1) http://pvinsights.com/.

(2) Kerr, M. J.; Cuevas, A.; Campbell, P. Limiting Efficiency of Crystalline Silicon Solar Cells Due to Coulomb-Enhanced Auger Recombination. *Prog. Photovoltaics Res. Appl.* **2003**, *11* (2), 97–104.

(3) Richter, A.; Hermle, M.; Glunz, S. . Reassessment of the Limiting Efficiency for Crystalline Silicon Solar Cells. *IEEE J. Photovoltaics* **2013**, *3* (4), 1184–1191.

(4) Connolly, J. P.; Mencaraglia, D.; Renard, C.; Bouchier, D. Designing III–V Multijunction Solar Cells on Silicon. *Prog. Photovoltaics Res. Appl.* **2014**, *22* (7), 810–820.

(5) Mailoa, J. P.; Bailie, C. D.; Johlin, E. C.; Hoke, E. T.; Akey, A. J.; Nguyen, W. H.; McGehee, M. D.; Buonassisi, T. A 2-Terminal Perovskite/Silicon Multijunction Solar Cell Enabled by a Silicon Tunnel Junction. *Appl. Phys. Lett.* **2015**, *106* (12), 121105.

(6) Bailie, C. D.; McGehee, M. D. High-Efficiency Tandem Perovskite Solar Cells. *MRS Bull.* **2015**, *40* (8), 681–685.

(7) Essig, S.; Allebé, C.; Remo, T.; Geisz, J. F.; Steiner, M. A.; Horowitz, K.; Barraud, L.; Ward, J. S.; Schnabel, M.; Descoeudres, A.; et al. Raising the One-Sun Conversion Efficiency of III-V/Si Solar Cells to 32.8% for Two Junctions and 35.9% for Three Junctions. *Nat. Energy* **2017**, *2* (9), 17144.

(8) Green, M. A.; Hishikawa, Y.; Dunlop, E. D.; Levi, D. H.; Hohl-Ebinger, J.; Ho-Baillie, A. W. Y. Solar Cell Efficiency Tables (Version 51). *Prog. Photovoltaics Res. Appl.* **2018**, *26* (1), 3–12.

(9) Masuko, K.; Shigematsu, M.; Hashiguchi, T.; Fujishima, D.; Kai, M.; Yoshimura, N.; Yamaguchi, T.; Ichihashi, Y.; Mishima, T.; Matsubara, N.; et al. Achievement of More than 25% Conversion Efficiency with Crystalline Silicon Heterojunction Solar Cell. *IEEE J. Photovoltaics* **2014**, *4* (6), 1433–1435.

(10) Adachi, D.; Hernández, J. L.; Yamamoto, K. Impact of Carrier Recombination on Fill Factor for Large Area Heterojunction Crystalline Silicon Solar Cell with 25.1% Efficiency. *Appl. Phys. Lett.* **2015**, *107* (23), 23–26.

(11) Smith, D. D.; Reich, G.; Baldrias, M.; Reich, M.; Boitnott, N.; Bunea, G. 2016 IEEE 43rd Photovoltaic Specialists Conference (PVSC). In *Silicon solar cells with total area efficiency above 25 %*; 2016; p 3351.

(12) Yoshikawa, K.; Kawasaki, H.; Yoshida, W.; Irie, T.; Konishi, K.; Nakano, K.; Uto, T.; Adachi, D.; Kanematsu, M.; Uzu, H.; et al. Silicon Heterojunction Solar Cell with Interdigitated Back Contacts for a Photoconversion Efficiency over 26%. *Nat. Energy* **2017**, *2* (5), 17032.

(13) Yastrebova, N. V. High-Efficiciency Multijunction Solar Cells: Current Status and Future Potential. Centre for Research in Photonics, University of Ottawa 2007.

(14) Peters, C. Thin Film Tandem Solar Cells - Coursework for Physics 240, Stanford University. 2010.

(15) Geisz, J. F.; Friedman, D. J. III N V Semiconductors for Solar Photovoltaic Applications. *Semicond. Sci. Technol.* **2002**, *17* (8), 769–777.

(16) Jain, N.; Hudait, M. K. III–V Multijunction Solar Cell Integration with Silicon: Present Status, Challenges and Future Outlook. *Energy Harvest. Syst.* **2014**, *1* (3–4), 121–145.

(17) Geisz, J. F.; Olson, J. M.; Friedman, D. J.; Jones, K. M.; Reedy, R. C.; Romero, M. J. Conference Record of the Thirty-First IEEE Photovoltaic Specialists Conference, 2005. In *Mattice-matched GaNPAs-on-Silicon Tandem Solar Cells.*; 2005; pp 695–698.

(18) Ager, J. W.; Reichertz, L. A.; Yu, K. M.; Schaff, W. J.; Williamson, T. L.; Hoffbauer, M. A.; Haegel, N. M.; Walukiewicz, W. 2008 33rd IEEE Photovoltaic Specialists Conference. In *InGaN/Si heterojunction tandem solar cells*; 2008.

(19) Tran, B. T.; Chang, E. Y.; Trinh, H. D.; Lee, C. T.; Sahoo, K. C.; Lin, K. L.; Huang, M. C.; Yu, H. W.; Luong, T. T.; Chung, C. C.; et al. Fabrication and Characterization of N-In0.4Ga0.6N/p-Si Solar Cell. *Sol. Energy Mater. Sol. Cells* **2012**, *102*, 208–211.

(20) Geisz, J. F.; Olson, J. M.; Romero, M. J.; Jiang, C. S.; Norman, A. G. Conference Record of the 2006 IEEE 4th World Conference on Photovoltaic Energy Conversion, WCPEC-4. In *Lattice-mismatched GaAsP Solar Cells Grown on Silicon by OMVPE*; 2007; Vol. 1, pp 772–775.

(21) Lueck, M. R.; Andre, C. L.; Pitera, A. J.; Lee, M. L.; Fitzgerald, E. A.; Ringel, S. A. Dual Junction GaInP/GaAs Solar Cells Grown on Metamorphic SiGe/Si Substrates with High Open Circuit Voltage. *IEEE Electron Device Lett.* **2006**, *27* (3), 142–144.

(22) Dimroth, F.; Roesener, T.; Essig, S.; Weuffen, C.; Wekkeli, A.; Oliva, E.; Siefer, G.; Volz, K.; Hannappel, T.; Haussler, D.; et al. Comparison of Direct Growth and Wafer Bonding for the Fabrication of GaInP/GaAs Dual-Junction Solar Cells on Silicon. *IEEE J. Photovoltaics* **2014**, *4* (2), 620–625.

(23) Derendorf, K.; Essig, S.; Oliva, E.; Klinger, V.; Roesener, T.; Philipps, S. P.; Benick, J.; Hermle, M.; Schachtner, M.; Siefer, G.; et al. Fabrication of GaInP/GaAs//Si Solar Cells by Surface Activated Direct Wafer Bonding. *IEEE J. Photovoltaics* **2013**, *3* (4), 1423–1428.

(24) Hironori Taguchi, Naoaki Okada, T.; Soga; Takashi; Jimbo; Masayoshi; Umeno. GaAs / Si TANDEM SOLAR CELL USING EPITAXIAL LIFT-OFF TECHNIQUE. **2003**, 769–772.

(25) Tanabe, K.; Watanabe, K.; Arakawa, Y. III-V/Si Hybrid Photonic Devices by Direct Fusion Bonding. *Sci. Rep.* **2012**, *2*, 349.

(26) Hochbaum, A. I.; Yang, P. Semiconductor Nanowires for Energy Conversion. *Chem. Rev.* **2010**, *110* (10), 527–546.

(27) Law, M.; Goldberger, J.; Yang, P. Semiconductor Nanowires and Nanotubes. *Annu. Rev. Mater. Res.* **2004**, *34* (1), 83–122.

(28) Bozhi Tian, Thomas J. Kempa, C. M. L. 2009 Renewable Energy Issue. *Chem. Soc. Rev.* **2009**, *38* (1), 165–184.

(29) Fan, Z.; Ruebusch, D. J.; Rathore, A. A.; Kapadia, R.; Ergen, O.; Leu, P. W.; Javey, A. Challenges and Prospects of Nanopillar-Based Solar Cells. *Nano Res.* **2009**, *2* (11), 829–

843.

(30) Yu, K.; Chen, J. Enhancing Solar Cell Efficiencies through 1-D Nanostructures. *Nanoscale Res. Lett.* **2009**, *4*, 1–10.

(31) Garnett, E.; Yang, P. Light Trapping in Silicon Nanowire Solar Cells. *Nano Lett.* **2010**, *10* (3), 1082–1087.

(32) Cao, L.; Park, J. S.; Fan, P.; Clemens, B.; Brongersma, M. L. Resonant Germanium Nanoantenna Photodetectors. *Nano Lett.* **2010**, *10* (4), 1229–1233.

(33) Greene, L. E.; Law, M.; Yuhas, B. D.; Yang, P. ZnO - TiO 2 Core - Shell Nanorod / P3HT Solar Cells. *J. Phys. Chem. C* **2007**, *111* (50), 18451–18456.

(34) Takanezawa, K.; Tajima, K.; Hashimoto, K. Efficiency Enhancement of Polymer Photovoltaic Devices Hybridized with ZnO Nanorod Arrays by the Introduction of a Vanadium Oxide Buffer Layer. *Appl. Phys. Lett.* **2008**, *93* (6), 10–13.

(35) Yuhas, B. D.; Yang, P. Nanowire-Based All-Oxide Solar Cells. *J. Am. Chem. Soc.* **2009**, *131* (10), 3756–3761.

(36) Varghese, O. K.; Paulose, M.; Grimes, C. A. Long Vertically Aligned Titania Nanotubes on Transparent Conducting Oxide for Highly Efficient Solar Cells. *Nat. Nanotechnol.* **2009**, *4* (9), 592–597.

(37) Wang, K.; Chen, J. J.; Zeng, Z. M.; Tarr, J.; Zhou, W. L.; Zhang, Y.; Yan, Y. F.; Jiang, C. S.; Pern, J.; Mascarenhas, A. Synthesis and Photovoltaic Effect of Vertically Aligned ZnO/ZnS Core/Shell Nanowire Arrays. *Appl. Phys. Lett.* **2010**, *96* (12), 15–18.

(38) Fan, Z.; Razavi, H.; Do, J.; Moriwaki, A.; Ergen, O.; Chueh, Y.; Leu, P. W.; Ho, J. C.; Takahashi, T.; Reichertz, L. A.; et al. Three-Dimensional Nanopillar-Array Photovoltaics on Low-Cost and Flexible Substrates. *Nat. Mater.* **2009**, *8* (8), 648–653.

(39) Lévy-Clément, C.; Tena-Zaera, R.; Ryan, M. A.; Katty, A.; Hodes, G. CdSe-Sensitized p-CuSCN/Nanowire n-ZnO Heterojunctions. *Adv. Mater.* **2005**, *17* (12), 1512–1515.

(40) Dong, Y. J.; Tian, B. Z.; Kempa, T. J.; Lieber, C. M. Coaxial Group III- Nitride Nanowire Photovoltaics. *Nano Lett.* **2009**, *9*, 2183–2187.

(41) Williams, S. S.; Hampton, M. J.; Gowrishankar, V.; Ding, I. K.; Templeton, J. L.; Samulski, E. T.; DeSimone, J. M.; McGehee, M. D. Nanostructured Titania-Polymer Photovoltaic Devices Made Using PFPE-Based Nanomolding Techniques. *Chem. Mater.* **2008**, *20* (16), 5229–5234.

(42) Law, M.; Greene, L. E.; Johnson, J. C.; Saykally, R.; Yang, P. Nanowire Dye-Sensitized Solar Cells. *Nat. Mater.* **2005**, *4* (6), 455–459.

(43) Briseno, A. L.; Holcombe, T. W.; Boukai, A. I.; Garnett, E. C.; Shelton, S. W.; Fréchet, J. J. M.; Yang, P. Oligo- and Polythiophene/ZnO Hybrid Nanowire Solar Cells. *Nano Lett.* **2010**, *10* (1), 334–340.

(44) Ihn, S.-G.; Song, J.-I.; Kim, Y.-H.; Lee, J. Y. GaAs Nanowires on Si Substrates Grown by a Solid Source Molecular Beam Epitaxy. *Appl. Phys. Lett.* **2006**, *89* (5), 053106.

(45) Paek, J. H.; Nishiwaki, T.; Yamaguchi, M.; Sawaki, N. MBE-VLS Growth of GaAs

Nanowires on (111)Si Substrate. *Phys. Status Solidi Curr. Top. Solid State Phys.* **2009**, *6*, 1436–1440.

(46) Green, M. A. *Solar Cells: Operating Principles, Technology and System Applications*, Englewood.; New South Wales, University, Kensington, Australia, 1982.

(47) Hecht E. *Optics*, Pearson.; San Francisco, 2002.

(48) Zhao, J.; Green, M. A. Optimized Antireflection Coatings for High Efficiency Silicon Solar Cells. *IEEE Trans. Electron Devices* **1991**, *38* (8), 1925–1934.

(49) Zhu, J.; Yu, Z.; Burkhard, G. F.; Hsu, C.; Connor, S. T.; Xu, Y.; Wang, Q.; Mcgehee, M.; Fan, S.; Cui, Y. Optical Absorption Enhancement in Amorphous Silicon Nanowire and Nanocone Arrays. *Nano Lett.* **2009**, *9* (1), 279–282.

(50) Muskens, O. L.; Rivas, J. G.; Algra, R. E.; Bakkers, E. P. A. M.; Lagendijk, A. Design of Light Scattering in Nanowire Materials for Photovoltaic Applications. *Nano Lett.* **2008**, *8* (9), 2638–2642.

(51) Tsakalakos, L.; Balch, J.; Fronheiser, J.; Korevaar, B. A.; Sulima, O.; Rand, J. Silicon Nanowire Solar Cells. *Appl. Phys. Lett.* **2007**, *91* (110), 233117.

(52) Tang, Y. B.; Chen, Z. H.; Song, H. S.; Lee, C. S.; Cong, H. T.; Cheng, H. M.; Zhang, W. J.; Bello, I.; Lee, S. T. Vertically Aligned P-Type Single-Crystalline GaN Nanorod Arrays on n-Type Si for Heterojunction Photovoltaic Cells. *Nano Lett.* **2008**, *8* (12), 4191–4195.

(53) Fan, Z.; Kapadia, R.; Leu, P. W.; Zhang, X.; Chueh, Y. L.; Takei, K.; Yu, K.; Jamshidi, A.; Rathore, A. A.; Ruebusch, D. J.; et al. Ordered Arrays of Dual-Diameter Nanopillars for Maximized Optical Absorption. *Nano Lett.* **2010**, *10* (10), 3823–3827.

(54) Diedenhofen, S. L.; Grzela, G.; Haverkamp, E.; Bauhuis, G.; Schermer, J.; Rivas, J. G. Broadband and Omnidirectional Anti-Reflection Layer for III/V Multi-Junction Solar Cells. *Sol. Energy Mater. Sol. Cells* **2012**, *101*, 308–314.

(55) Colombo, C.; Heiβ, M.; Grätzel, M.; Fontcuberta i Morral, A. Gallium Arsenide P-i-n Radial Structures for Photovoltaic Applications. *Appl. Phys. Lett.* **2009**, *94* (17), 173108.

(56) Kupec, J.; Stoop, R. L.; Witzigmann, B. Light Absorption and Emission in Nanowire Array Solar Cells. *Opt. Express* **2010**, *18* (26), 27589.

(57) Hu, L.; Chen, G. Analysis of Optical Absorption in Silicon Nanowire Arrays for Photovoltaic Applications. *Nano Lett.* **2007**, *7* (11), 3249–3252.

(58) Anttu, N.; Xu, H. Q. Coupling of Light into Nanowire Arrays and Subsequent Absorption. *J. Nanosci. Nanotechnol.* **2010**, *10* (11), 7183–7187.

(59) Muskens, O. L.; Diedenhofen, S. L.; Kaas, B. C.; Algra, R. E.; Bakkers, E. P. A. M.; Rivas, J. G.; Lagendijk, A. Large Photonic Strength of Highly Tunable Resonant Nanowire Materials. *Nano Lett.* **2009**, *9* (3), 930–934.

(60) Garnett, E. C.; Brongersma, M. L.; Cui, Y.; McGehee, M. D. Nanowire Solar Cells. *Annu. Rev. Mater. Res.* **2011**, *41* (1), 269–295.

(61) Ginley, D.; Green, M. A.; Collins, R. Solar Energy Conversion toward 1 Terawatt. *MRS*

Bull. **2008**, *33* (4), 355–364.

(62) Kuykendall, T.; Ulrich, P.; Aloni, S.; Yang, P. Complete Composition Tunability of InGaN Nanowires Using a Combinatorial Approach. *Nat. Mater.* **2007**, *6* (12), 951–956.

(63) Kayes, B. M.; Atwater, H. a.; Lewis, N. S. Comparison of the Device Physics Principles of Planar and Radial P-n Junction Nanorod Solar Cells. *J. Appl. Phys.* **2005**, *97* (11), 1–11.

(64) Yao, M.; Huang, N.; Cong, S.; Chi, C.; Seyedi, M. A.; Lin, Y.; Cao, Y.; Povinelli, M. L.; Dapkus, P. D.; Zhou, C. GaAs Nanowire Array Solar Cells with Axial p − i − n Junctions. *Nano Lett.* **2014**, *14* (6), 3293–3303.

(65) Gutsche, C.; Lysov, A.; Braam, D.; Regolin, I.; Keller, G.; Li, Z.-A.; Geller, M.; Spasova, M.; Prost, W.; Tegude, F.-J. N-GaAs/InGaP/p-GaAs Core-Multishell Nanowire Diodes for Efficient Light-to-Current Conversion. *Adv. Funct. Mater.* **2012**, *22* (5), 929–936.

(66) Huang, N.; Lin, C.; Povinelli, M. L. Limiting Efficiencies of Tandem Solar Cells Consisting of III-V Nanowire Arrays on Silicon. *J. Appl. Phys.* **2012**, *112*, 064321.

(67) Tian, B.; Zheng, X.; Kempa, T. J.; Fang, Y.; Yu, N.; Yu, G.; Huang, J.; Lieber, C. M. Coaxial Silicon Nanowires as Solar Cells and Nanoelectronic Power Sources. *Nature* **2007**, *449*, 885–890.

(68) Zhang, Y.; Wang, L. W.; Mascarenhas, A. “Quantum Coaxial Cables” for Solar Energy Harvesting. *Nano Lett.* **2007**, *7* (5), 1264–1269.

(69) Garnett, E. C.; Yang, P. Silicon Nanowire Radial p - n Junction Solar Cells. *J. Am. Chem. Soc.* **2008**, *130*, 9224–9225.

(70) Czaban, J. A.; Thompson, D. A.; LaPierre, R. R. GaAs Core- Shell Nanowires for Photovoltaic Applications. *Nano Lett.* **2008**, *9* (1), 148–154.

(71) Wei, W.; Bao, X.; Soci, C.; Ding, Y.; Wang, Z.; Wang, D. Direct Heteroepitaxy of Vertical InAs Nanowire Array on Si Substrates for Broadband Photovoltaics and Photodetection. *Nano Lett.* **2009**, *9* (8), 2926–2934.

(72) Goto, H.; Nosaki, K.; Tomioka, K.; Hara, S.; Hiruma, K.; Motohisa, J.; Fukui, T. Growth of Core–Shell InP Nanowires for Photovoltaic Application by Selective-Area Metal Organic Vapor Phase Epitaxy. *Appl. Phys. Express* **2009**, *2*, 035004.

(73) Lin, C.; Povinelli, M. L. The Effect of Plasmonic Particles on Solar Absorption in Vertically Aligned Silicon Nanowire Arrays. *Appl. Phys. Lett.* **2010**, *97* (7), 071110.

(74) Shin, J. C.; Kim, K. H.; Yu, K. J.; Hu, H.; Yin, L.; Ning, C.; Rogers, J. A.; Zuo, J.; Li, X. InxGa1-xAs Nanowires on Silicon: One-Dimensional Heterogeneous Epitaxy, Bandgap Engineering, and Photovoltaics. *Nano Lett.* **2011**, *11* (11), 4831–4838.

(75) Tomioka, K.; Tanaka, T.; Hara, S.; Hiruma, K.; Fukui, T. III – V Nanowires on Si Substrate : Selective-Area Growth and Device Applications. *IEEE J. Sel. Top. Quantum Electron.* **2011**, *17* (4), 1112–1129.

(76) Tang, J.; Huo, Z.; Brittman, S.; Gao, H.; Yang, P. Solution-Processed Core – Shell Nanowires for Efficient Photovoltaic Cells. *Nat. Nanotechnol.* **2011**, *6* (9), 568–572.

(77) Lapierre, R. R. Numerical Model of Current-Voltage Characteristics and Efficiency of GaAs Nanowire Solar Cells. *J. Appl. Phys.* **2011**, *109* (3).

(78) Mariani, G.; Wong, P. S.; Katzenmeyer, A. M.; Léonard, F.; Shapiro, J.; Huffaker, D. L. Patterned Radial GaAs Nanopillar Solar Cells. *Nano Lett.* **2011**, *11* (6), 2490–2494.

(79) Huang, N.; Lin, C.; Povinelli, M. L. Broadband Absorption of Semiconductor Nanowire Arrays for Photovoltaic Applications. *J. Opt.* **2012**, *14* (2), 024004.

(80) Kempa, T. J.; Cahoon, J. F.; Kim, S.; Day, R. W.; Bell, D. C.; Park, H.; Lieber, C. M. Coaxial Multishell Nanowires with High-Quality Electronic Interfaces and Tunable Optical Cavities for Ultrathin Photovoltaics. *PNAS* **2012**, *109* (5), 1407–1412.

(81) Heurlin, M.; Lindgren, D.; Deppert, K.; Samuelson, L.; Magnusson, M. H.; Ek, M. L.; Wallenberg, R. Continuous Gas-Phase Synthesis of Nanowires with Tunable Properties. *Nature* **2012**, *492* (7427), 90–94.

(82) Mariani, G.; Zhou, Z.; Scofield, A.; Huffaker, D. L. Direct-Bandgap Epitaxial Core-Multishell Nanopillar Photovoltaics Featuring Subwavelength Optical Concentrators. *Nano Lett.* **2013**, *13* (4), 1632–1637.

(83) Hu, S.; Chi, C.; Fountaine, K. T.; Yao, M.; Atwater, H. A.; Dapkus, P. D.; Lewis, S. Optical, Electrical, and Solar Energy-Conversion Properties of Gallium Arsenide Nanowire-Array Photoanodes. *Energy Environ. Sci.* **2013**, *6*, 1879–1890.

(84) Wallentin, J.; Anttu, N.; Asoli, D.; Huffman, M.; Åberg, I.; Magnusson, M. H.; Siefer, G.; Fuss-Kailuweit, P.; Dimroth, F.; Witzigmann, B.; et al. InP Nanowire Array Solar Cells Achieving 13.8% Efficiency by Exceeding the Ray Optics Limit. *Science (80-.).* **2013**, *339* (6123), 1057–1060.

(85) Holm, J. V.; Jørgensen, H. I.; Krogstrup, P.; Nygård, J.; Liu, H.; Aagesen, M. Surface-Passivated GaAsP Single-Nanowire Solar Cells Exceeding 10% Efficiency Grown on Silicon. *Nat. Commun.* **2013**, *4*, 1498.

(86) Cui, Y.; Wang, J.; Plissard, S. R.; Cavalli, A.; Vu, T. T. T.; van Veldhoven, R. P. J.; Gao, L.; Trainor, M.; Verheijen, M. A.; Haverkort, J. E. M.; et al. Efficiency Enhancement of InP Nanowire Solar Cells by Surface Cleaning. *Nano Lett.* **2013**, *13* (9), 4113–4117.

(87) Nakai, E.; Chen, M.; Yoshimura, M.; Tomioka, K.; Fukui, T. InGaAs Axial-Junction Nanowire-Array Solar Cells. *Jpn. J. Appl. Phys.* **2015**, *54*, 015201.

(88) Anttu, N. Shockley − Queisser Detailed Balance Efficiency Limit for Nanowire Solar Cells. *ACS Photonics* **2015**, *2* (3), 446–453.

(89) Åberg, I.; Vescovi, G.; Asoli, D.; Naseem, U.; Gilboy, J. P.; Sundvall, C.; Dahlgren, A.; Svensson, K. E.; Anttu, N.; Björk, M. T.; et al. A GaAs Nanowire Array Solar Cell with 15 . 3 % Efficiency at 1 Sun. *IEEE J. Photovoltaics* **2015**, *6* (1), 185–190.

(90) Boulanger, J. P.; Chia, A. C. E.; Wood, B.; Yazdi, S.; Kasama, T.; Aagesen, M.; LaPierre, R. R. Characterization of a Ga-Assisted GaAs Nanowire Array Solar Cell on Si Substrate. *IEEE J. Photovoltaics* **2016**, *6* (3), 661–667.

(91) Dam, D. Van; Hoof, N. J. J. Van; Cui, Y.; Veldhoven, P. J. Van; Bakkers, E. P. A. M.; Go, J.; Haverkort, J. E. M. High-Efficiency Nanowire Solar Cells with Omnidirectionally

Enhanced Absorption Due to Self-Aligned Indium − Tin − Oxide Mie Scatterers. *ACS Nano* **2016**, *10*, 11414–11419.

(92) Mariani, G.; Scofield, A. C.; Hung, C.-H.; Huffaker, D. L. GaAs Nanopillar-Array Solar Cells Employing in Situ Surface Passivation. *Nat. Commun.* **2013**, *4*, 1497.

(93) Krogstrup, P.; Jørgensen, H. I.; Heiss, M.; Demichel, O.; Holm, J. V.; Aagesen, M.; Nygard, J.; Fontcuberta I Morral, A. Single-Nanowire Solar Cells beyond the Shockley-Queisser Limit. *Nat. Photonics* **2013**, *7* (4), 306–310.

(94) Henry, C. H. Limiting Efficiencies of Ideal Single and Multiple Energy Gap Terrestrial Solar Cells. *J. Appl. Phys.* **1980**, *51* (8), 4494.

(95) Jackson, J. B.; Kapoor, D.; Jun, S.; Miller, M. S.; Jackson, J. B.; Kapoor, D.; Miller, M. S. Integrated Silicon Nanowire Diodes and the Effects of Gold Doping from the Growth Catalyst. *J. Appl. Phys.* **2007**, *102*, 054310.

(96) Schmidt, V.; Wittemann, J. V.; Senz, S.; Gósele, U. Silicon Nanowires: A Review on Aspects of Their Growth and Their Electrical Properties. *Adv. Mater.* **2009**, *21* (25–26), 2681–2702.

(97) Bar-Sadan, M.; Barthel, J.; Shtrikman, H.; Houben, L. Direct Imaging of Single Au Atoms within GaAs Nanowires - Supporting Information. *Nano Lett.* **2012**, *12*, 2352–2356.

(98) Tambe, M. J.; Ren, S.; Gradečak, S. Effects of Gold Diffusion on N-Type Doping of GaAs Nanowires. *Nano Lett.* **2010**, *10* (11), 4584–4589.

(99) Breuer, S.; Pfüller, C.; Flissikowski, T.; Brandt, O.; Grahn, H. T.; Geelhaar, L.; Riechert, H. Suitability of Au-and Self-Assisted GaAs Nanowires for Optoelectronic Applications. *Nano Lett.* **2011**, *11* (3), 1276–1279.

(100) Wen, L.; Zhao, Z.; Li, X.; Shen, Y.; Guo, H.; Wang, Y. Theoretical Analysis and Modeling of Light Trapping in High Efficicency GaAs Nanowire Array Solar Cells. *Appl. Phys. Lett.* **2011**, *99*, 143116.

(101) Wu, P. M.; Anttu, N.; Xu, H. Q.; Samuelson, L.; Pistol, M. Colorful InAs Nanowire Arrays: From Strong to Weak Absorption. *Nano Lett.* **2012**, *12*, 1990–1995.

(102) Fontcuberta i Morral, A.; Colombo, C.; Abstreiter, G.; Arbiol, J.; Morante, J. R. Nucleation Mechanism of Gallium-Assisted Molecular Beam Epitaxy Growth of Gallium Arsenide Nanowires. *Appl. Phys. Lett.* **2008**, *92* (6), 063112.

(103) Dubois, S.; Palais, O.; Pasquinelli, M.; Martinuzzi, S.; Jaussaud, C. Influence of Substitutional Metallic Impurities on the Performances of P-Type Crystalline Silicon Solar Cells: The Case of Gold. *J. Appl. Phys.* **2006**, *100*, 123502.

(104) Kempa, T. J.; Tian, B.; Kim, D. R.; Jinsong, H.; Xiaolin, Z.; Lieber, C. M. Single and Tandem Axial P-i-n Nanowire Photovoltaic Devices. *Nano Lett.* **2008**, *8* (10), 3456–3460.

(105) Heurlin, M.; Wickert, P.; Fält, S.; Borgström, M. T.; Deppert, K.; Samuelson, L.; Magnusson, M. H. Axial InP Nanowire Tandem Junction Grown on a Silicon Substrate. *Nano Lett.* **2011**, *11* (5), 2028–2031.

(106) Lapierre, R. R. Theoretical Conversion Efficiency of a Two-Junction III-V Nanowire on Si Solar Cell. *J. Appl. Phys.* **2011**, *110* (1), 014310.

(107) Demichel, O.; Heiss, M.; Bleuse, J.; Mariette, H.; Fontcuberta i Morral, A. Impact of Surfaces on the Optical Properties of GaAs Nanowires. *Appl. Phys. Lett.* **2010**, *97* (20), 201907.

(108) Hu, Y.; Li, M.; He, J. J.; LaPierre, R. R. Current Matching and Efficiency Optimization in a Two-Junction Nanowire-on-Silicon Solar Cell. *Nanotechnology* **2013**, *24* (6), 065402.

(109) Bu, S.; Li, X.; Wen, L.; Zeng, X.; Zhao, Y.; Wang, W.; Wang, Y. Optical and Electrical Simulations of Two-Junction III-V Nanowires on Si Solar Cell. *Appl. Phys. Lett.* **2013**, *102* (3), 031106.

(110) Wang, Y.; Zhang, Y.; Zhang, D.; He, S.; Li, X. Design High-Efficiency III–V Nanowire/Si Two-Junction Solar Cell. *Nanoscale Res. Lett.* **2015**, *10* (1), 269.

(111) Yao, M.; Cong, S.; Arab, S.; Huang, N.; Povinelli, M. L.; Cronin, S. B.; Dapkus, P. D.; Zhou, C. Tandem Solar Cells Using GaAs Nanowires on Si: Design, Fabrication, and Observation of Voltage Addition. *Nano Lett.* **2015**, *15* (11), 7217–7224.

(112) Virkar, A. Lecture notes, University of Utah

https://pubweb.eng.utah.edu/~lzang/images/lecture-30.pdf.

(113) Ibach, H.; Lueth, H. *Solid State Physics*; Springer Verlag, 2003.

(114) Hermann, M. H.; H. Sitter. *Molecular Beam Epitaxy - Fundamentals and Current Status*, Series in.; Springer Verlag, 1996.

(115) Depertment of Physiscs, University of Warwick

https://warwick.ac.uk/fac/sci/physics/current/postgraduate/regs/mpagswarwick/ex5/growth/pvd/.

(116) Klein, J. Epitaktische Heterostrukturen Aus Dotierten Manganaten, Universität zu Köln, 2001.

(117) Graduate School of Engineering, Tohoku University

http://www.material.tohoku.ac.jp/~kaimenb/B_RHEED.html.

(118) Rudolph, D.; Hertenberger, S.; Bolte, S.; Paosangthong, W.; Spirkoska, D.; Döblinger, M.; Bichler, M.; Finley, J. J.; Abstreiter, G.; Koblmüller, G. Direct Observation of a Noncatalytic Growth Regime for GaAs Nanowires. *Nano Lett.* **2011**, *11* (9), 3848–3854.

(119) Dai, X.; Olivier, A.; Wilhelm, C.; Dayeh, S. A.; Soci, C. Advanced III-V Nanowire Growth toward Large-Scale Integration. In *Semiconductor Nanowires: Materials, Synthesis, Characterization and Applications*; Elsevier Ltd, 2015; pp 71–124.

(120) Dursap, T. Crystal Phase, Ga Droplet Catalyst and Patterning Studies of Self-Catalyzed GaAs Nanowires, Master 2 Report, Ecole Centrale de Lyon, 2018.

(121) Dursap, T.; Vettori, M.; Botella, C.; Regreny, P.; Danescu, A.; Bugnet, M.; Patriarche, G.; Gendry, M.; Penuelas, J. Crystal Phase Engineering of Self-Catalyzed GaAs

Nanowires: A RHEED Study (Article in Progress of Publication). **2019**.

(122) Dick, K. A.; Caroff, P. Metal-Seeded Growth of III–V Semiconductor Nanowires: Towards Gold-Free Synthesis. *Nanoscale* **2014**, *6* (6), 3006.

(123) Wagner, R. S.; Ellis, W. C. Vapor-Liquid-Solid Mechanism of Single Crystal Growth. *Appl. Phys. Lett.* **1964**, *4* (5), 89–90.

(124) Givargizov, E. I. Fundamental Aspects of VLS Growth. *Vap. Growth Ep.* **1975**, *31*, 20–30.

(125) Dubrovskii, V. G.; Sibirev, N. V. Growth Rate of a Crystal Facet of Arbitrary Size and Growth Kinetics of Vertical Nanowires. *Phys. Rev. E - Stat. Physics, Plasmas, Fluids, Relat. Interdiscip. Top.* **2004**, *70* (3), 031604.

(126) Dubrovskii, V. G.; Cirlin, G. E.; Soshnikov, I. P.; Tonkikh, A. A.; Sibirev, N. V.; Samsonenko, Y. B.; Ustinov, V. M. Diffusion-Induced Growth of GaAs Nanowhiskers during Molecular Beam Epitaxy: Theory and Experiment. *Phys. Rev. B - Condens. Matter Mater. Phys.* **2005**, *71* (20), 205325.

(127) Dubrovskiĭ, V. G.; Sibirev, N. V.; Suris, R. A.; Cirlin, G. É.; Ustinov, V. M.; Tchernysheva, M.; Harmand, J. C. The Role of Surface Diffusion of Adatoms in the Formation of Nanowire Crystals. *Semiconductors* **2006**, *40* (9), 1075–1082.

(128) Glas, F.; Harmand, J. C. Calculation of the Temperature Profile in Nanowhiskers Growing on a Hot Substrate. *Phys. Rev. B - Condens. Matter Mater. Phys.* **2006**, *73* (15), 155320.

(129) Dubrovskii, V. G.; Sibirev, N. V. General Form of the Dependences of Nanowire Growth Rate on the Nanowire Radius. *J. Cryst. Growth* **2007**, *304* (2), 504–513.

(130) Glas, F.; Harmand, J.-C.; Patriarche, G. Why Does Wurtzite Form in Nanowires of III-V Zinc Blende Semiconductors? *Phys. Rev. Lett.* **2007**, *99* (14), 146101.

(131) Dubrovskii, V. G.; Sibirev, N. V. Growth Thermodynamics of Nanowires and Its Application to Polytypism of Zinc Blende III-V Nanowires. *Phys. Rev. B - Condens. Matter Mater. Phys.* **2008**, *77* (3), 035414.

(132) Dubrovskii, V. G.; Sibirev, N. V.; Harmand, J. C.; Glas, F. Growth Kinetics and Crystal Structure of Semiconductor Nanowires. *Phys. Rev. B* **2008**, *78* (23), 235301.

(133) Cirlin, G. E.; Dubrovskii, V. G.; Samsonenko, Y. B.; Bouravleuv, A. D.; Durose, K.; Proskuryakov, Y. Y.; Mendes, B.; Bowen, L.; Kaliteevski, M. A.; Abram, R. A.; et al. Self-Catalyzed, Pure Zincblende GaAs Nanowires Grown on Si(111) by Molecular Beam Epitaxy. *Phys. Rev. B* **2010**, *82* (3), 035302.

(134) Krogstrup, P.; Curiotto, S.; Johnson, E.; Aagesen, M.; Nygård, J.; Chatain, D. Impact of the Liquid Phase Shape on the Structure of III-V Nanowires. *Phys. Rev. Lett.* **2011**, *106* (12), 125505.

(135) Yeh, C.; Lu, Z. W.; Froyen, S.; Zunger, A. Zinc-Blende - Wurtzite Polytypism in Semiconductors. *Phys. Rev. B* **1992**, *46* (16), 10086–10097.

(136) Krogstrup, P.; Jørgensen, H. I.; Johnson, E.; Madsen, M. H.; Sørensen, C. B.;

Fontcuberta i Morral, A.; Aagesen, M.; Nygård, J.; Glas, F. Advances in the Theory of III–V Nanowire Growth Dynamics. *J. Phys. D. Appl. Phys.* **2013**, *46* (31), 313001.

(137) Yu, X.; Wang, H.; Lu, J.; Zhao, J.; Misuraca, J.; Xiong, P.; Von Molnár, S. Evidence for Structural Phase Transitions Induced by the Triple Phase Line Shift in Self-Catalyzed GaAs Nanowires. *Nano Lett.* **2012**, *12* (10), 5436–5442.

(138) Jacobsson, D.; Panciera, F.; Tersoff, J.; Reuter, M. C.; Lehmann, S.; Hofmann, S.; Dick, K. A.; Ross, F. M. Interface Dynamics and Crystal Phase Switching in GaAs Nanowires. *Nature* **2016**, *531* (7594), 317–322.

(139) Kim, W.; Dubrovskii, V. G.; Vukajlovic-Plestina, J.; Tütüncüoglu, G.; Francaviglia, L.; Güniat, L.; Potts, H.; Friedl, M.; Leran, J.-B.; Fontcuberta i Morral, A. Bi-Stability of Contact Angle and Its Role in Achieving Quantum-Thin Self-Assisted GaAs Nanowires. *Nano Lett.* **2018**, *18*, 49–57.

(140) Colombo, C.; Spirkoska, D.; Frimmer, M.; Abstreiter, G.; Fontcuberta i Morral, A. Ga-Assisted Catalyst-Free Growth Mechanism of GaAs Nanowires by Molecular Beam Epitaxy. *Phys. Rev. B - Condens. Matter Mater. Phys.* **2008**, *77*, 155326.

(141) Plissard, S.; Dick, K. A.; Larrieu, G.; Godey, S.; Addad, A.; Wallart, X.; Caroff, P. Gold-Free Growth of GaAs Nanowires on Silicon: Arrays and Polytypism. *Nanotechnology* **2010**, *21* (38), 385602.

(142) Madsen, M.; Aagesen, M.; Krogstrup, P.; Sørensen, C.; Nygård, J. Influence of the Oxide Layer for Growth of Self-Assisted InAs Nanowires on Si(111). *Nanoscale Res. Lett.* **2011**, *6* (1), 516.

(143) Benali, A. Nanofils de Ga(Al)As Sur Silicium Pour Le Photovoltaïque de 3eme Génération : Simulation et Croissance Auto-Catalysée, Ecole Centrale de Lyon, 2017.

(144) Becdelievre, J. Etude Des Propriétés Électriques et Mécaniques de Nanofils de GaAs : Vers Une Modulation Du Transport Par Effet Piézoélectrique Ou Ferroélectrique, Ecole Centrale de Lyon, 2017.

(145) Guan, X. Growth of Semiconductor (Core) / Functional Oxide (Shell) Nanowires: Application to Photoelectrochemical Water Splitting, Ecole Centrale de Lyon, 2017.

(146) Tauchnitz, T.; Nurmamytov, T.; Hübner, R.; Engler, M.; Facsko, S.; Schneider, H.; Helm, M.; Dimakis, E. Decoupling the Two Roles of Ga Droplets in the Self-Catalyzed Growth of GaAs Nanowires on SiOx/Si(111) Substrates. *Cryst. Growth Des.* **2017**, *17* (10), 5276–5282.

(147) Matteini, F.; Tütüncüoglu, G.; Potts, H.; Jabeen, F.; Fontcuberta i Morral, A. Wetting of Ga on SiO x and Its Impact on GaAs Nanowire Growth. *Cryst. Growth Des.* **2015**, *15* (7), 3105–3109.

(148) Tchernycheva, M.; Travers, L.; Patriarche, G.; Glas, F.; Harmand, J. C.; Cirlin, G. E.; Dubrovskii, V. G. Au-Assisted Molecular Beam Epitaxy of InAs Nanowires: Growth and Theoretical Analysis. *J. Appl. Phys.* **2007**, *102* (9), 094313.

(149) Zhang, X.; Dubrovskii, V. G.; Sibirev, N. V; Cirlin, G. E.; Sartel, C.; Tchernycheva, M.; Harmand, J. C.; Glas, F. Growth of Inclined GaAs Nanowires by Molecular Beam

Epitaxy : Theory and Experiment. *Nanoscale Res. Lett.* **2010**, *5*, 1692–1697.

(150) Glas, F.; Ramdani, M. R.; Patriarche, G.; Harmand, J.-C. Predictive Modeling of Self-Catalyzed III-V Nanowire Growth. *Phys. Rev. B* **2013**, *88* (19), 195304.

(151) Foxon, C. T.; Novikov, S. V.; Hall, J. L.; Campion, R. P.; Cherns, D.; Griffiths, I.; Khongphetsak, S. A Complementary Geometric Model for the Growth of GaN Nanocolumns Prepared by Plasma-Assisted Molecular Beam Epitaxy. *J. Cryst. Growth* **2009**, *311* (13), 3423–3427.

(152) Galopin, E.; Largeau, L.; Patriarche, G.; Travers, L.; Glas, F.; Harmand, J. C. Morphology of Self-Catalyzed GaN Nanowires and Chronology of Their Formation by Molecular Beam Epitaxy. *Nanotechnology* **2011**, *22*, 245606.

(153) Ramdani, M. R.; Harmand, J. C.; Glas, F.; Patriarche, G.; Travers, L. Arsenic Pathways in Self-Catalyzed Growth of GaAs Nanowires. *Cryst. Growth Des.* **2013**, *13* (1), 91–96.

(154) Rudolph, D.; Hertenberger, S.; Bolte, S.; Paosangthong, W.; Spirkoska, D.; Döblinger, M.; Bichler, M.; Finley, J. J.; Abstreiter, G.; Koblmüller, G. Direct Observation of a Noncatalytic Growth Regime for GaAs Nanowires. *Nano Lett.* **2011**, *11* (9), 3848–3854.

(155) Glas, F. Vapor Fluxes on the Apical Droplet during Nanowire Growth by Molecular Beam Epitaxy. *Phys. Status Solidi Basic Res.* **2010**, *247* (2), 254–258.

(156) Shibata, M.; Stoyanov, S. S.; Ichikawa, M. Selective Growth of Nanometer-Scale Ga Dots on Si(111) Surface Windows Formed in an Ultrathin SiO2 Film. *Phys. Rev. B* **1999**, *59* (15), 289–295.

(157) Lee, S. C.; Brueck, S. R. J. Scaling of the Surface Migration Length in Nanoscale Patterned Growth. *Appl. Phys. Lett.* **2009**, *94* (15), 153110.

(158) Schroth, P.; Jakob, J.; Feigl, L.; Mostafavi Kashani, S. M.; Vogel, J.; Strempfer, J.; Keller, T. F.; Pietsch, U.; Baumbach, T. Radial Growth of Self-Catalyzed GaAs Nanowires and the Evolution of the Liquid Ga-Droplet Studied by Time-Resolved in Situ X-Ray Diffraction. *Nano Lett.* **2018**, *18* (1), 101–108.

(159) Dubrovskii, V. G.; Xu, T.; Álvarez, A. D.; Plissard, S. R.; Caroff, P.; Glas, F.; Grandidier, B. Self-Equilibration of the Diameter of Ga-Catalyzed GaAs Nanowires. *Nano Lett.* **2015**, *15* (8), 5580–5584.

(160) Oehler, F.; Cattoni, A.; Scaccabarozzi, A.; Patriarche, G.; Glas, F.; Harmand, J. C. Measuring and Modeling the Growth Dynamics of Self-Catalyzed GaP Nanowire Arrays. *Nano Lett.* **2018**, *18* (2), 701–708.

(161) Tateno, K.; Gotoh, H.; Watanabe, Y. Multi-Quantum Structures of GaAs/AlGaAs Free-Standing Nanowires. *Japanese J. Appl. Physics, Part 1 Regul. Pap. Short Notes Rev. Pap.* **2006**, *45* (4 B), 3568–3572.

(162) Ishikawa, K.; Yamamoto, N.; Tateno, K.; Watanabe, Y. Characterization of Individual GaAs/AlGaAs Self-Standing Nanowires by Cathodoluminescence Technique Using Transmission Electron Microscope. *Japanese J. Appl. Physics, Part 1 Regul. Pap. Short Notes Rev. Pap.* **2008**, *47* (8 PART 1), 6596–6600.

(163) Hayashida, A.; Sato, T.; Hara, S.; Motohisa, J.; Hiruma, K.; Fukui, T. Fabrication and

Characterization of GaAs Quantum Well Buried in AlGaAs/GaAs Heterostructure Nanowires. *J. Cryst. Growth* **2010**, *312* (24), 3592–3598.

(164) Priante, G.; Glas, F.; Patriarche, G.; Pantzas, K.; Oehler, F.; Harmand, J.-C. Sharpening the Interfaces of Axial Heterostructures in Self-Catalyzed AlGaAs Nanowires: Experiment and Theory. *Nano Lett.* **2016**, *16*, 1917–1924.

(165) Wu, Z. H.; Sun, M.; Mei, X. Y.; Ruda, H. E. Growth and Photoluminescence Characteristics of AlGaAs Nanowires. *Appl. Phys. Lett.* **2004**, *85* (4), 657–659.

(166) Chen, C.; Shehata, S.; Fradin, C.; LaPierre, R.; Couteau, C.; Weihs, G. Self-Directed Growth of AlGaAs Core-Shell Nanowires for Visible Light Applications. *Nano Lett.* **2007**, *7* (9), 2584–2589.

(167) Chen, C.; Braidy, N.; Couteau, C.; Fradin, C.; Weihs, G.; LaPierre, R. Multiple Quantum Well AlGaAs Nanowires. *Nano Lett.* **2008**, *8* (2), 495–499.

(168) Barettin, D.; Platonov, A. V; Pecchia, A.; Kats, V. N.; Cirlin, G. E.; Soshnikov, I. P.; Bouravleuv, A. D.; Besombes, L.; Mariette, H.; Maur, M. A. der; et al. Model of a GaAs Quantum Dot Embedded in a Polymorph AlGaAs Nanowire. *Ieee J. Sel. Top. Quantum Electron.* **2013**, *19* (5), 1901209.

(169) Wicks, C. E.; Block, F. E. Thermodynamic Properties of 65 Elements - Their Oxides, Halides, Carbides, and Nitrides. Bureau of Mines, United States Government Printing Office: Washington 1963.

(170) Williams, R. S.; Wehner, P. S.; Apai, G.; Stöhr, J.; Shirley, D. A.; Kowalczyk, S. P. Angle- and Energy-Dependent Core-Level Photoelectron Energy Loss Studies in Al and In. *J. Electron Spectros. Relat. Phenomena* **1977**, *12* (4), 477–492.

(171) Tomioka, K.; Motohisa, J.; Hara, S.; Hiruma, K.; Fukui, T. GaAs/AlGaAs Core Multishell Nanowire-Based Light-Emitting Diodes on Si. *Nano Lett.* **2010**, *10* (5), 1639–1644.

(172) Gallo, E. M.; Chen, G.; Currie, M.; Mcguckin, T.; Prete, P.; Lovergine, N.; Nabet, B.; Spanier, J. E. Picosecond Response Times in GaAs / AlGaAs Core / Shell Nanowire-Based Photodetectors Picosecond Response Times in GaAs / AlGaAs Core / Shell Nanowire-Based Photodetectors. *Appl. Phys. Lett.* **2011**, *98*, 241113.

(173) Winnerl, J.; Treu, J.; Mayer, B.; Rudolph, D.; Schnell, J.; Morko, S.; Finley, J. J.; Bracher, G.; Abstreiter, G.; Koblmu, G. Lasing from Individual GaAs-AlGaAs Core-Shell Nanowires up to Room Temperature. *Nat. Commun.* **2013**, *4*, 2931.

(174) Saxena, D.; Mokkapati, S.; Parkinson, P.; Jiang, N.; Gao, Q.; Tan, H. H. Optically Pumped Room-Temperature GaAs Nanowire Lasers. *Nat. Photonics* **2013**, *7*, 963.

(175) Dai, X.; Zhang, S.; Wang, Z.; Adamo, G.; Liu, H.; Huang, Y.; Couteau, C.; Soci, C. GaAs/AlGaAs Nanowire Photodetector. *Nano Lett.* **2014**, *14* (5), 2688–2693.

(176) Ho, J.; Tatebayashi, J.; Sergent, S.; Fong, C. F.; Iwamoto, S.; Arakawa, Y. Low-Threshold near-Infrared GaAs − AlGaAs Core − Shell Nanowire Plasmon Laser. *ACS Photonics* **2015**, *2* (1), 165–171.

(177) Piazza, V.; Vettori, M.; Ahmed, A.; Chauvin, N.; Patriarche, G.; Fave, A.; Gendry, M.; Tchernycheva, M. Nanoscale Investigation of Radial P-n Junction in Self-Catalyzed

GaAs Nanowires Grown on Si (111). *Nanoscale* **2018**, *10* (43), 20207–20217.

(178) Vettori, M.; Piazza, V.; Cattoni, A.; Scaccabarozzi, A.; Patriarche, G.; Regreny, P.; Chauvin, N.; Botella, C.; Grenet, G.; Penuelas, J.; et al. Growth Optimization and Characterization of Regular Arrays of GaAs/AlGaAs Core/Shell Nanowires for Tandem Solar Cells on Silicon. *Nanotechnology* **2019**, *30*, 084005.

(179) Hilse, M.; Ramsteiner, M.; Breuer, S.; Geelhaar, L.; Riechert, H. Incorporation of the Dopants Si and Be into GaAs Nanowires. *Appl. Phys. Lett.* **2010**, *96* (19), 10–12.

(180) Zhang, Y.; Sun, Z.; Sanchez, A. M.; Ramsteiner, M.; Aagesen, M.; Wu, J.; Kim, D.; Jurczak, P.; Huo, S.; Lauhon, L. J.; et al. Doping of Self-Catalyzed Nanowires under the Influence of Droplets. *Nano Lett.* **2018**, *18*, 81–87.

(181) Dimakis, E.; Ramsteiner, M.; Tahraoui, A.; Riechert, H.; Geelhaar, L. Shell-Doping of GaAs Nanowires with Si for n-Type Conductivity. *Nano Res.* **2012**, *5* (11), 796–804.

(182) Titova, L. V; Hoang, T. B.; Jackson, H. E.; Smith, L. M.; Yarrison-Rice, J. M.; Kim, Y.; Joyce, H. J.; Tan, H.; Jagadish, C. Temperature Dependence of Photoluminescence from Single Core-Shell GaAs – AlGaAs Nanowires. *Appl. Phys. Lett.* **2006**, *89* (2006), 173126.

(183) Perera, S.; Fickenscher, M. A.; Jackson, H. E.; Smith, L. M.; Yarrison-rice, J. M.; Joyce, H. J.; Gao, Q.; Tan, H. H.; Jagadish, C.; Zhang, X.; et al. Nearly Intrinsic Exciton Lifetimes in Single Twin-Free GaAs / AlGaAs Core-Shell Nanowire Heterostructures. *Appl. Phys. Lett.* **2008**, *93*, 053110.

(184) Krogstrup, P.; Popovitz-Biro, R.; Johnson, E.; Madsen, M. H.; Nygård, J.; Shtrikman, H. Structural Phase Control in Self-Catalyzed Growth of GaAs Nanowires on Silicon (111). *Nano Lett.* **2010**, *10* (11), 4475–4482.

(185) Heiss, M.; Conesa-Boj, S.; Ren, J.; Tseng, H.-H.; Gali, A.; Rudolph, A.; Uccelli, E.; Peiró, F.; Morante, J. R.; Schuh, D.; et al. Direct Correlation of Crystal Structure and Optical Properties in Wurtzite/Zinc-Blende GaAs Nanowire Heterostructures. *Phys. Rev. B* **2011**, *83* (4), 045303.

(186) Ben Sedrine, N.; Ribeiro-Andrade, R.; Gustafsson, A.; Soares, M. R.; Bourgard, J.; Teixeira, J. P.; Salomé, P. M. P.; Correia, M. R.; Moreira, M. V. B.; De Oliveira, A. G.; et al. Fluctuating Potentials in GaAs:Si Nanowires: Critical Reduction of the Influence of Polytypism on the Electronic Structure. *Nanoscale* **2018**, *10* (8), 3697–3708.

(187) Dhaka, V.; Oksanen, J.; Jiang, H.; Haggren, T.; Nykänen, A.; Sanatinia, R.; Kakko, J. P.; Huhtio, T.; Mattila, M.; Ruokolainen, J.; et al. Aluminum-Induced Photoluminescence Red Shifts in Core-Shell GaAs/AlxGa1-XAs Nanowires. *Nano Lett.* **2013**, *13* (8), 3581–3588.

(188) Fontana, Y.; Corfdir, P.; Van Hattem, B.; Russo-Averchi, E.; Heiss, M.; Sonderegger, S.; Magen, C.; Arbiol, J.; Phillips, R. T.; Fontcuberta i Morral, A. Exciton Footprint of Self-Assembled AlGaAs Quantum Dots in Core-Shell Nanowires. *Phys. Rev. B - Condens. Matter Mater. Phys.* **2014**, *90* (7), 075307.

(189) Francaviglia, L.; Fontana, Y.; Conesa-Boj, S.; Tütüncüoglu, G.; Duchêne, L.; Tanasescu, M. B.; Matteini, F.; Fontcuberta i Morral, A. Quantum Dots in the GaAs/AlxGa1-XAs

Core-Shell Nanowires: Statistical Occurrence as a Function of the Shell Thickness. *Appl. Phys. Lett.* **2015**, *107* (3), 033106.

(190) Loitsch, B.; Jeon, N.; Döblinger, M.; Winnerl, J.; Parzinger, E.; Matich, S.; Wurstbauer, U.; Riedl, H.; Abstreiter, G.; Finley, J. J.; et al. Suppression of Alloy Fluctuations in GaAs-AlGaAs Core-Shell Nanowires. *Appl. Phys. Lett.* **2016**, *109* (9), 93105.

(191) Vainorius, N.; Jacobsson, D.; Lehmann, S.; Gustafsson, A.; Dick, K. A.; Samuelson, L.; Pistol, M. E. Observation of Type-II Recombination in Single Wurtzite/Zinc-Blende GaAs Heterojunction Nanowires. *Phys. Rev. B - Condens. Matter Mater. Phys.* **2014**, *89* (16), 1–8.

(192) Spirkoska, D.; Efros, A. L.; Lambrecht, W. R. L.; Cheiwchanchamnangij, T.; Fontcuberta i Morral, A.; Abstreiter, G. Valence Band Structure of Polytypic Zinc-Blende/Wurtzite GaAs Nanowires Probed by Polarization-Dependent Photoluminescence. *Phys. Rev. B - Condens. Matter Mater. Phys.* **2012**, *85* (4), 045309.

(193) Jahn, U.; Lähnemann, J.; Pfüller, C.; Brandt, O.; Breuer, S.; Jenichen, B.; Ramsteiner, M.; Geelhaar, L.; Riechert, H. Luminescence of GaAs Nanowires Consisting of Wurtzite and Zinc-Blende Segments. *Phys. Rev. B - Condens. Matter Mater. Phys.* **2012**, *85* (4), 045323.

(194) Bolinsson, J.; Ek, M.; Trägårdh, J.; Mergenthaler, K.; Jacobsson, D.; Pistol, M. E.; Samuelson, L.; Gustafsson, A. GaAs/AlGaAs Heterostructure Nanowires Studied by Cathodoluminescence. *Nano Res.* **2014**, *7* (4), 473–490.

(195) Lavenus, P.; Messanvi, A.; Rigutti, L.; De Luna Bugallo, A.; Zhang, H.; Bayle, F.; Julien, F. H.; Eymery, J.; Durand, C.; Tchernycheva, M. Experimental and Theoretical Analysis of Transport Properties of Core-Shell Wire Light Emitting Diodes Probed by Electron Beam Induced Current Microscopy. *Nanotechnology* **2014**, *25* (25), 255201.

(196) Cheng, C. W.; Shiu, K. T.; Li, N.; Han, S. J.; Shi, L.; Sadana, D. K. Epitaxial Lift-off Process for Gallium Arsenide Substrate Reuse and Flexible Electronics. *Nat. Commun.* **2013**, *4*, 1577.

(197) Luque, A.; Hegedus, S. S. *Handbook of Photovoltaic Science and Engineering*; Wiley: Chichester, 2003.

(198) Weihofen, R.; Weiser, G.; Starck, C.; Simes, R. J. Energy Gaps in Strained In1-XGaxAs/In1-YGayAszP1-z Quantum Wells Grown on (001) InP. *Phys. Rev. B* **1995**, *51* (7), 4296–4305.

(199) Maryasin, V.; Bucci, D.; Rafhay, Q.; Panicco, F.; Michallon, J.; Kaminski-Cachopo, A. Technological Guidelines for the Design of Tandem III-V Nanowire on Si Solar Cells from Opto-Electrical Simulations. *Sol. Energy Mater. Sol. Cells* **2017**, *172* (July), 314–323.

(200) Michallon, J.; Bucci, D.; Morand, A.; Zanuccoli, M.; Consonni, V.; Kaminski-Cachopo, A. Light Trapping in ZnO Nanowire Arrays Covered with an Absorbing Shell for Solar Cells. *Opt. Express* **2014**, *22* (S4), A1174–A1189.

(201) Chia, A. C. E.; LaPierre, R. R. Electrostatic Model of Radial Pn Junction Nanowires. *J. Appl. Phys.* **2013**, *114*, 074317.

(202) Li, Z.; Wenas, Y. C.; Fu, L.; Mokkapati, S.; Tan, H. H.; Jagadish, C. Influence of Electrical Design on Core – Shell GaAs Nanowire Array Solar Cells. *IEEE J. Photovoltaics* **2015**, *5* (3), 854–864.

(203) Madiomanana, K.; Bahri, M.; Rodriguez, J. B.; Largeau, L.; Cerutti, L.; Mauguin, O.; Castellano, A.; Patriarche, G.; Tournié, E. Silicon Surface Preparation for III-V Molecular Beam Epitaxy. *J. Cryst. Growth* **2015**, *413*, 17–24.

(204) Bauer, B.; Rudolph, A.; Soda, M.; Fontcuberta i Morral, A.; Zweck, J.; Schuh, D.; Reiger, E. Position Controlled Self-Catalyzed Growth of GaAs Nanowires by Molecular Beam Epitaxy. *Nanotechnology* **2010**, *21* (43), 435601.

(205) Plissard, S.; Larrieu, G.; Wallart, X.; Caroff, P. High Yield of Self-Catalyzed GaAs Nanowire Arrays Grown on Silicon via Gallium Droplet Positioning. *Nanotechnology* **2011**, *22* (27), 275602.

(206) Zhang, Y.; Wu, J.; Aagesen, M.; Holm, J.; Hatch, S.; Tang, M.; Huo, S.; Liu, H. Self-Catalyzed Ternary Core-Shell GaAsP Nanowire Arrays Grown on Patterned Si Substrates by Molecular Beam Epitaxy. *Nano Lett.* **2014**, *14* (8), 4542–4547.

(207) Munshi, A. M.; Dheeraj, D. L.; Fauske, V. T.; Kim, D. C.; Huh, J.; Reinertsen, J. F.; Ahtapodov, L.; Lee, K. D.; Heidari, B.; van Helvoort, A. T. J.; et al. Position-Controlled Uniform GaAs Nanowires on Silicon Using Nanoimprint Lithography. *Nano Lett.* **2014**, *14* (2), 960–966.

(208) Tomioka, K.; Fukui, T. Recent Progress in Integration of III–V Nanowire Transistors on Si Substrate by Selective-Area Growth. *J. Phys. D. Appl. Phys.* **2014**, *47* (39), 394001.

(209) Heiss, M.; Russo-Averchi, E.; Dalmau-Mallorquí, A.; Tütüncüoğlu, G.; Matteini, F.; Rüffer, D.; Conesa-Boj, S.; Demichel, O.; Alarcon-Lladó, E.; Fontcuberta i Morral, A. III-V Nanowire Arrays: Growth and Light Interaction. *Nanotechnology* **2014**, *25* (1), 014015.

(210) Russo-Averchi, E.; Vukajlovic Plestina, J.; Tütüncüoğlu, G.; Matteini, F.; Dalmau-Mallorquí, A.; De La Mata, M.; Rüffer, D.; Potts, H. A.; Arbiol, J.; Conesa-Boj, S.; et al. High Yield of GaAs Nanowire Arrays on Si Mediated by the Pinning and Contact Angle of Ga. *Nano Lett.* **2015**, *15* (5), 2869–2874.

(211) Vukajlovic-Plestina, J.; Kim, W.; Dubrovski, V. G.; Tütüncüoğlu, G.; Lagier, M.; Potts, H.; Friedl, M.; Fontcuberta i Morral, A. Engineering the Size Distributions of Ordered GaAs Nanowires on Silicon. *Nano Lett.* **2017**, *17* (7), 4101–4108.

(212) Tan, S. L.; Genuist, Y.; den Hertog, M. I.; Bellet-Amalric, E.; Mariette, H.; Pelekanos, N. T. Highly Uniform Zinc Blende GaAs Nanowires on Si (111) Using a Controlled Chemical Oxide Template. *Nanotechnology* **2017**, *28*, 255602.

(213) Küpers, H.; Tahraoui, A.; Lewis, R. B.; Rauwerdink, S.; Matalla, M.; Krüger, O.; Bastiman, F.; Riechert, H.; Geelhaar, L. Surface Preparation and Patterning by Nano Imprint Lithography for the Selective Area Growth of GaAs Nanowires on Si(111). *Semicond. Sci. Technol.* **2017**, *32* (111), 115003.

(214) Breuer, S. Molecular Beam Epitaxy of GaAs Nanowires and Their Suitability for Optoelectronic Applications, Humboldt-Universitaet zu Belin, 2011.

(215) Tomioka, K.; Motohisa, J.; Hara, S.; Fukui, T. Control of InAs Nanowire Growth Directions on Si. *Nano Lett.* **2008**, *8* (10), 3475–3480.

(216) ISP OPTICS. Si specifications

https://www.google.com/url?sa=t&rct=j&q=&esrc=s&source=web&cd=3&ved=2ahUKEwiszKiwp5PfAhULXRoKHaxBCSEQFjACegQICRAC&url=https%3A%2F%2Fwww.janis.com%2FLibraries%2FWindow_Transmissions%2FSilicon_Si_TransmissionCurveDataSheet.sflb.ashx&usg=AOvVaw0ELDawGnw40Gv1.

(217) AZO Materials. Physical parameters of silica

https://www.azom.com/properties.aspx?ArticleID=1114.

(218) Yamane, T.; Nagai, N.; Katayama, S. I.; Todoki, M. Measurement of Thermal Conductivity of Silicon Dioxide Thin Films Using a 3ω Method. *J. Appl. Phys.* **2002**, *91* (12), 9772–9776.

(219) Maycock, P. D. Thermal Conductivity of Silicon, Germanium, III-V Compounds and III-V Alloys. *Solid State Electron.* **1967**, *10* (3), 161–168.

(220) Nolan, M.; Perova, T.; Moore, R. A.; Gamble, H. S. Boron Diffusion from a Spin-on Source during Rapid Thermal Processing. *J. Non. Cryst. Solids* **1999**, *254*, 89–93.

(221) Fave, A.; Lelièvre, J. F.; Gallet, T.; Su, Q.; Lemiti, M. Fabrication of Si Tunnel Diodes for C-Si Based Tandem Solar Cells Using Proximity Rapid Thermal Diffusion. *Energy Procedia* **2017**, *124*, 577–583.

(222) Wu, H.; Ru, G.; Zhang, Y.; Jin, C.; Mizuno, B.; Jiang, Y.; Qu, X.; Li, B. Electrochemical Capacitance-Voltage Characterization of Plasma-Doped Ultra-Shallow Junctions. *Front. Electr. Electron. Eng. China* **2008**, *3* (1), 116–119.

(223) Yao, M.; Huang, N.; Cong, S.; Chi, C.; Seyedi, M. A.; Lin, Y.; Cao, Y.; Povinelli, M. L.; Dapkus, P. D.; Zhou, C. GaAs Nanowire Array Solar Cells with Axial P-i-n Junctions. *Nano Lett.* **2014**, *14* (6), 3293–3303.

(224) Patkar, M. P.; Chin, T. P.; Woodall, J. M.; Lundstrom, M. S.; Melloch, M. R. Very Low Resistance Nonalloyed Ohmic Contacts Using Lowtemperature Molecular Beam Epitaxy of GaAs. *Appl. Phys. Express* **1995**, *66*, 1412.

(225) Zhang, J.; Chia, A. C. E.; LaPierre, R. R. Low Resistance Indium Tin Oxide Contact to N-GaAs Nanowires. *Semicond. Sci. Technol.* **2014**, *29*, 054002.

Annex 1: Characterization techniques

1.1 Transmission Electron Microscopy

Transmission Electron Microscopy (TEM) is a powerful characterization technique capable of providing much information about morphology, crystal structure and composition of a sample. Based on the transmission of an electron beam through the specimen and on its diffraction, TEM can be described approximately as an electron scattering process which can result in constructive or destructive interference according to the Bragg law:

$$2d \sin \vartheta = n\lambda$$

Where ϑ is the angle of incidence, d the distance between reticular planes, λ the wavelength of the electron beam and n an integer number.

For the process to occur, the sample must be sufficiently thin. In the case of bulk materials, it is therefore necessary to reduce the thickness of the sample: this is a destructive step carried out firstly mechanically and then by chemical etching or ion bombardment. However, in the case of NWs there is no need for such a pre-treatment, their size being already small enough to allow the transmission of electrons. These arrive on the sample with an energy between 50 and 200 KeV, then originating the diffraction pattern. Since the final result of a TEM analysis depends on the number of electrons transmitted through the sample, the image obtained is presented in greyscale, in which the darker spots are originated by those elements of the specimen having higher atomic number.

TEM facilities are kept under UHV so as to permit the electron beam to reach the sample and include several parts and comparts, of which the main ones are the electron gun, a set of magnetic lenses and electric plates to control the electron beam and focus it on the specimen, a sample holder, a set of objective lenses to collect the diffracted electrons and another one of intermediate lenses to magnify the image and project them on a fluorescent screen. This one may consist either in a phosphorus screen or in a charge coupled device (CCD), connected to an image recording system (Figure 1). Depending on the objective lenses and slits adopted to collect the diffracted electrons, the instrument can be used to collect either structural images or diffraction pattern from a selected area.

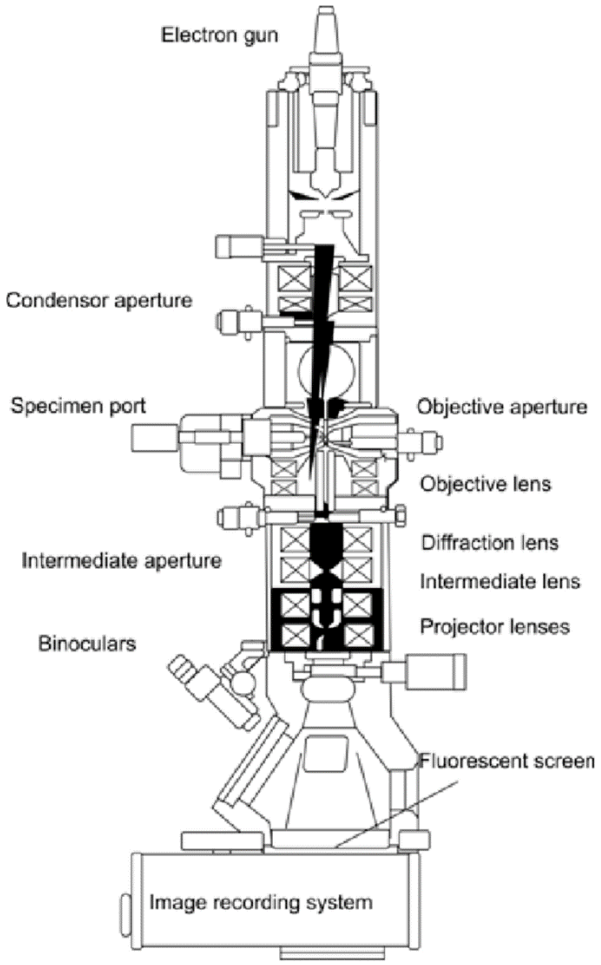

Figure 1. Schematics of a TEM instrument.[1]

The energy of the electrons is directly related with their wavelength, thus determining their ultimate resolution. Being the electron wavelengths much smaller than the atomic separations in the solid (e.g. ≈ 2.5 pm for electrons at 200 KeV), TEM can theoretically achieve sub-atomic scale resolution, but in reality this value is precluded by the spherical and chromatic aberrations of the magnetic lenses, so that the maximal resolution obtained by TEM is about 0.5 Å. However, the development of highly performing monochromators and correctors has led to the improvement of the technique into the so-called High Resolution Transmission Electron Microscopy (HR-TEM), which eventually permits to reach point resolution below 0.5 Å, allowing for direct imaging of the atomic structure of the specimens.

TEM can be employed also to investigate the composition of a sample by Energy-Dispersive X-ray spectroscopy (EDX). Bombarding the specimen with high-energy beam expels core electrons of atoms and originates holes which are filled by electrons from the shell. Because of the conservation of energy, electronic decays from high-energy states to lower ones occur with the emission of photons, whose energy equals the difference

between the two states. The energy of these photons is typically in the x-ray range and characteristic of the atomic number; therefore, collecting the photons as a function of their wavelength allows investigating the elemental composition of the specimen. Moreover, the fact of performing EDX analyses in TEM with finely focused electron beams (the diameter being lower than 10 nm) and the possibility of collecting data in scanning mode allow also to localise the elements detected in the sample, thus permitting to analyse not only the overall composition but also the elemental distribution in a specimen. For these reasons, EDX is a very powerful tool which can provide many relevant information, and concerning NWs this technique is particularly suitable for studying the configuration of radial or axial heterostructures.

All TEM/STEM and EDX analyses carried out in this thesis work were performed by G. Patriarche at C2N on a FEI Titan Themis 200 working at 200 kV and equipped with a geometrical aberration corrector on the probe (STEM mode). For the observations in STEM mode, the probe resolution is about 0.1 nm and the probe current 70 pA. The EDX analysis system consists of 4 detectors (to reach an angular solid angle of 0.8 steradian) and a Ceta 16M camera for the TEM images.

1.2 X-ray Photoelectron Spectroscopy

X-ray photoelectron spectroscopy (XPS) is an important technique for surface analysis based on collecting photoelectrons emitted from specimens irradiated by a beam of X-rays. A schematic representation of a XPS equipment is reported in Figure 2. The instrumental setup of XPS consists of an UHV chamber equipped with a focused monochromatic x-ray source, electron collection lenses, electron energy detector and analyser.

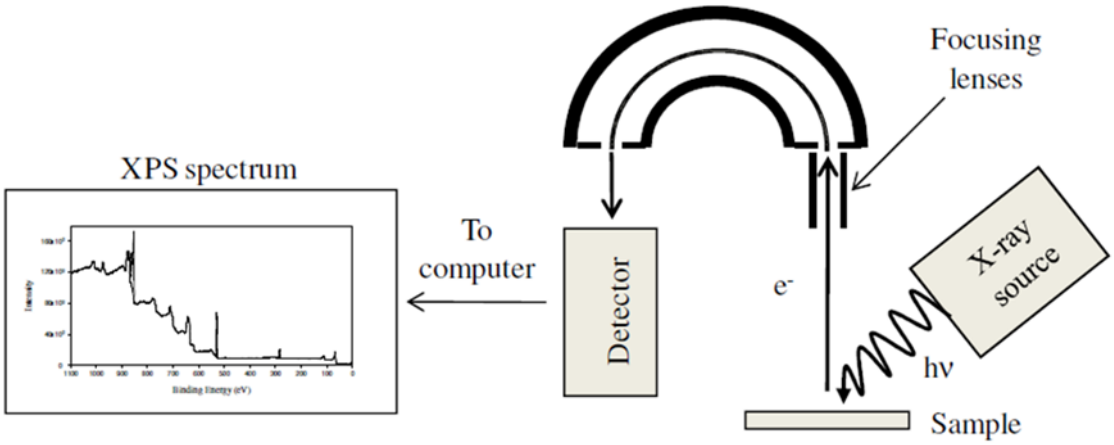

Figure 2. Schematics of a XPS setup.[2]

The whole process can be considered as an application of the photoelectric effect, so that if the material is exposed to radiation with a certain frequency there is a finite probability that photons are absorbed and electrons emitted from the sample. The kinetic energy of each of the emitted photoelectrons E_{kin} can be determined by using the equation:

$$E_{kin} = h\nu - E_b - \phi_s$$

where hν is the radiation energy (with h as the Planck constant and ν the frequency of the photons), E_b the electron binding energy and ϕ_s the work function dependent on both the spectrometer and the material.

Photoelectrons can be originated both from core levels and from the valence band. Knowing the kinetic energy of the emitted core level photoelectrons which is measured with the spectrometer, it is possible to identify the various chemical elements of a sample. The kinetic energy of photoelectrons being also influenced by the chemical environment of the emitting atoms, XPS measurements allow to obtain information on it. Chemical shifts can be quantitatively estimated taking into account factors such as local potentials, charge transfers to nearby atoms and electronic correlation effects.

Photoelectrons generated in solids in the usual range of energies (250-1500 eV) have mean free path around 0.8-1.5 nm before undergoing inelastic scattering and losing all information related to their kinetic energy (Figure 3). Therefore, only those electrons generated in the first atomic layers can be collected by the instrument, and this makes XPS an extremely suitable technique for surface analysis.

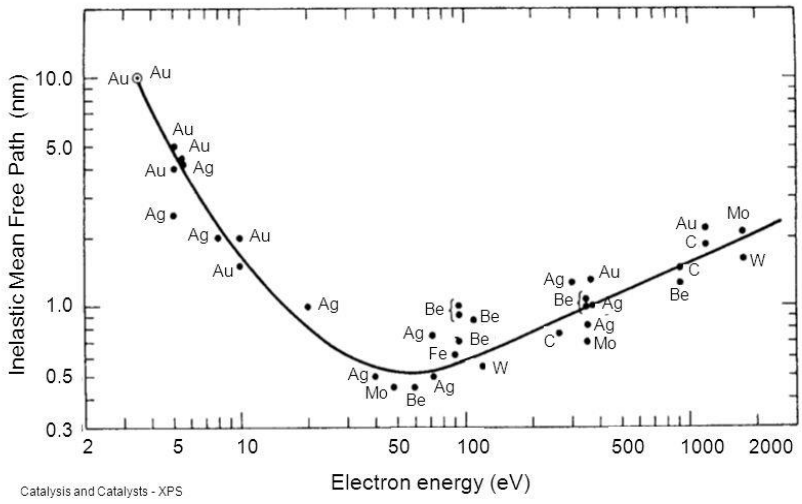

Figure 3. Inelastic mean free path of electrons as a function of kinetic energy.[3]

Concerning the measurements carried out in this work, our XPS chamber is equipped with a focused monochromatic x-ray source Al K_α = 1486.6 eV and is connected in UHV to the MBE reactor, thus allowing to perform *in situ* analysis after the growth preventing possible surface contaminations from the outer atmosphere.

1.3 Photoluminescence spectroscopy

Photoluminescence (PL) spectroscopy is widely used to investigate the optoelectronic properties of semiconductors, and constitutes a non-invasive characterization process via photonic excitation. The mechanism underlying PL is the formation of electron-hole pairs from inter-band transitions caused by photo-excitation with radiations having higher energy than the semiconductor band gap. The carrier separation is followed by electron-hole radiative recombinations originating the PL. Recombinations may involve free carriers, acceptors and/or donors, and free and bounded excitons. Information concerning the material properties can be obtained by observing the energy, intensity and shape of the various emission lines recorded and plot as a function of the energy. Typically, a PL setup includes a light source, a system of focalisation lenses, a support for the sample consisting in a liquid-helium cooled cryostat, a system of collection lenses, a monochromator and a detector (Figure 4). Lasers in the UV or visible range are the most commonly used light sources in PL, since they offer high brightness and monochromaticity.

The INL laboratory is provided with a PL equipment including a laser source with wavelength equal to 532 nm. The sample can be inserted in a cryostat/heater system which permits analysis in a very wide range of temperatures (10-300 K), while a pump keeps the sample in vacuum (10^{-5}-10^{-7} Torr). A different configuration uses a laser source whose wavelength is 515 nm: this can be used to perform time-resolved PL analysis (TRPL), which eventually allows determining the average life time of the carriers.

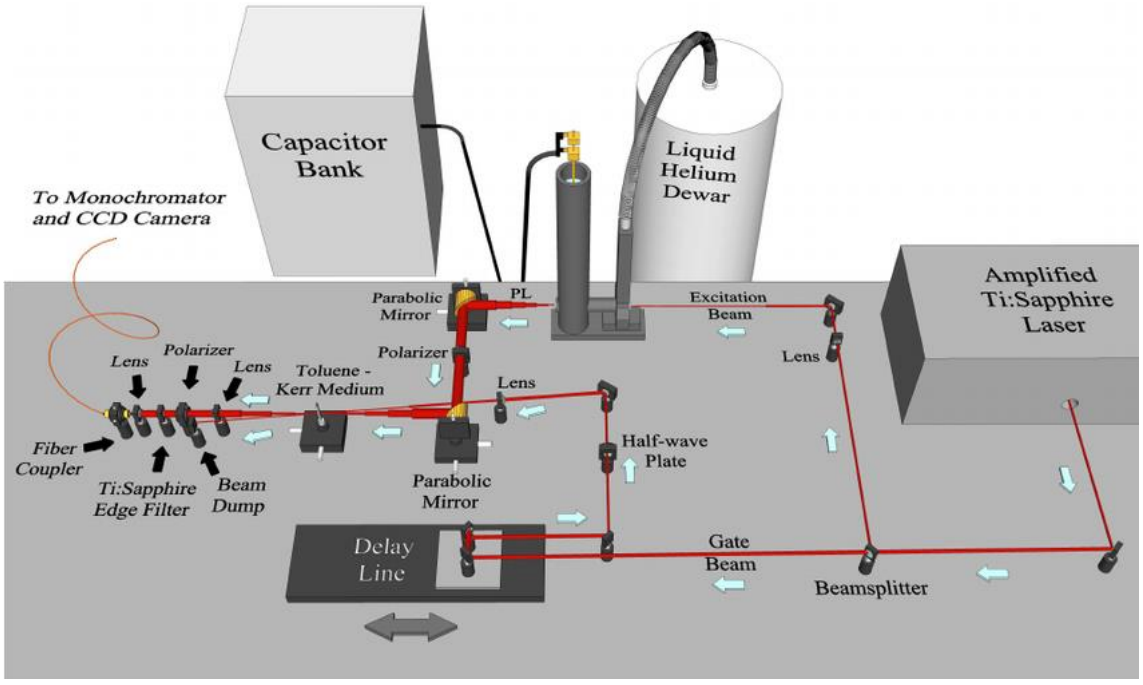

Figure 4. Schematics of a PL setup.[4]

1.4 Electron Beam Induced Current microscopy

Charge Collection Microscopy (CCM) is an ensemble of analytical techniques in which an excitation source is used to scan the surface of an electrically-contacted sample and study the spatial distribution of the electrical properties of semiconductor nanostructures, in a process of current mapping which can detect both electrical inhomogeneities and morphological failures. CCM employs an excitation source to generate a local excess of carriers, which can be collected and measured in presence of an electric field. Generally speaking, excitation sources can be both optical (laser) and electronic beams; in the second case, the technique constitutes the so-called Electron Beam Induced Current (EBIC) microscopy, which offers higher resolution compared to its optical counterpart, especially if coupled with Scanning TEM (STEM) setup.

EBIC microscopy can therefore be defined as a probe-scanning technique for the nanoscale investigation of an internal field. When the electron beam hits the sample, the interaction between the electrons and the matter causes electron scattering within a nanometric volume (the so-called interaction volume), as reported in Figure 5(a); similarly to photons, the electrons into this volume have enough energy to excite electron/hole pairs and, if an internal field is present, this will cause the drift of the excess carriers forming the so-called induced current (Figure 5(b)), which can be eventually extracted into an external circuit and measured.

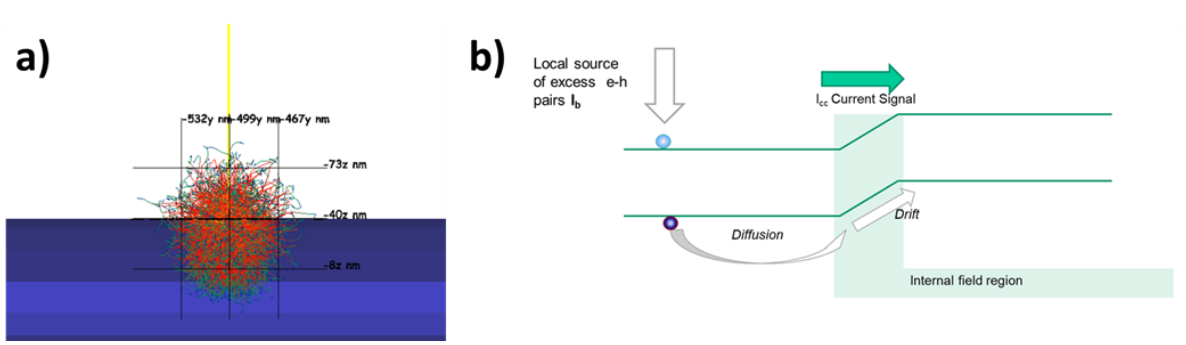

Figure 5. (a) Simulation of electron/matter interaction for an excitation beam accelerated at 2 kV with current equal to 5 µA. (b) Schematics of the induced current generation.[5]

EBIC setups generally consist of an electron source, an electrical contact on the sample to collect the induced current, and a bias/current amplifier, as shown in Figure 6. Since the excitation source should be a scanning beam, most of devices usually employed for EBIC analyses are nothing but an adaptation of scanning electron microscopy (SEM) instruments, provided with the components for current measuring. This approach is extremely convenient, the morphological images of the samples being important to the interpretation of the EBIC map.

The instrument used to perform the analysis reported in this thesis is a Hitachi SU8000 with Gatan control system and Kleindiek PS4 as *in situ* electrical contact.

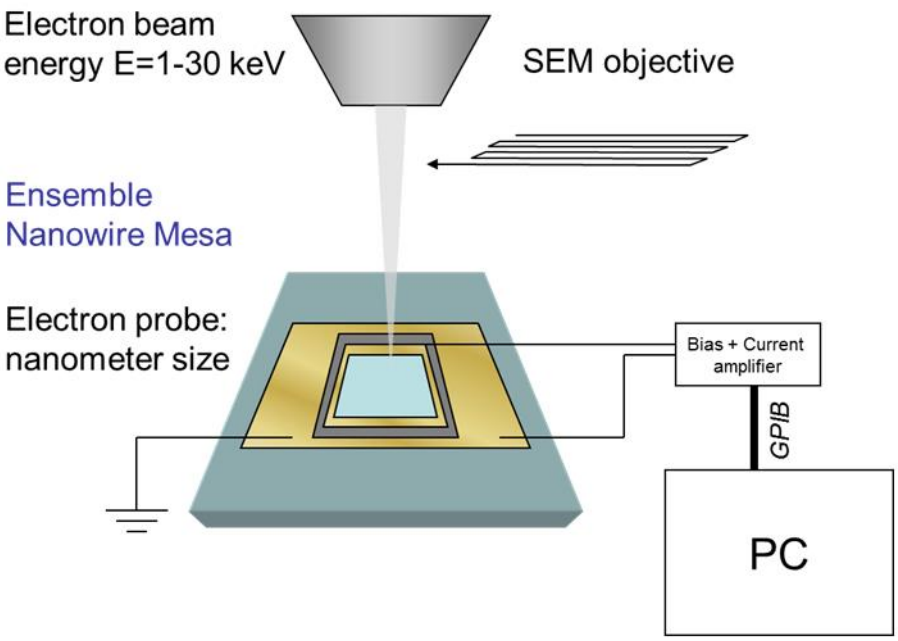

Figure 6. Schematics of an EBIC setup.[5]

EBIC microscopes allow characterizing both single NWs and NW arrays. In the first case, the electrical contacts can be either fabricated by electron beam lithography on dispersed NWs or obtained by direct contact with metal micro- or nano-manipulators, the latter option being generally preferable since it does not require long preparation time and permits the characterization on free-standing structures. In the second case, NW arrays can be encapsulated and electrically contacted with transparent conductive oxides, such as ITO.

Thanks to the capacity of probing the electrical activity at the nanoscale, EBIC can give important insight about core/shell radial junctions. For example, in the case of p-n core-shell NW-based light emitting diodes (LEDs), the EBIC analysis can provide information about the resistivity of the core and the shell by cleaving the structure and exposing its section to the electron beam, thus mapping the electrical activity of the junction. Moreover, this technique allows to visualize the electrical activity along the axial profile of single NWs, to evaluate the electrical homogeneities of arrays and possibly to measure the doping levels as well as the diffusion length and the average life-time of the carriers.[6] These information are very important to perform a proper characterization of NW structures suitable for the fabrication of PV cells, thus making EBIC an important tool of investigation for the purpose of this thesis.

References

(1) ResearchGate https://www.researchgate.net/figure/233-Scheme-of-optics-in-a-basic-TEM_fig15_46278733.

(2) Payne, B. P. X-Ray Photoelectron Spectroscopy Studies on the Oxidation Processes of Nickel, Chromium and Their Alloys, University of Western Ontario, 2011.

(3) SlideServe - X-ray Electron Spectroscopy (XPS) https://www.slideserve.com/gallia/x-ray-electron-spectroscopy-xps.

(4) ResearchGate https://www.researchgate.net/figure/Illustration-of-the-optical-Kerr-gate-setup-for-time-resolved-photoluminescence_fig2_259585779.

(5) Piazza, V.; Vettori, M.; Ahmed, A.; Chauvin, N.; Patriarche, G.; Fave, A.; Gendry, M.; Tchernycheva, M. Nanowire Week 2017, Lund, Poster: Nanoscale Investigation of Radial p-n Junction in Self-Catalyzed GaAs Nanowires Grown on Si (111). 2017.

(6) Piazza, V.; Mancini, L.; Chen, H. L.; Collin, S.; Tchernycheva, M. Nanoscale Analyses Applied to Nanowire Devices. In *Semiconductors and Semimetals*; 2018; Vol. 98, pp 231–319.

ANNEX 2: Numerical simulations of the VLS growth process

in collaboration with A. Danescu

Table of contents

1 Introduction

In order to clarify the experimental evidence of NW growth with different group III sources we propose in the following quantitative estimates of the evolution of the liquid droplet and NW parameters based on simplified models similar to those already proposed in [1].

We implement and discuss predictions of two growth models :

- Model 1 : a simplified version taking into account the amount of material feeding the liquid droplet under the assumption of constant NW radius and
- Model 2 : a more complex version that account for variable NW radius.

The physics of VLS nanowire growth can be summarized as follows : external fixed fluxes of group III and group V atoms feed the liquid droplet through the so-called “direct flues” for which the amount of matter is proportional to the area of the projected surface of the droplet on the normal plane to the flux direction. It is commonly accepted that no other sources (diffusion, etc.) of group V adatoms are involved in the growth process at the growth temperature. Moreover, at growth conditions the group III adatoms attachment is very close to 1 so that diffusion on the substrate and diffusion along the NW facets should be also accounted for. Incorporation in the droplet of different quantities of group III and V adatoms leads to an evolution of its concentration. When

the group V saturation threshold in the droplet exceeds a given value, a solid III-V mono-layer crystallizes at the LS interface. As this mono-layer needs the same amount of group III and group V atoms the concentration is the droplet drops at a level lower that the saturation limit. Amount of material not concerned by the solidification process but incorporated in the liquid droplet modifies the droplet volume so that for simplicity in Model I we shall assume that: (a) the NW radius is fixed, (b) the droplet is pinned at the triple point and (c) the geometry of the triple line has rotational symmetry. Under this assumptions crystallization process modifies the droplet volume and wetting angle at the triple point during growth.

This brief qualitative description can be formalized as a system of nonlinear ordinary differential equations (ODE) relating the amount of group V and III adatoms, diffusion lengths, droplet radius, droplet concentration and NW length accompanied by a set of inequalities involving the droplet saturation condition and admissible weeding angles. To investigate quantitative and qualitative features of this system of ODE one will use time-discretization and numerical approximation algorithms. To simplify the presentation we shall describe further the discrete algorithm, involving the modifications of various parameters of the process in an infinitesimal time interval $(t, t+\Delta t)$.

We start with Model 1 and discuss its qualitative features, the identification procedure of the model parameters and its quantitative predictions. Guided by the experimental evidence we extend it to Model 2 that takes into account time-dependent NW radius and wetting angle lower and upper bounds allowing for the predition of ZB and/or WZ GaAs structure.

2 Model with fixed NW radius (Model 1)

2.1 Preliminaries

Area exposed to the direct flux Let α_{Ga} and α_{As} denote the angles formed by sources of group V and III elements respectively with the normal to the substrate plane and let r denote the NW radius. At fixed droplet radius R and wetting angle β, the orientation of adatom sources (III or V) determine the droplet area which is exposed to the direct flux, a result given in [2]. The explicit formula is :

$$S(\alpha,\beta,r) = R^2 \cdot \begin{cases} \pi \quad \text{if } R(\beta) \geqslant r/\cos\alpha \quad \text{and} \quad \beta \geqslant \pi/2, \\ \left(\dfrac{\pi}{2} - \arcsin\left(\dfrac{\cos\beta}{\sin\alpha}\right) - \cos\beta\sqrt{\sin^2\beta - \cos^2\alpha} + \cos\alpha\sin^2\beta \arcsin\dfrac{\sqrt{\sin^2\beta-\cos^2\alpha}}{\sin\alpha\sin\beta}\right) \\ \qquad\qquad \text{if } R(\beta) < r/\cos\alpha \quad \text{and} \quad \beta \geqslant \pi/2, \\ \pi\sin^2\beta \quad \text{if } R(\beta) \geqslant r/\sin\alpha \quad \text{and} \quad \beta < \pi/2, \\ \left(\cos\alpha\sin^2\beta\left(\dfrac{\pi}{2} + \arcsin\left(\dfrac{\tan\beta}{\tan\alpha}\right)\right) - \cos\beta\sqrt{\sin^2\beta-\cos^2\alpha} + \arcsin\dfrac{\sqrt{\sin^2\beta-\cos^2\alpha}}{\sin\alpha}\right) \\ \qquad\qquad \text{if } R(\beta) < r/\sin\alpha \quad \text{and} \quad \beta < \pi/2. \end{cases} \tag{1}$$

and the graph of the function $S(\alpha, \beta, 30)$ is illustrated below.

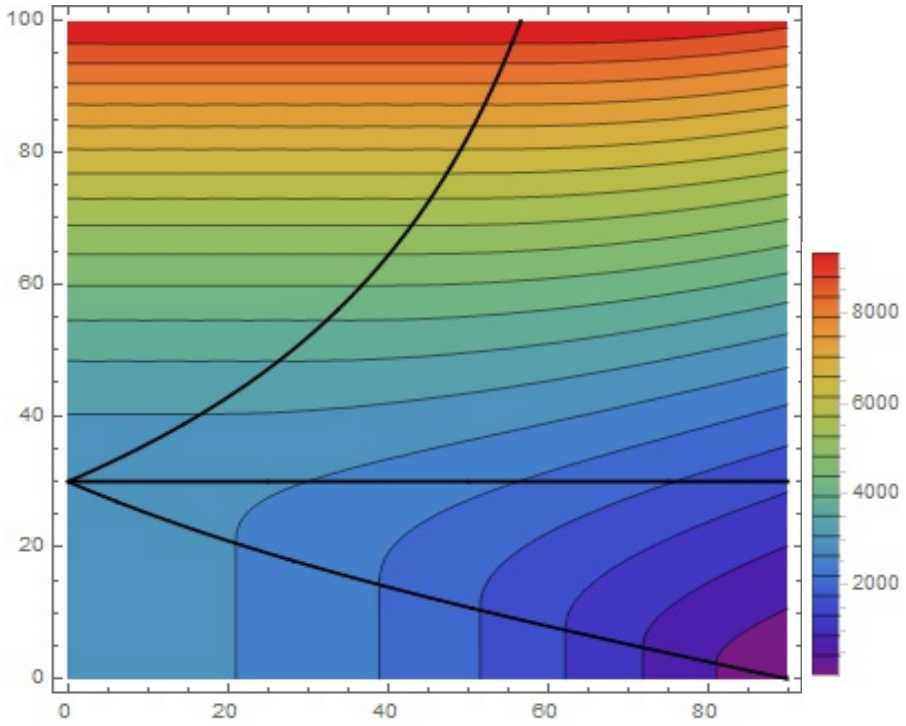

Figure 1. Capture surface as a function of source position (horizontal coordinate) and droplet heigth (vertical coordinate) for $r = 30$ nm. In black the curves representing the boundaries of various cases in (1).

The three section of interest in this graph are the vertical sections at $\alpha = 9.32°$, $\alpha = 27.89°$ and $\alpha = 40.99°$. These three section are prsented below :

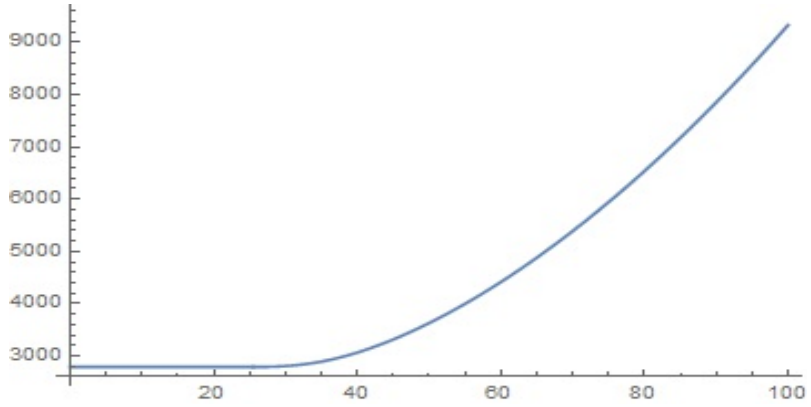

Figure 2. Surface of capture $S(9.32, h, 30)$ as a function of the droplet height.

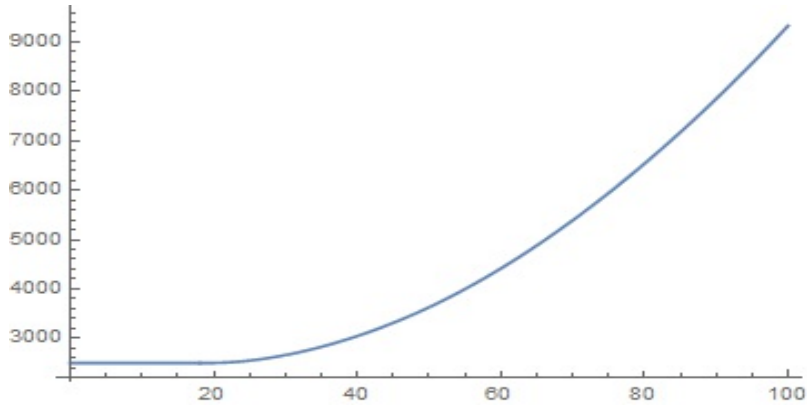

Figure 3. Surface of capture $S(27.89, h, 30)$ as a function of the droplet height.

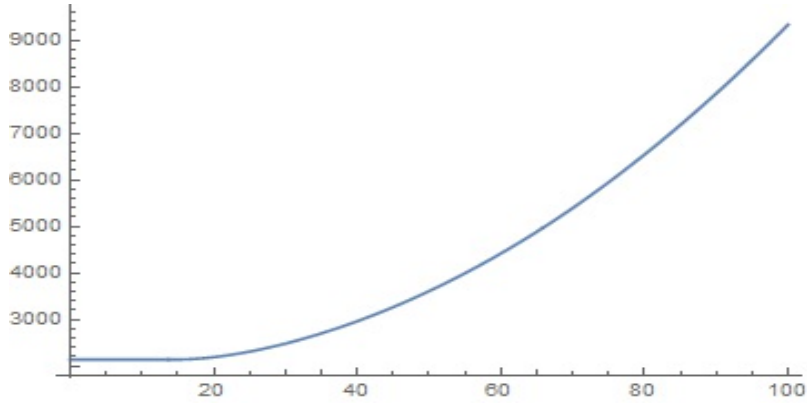

Figure 4. Surface of capture $S(40.99, h, 30)$ as a function of the droplet height.

Ga and As fluxes The group III adatoms flux, further denoted q_{Ga}, is fixed at a value that provides a layer-by-layer vertical growth velocity of 0.5 ML/min which, by assuming full attachement, correspond to a "vertical" flux

$$q_{\mathrm{Ga}} = 3.1325\,(\mathrm{adatoms}\cdot s^{-1}\cdot \mathrm{nm}^{-2}), \tag{2}$$

The value corresponding to the flux for the element V adatoms can be computed using and gives for the vertical flux

$$q_{\mathrm{As}} = 15.1789\,(\mathrm{adatoms}\cdot s^{-1}\cdot \mathrm{nm}^{-2}). \tag{3}$$

Droplet saturation condition and amont of species in the droplet If V denotes the droplet volume and c denotes the As concentration in the droplet, defined as $c = N_{\mathrm{As}}/(N_{\mathrm{As}} + N_{\mathrm{Ga}})$, then the amount of As adatons and Ga adatoms can be computed straightforward by using molar mass and mass density for each species and the Avogadro number (N_A). Indeed, we have successively

$$V = V_{\mathrm{As}} + V_{\mathrm{Ga}} = \frac{m_{\mathrm{As}}}{\rho_{\mathrm{As}}} + \frac{m_{\mathrm{Ga}}}{\rho_{\mathrm{Ga}}} = \frac{M_{\mathrm{As}} N_{\mathrm{As}}}{N_A\,\rho_{\mathrm{As}}} + \frac{M_{\mathrm{Ga}} N_{\mathrm{Ga}}}{N_A\,\rho_{\mathrm{Ga}}} = N_{\mathrm{As}}\left(\frac{M_{\mathrm{As}}}{N_A\,\rho_{\mathrm{As}}} + \frac{M_{\mathrm{Ga}}}{N_A\,\rho_{\mathrm{Ga}}}\left(\frac{1}{c} - 1\right)\right)$$

which gives

$$N_{\mathrm{As}} = V\left(\frac{M_{\mathrm{As}}}{N_A\,\rho_{\mathrm{As}}} + \frac{M_{\mathrm{Ga}}}{N_A\,\rho_{\mathrm{Ga}}}\left(\frac{1}{c} - 1\right)\right)^{-1}, \qquad N_{\mathrm{Ga}} = N_{\mathrm{As}}\left(\frac{1}{c} - 1\right). \tag{4}$$

2.2 Computation procedure

Let us assume that at time t : the droplet volume $V(t)$, the droplet radius $R(t)$, the wetting angle $\beta(t)$, the droplet concentration $c(t)$ and the nanowire length $L(t)$ are known.

1. **Compute the of adatoms feeding the droplet**:

   In a small time interval Δt there are three contributions for the quantity of Ga that feeds the droplet :

   a) **diffusion on the substrate** ; if λ_S denotes the diffusion length of the Ga atoms on the SiO_2 substrate the amount of Ga able to feed the droplet is, per unit time

   $$Q_S = \pi((r+\lambda_S)^2 - r^2)\, q_{\mathrm{Ga}} \tag{5}$$

   This contribution exists as long as the length of the NW is lower than the diffusion length λ_{NW}, since otherwise adatoms from the substrate cannot reach the triple point.

   b) **diffusion on the NW walls**: this contribution is proportional to the "exposed area of the NW surface, which is simply

   $$Q_{\mathrm{NW}} = 2r \min(\lambda_{\mathrm{NW}}, L)\, q_{\mathrm{Ga}} \tan\alpha_{\mathrm{Ga}} \tag{6}$$

   per unit time, where the minimum function accounts for situations when $L < \lambda_{\mathrm{NW}}$.

   c) **direct incorporation in the droplet**: this quantity can be computed using formula (1) and gives, per unit time :

   $$Q_D = S(\alpha_{\mathrm{Ga}}, \beta, r(t), R(t)) \frac{q_{\mathrm{Ga}}}{\cos\alpha_{\mathrm{Ga}}}. \tag{7}$$

   Thus the total amount of Ga adatoms feeding the droplet in an interval Δt is

   $$Q_{\mathrm{Ga}} = (Q_S + Q_{\mathrm{NW}} + Q_D)\, \Delta t. \tag{8}$$

   In a similar way the amount of As adatoms is straightforward given by

   $$Q_{\mathrm{As}} = S(\alpha_{\mathrm{As}}, \beta, r(t), R(t)) q_{\mathrm{As}} \Delta t. \tag{9}$$

2. **Compute the droplet concentration and amount of adatoms available for the solidification** :

   In the time-interval $(t, t+\Delta t)$ the amount of Ga and As in the droplet increase from N_{As} and N_{Ga} given by relation (4) to

   $$N_{\mathrm{As}}(t+\Delta t) = N_{\mathrm{As}}(t) + Q_{\mathrm{As}} \qquad N_{\mathrm{Ga}}(t+\Delta t) = N_{\mathrm{Ga}}(t) + Q_{\mathrm{Ga}} \tag{10}$$

so that the concentration becomes

$$c(t+\Delta t) = \frac{N_{\mathrm{As}}(t+\Delta t)}{N_{\mathrm{Ga}}(t+\Delta t) + N_{\mathrm{As}}(t+\Delta t)}. \tag{11}$$

If $c(t+\Delta t)$ exceeds the saturation threshold then : (i) a certain amount of Ga and As adatoms will form the solid phase at the interface between the NW and the droplet and (ii) the droplet concentration remain at the saturation threshold. To compute the amount of material that contributes to solidification we look for **the same amount of both species**, further denoted Q such that

$$\frac{N_{\mathrm{As}}(t+\Delta t) - Q}{N_{\mathrm{Ga}}(t+\Delta t) + N_{\mathrm{As}}(t+\Delta t) - 2Q} = c^\star \quad \text{and} \quad \frac{N_{\mathrm{As}}(t+\Delta t)}{N_{\mathrm{Ga}}(t+\Delta t) + N_{\mathrm{As}}(t+\Delta t)} = c(t+\Delta t) \tag{12}$$

which gives

$$Q = N_{\mathrm{As}}(t+\Delta t)\frac{c(t+\Delta t) - c^\star}{c(t+\Delta t)(1-2c^\star)}. \tag{13}$$

3. **Update the NW length**:

   Assuming a constant NW radius, the amount of Q adatoms of Ga and Q adatoms of As will form a GaAs crystal (whose lattice parametr is known) over a surface of area πr^2. Thus the NW length will increase by an amount of

$$L(t+\Delta t) = L(t) + Q\,\frac{a^3_{\mathrm{GaAs}}}{4\pi r^2}. \tag{14}$$

   Obviously, the seond term above is not always an integer multiple of the lattice parameter, but this is essentially an artefact due to time discretization scheme, so that it has no particular incidence on the final result of the simulation.

4. **Update the droplet radius and wetting angle**:

   Solidification of a certain amount of Ga and As, imposed by the concentration threshold, modifies at $(t+\Delta t)$ the amouint of Ga and As adatoms in the liquid droplet. After solidifcation the droplet contains $N_{\mathrm{As}}(t+\Delta t) - Q$ adatoms of As and $N_{\mathrm{Ga}}(t+\Delta t) - Q$ adatoms of Ga. The corresponding total volume of the droplet can be computed using relations (4.1) with $c^\star$ instead of c and $N_{\mathrm{As}}(t+\Delta t)$ in the left-hand side, i.e.

$$V(t+\Delta t) = N_{\mathrm{As}}(t+\Delta t)\left(\frac{M_{\mathrm{As}}}{N_A\,\rho_{\mathrm{As}}} + \frac{M_{\mathrm{Ga}}}{N_A\,\rho_{\mathrm{Ga}}}\left(\frac{1}{c^\star} - 1\right)\right). \tag{15}$$

   Since the NW radius is fixed, the volume $V(t+\Delta t)$ determine the droplet radius $R(t+\Delta t)$ by using the inverse function of the two-branch relation $V(R)$ given by

$$V(R)\begin{cases} V_{\mathrm{inf}}(R) = \dfrac{\pi}{3}\big(R - \sqrt{R^2-r^2}\big)^2\big(2R + \sqrt{R^2-r^2}\big) & \text{if } \beta > \pi/2 \\ V_{\mathrm{sup}}(R) = \dfrac{\pi}{3}\big(R + \sqrt{R^2-r^2}\big)^2\big(2R - \sqrt{R^2-r^2}\big) & \text{if } \beta \leqslant \pi/2. \end{cases} \tag{16}$$

Then the wetting angle can be updated by using elementry geometry once since the droplet radius is known. We obtain :

$$\begin{aligned} \beta(t+\Delta t) &= \frac{\pi}{2} + \arccos(r/R) \text{ if } V(t+\Delta t) > \frac{2\pi r^3}{3}, \\ \beta(t+\Delta t) &= \arcsin(r/R) \text{ if } V(t+\Delta t) \leqslant \frac{2\pi r^3}{3}. \end{aligned} \tag{17}$$

At the end of these update steps we have compute $R(t+\Delta t), L(t+\Delta t), \beta(t+\Delta t)$ and $V(t+\Delta t)$ so we can proceed to the next time-step itteration.

2.3 Initial conditions

In our simulations the positions of Ga and As sources with respect to the normal to the substrate surface were computed from the geometry of the MBE reactor. We have considered

$$\alpha_{\mathrm{Ga5}} = 27.89^\circ, \quad \alpha_{\mathrm{Ga7}} = 9.32^\circ, \quad \alpha_{\mathrm{As}} = 40.99^\circ. \tag{18}$$

The value of the critical concentration threshold was taken from the litterature at $c = 0.026$. The diffusion length for Ga adatoms on SiO_2 is fixed to $\lambda_S = 100\,\mathrm{nm}$ while the diffusion length of Ga atoms on GaAs is reported in the litterature in the range $(1\,\mu m,\ 1.5\,\mu m)$. Typical simulation started with a half-sphere volume of the droplet, i.e. $R(0) = r = 30\,\mathrm{nm}$ and $V(0) = \frac{2\pi r^3}{3}\,\mathrm{nm}^3 = 56540$ nm^2 which gives obviously $\beta(0) = \pi/2$. The saturation condition is fixed at a concentration thresohld $c(0) = c^\star$ and initial length of the NW was fixed at $L(0) = 0$.

2.4 Remarks

Not explicitly stated above there are several assumption concerning the limitations of the model.

a) One of them concerns the NW density : at average dnesity lower the $\simeq 2\lambda_S$ the model can be applied. Avove this limit there is a certain amount of Ga which has to be shared between several droplets, so that the initial contribution of the substrate diffusion decrease. As we shall show in the following this has some impact only on the transitory regime (explained below). The NW density has also some impact on the adatoms arriving at the triple point via the NW facets, due to a shadowing effect.

b) From a technical point of view an additional test should stop the computation if the droplet becomes to small or to large.

c) For technical reasons, the description using $V(R)$, which is a function containing two branches is not the best choice, and is handled with some additional computational cost. The best choice is to use the one-to-one correspondance between the droplet height and its volume. Once the height of the droplet is known the radius can be uniquely determined from simple geometric arguments. Using this description we have

$$R = \frac{r^2 + h^2}{2h}, \qquad \beta = \frac{\pi}{2} + \arcsin\left(\frac{h^2 - r^2}{h^2 + r^2}\right). \tag{19}$$

d) Desorbtion along the substrate and along the facets of the NW is not explicitly considered here but can be incorporated easily. In the above model this is equivalent of changing the diffusion lengths λ_S and λ_{NW}.

3 Numerical results

A typical result obtained with : the initial data given in subsection 2.3, a time step of $\Delta t = 0.5\,s$ over a time interval of $T = 50\,\text{min}$ is represented in Fig. 5.

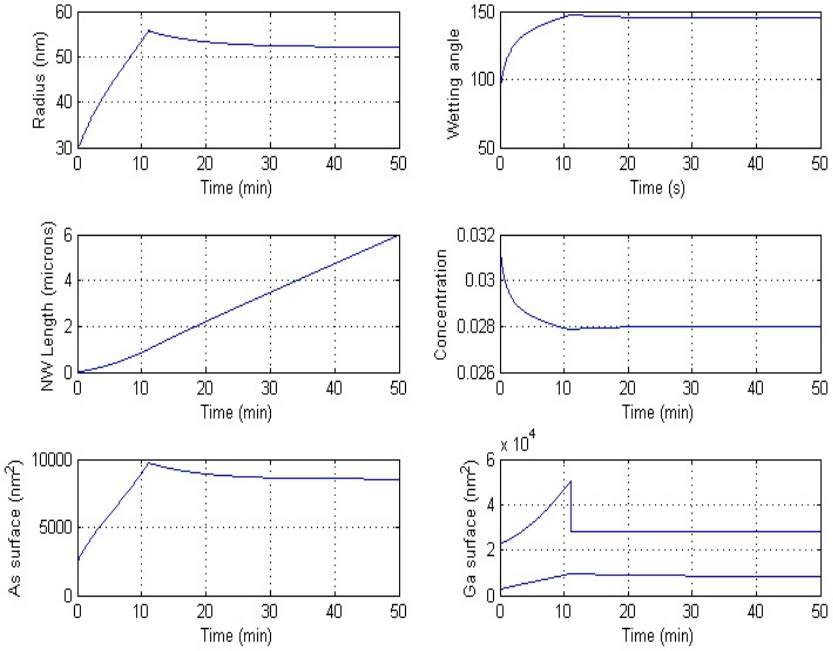

Figure 5. Typical evolution of various parameters (R, β, L, c) as well the capture surfaces for Ga and As during the NW growth. The value of the concentration is $c(t+\Delta t)$ before crystallization of the solid phase (thus always $c > c^\star$). The two curves on the Ga surface graph are proportional to tha amount of Ga adatons entering the droplet via diffusion (upper curve) and direct flux (lower curve).

It is interesting to notice the following behavior : we recognize a transient growth regime up to $t = 40'$ which becomes asymptotic stationnary. As expected at $t \simeq 11\,\text{min.}$, when the NW length equals $L = 1\,\mu m$ (which is exactly the input value for λ_{NW}) the adatoms arriving at the triple point via diffusion on the substrate are lost. This can be recognized as a discontinuity in the amount of Ga adatoms and leads to a decrease of the droplet size and consequently, a reduction of the amount of As adatoms by direct flux. After this point the system evolves toward a stationnary evolution (result predicted also by simple models of Dubrovskii [3]: this regime is characrerized by a constant longitudinal velocity obtained as an exact balance between the quantities of As and Ga adatoms. As can be noticed below this regime is (almost) independent on the initial conditions and depends only on the flux ratio between the group V and III elements as weel as the positions α_{Ga} and α_{As} of Ga and As sources respectively.

Indeed, stationnary growth condition can be obtained from the equality between the amount of Ga and As adatoms. In above notation the grotwh is stationnary iff

$$\frac{2r\lambda_{\text{NW}} \sin\alpha_{\text{Ga}} + S(\alpha_{\text{Ga}}, \beta, r(t))}{S(\alpha_{\text{As}}, \beta, r(t))} = \cos\alpha_{\text{Ga}} \frac{q_{\text{As}}}{q_{\text{Ga}}} \tag{20}$$

which represents the "balance" of Ga and As adatoms. This formula provides important informations about the stationnary regime and guide the identification strategy.

3.1 Identification strategy

From the experimental data the longitudinal growth velocity can be measured so that, the amount of As adatoms needed can be easily computed. As at fixed NW radius r and As source position α_{As} the surface of the droplet exposed to the As flux is known, the above condition select a unique asymptotic droplet radius R and wetting angle β.

Using the Ga5 experimental data we find a longitudinal growth velocity

$$v = 1.9066\,\mathrm{nm/sec}.$$

which represents V = 5390 nm^3/sec or equivalent an amount of As adatoms given by 119350 atoms/sec. This gives a projected surface of $\frac{119350}{15.1789} = 7862\ \mathrm{nm}^2$ which, by using the result in Fig. 3, gives in the stationnary regime :

$$h = 90\,\mathrm{nm}, \quad R = 50\,\mathrm{nm}, \quad \beta = 143^\circ$$

in agreement with the numerical results in Fig. 5. From relation (20) we can compute the diffusion length on the NW facets which gives exactly this stationnary regime, and we obtain

$$L_{\mathrm{NF}} = \frac{4.2786 \cdot S(90, 41^\circ) - S(90, 27^\circ)}{2r \sin(27^\circ)} = 918\,\mathrm{nm}$$

which is close to values reported by Schroth *et al.* [4]. With this diffusion length the longitudinal velocity for Ga5 is exact. The result of the simulation is presented in Fig. 6.

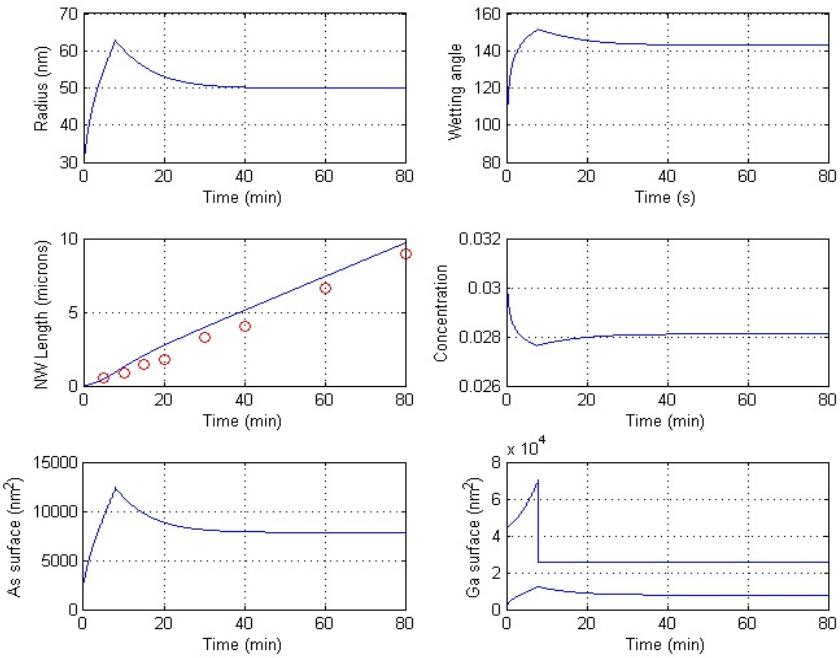

Figure 6. Simulation results (continuous blue curve) obtained with a diffusion length $\lambda_{\mathrm{NW}} = 918\,\mathrm{nm}$ and $\lambda_S = 100$ nm for $\Delta t = 0.5$ sec and 9600 time steps. The longitudinal velocity, the asymptotic weeting angle and droplet radius are correct but the starting point in the stationnary regime is to high.

To improve the previous simulation one has to decrease the diffusion length λ_S which in consequence, decrease the NW length at the beginning of the stationnary regime. The results obtained with $\lambda_S = 65\text{nm}$ are illustrated below in Fig. 7.

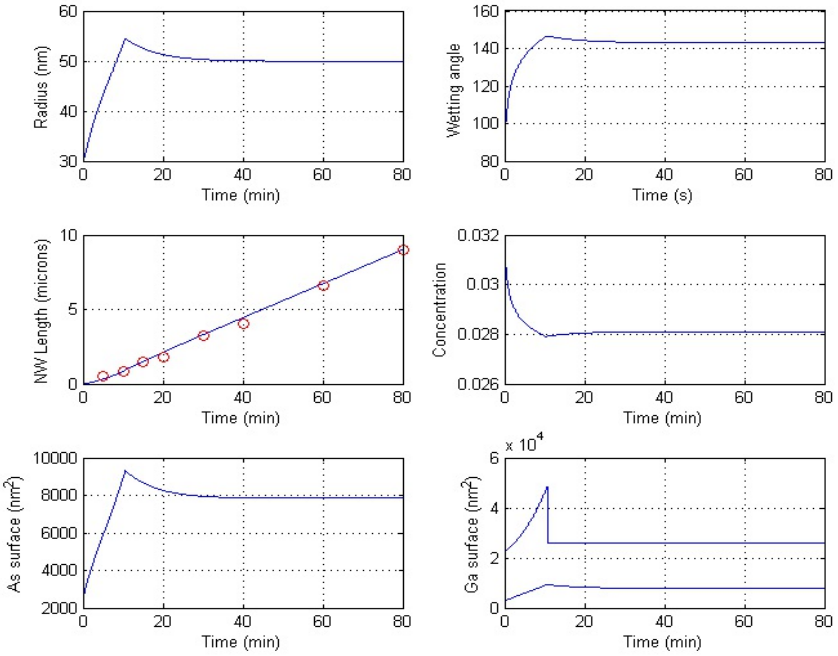

Figure 7. With $\lambda_S = 65$ nm the experimental data (red circles) for Ga5 source are fitted by the simulation results (blue continuous curves).

One can show that low diffusion length λ_S leads to a decrease of the simulation results keeping the longitudinal velocity constant. The effect of the initial volume on the simulation results should be further investigated.

3.2 Application to Ga7 source

Using the best values obtained from stationnary data one can simulate the NW evolution using the Ga7 source. The result is illustrated in Fig. 8. Changing the source we still notice a transitory regime followed by a stationnary evolution of the NW length. While the transitory regime is well reproduced the constant velocity growth in the stationnary regime predicted by the simulation is to low.

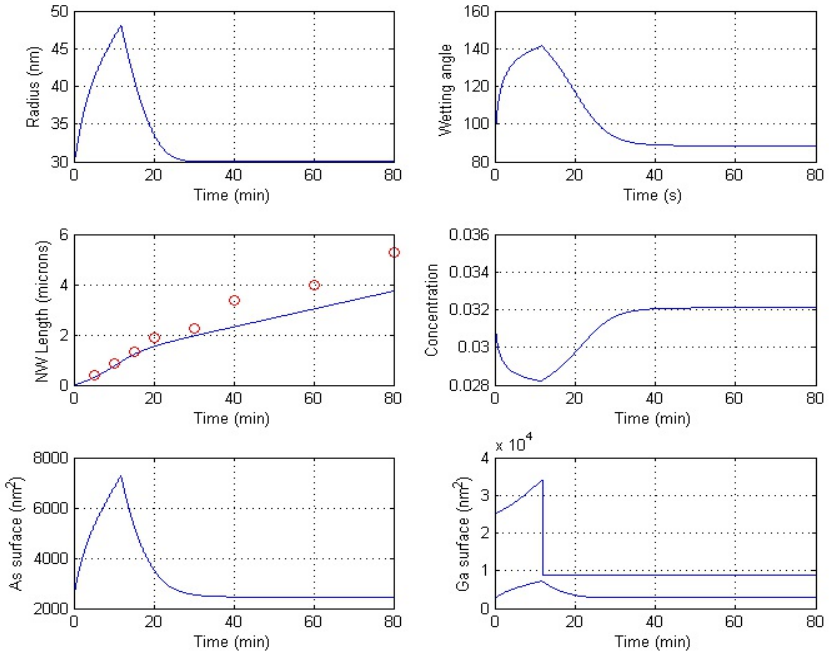

Figure 8. Simlation results obtained by using $\lambda_S = 65$ nm and $\lambda_{\mathrm{NW}} = 918$ nm (continuous blue line) and experimental data (red circles).

References :

1. Tchernycheva, M.; Travers, L.; Patriarche, G.; Glas, F.; Harmand, J. C.; Cirlin, G. E.; Dubrovskii, V. G. Au-Assisted Molecular Beam Epitaxy of InAs Nanowires: Growth and Theoretical Analysis. *J. Appl. Phys.* **2007**, 102 (9), 094313.

2. Glas, F. Vapor Fluxes on the Apical Droplet during Nanowire Growth by Molecular Beam Epitaxy. *Phys. Status Solidi Basic Res.* **2010**, 247 (2), 254–258.

3. Dubrovskii, V. G.; Xu, T.; Álvarez, A. D.; Plissard, S. R.; Caroff, P.; Glas, F.; Grandidier, B. Self-Equilibration of the Diameter of Ga-Catalyzed GaAs Nanowires. *Nano Lett.* **2015**, 15 (8), 5580–5584.

4. Schroth, P.; Jakob, J.; Feigl, L.; Mostafavi Kashani, S. M.; Vogel, J.; Strempfer, J.; Keller, T. F.; Pietsch, U.; Baumbach, T. Radial Growth of Self-Catalyzed GaAs Nanowires and the Evolution of the Liquid Ga-Droplet Studied by Time-Resolved in Situ X-Ray Diffraction. *Nano Lett.* **2018**, 18 (1), 101–108.

Abstract

The objective of this thesis is to achieve monolithical integration of $Al_{0.2}Ga_{0.8}As$-based nanowires (NWs) on Si substrates by molecular beam epitaxy via the self-assisted vapour-liquid-solid (VLS) method and develop a NWs-based tandem solar cell (TSC).

In order to fulfil this purpose, we firstly focused our attention on the growth of GaAs NWs this being a key-step for the development of p-GaAs/p.i.n-$Al_{0.2}Ga_{0.8}As$ core/shell NWs, which are expected to constitute the top cell of the TSC. We have shown, in particular, the influence of the incidence angle of the Ga flux on the GaAs NW growth kinetic. A theoretical model and numerical simulations were performed to explain these experimental results.

Subsequently, we employed the skills acquired to grow p-GaAs/p.i.n-$Al_{0.2}Ga_{0.8}As$ core/shell NWs on epi-ready Si substrates. EBIC characterizations performed on these NWs have shown that they are potential building blocks for a photovoltaic cell. We then committed to growing them on patterned Si substrates so as to obtain regular arrays of NWs. We have developed a protocol, based on a thermal pre-treatment, which allows obtaining high vertical yields of such NWs (80-90 %) on patterned Si substrates (on a surface of 0.9 x 0.9 mm^2).

Finally, we dedicated part of our work to define the optimal fabrication process for the TSC, focusing our attention to the development of the TSC tunnel junction, the NW encapsulation and the top contacting of the NWs.

KEY WORDS: AlGaAs-based nanowires, core/shell structures, radial junction, EBIC, ordered arrays, self- catalysed, heterogeneous integration, photovoltaics, tandem solar cell

Résumé

L'objectif de cette thèse est de réaliser l'intégration monolithique de nanofils (NFs) à base de l'alliage $Al_{0.2}Ga_{0.8}As$ sur des substrats de Si par épitaxie par jets moléculaires via la méthode vapeur-liquide-solide (VLS) auto-assistée et de développer une cellule solaire tandem (TSC) à base de ces NFs.

Pour atteindre cet objectif, nous avons tout d'abord étudié la croissance de NFs GaAs, étape clé pour le développement des NFs p-GaAs/p.i.n-$Al_{0.2}Ga_{0.8}As$ coeur/coquille, qui devraient constituer la cellule supérieure de la TSC. Nous avons montré, en particulier, l'influence de l'angle d'incidence du flux de Ga sur la cinétique de croissance des NFs GaAs. Un modèle théorique et des simulations numériques ont été réalisées pour expliquer ces résultats expérimentaux.

Nous avons ensuite utilisé le savoir-faire acquis pour faire croître des NFs p-GaAs/p.i.n-$Al_{0,2}Ga_{0,8}As$ coeur/coquille sur des substrats de Si prêts pour l'emploi. Les caractérisations EBIC réalisées sur ces NFs ont montré qu'ils sont des candidats potentiels pour la réalisation d'une cellule photovoltaïque. Nous avons ensuite fait croître ces NFs sur des substrats de Si patternés afin d'obtenir des réseaux réguliers de ces NFs. Nous avons développé un protocole, basé sur un pré-traitement thermique, qui permet d'obtenir des rendements élevés de NFs verticaux (80-90 %) sur une surface patternée de 0,9 x 0,9 mm^2.

Enfin, nous avons consacré une partie de notre travail à définir le procédé de fabrication optimal pour la TSC, en concentrant notre attention sur le développement de la jonction tunnel de la TSC, l'encapsulation des NFs et le contact électrique supérieur du réseau de NFs.

MOT-CLEFS : Nanofils à base d'AlGaAs, structures coeur/coquille, jonction radiale, EBIC, réseaux ordonnés, intégration hétérogène, photovoltaïque, cellule solaire en tandem.